ACTA TECHNICA

ACADEMIAE SCIENTIARUM HUNGARICAE

EDITOR-IN-CHIEF: P. MICHELBERGER

VOLUME 105
NUMBERS 1–2

ENERGY ENGINEERING — E/4

AKADÉMIAI KIADÓ, BUDAPEST 1993

ACTA TECHN. HUNG.

ACTA TECHNICA

A JOURNAL OF THE HUNGARIAN ACADEMY OF SCIENCES

Acta Technica publishes original papers, preliminary reports and reviews in English, which contribute to the advancement of engineering sciences.

Acta Technica is published by

AKADÉMIAI KIADÓ
Publishing House of the Hungarian Academy of Sciences
H-1117 Budapest, Prielle K. u. 19—35

Subscription information

Orders should be addressed to

AKADÉMIAI KIADÓ
H-1519 Budapest, P.O. Box 245

Subscription price for Volume 105 (1993) in 4 issues US$ 80.00, including normal postage, airmail delivery US$ 20.00.

Acta Technica is abstracted/indexed in Applied Mechanics Reviews, Current Contents–Engineering, Technology and Applied Sciences, GeoRef Information System, Science Abstracts.

CONTENTS

Acta Technica Acad.Sci.Hung., 105(1-2), pp. 3-17 (1993)

ON-LOAD MECHANICAL CLEANING OF HEAT EXCHANGERS BY MEANS OF BRUSHES

FODOR, L.[1] - GŐSI, P.[2] - KOSTKA, P.[3] - TÓTH, J.[4]

(Received: 3 January 1991)

Described here is a continuous brush-type heat-exchanger cleaning system developed and used for the condenser of a 4.5 MW steam turbine of TVM, a chemical plant. A measurement system has been provided not only for the unit equipped with the cleaning system but also for another unit of identical construction but operated without on-load cleaning of the condenser so that, by comparison, the economic efficiency of on-load cleaning can be determined.

NOTATIONS

D_I	pipe ID
D_O	pipe OD
D_E	equivalent pipe diameter $D_E = (D_O - D_I)/\ln(D_O/D_I)$
δ	pipe wall thickness
λ	coefficient of thermal conductivity of pipe
α_W	internal heat transfer coefficient (water-side)
α_S	external heat transfer coefficient (steam-side)
$\sum R_F$	thermal resistance due to fouling
k	overall heat transfer coefficient
t	inlet water temperature
t_c	condensing temperature
Δt_{ln}	logarithmic mean temperature difference
Δ	condenser end-temperature difference

[1]Fodor, László, H-2074 Perbál, Lakótelep C/7, Hungary

[2]Gősi, Péter, H-1025 Budapest, Felsőzöldmáli út 5/b, Hungary

[3]Kostka, Pál, H-1031 Budapest, Csónakház u. 8, Hungary

[4]Tóth, János, H-5000 Szolnok, Meder u. 20, Hungary

Akadémiai Kiadó, Budapest

v water velocity

s steam load, steam mass flow

τ time

Subscripts:

C clean condition

F fouled condition

M value based on measurement

CA calculated value

o condition in case of parameters t_o, v_o, s_o

1 condition in case of parameters t_1, v_1, s_1

X condition in case of parameters t_x, v_x, s_x

Introduction

Damages due to fouling of the surfaces exposed to the coolant are significant in case of water-cooled heat exchangers. E.g. in case of steam turbine condensers of this type, the overall heat transfer coefficient decreases, a loss of vacuum takes place and as a result, the effective turbine output decreases with the steam consumption remaining unchanged. To reduce damages and to avoid breakdowns, it is necessary that the heat-exchange surfaces be cleaned during operation.

Use of the conventional cleaning methods necessitates that the heat exchanger to be cleaned be put out of service. In this case, the loss in electricity generation is often considerable. Chemical cleaning e.g. by continuous feed of chemicals to the coolant results in damages to the environment and the costs of chemicals are not negligible either. Because of these disadvantages, equipment for mechanical cleaning of heat exchangers during operation are being used increasingly. From among equipment of this type, ball-type and brush-type systems are most widely used.

The advantage of continuous cleaning over periodical cleaning is illustrated in Fig. 1. In case of continuous cleaning, the overall heat transfer coefficient remains practically constant while in case of periodical cleaning, the initial value of the overall heat transfer coefficient can never be restored again (Fig. 1).

Ball-type cleaning systems use balls made of elastic material, the size of which is adjusted to the inner diameter of the heat-exchange pipes. The balls are introduced with the cooling water and pressed through

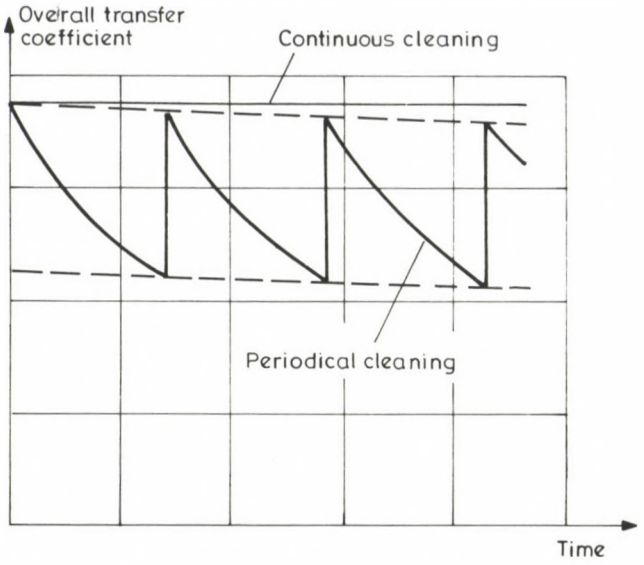

Fig. 1. Values of overall heat transfer coefficient in case of continuous and periodical cleaning

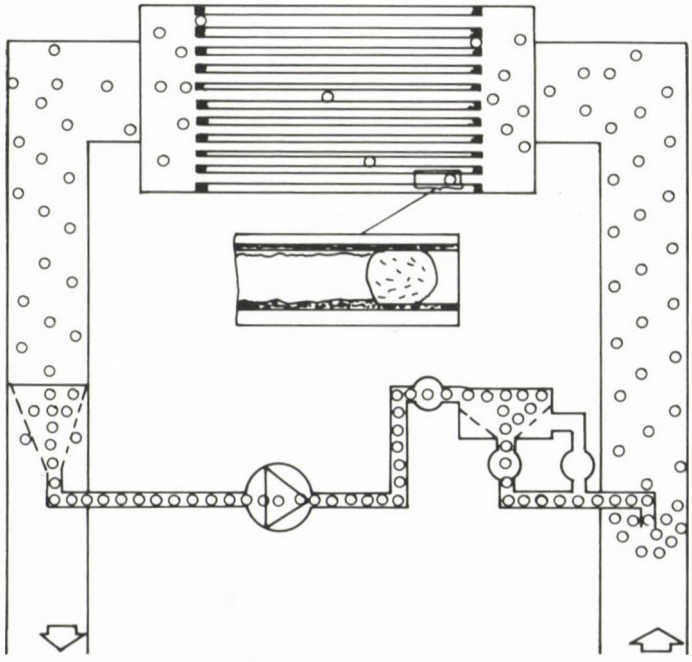

Fig. 2. Schematic diagram of ball-type heat-exchanger cleaning

the pipes to be cleaned by the coolant flowing in the system. While passing through the pipes, the balls remove sedimentation from the internal wall of the heat-exchange pipes (Fig. 2). The balls leaving the heat exchanger are collected by a filter where the balls unsuited for further use are at the same time removed from the system.

Brush-type cleaning systems use one brush and two catch baskets for each heat-exchange pipe. The baskets are designed so as to catch the brush brought by the flowing water without hindering the water in flowing through the pipes (Fig. 3). The direction of water flow shall be changed periodically, depending on the extent of fouling of the pipes. Quite a number of different reversing devices have been developed for this purpose by different companies (reversal is also possible by means of four butterfly valves of co-ordinated operation).

Both the ball-type and the brush-type systems have advantages and disadvantages, but they are not dealt with in detail in this paper. For large-size equipment (e.g. turbine condensers with a capacity of several hundred MW), use of the ball-type system is preferable while in case of smaller heat exchangers, the choice of the appropriate cleaning system depends largely on the local conditions.

In this paper, we describe a brush-type cleaning system used for the 4.5 MW steam turbine condenser of TVM (Tiszamenti Chemical Works), the test methods used, the results of measurement, the operation experience with and the economic efficiency of the system. Installation of the equipment has been financed by TVM while the tests have been supported by OKKFT G/4 Program Office. Based on the favourable operational experience with the cleaning system further developments are being carried on with the support of OMFB (development of flow diverter, installation and examination of cleaning systems in the food industry, etc.). This work is expected to be finished by the end of 1992.

1. Description of the system

The brush-type cleaning system has been installed at the power plant of TVM. Two condensing turbine units of a rated capacity of 4.5 MW each, denoted by I and II, are operated at the power plant. The condensers are supplied with cooling water from a ring duct with 2 branch pipes for each unit, first for unit I and then for unit II when viewed in the direction

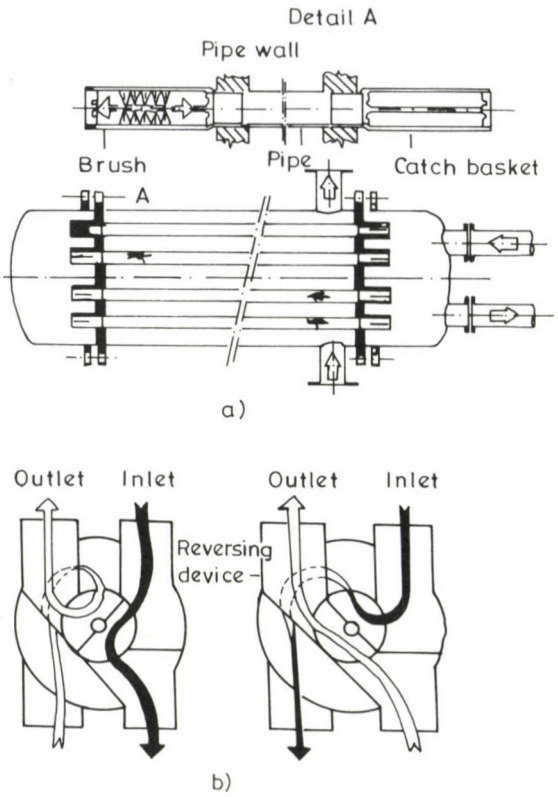

Fig. 3. Schematic diagram of brush-type heat-exchanger cleaning

of flow. (Water-side parts of the condensers are divided in two parts each.) The warmed cooling water is recooled by cooling towers.

Before brush-type cleaning was introduced, the values of vacuum and the specific production figures for unit II had been rather inferior to the similar values for unit I. Therefore, the cleaning system was built into unit II. The brushes and the plastic baskets were purchased from MESROC Ltd., a German partner, while the reversing device with 4 butterfly valves was produced by TVM. The butterfly valves are operated by imported pneumatic motors. The arrangement of the baskets and brushes and the lay-out of the condenser are illustrated in Figs 4 and 5, respectively.

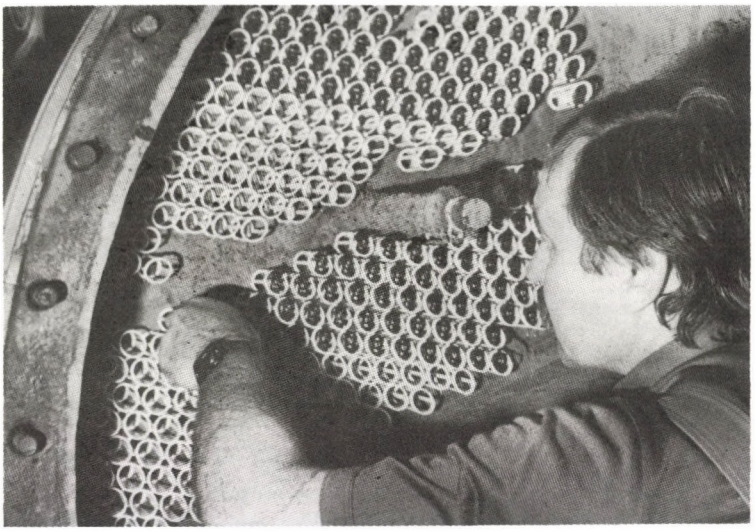

Fig. 4. Arrangement of brushes and catch baskets

2. Test method

A measurement system for automatic data collection has been provided for both units, that is, for unit II with continuous cleaning and unit I of similar construction, operated without continuous cleaning. The measurement systems were in operation in the year before installation of the cleaning system. After the cleaning equipment had been put into service, measurements were carried out for both units simultaneously during a period of three months of continuous operation.

So far the measurements have been designed first of all to supply reliable data for economic efficiency calculations. Therefore, three different factors have been taken as a basis for evaluation, in particular, change of the overall heat transfer coefficient, direct comparison of condensing temperatures and values of specific heat consumption. The results obtained on the basis of the three factors are approximately identical. Discussed below is only the most generally applicable method based on change of the overall heat transfer coefficient.

In the ideal case, that is, constant temperature and flow rate of cooling water and constant steam load during operation of the condenser, determination of the overall heat transfer coefficient as a function of time would be a sufficient method for evaluation of the effect of fouling (or cleaning). However, the conditions of operation are less ideal in case

of measurements in practice. Therefore, the values of the overall heat transfer coefficient measured directly must be converted into common parameters (water flow rate, water temperature and steam load). Although we have been successful in making measurements at approximately constant values of water temperature and flow rate in the range of a higher and a lower generator power (steam load), this is seldom possible in practice. And in case of minor fouling, the effect of changes in water temperature and flow rate and steam load may be comparable with the effect of fouling.

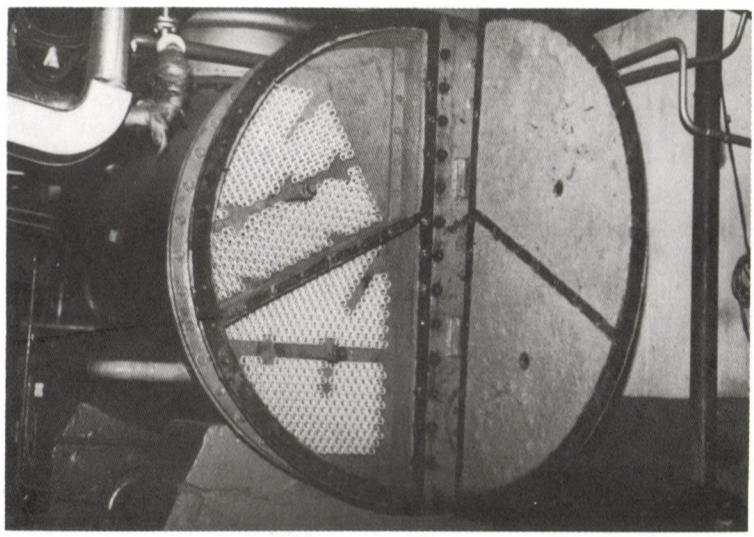

Fig. 5. Cleaning devices arranged in one part of the condenser

The overall heat transfer coefficient of a clean heat exchanger under operating conditions 1 (see explanation of the symbols), related to the external surface, is

$$\frac{1}{k_{C1CA}} = \frac{D_0}{D_I}\frac{1}{\alpha_{W1}} + \frac{D_0}{D_E}\frac{\delta}{\lambda} + \frac{1}{\alpha_{S1}} \qquad (1)$$

while that of a fouled heat exchanger:

$$\frac{1}{k_{F1CA}} = \frac{D_0}{D_I}\frac{1}{\alpha_{W1}} + \frac{D_0}{D_E}\frac{\delta}{\lambda} + \frac{1}{\alpha_{S1}} + \Sigma R_F \qquad (2)$$

In case of constant water temperature and flow rate as well as steam load (t, v and s, respectively), a change of the overall heat transfer coefficient results from fouling alone:

$$\Sigma R_F = \frac{1}{k_{F1CA}} - \frac{1}{k_{C1CA}} \tag{3}$$

On the analogy of equation (3), the value of ΣR_F can be expressed also by overall heat transfer coefficients measured directly:

$$\Sigma R_F = \frac{1}{k_{F1M}} - \frac{1}{k_{C1M}} \tag{4}$$

In case of fouling ΣR_F developed by time τ, the following formula can be used to calculate the overall heat transfer coefficient under operating conditions X (that is, for parameters t_x, v_x, s_x):

$$\frac{1}{k_{FXCA}} = \frac{D_O}{D_I}\frac{1}{\alpha_{WX}} + \frac{D_O}{D_E}\frac{\delta}{\lambda} + \frac{1}{\alpha_{SX}} + \Sigma R_F \tag{5}$$

In equations (5) and (2), the relationship between α_{WX} and α_{W1}, α_{SX} and α_{S1}, respectively, shall be determined by calculation. The value of overall heat transfer coefficient, if determined by means of the calculation method used in general for a clean heat exchanger, will certainly differ from the value measured directly, first of all as a result of the difference between the two measured and two calculated values of the heat transfer coefficient. However, as a good approximation, it can be assumed that

$$\alpha_{WCA} = C_1 \alpha_{WM} \tag{6}$$

and

$$\alpha_{SCA} = C_2 \alpha_{SM} \tag{7}$$

over the entire range studied.

Since the measurements under operating conditions make no distinction between factors C_1 and C_2, a suitably selected correction factor shall be used between the calculated and measured values. The following correction factor will result in only a negligible error over the entire range affected:

$$C = \frac{\frac{D_0}{D_I}\left(\frac{1}{\alpha_{WM}} + \frac{1}{\alpha_{SM}}\right)}{\frac{D_0}{D_I}\left(\frac{1}{\alpha_{WCA}} + \frac{1}{\alpha_{SCA}}\right)} \qquad (8)$$

Relationship (8) is obtained by calculating the appropriate C from the terms containing the heat transfer coefficients like in case of the overall heat transfer coefficient. The functional connection between C, C_1 and C_2 can be written by writing the expressions on the right side of equations (6) and (7) in place of α_{WCA} and α_{SCA} in equation (8).

Hence, coefficient C according to formula (8) can be considered constant under operating conditions 1 and X. With the numerator of equation (8) expressed from the basic relationship for the overall heat transfer coefficient, the following equation is obtained:

$$\frac{\frac{1}{k_{F1M}} - \frac{D_0}{D_E}\frac{\delta}{\lambda} - \Sigma R_F}{\frac{D_0}{D_I}\left(\frac{1}{\alpha_{W1}} + \frac{1}{\alpha_{S1}}\right)} = \frac{\frac{1}{k_{FXM}} - \frac{D_0}{D_E}\frac{\delta}{\lambda} - \Sigma R_F}{\frac{D_0}{D_I}\left(\frac{1}{\alpha_{WX}} + \frac{1}{\alpha_{SX}}\right)} = C \qquad (9)$$

On the analogy of equation (9), the following equation can be written e.g. for operating conditions 1 (clean condition) and 0 (for parameters t_1, v_1, s_1 and t_o, v_o, s_o, respectively):

$$\frac{\frac{1}{k_{C1M}} - \frac{D_0}{D_E}\frac{\delta}{\lambda}}{\frac{D_0}{D_I}\left(\frac{1}{\alpha_{W1}} + \frac{1}{\alpha_{S1}}\right)} = \frac{\frac{1}{k_{COM}} - \frac{D_0}{D_E}\frac{\delta}{\lambda}}{\frac{D_0}{D_I}\left(\frac{1}{\alpha_{WO}} + \frac{1}{\alpha_{SO}}\right)} \qquad (10)$$

By means of the overall heat transfer coefficient measured under operating condition 1, the overall heat transfer coefficient for arbitrary operating conditions X can be expressed from equation (9) by use of (4) and (10):

$$\frac{1}{k_{FXM}} = C\left[\frac{D_0}{D_I}\left(\frac{1}{\alpha_{WX}} - \frac{1}{\alpha_{W1}}\right) + \frac{1}{\alpha_{SX}} - \frac{1}{\alpha_{S1}}\right] + \frac{1}{k_{F1M}} \qquad (11)$$

where the value of C is obtained similarly from (9), using (4) and (10):

$$C = \frac{1}{\frac{D_O}{D_I}\frac{1}{\alpha_{WO}} + \frac{1}{\alpha_{SO}}} \left[\frac{1}{k_{COM}} - \frac{D_O}{D_E}\frac{\delta}{\lambda} \right] \qquad (12)$$

Hence, to convert overall heat transfer coefficient k_{FIM} determined on the basis of directly measured data at time τ from parameters 1 to (common) parameters X, it is necessary that

- overall heat transfer coefficient k_{COM} for parameters t_o, v_o, s_o at time $\tau = 0$ that is in clean condition and
- overall heat transfer coefficient k_{FIM} for parameters t_1, v_1, s_1 at time be known and
- internal (water-side) and external (steam-side) heat transfer coefficients α_W and α_S, respectively, be calculated for parameters t_o, v_o, s_o, t_1, v_1, s_1 and t_x, v_x, s_x on the basis of the appropriate relationships.

Attention shall be paid to leakage proofness and air vent during condenser measurements, since a change of the conditions prevailing in the condenser may affect the overall heat transfer coefficient.

Knowing the change of the overall heat transfer coefficient with time, the usual calculations for steam cycles can be carried out.

3. Results of measurements, operating experience

The brush-type heat-exchanger cleaning system was put into service in May 1989. In the course of tests by means of the reversing device, the value of vacuum was found to change only slightly, by about 2 to 3%, during reversal, provided, the right and left side of the condenser of a common plenum for steam but divided in two parts in respect of water supply was cleaned independently, that is, not simultaneously. (This value is in agreement with the results of calculations for analysis of the effect of reversal made before installation. Figure 6 shows the typical change of temperature, flow rate and vacuum as a result of reversal, illustrated diagrammatically on the basis of the model developed for the purposes of calculation.)

From the set of data available, data measured in low-load operation (at a generator power of 2620-2716 kW) and high-load operation (4240-

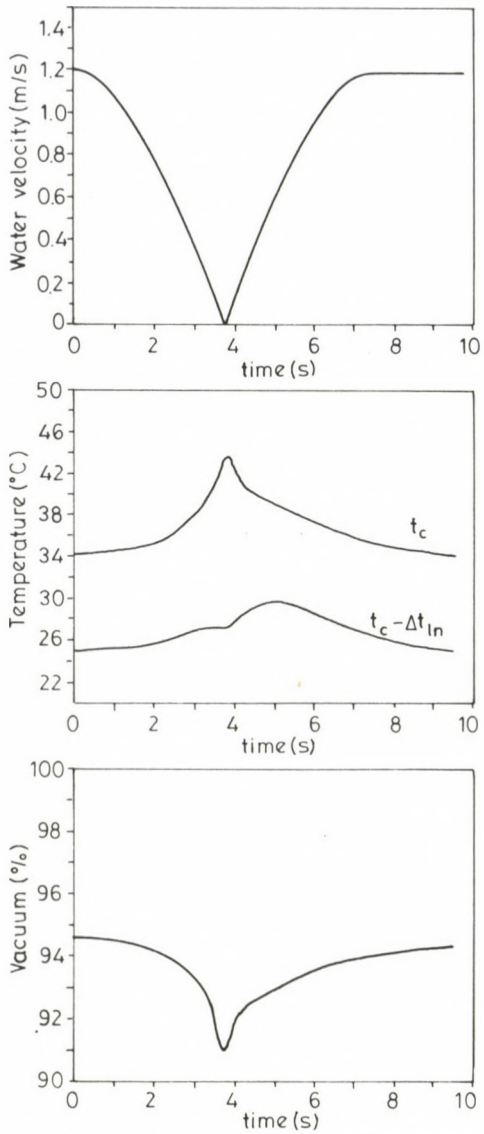

Fig. 6. Values of water velocity, temperature and vacuum as a function of time upon reversal (results obtained by means of a computer model)

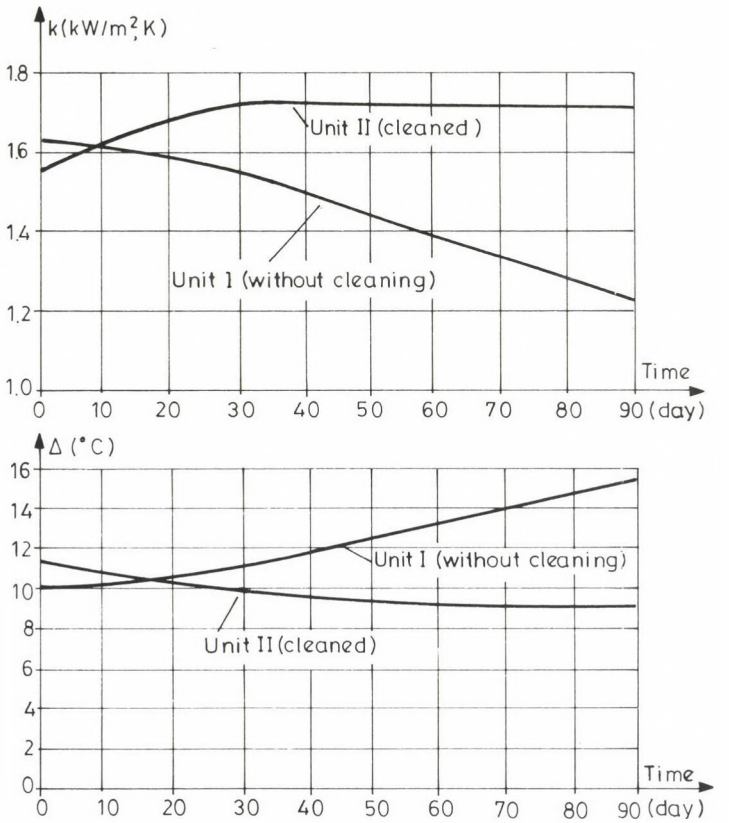

Fig. 7. Values of overall heat transfer coefficient and end-temperature difference as a function of time in the generator power range of 2620-2716 kW

4332 kW) have been evaluated independently for each mode of operation. The most important results of measurements are presented in Figs 6 to 9.

Figure 7 shows the change of the most important characteristics measured in a generator power range of 2620-2716 kW for units II and I (operated with and without continuous brush-type cleaning equipment, respectively), the abscissa being the time axis, while the values along the vertical axes being the overall heat transfer coefficient measured but converted into identical (average) water flow rate, steam load and water temperature (par 1.3), as well as the condenser end-temperature difference. In compliance with what has been described in par 2, the diagram suggests that the condenser of unit I worked better than that of unit II at the beginning of the tests. However, in case of unit II operated in application with the cleaning equipment, the overall heat transfer coef-

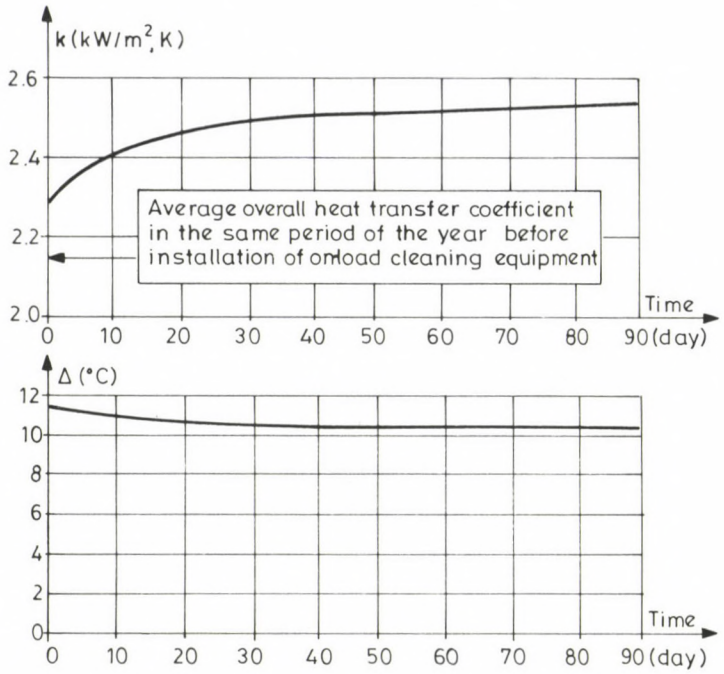

Fig. 8. Values of overall heat transfer coefficient and end-temperature difference as a function of time in the generator power range of 4268-4320 kW

ficient increased asymptotically as a function of time whereas in case of unit I, the overall heat transfer decreased considerably as a result of fouling.

Figure 8 illustrates the change of the overall heat transfer coefficient and end-temperature difference with time for the condenser of unit II operated with continuous cleaning similarly to Fig. 7, but now at a generator power of 4268-4320 kW. For the sake of comparison, the average value of overall heat transfer coefficient (measured for the same unit in the same period of the previous year as before installation of the cleaning equipment) has also been indicated along the vertical axis.

In Fig. 9, the changes of water pressure losses in the condensers of units I and II are illustrated as a function of time. As seen, the loss of pressure increased considerably in case of unit I as a result of fouling.

During the test period of about three months, the machine equipped with the cleaning equipment was operated continuously and the operation of the cleaning system was most efficient. After operation for three months, the condenser covers were removed to find that the heat-exchange surfaces

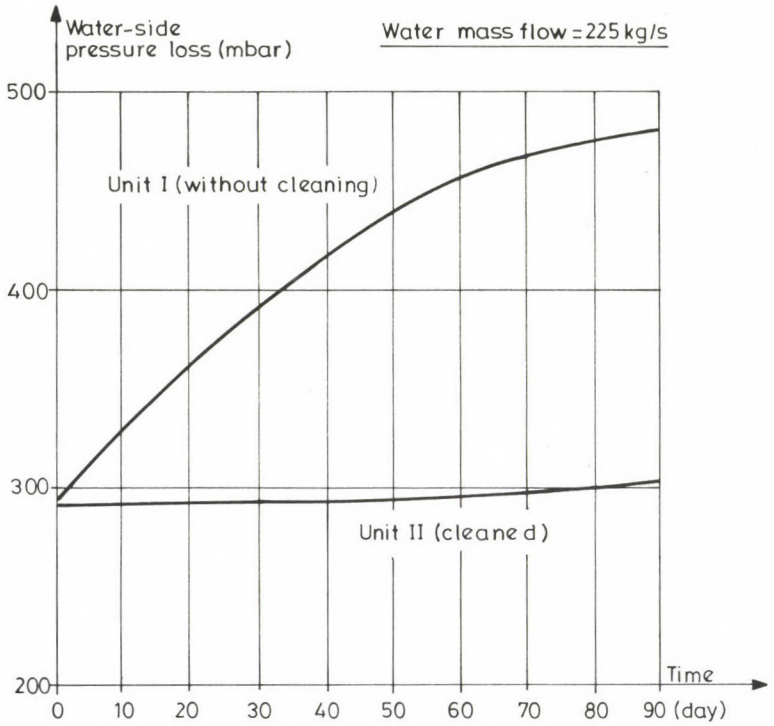

Fig. 9. Change of water pressure losses as a function of time

were perfectly clean, except for a few pipes. A few brushes got stuck in the interior of the fouled pipes because of the higher than permissible variation of the pipe diameter (the slight increase in pressure loss according to Fig. 9 can most likely be attributed to the same reason). To eliminate this trouble, the diameter of the conic guide fittings at the end of these brushes had to be reduced slightly.

4. Economic efficiency, rate of return

On the basis of earlier operating experience, the annual schedule of the unit investigated can be approximated as follows:

In winter (from October to April), the turbine is operated at a generator power of 2620 kW for 2253 hours only. In summer (from May to September), the unit is operated continuously, for 2116 hours in the low-load mode (2620 kW), while for 1556 hours in the high-load mode (4332 kW).

As a result of continuous on-load cleaning instead of the earlier periodical (monthly) cleaning, an additional 423270 kWh has been generated annually with invariable heat input. Another electricity gain of 231040 kWh/year results from the fact that no standstill for cleaning is required in the summer. On the basis of the so-called 'mixed electricity price' of Ft 2/kWh used in TVM, the total additional electricity generation of 654310 kWh/year results in a profit of MFt 1.31 annually. With this profit, compared with the investment costs of MFt 2.435, a rate of return of 1.86 years is obtained, a rather favourable rate as compared with similar investments in the energy sector. Hence, an increasing use of systems of this type for similar or smaller heat exchangers seems to be most reasonable, while in case of favourable operating experience, use of the cleaning system for smaller power plant units is worth considering.

Acta Technica Acad.Sci.Hung., 105(1-2), pp. 19-40 (1993)

COMPUTER AIDED DESIGN OF OPTIMIZED STRANDED CONDUCTORS

GÜNTNER, O.* - DANYEK, GY.**

(Received: 3 January 1991)

As a result of joint research and development work of MKM (Hungarian Cable Works) and VEIKI (Research Institute of Electricity Industry), Hungary has been the first to use aluminium-steel stranded conductors of optimized stranding geometry and reduced loss. Since 1982, about 10 000 tons of low-loss conductors have been built into overhead transmission line oy MVMT (Hungarian Electricity Works Trust), expected to save about DM 25 million for the Hungarian economy in a service period of 35 years. In 1987-1988, the Austrian Ministry of Science and Research as well as the Technical University of Vienna contributed to continue theoretical research by granting a scholarship for one of the Hungarian research workers to work abroad.

This work describes the results achieved in the period after 1987.

According to a report /1/ presented at the 1986 summer session of IEEE, "the deficit resulting from the increased energy losses due to a.c. load in aluminium-steel stranded conductors used for power lines may be comparable with the investment costs of the conductor in a service period of 50 years.

Because of the high value of a.c. resistance, some electricity suppliers avoid using aluminium-steel stranded wires with three or five aluminium layers in the network".

Research is going on all over the world to reduce the energy losses of ACSR conductors /1, 3, 4, 9, 10/.

Although the most important principles of the design of optimized structures like e.g. reduction of the axial field strength developing in the interior of the conductor had been recognized internationally /1/, so far the theory has found practical application on a large scale only in Hungary /4, 11/.

Research has been run in co-operation with the Hungarian Cable Works

*Güntner, Ottó, H-1182 Budapest, Batthyány u. 190/b, Hungary

**Danyek, Gyula, H-1022 Budapest, Törökvész út 16/c, Hungary

Akadémiai Kiadó, Budapest

in our Institute to reduce the energy losses and to develop energy-saving stranded conductors. As a result, the source of increasing losses has been identified and a method to reduce the losses has been found. As a result of theoretical research, structural modifications have been introduced, resulting in a reduction of 3-6% of the energy losses of stranded conductors.

VEIKI was the first to detect in 1977 the uneven current distribution in the aluminium layers of aluminium-steel stranded conductors in case of a.c. load /2/.

This new result permitted the earlier calculation processes /3/ to be supervised, the conventional stranded structures to be improved and new low-loss stranded conductors to be patented /4/.

The test results obtained from the first new conductor structures manufactured were published as early as in 1980 /5/. It was proved that even minimum changes in the stranding parameters affected the a.c. resistance of the stranded conductor considerably /6, 11, 12/. Because of the nonlinear magnetic characteristic of the iron core, the expectable operating parameters of new structures can be determined by time consuming calculation processes only, including sometimes iteration. Therefore, research work in the period after 1987 was designed to develop a computer program permitting the technical and economic effects of any constructional modification to be followed mathematically.

The computer program available as a result of research

- permits technically and economically optimum stranded structure to be developed,
- helps traders to determine the economic efficiency of stranded wire parameters and new energy saving conductors in tender specifications,
- permits optimum utilization of the conductors in the network by electricity suppliers,
- permits the products to be improved by the manufacturers in accordance with the recent requirements on the world market.

The methods of calculation used in the program have been tested by means of laboratory experiments.

The theoretical research work is described in detail in the doctor's thesis submitted to the Technical University of Vienna /7/.

1. Recent requirements on the world market

The investment costs of phase conductors of a 400 kV overhead line amount to 20% of total construction costs of the overhead line /8/. The value of additional a.c. energy losses of aluminium-steel stranded wires during the service life of the conductor may lie even above this value /1, 7, 9, 10/. Because of the high investment costs and considerable energy losses, demand for conductors of improved economic efficiency and increased service life has been increasing on the world market.

The increasing requirements imposed upon the quality of stranded conductors are reflected first of all in the recent tenders. Tensile strength and d.c. resistance alone, used earlier as a basis for evaluation of stranded conductors, are by far not enough today. Recent tenders include more than 13 technical parameters. To compete successfully, the manufacturers have to specify parameters of a large number for conventional conductors on the one hand and to develop new, more favourable constructions on the other hand.

According to experience, the time available for supply of tender parameters is too short to permitthe conductor to be manufactured and tested in laboratory. Therefore, the manufacturers often miss the tender. As a result of the computer aided process, the tender parameters, for any stranded structure are available within minutes.

For determination of the electric, mechanical and economical characteristics, we had to supervise the conventional methods of calculation on the one hand and to develop new processes on the other hand. Development of a new method for calculation of the a.c. resistance, taking the uneven current distribution within the aluminium layers into consideration, has been indispensable for both the tender parameters and design of energy saving stranded wires.

2. Investigation of the method used earlier for calculation of current distribution and a.c. resistance of ACSR conductors

In calculation for energy losses, aluminium-steel conductors can be treated as an iron-core coil. In earlier calculations, the increase of resistance in case of a.c. load has been attributed almost entirely to iron losses resulting from axial magnetic field strength /3/.

For calculation of the axial magnetic field strength taking place in the interior of a stranded conductor with more aluminium layers, the aluminium layers were replaced by one single coil with a number of turns per meter according to the following formula:

$$N = \frac{\sum_{i=1}^{j} \frac{n_i}{h_i} (-1)^i}{n} \quad \text{(turns/m)} \qquad (1)$$

where

N number of turns per meter in the coil (turns/m)

n_i number of aluminium strands in layer i

h_i pitch of aluminium strands in layer i (m)

n number of aluminium wires

j number of conductor layers

Using relationship (1), increase of the resistance was calculated as follows /3/

$$\Delta R = \frac{\mu A_V \left(\sum_{i=1}^{j} \frac{n_i}{h_i} (-1)^i \right)^2 \omega}{n^2} \cdot \operatorname{tg} \phi \ (\Omega/m) \qquad (2)$$

where

μ permeability of the steel core in case of a field strength determined by loading current (Vs/Am)

ϕ phase angle between loading current and voltage induced in the aluminium layer (^{o})

ω angular frequency (rad/s)

A_V steel core cross section (m^2)

Increase of the resistance is described by relationship (2) erroneously because

- it assumes a uniform current distribution among the aluminium layers and
- it uses $\operatorname{tg}\phi$ instead of the correct multiplier of $\sin\phi \cos\phi$.

a) Detection of uneven current distribution by laboratory measurements

Uneven current distribution among the aluminium layers was detected by measuring the temperature rise of the aluminium layers and steel core

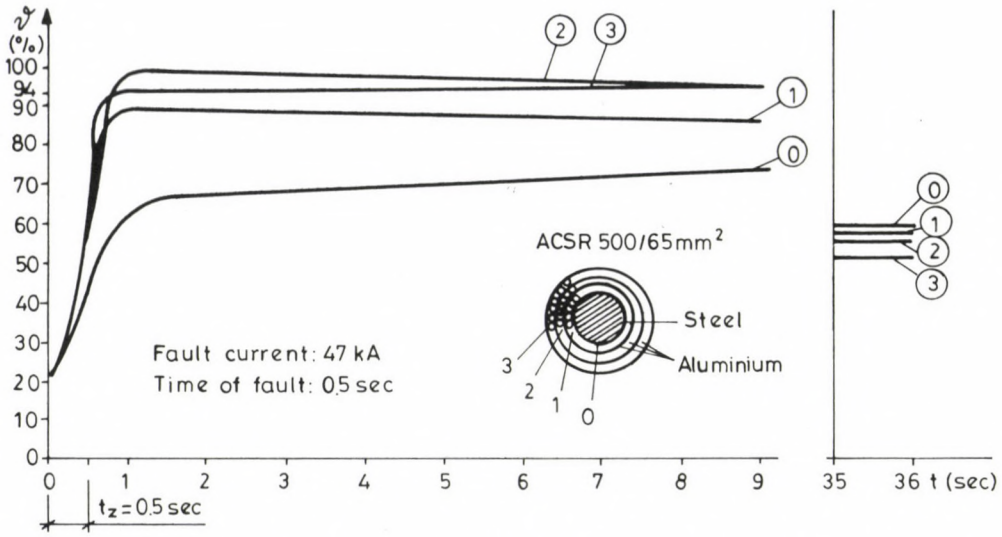

Fig. 1. Temperature rise in ACSR conductor upon short-circuit

under short-circuit conditions /2/ by means of thermocouples built in between the wires (Fig. 1) in 1977.

Highest current intensity could be detected in the middle layer.

The difference between the layers in current density increases in the range of the normal service currents where the permeability of the steel core lies by an order of magnitude above the value in case of short circuit.

b) Using the phase angle between induced voltage and loading current correctly

For testing the relationship (2) the substitutional connection diagram (Fig. 2) and the vector diagram (Fig. 3) for a stranded conductor with one aluminium layer have been plotted. The following symbols have been used in the diagrams:

U_T Voltage measurable at the terminals of the test circuit consisting of stranded conductor and connecting cables.

U_l Voltage drop at internal impedance of the stranded conductor.

U_i Voltage induced in the aluminium layer by resultant axial magnetic strength.

I_l Loading current flowing in the aluminium layer.

I_s Current flowing in the secondary circuit mapping the iron losses.

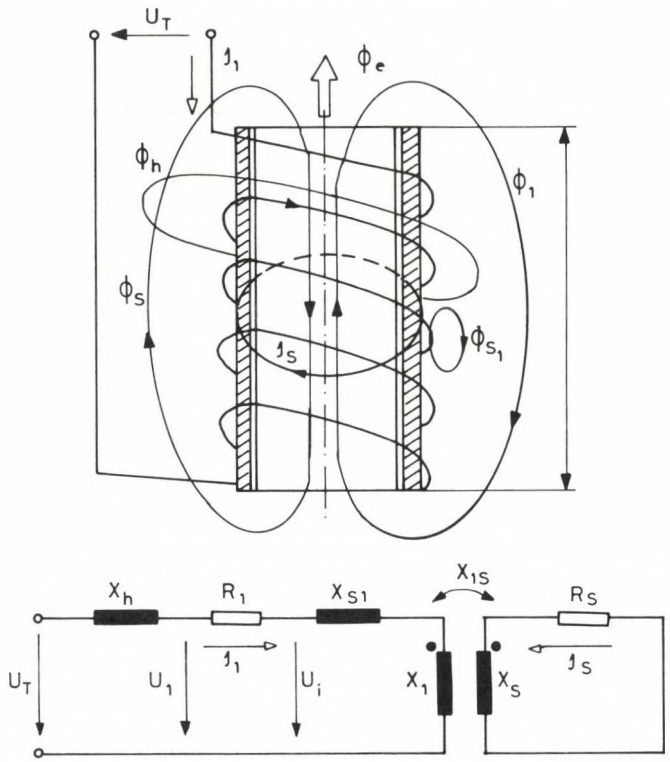

Fig. 2. Substitutional connection diagram of ACSR conductor with one aluminium layer

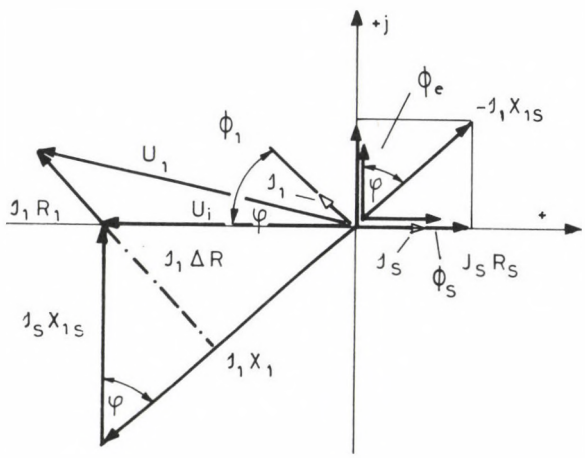

Fig. 3. Vector diagram of ACSR conductor with one aluminium layer

ϕ_h Tangential flux in the domain surrounded by the stranded wire surface and the connecting cables, brought about by loading current flowing in the conductor.

ϕ_l Axial flux in the steel core brought about by loading current flowing in the aluminium layer.

ϕ_s Axial flux in the steel core brought about by secondary current mapping iron losses.

ϕ_e Resultant axial flux in the steel core, brought about by loading current flowing in the aluminium layer and secondary current mapping the iron losses.

X_h Reactance of circuit surrounded with the conductor surface and connecting cables.

X_{sl} Leakage reactance.

X_l Reactance of the iron-core coil, substituting the aluminium layer.

X_s Reactance of the secondary circuit mapping the iron losses.

X_{ls} Mutual reactance of aluminium layer and secondary circuit mapping the iron losses.

R_l Resistance of aluminium layer.

R_s Resistance of secondary circuit mapping the iron losses.

ΔR Increment of resistance of the stranded conductor as a result of a.c. load.

ϕ Phase angle between loading current and fundamental harmonic voltage induced in the aluminium layer.

Value of the increment in resistance on the basis of the vector diagram:

$$\Delta R = X_l \sin\phi \cdot \cos\phi \qquad (\Omega/m) \qquad (3)$$

Substituting $X_l = \omega \cdot \mu . A_v . N^2$:

$$\Delta R = \omega \cdot \mu \cdot A_v \cdot N^2 \sin\phi \cdot \cos\phi \qquad (\Omega/m) \qquad (4)$$

The values of $\mu_r \sin\phi \cos\phi$ as a function of field strength have been calculated for the steel core on the basis of μ_r and ϱ curves determined by measurements (Fig. 4). The increment of resistance measured for the entire stranded conductor is in good conjunction with the calculated values.

Relationship (4) applies only to stranded wires with one conducting layer. To calculate the resistance of multilayer stranded wires, the connection diagram according to Fig. 2 had to be further developed.

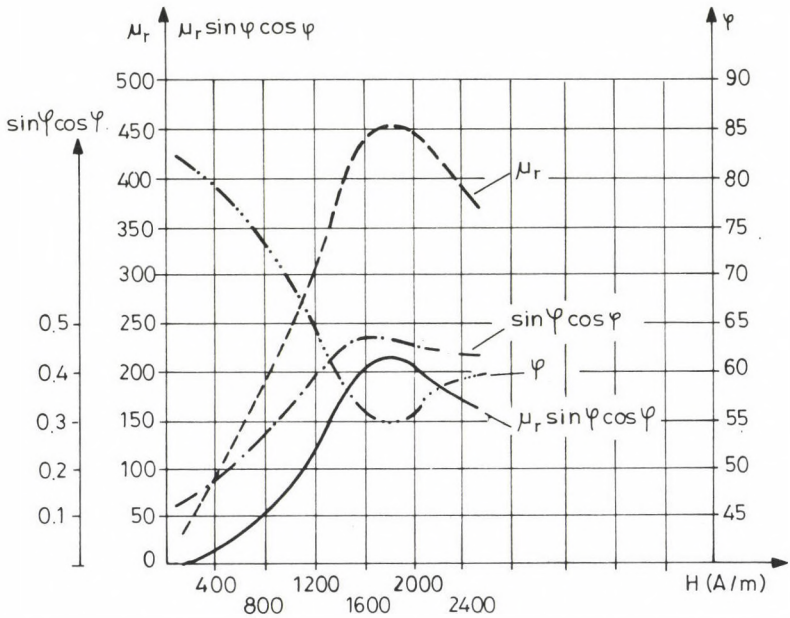

Fig. 4. Results of μ_r . $\sin\phi$. $\cos\phi$ measurements as a function of field strength

3. New method for calculation of current distribution and a.c. resistance of ACSR conductors

In the course of research, substitution of one single coil for the conducting layers was found to be the wrong practice because of the uneven current distribution among the layers.

Theoretically, we have proved that the aluminium layers are connected in parallel /17/. Therefore, the substitutional connection of the stranded wire with three aluminium layers is modified according to Fig. 5.

The Figure permitted

- the current distribution to be determined and
- the losses occurring in the different aluminium layers and steel core mapped by the secondary circuit to be calculated.

The process developed is advantageous, among others, in that the equations can be solved without iteration in spite of nonlinear curves μ and ϕ /7/. Thus the program is considerably simplified and the time required for running becomes shorter.

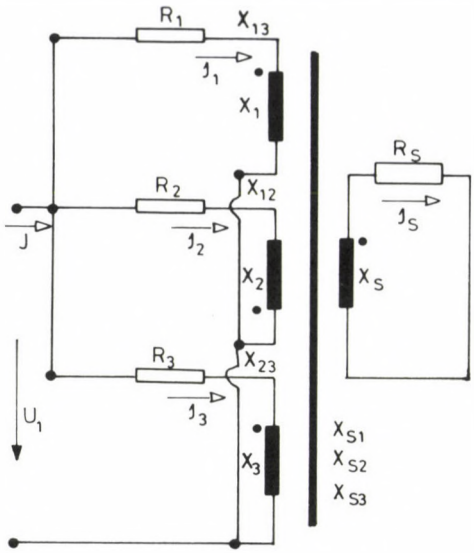

Fig. 5. Substitutional connection diagram of ACSR conductors with three aluminium layers

3.1. Current distribution in an ACSR conductor with three aluminium layers

On the basis of Fig. 5, the current distribution in a 500/65 mm^2 ACSR conductor with three aluminium layers could be determined as a function of loading current (Fig. 6). It was found that in the normal service current range of 1000 A, the current conducted by the aluminium layer in the middle /2/ was 27% higher at a.c. load than in case of direct current. In the outer layer /3/, the current intensity decreased by 10% while in the inner layer /1/ by 24%. According to temperature rise test on short-circuit conditions made in 1977, the current intensities show an identical distribution (Fig. 1). A change of the stranding geometry results in a reduction of the resultant axial magnetic field strength brought about in the steel core by the aluminium layers to approx. 1/3. In this case, the current distribution becomes more homogeneous and thus the additional losses in the aluminium layers decrease. Also iron losses are reduced as a result of the reduced field strength. Hence, reduction of field strength is the best method to optimize stranded structures in respect of losses.

The vector diagram of ACSR conductors with three conducting layers has been plotted to give a simple physical explanation of uneven current distribution. In a qualitative form, the vector diagram is given in Fig. 7.

The currents flowing in the aluminium layer and the eddy currents occurring in the steel core bring about a resultant axial flux ϕ_e in the

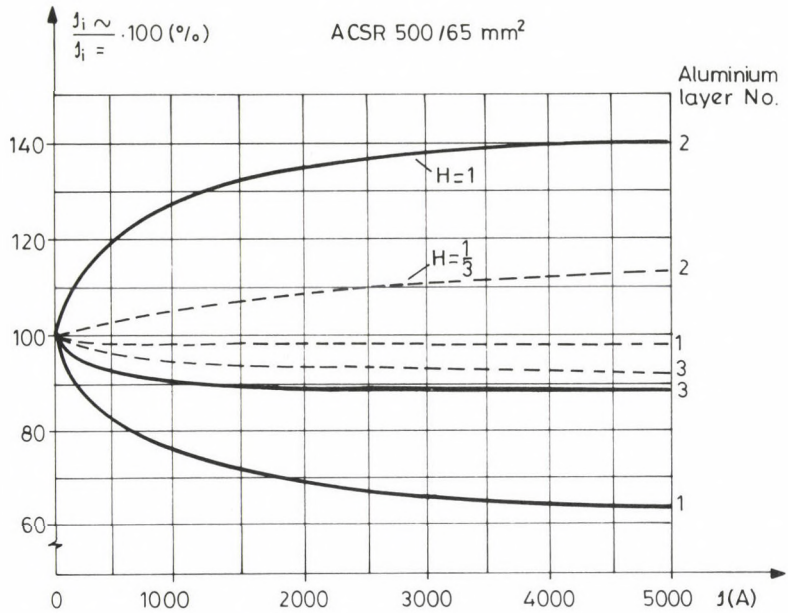

Fig. 6. Current distribution in ACSR conductor with three aluminium layers

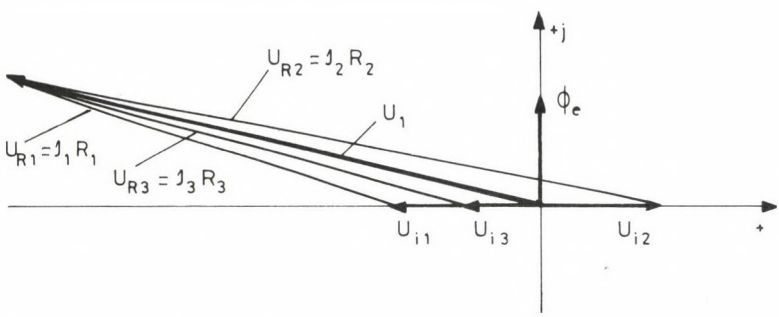

Fig. 7. Vector diagram of ACSR conductor with three aluminium layers

interior of the stranded wire, inducing voltage in the different layers, the ratio of which corresponds to the number of turns ($U_{i1}/U_{i2}/U_{i3}$ = = $N_1/N_2/N_3$).

Since the direction of the turns in the middle layer is inverse, U_{i2} is of opposite sense. Component IR depending on the layer current and layer resistance is added to the induced voltage. The resultant of the IR and the induced voltage gives the voltage drop (U) at internal impedance per unit section of the stranded conductor.

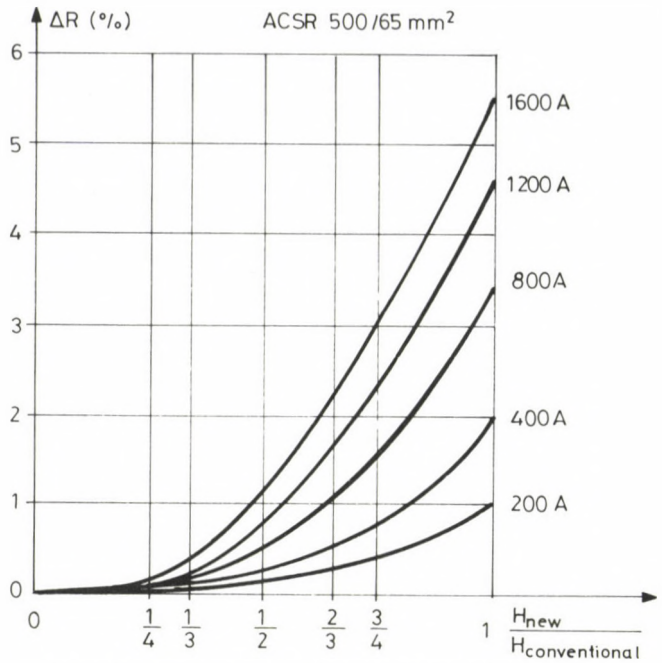

Fig. 8. Effect of axial magnetic field strength on additional a.c. resistance of the conductor

The ratio of layer currents at a.c. and d.c. load is given by relationship

$$\frac{I_{i\sim}}{I_{i=}} = \frac{U_{Ri}}{U} \tag{5}$$

The vector diagram explains the inhomogeneous fault current distribution according to Fig. 1 illustratively. One of the most important conclusions is that maximum current intensity will be caused rather in the middle layer by the compensating currents resulting from the axial flux and the stranding than in the outer layer attributed to the skin effect resulting from tangential flux within the conductor.

3.2 Dependence of a.c. resistance of ACSR conductors with three conducting layers on field strength

In the knowledge of currents flowing in the aluminium layers and in the secondary circuit mapping the iron losses, the increment in resistance of the stranded conductor can be determined.

As shown in Fig. 7, by decreasing the resultant flux and/or field strength the current distribution becomes more homogeneous and thus the increment in resistance is less.

This method to reduce losses had been recommended also abroad but has not found practical application in networks so far /10/.

The result of our research work devised on the basis of a simplified diagram, directly applicable in practice, is illustrated in Fig. 8.

Reduction of the field strength as a result of constructional modification in case of given loading current is considerable at the beginning while it results then in a decreasing rate of reduction of the resistance.

According to earlier results of research /4/, the construction of stranded conductors with reduced losses should be such as to compensate for almost 100% of axial magnetic field strength. However, as proved by Fig. 8, a reduction of 30% of the field strength results in a reduction of 50% of additional a.c. resistance.

Hence, full compensation for axial magnetic field strength within the conductor is not necessary. In practice, a reduction of 50-65% being allowed of a mechanically permissible constructional modification is sufficient. The standards permit the stranding parameters to be selected optionally within certain limits. Accordingly, the deviation of the values of a.c. resistance of different versions of 500/65 m^2 ACSR conductors from each other may be as high as 3.4%. The optimum structure can be chosen only in the knowledge of the accurate calculation method by means of a computer.

4. Use of the results of research for design of low-loss stranded conductors

The extent of possible reduction of resistance by reduction of the field strength is illustrated in Fig. 9. Curve 1 shows the dependence of the a.c. resistance of the conventional stranded conductor upon the current while curve 2 describes a structure where a reduction of 1.8% of d.c. resistance and 3.4% of a.c. resistance was achieved by increase of the stranding factor in every conducting layer.

The optimum structure developed by us is illustrated by curve 3. Dissimilarly to version 2, the purpose of the constructional modification has been to minimize rather axial magnetic field strength than d.c. resistance.

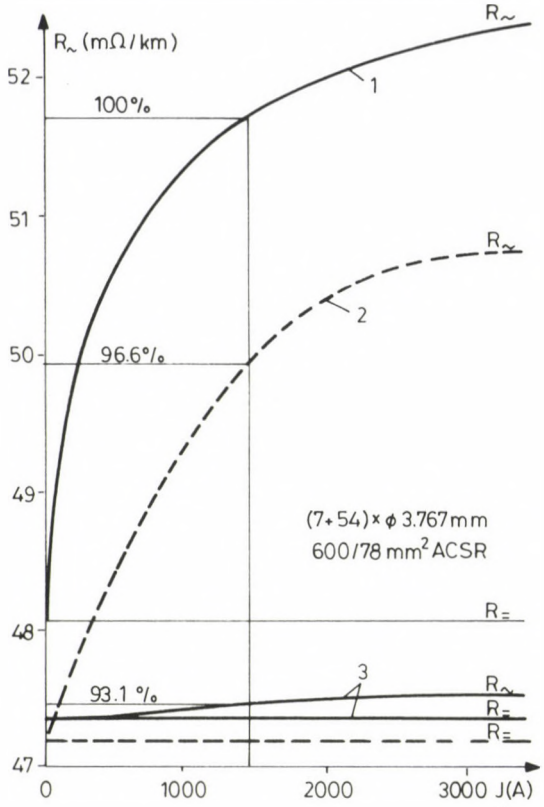

Fig. 9. Conductor optimized by means of a computer aided method
(1 - conventional stranded conductor, 2 - conductor of improved properties of foreign make, 3 - optimized conductor)

Although the d.c. resistance of version 3 is higher than that of version 2, the resultant a.c. resistance lies 3.5% below the value of standard loading current. As compared with the original construction, the resistance could be reduced by 6.9%.

The results of research warn against taking the catalogue values of d.c. resistance as a basis for evaluation of the economic efficiency of stranded conductors.

The value of a.c. resistance alone cannot be a basis for comparison of the different structures in respect of economic efficiency. Namely, as the stranding parameters are modified, also the weight of the aluminium conductor built into the cable changes. Using these two values, the improvement of the conductor has been determined for different structures of reduced axial field strength on the basis of German and Austrian economic parameters (Fig. 10). The capital value method has been used for calculation /9/.

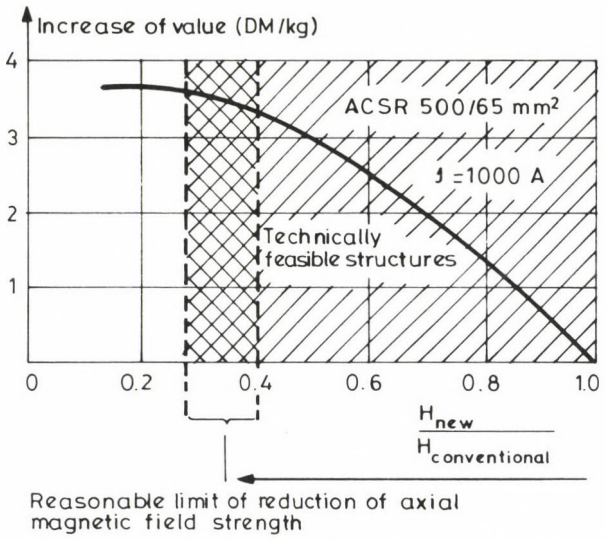

Fig. 10. Improvement of the conductor as a function of axial magnetic field strength in case of energy saving stranded conductors

By means of the Figure, a reasonable limit can be determined for reduction of field strength. Reduction of axial field strength by 30-40% was found to increase the value of the 500/65 mm^2 ACSR conductor studied by more than 3 DM/kg, taking into consideration the actual current loads in the network. A significant improvement is not expectable from additional reduction of the field strength and at the same time, in case of reduction of the field strength below a reasonable value, the mechanical properties would be affected unfavourably.

The computer program developed is described below.

5. Description of the computer program

The program developed on IBM compatible computers serves to determine the tender characteristics, including standard and special electrical, mechanical, constructional and, in case of double-metallic structures, comparative economic parameters for stranded conductors with max. three layers, made of single or double metal(s).

The program is suited for prompt calculation of the values listed below for optional input values, in 5 variations, on the basis of the

relevant IEC 207-210 specifications, taking into account the material constants of 6 different national standards, and to display them diagrammatically or in tabulated form.

The program permits hard copies both with words and graphics to be printed by means of an EPSON FX printer (in EPSON mode) for EGA (350x540) and Hercules (348x720) monitor drivers.

Values supplied

Electrical values:

- Resultant a.c. resistance
- A.c. resistance as a function of current (in case of double-metallic structures), magnetic characteristics of steel-core and geometry, in the range of 0 to min. 12 kA
- Internal reactance of stranded conductor, similarly as a function of current, magnetic characteristics of steel-core and geometry
- Permissible value of loading current according to DIN in case of an ambient temperature of 35 ^{o}C and a conductor temperature of max. 80 ^{o}C, under no wind conditions or in case of a wind speed of 0.6 m/s

Geometrical and mechanical values:

- Cross section of aluminium conductor
- Cross section of steel core
- Resultant weight of aluminium layers
- Weight of steel core
- Resultant weight of stranded conductor
- Resultant tensile strength
- Torsional moment
- Initial and final modulus of elasticity
- Resultant coefficient of thermal expansion
- Geometrical mean radius (GMR) of the conductor

Constructional parameters:

- Wire diameter
- Angle of stranding (calculated on the basis of the stranding factor to be specified)
- Mean diameter of layers

Comparative economic efficiency:

Data of max. 5 variations are processed by the program. Taking variation 1 as a basis (West German data), the improvement of the conductor per kg is given in DM for stranded conductors according to variations 2

thru 5, using the method of calculation of capital return in case of double-metallic structures.

This means essentially savings in investment and energy costs per kg of stranded conductors according to variations 2 thru 5 over the service life of the stranded conductor (35 years in the present case).

Hence, any price increase by the manufacturer which lies below the calculated improvement is realistic on the market. The program takes a.c. resistance and the change in mass as a basis for evaluation of the economic efficiency of the different stranded conductors.

Special tender characteristics:

- A.c. resistance as a function of frequency (max. 5000 Hz)
- Internal reactance of the conductor as a function of frequency (max. 5000 Hz)
- Positive-sequence reactance of one-system overhead line with single or bundle conductor as a function of geometry of the overhead line
- Approximate tensile strength curve for the entire stranded conductor

Input data:

- Geometrical parameters:
  - Wire diameter per layer
  - Number of wires per layer
  - Stranding factor per layer
- Temperature:
  - Ambient temperature
  - Operating temperature of stranded conductor
  - Temperature gradient between the layers within the stranded conductor, in per cents
- Material characteristics (for 6 different standards):
  - Specific resistance of conductive material
  - Mechanical strength of steel (for 1% elongation)
  - Tensile strength of aluminium
  - Modulus of elasticity of steel and aluminium
  - Density of steel and aluminium
  - Coefficient of thermal expansion of steel and aluminium

An example is presented below for practical application of the program.

6. Example for practical application of the computer aided method

To illustrate the effect of change of the angle of stranding on the electrical, mechanical and economic parameters of the stranded conductor, two variations of the 500/65 mm^2 ACSR stranded conductor of minimum and maximum stranding factor according to standard DIN 48204 are presented. Figure 11 shows the input data identical for both variations except for the angles of stranding.

Geometrical properties

	Layers			
	Inner	Middle	Outer	Steel
Variation 1				
Nominal diameter of wire (mm)	3.45	3.45	3.45	3.45
Number of wires	12	18	24	7
Angle of stranding (deg)	76	75	74	84
Variation 2				
Nominal diameter of wire (mm)	3.45	3.45	3.45	3.45
Number of wires	12	18	24	7
Angle of stranding (deg)	82	80	79	84

Fig. 11. Input data of the computer program

Illustrated in Fig. 12 are, as a function of loading current,

- the current distribution in the aluminium layers
- the increment of resistance as a result of alternating current and
- the a.c. resistance.

Figure 13 shows the increment of resistance and the improvement of the conductor for five variations. In the economic efficiency calculations, the permissible value of the normal loading current has been estimated at 1000 A. (The parameters of variations 1 and 2 are given in Fig. 11.)

The increment of resistance of the improved construction (variation 2) at a loading current of 1000 A is by 3% lower than that of the conventional construction (variation 1). Further improvement of the stranding geometry may result in a reduction as much as 6% in resistance (curves No.

Calculated results

	Serial No. of workpoint				
	1	2	3	4	5
Variation 1					
Loading Current (A)	171	358	526	656	784
DC curr.distr. Layer 1 (%)	22.2	22.2	22.2	22.2	22.2
AC curr.distr. Layer 1 (%)	21.0	20.4	19.9	19.4	19.0
DC curr.distr. Layer 2 (%)	33.3	33.3	33.3	33.3	33.3
AC curr.distr. Layer 2 (%)	37.0	38.3	39.3	40.2	41.0
DC curr.distr. Layer 3 (%)	44.4	44.4	44.4	44.4	44.4
AC curr.distr. Layer 3 (%)	43.0	42.4	41.9	41.5	41.1
Alu.conduct. "R" increment (%)	2.52	3.14	3.69	4.21	4.63
Steel core "R" increment (%)	0.44	0.75	1.00	1.15	1.30
Residual AC "R" increment (%)	2.96	3.89	4.69	5.36	5.93
Resid. AC resistance (ohm/km) Conductor temperature: 60 °C	0.0690	0.0697	0.0702	0.0706	0.0710
Variation 2					
Loading Current (A)	229	455	638	763	878
DC curr.distr. Layer 1 (%)	22.2	22.2	22.2	22.2	22.2
AC curr.distr. Layer 1 (%)	22.0	21.8	21.6	21.4	21.2
DC curr.distr. Layer 2 (%)	33.3	33.3	33.3	33.3	33.3
AC curr.distr. Layer 2 (%)	34.3	34.8	35.4	36.0	36.5
DC curr.distr. Layer 3 (%)	44.4	44.4	44.4	44.4	44.4
AC curr.distr. Layer 3 (%)	44.2	43.9	43.6	43.3	43.0
Alu.conduct. "R" increment (%)	0.96	1.14	1.34	1.56	1.77
Steel core "R" increment (%)	0.25	0.47	0.69	0.87	1.06
Residual AC "R" increment (%)	1.21	1.62	20.3	2.43	2.83
Resid. AC resistance (ohm/km) Conductor temperature: 60 °C	0.0665	0.0668	0.0671	0.0673	0.0676

Fig. 12. Current distribution of a.c. resistance as a function of loading current

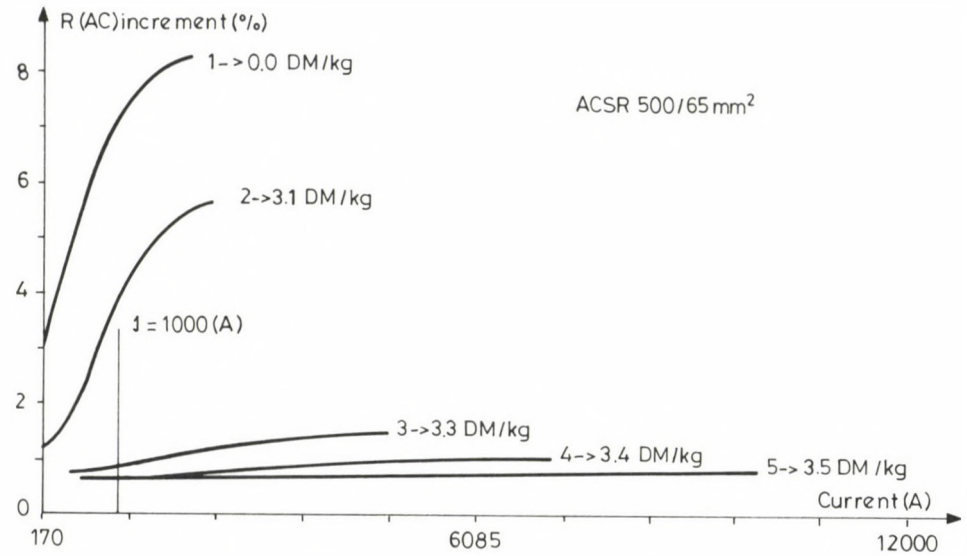

Fig. 13. Additional a.c. resistance of stranded conductors of different structure as a function of loading current

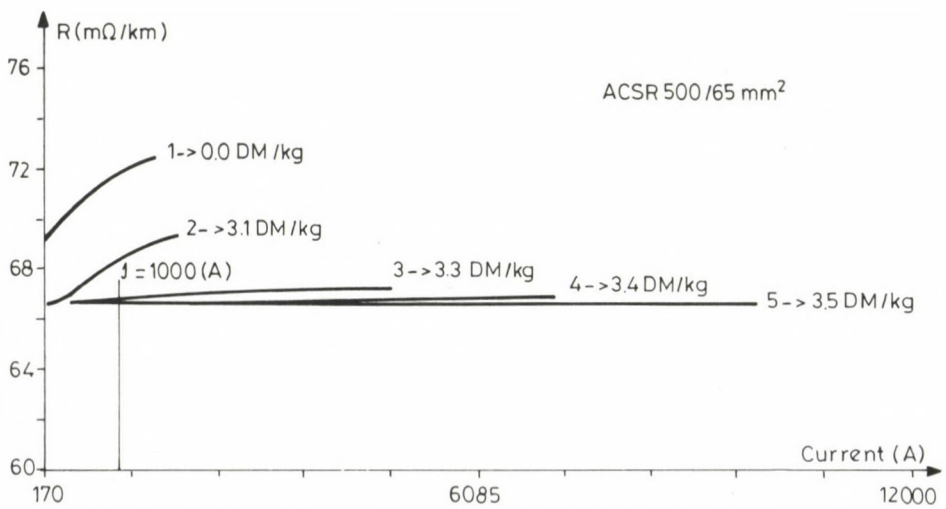

Fig. 14. A.c. resistance of stranded conductors of different structure as a function of loading current

3, 4, 5). However, due to the increased mass of the conductor material in the stranded cable, the improvement of the conductor does not increase accordingly. At any additional price lying below the calculated improvement, use of the new stranded conductor results in increased economic efficiency.

Figure 14 illustrates the a.c. resistance of five different stranded structures as a function of loading current. The value of 3.1 DM/kg, calculated for structure No. 2, can be achieved even with standard structures /15/.

Considering that the price of ACSR stranded conductors is 3.7 DM/kg at present, the constructional modification presented here resulted in an increase of 84% of the value.

Figure 15 shows the most important mechanical and geometrical characteristics of the two variations selected. As seen, the mechanical properties have not been affected unfavourably by the constructional modification. A reduction of the torsional moment of the new structure by more than 30% is favourable in respect of installation.

7. Possibilities of development of the program

Our computer program meets the recent, most up-to-date, international requirements /10/ and it is suited to

- determine every tender parameter of stranded conductors of any arbitrary stranding factor and
- calculate technical-economical characteristics required for choosing optimum structures.

The program includes no manufacturability test and it assumes therefore that only stranding parameters of technically feasible structures are included among the input data.

The tender and design program can be optionally extended to include the recent results achieved in this special field.

The following calculations are intended to add to the program:

- determination of maximum permissible loading current for ACSR stranded conductors with the temperature gradient between the aluminium layers and the uneven current distribution taken into consideration,
- manufacturability test in case of optional stranding parameters.

Mechanical features

	Layers			
	Inner	Middle	Outer	Steel
Variation 1				
Nominal diameter of wire (mm)	3.45	3.45	3.45	3.45
Number of wires	12	18	24	7
Angle of stranding (deg)	76.0	75.0	74.0	84.0
Stranding factor	10.08	10.05	9.74	19.93
Medium diameter of layer (mm)	13.80	20.70	27.60	6.90
(Active) turn number	5.75	4.12	3.31	1.00
Outer diameter of layer (mm)	17.25	24.15	31.05	10.35
Residual DC resistan. (ohm/km)	0.06705	(at cond. temp.: 60 °C)		
Cond./Steel area (mm^2/mm^2)	504.8/65.4			
Cond./ Stl. weight (kg/km/kg/km)	1412.7/519.8			
Total weight (kg/km)	1932.5			
Nominal breaking load (N)	164135.7			
Torsion torque (Nm/kN)	0.74			
Resid. modul of elasti. (N/mm^2)	66434.4			
Res.coe.of lin.exp. (1e-6/deg)	19.6			
Loading current (DIN 48402) (A)	913			
Variation 2				
Nominal diameter of wire (mm)	3.45	3.45	3.45	3.45
Number of wires	12	18	24	7
Angle of stranding (deg)	81.6	80.4	78.7	84.0
Stranding factor	17.02	15.92	13.98	19.93
Medium diameter of layer (mm)	13.80	20.70	27.60	6.90
(Active) turn number	3.41	2.60	2.30	1.00
Outer diameter of layer (mm)	17.25	24.15	31.05	10.35
Residual DC resistan. (ohm/km)	0.06572 (at cond. temp.: 60 °C)			
Cond./Steel area (mm^2/mm^2)	504.8/65.4			
Cond./Stl. weight (kg/km/kg/km)	1384.7/519.8			
Total weight (kg/km)	1904.5			
Nominal breaking load (N)	164135.7			
Torsion torque (Nm/kN)	0.51			
Resid. modul of elasti. (N/mm^2)	69288.6			
Res.coe.of lin.exp. (1e.6/deg)	19.6			
Loading current (DIN 48204) (A)	913			

Fig. 15. Mechanical and geometrical characteristics of the two variations investigated

REFERENCES

1. Barrett, J.S., Findlay, R.D.: A new model of AC resistance in ACSR conductors. IEEE Trans., Vol. PWRD-1, No. 2, 198-208 (April 1986)

2. Tóth, T., Güntner, O., Varga, L.: Problems of the short circuit strength of overhead lines. CIGRE Working Group 31-02 (1977).

3. Morgan, V.T.: Electrical characteristics of steel-cored aluminium conductors. Proc. IEE, Vol. 112, No. 2 (February 1965)

4. Güntner, O., Tóth, T., Marton, S., Bablena, L.: Steel reinforced stranded aluminium conductor. Patent description, patent No.: 178.833/51, Budapest (in Hungarian)

5. Güntner, O., Magyar, J., Tóth, T.: Steel reinforced aluminium overhead conductors of reduced loss. Research and Development (1980)

6. Bablena, L., Marton, S., Güntner, O., Tóth, T.: Low-aluminium low-energy aluminium-steel overhead conductor. Magyar Aluminium 7-8 (1982) (in Hungarian)

7. Güntner, O.: Auswirkung der innerhalb der Aluminium-Lagen auftretenden ungleichmässigen Stromverteilung auf die Energieübertragungsverluste von Stahl-Aluminium-Freileitungsseilen. Dissertation. Technische Universität Wien, Fakultät für Elektrotechnik, 1988

8. Stimmer, H.: Elektrische Energieübertragung und Verteilung. Vorlesungsunterlagen. Technische Universität Wien, Institut für Elektrische Anlagen und Hochspannungstechnik 1987/88

9. Köhler, W.: Die Wirtschaftlichkeit von Alumoweld beim Einsatz in Freileitungen. Elektrizitätswirtschaft, Sonderdruck Nr. 2760, Band 74 (1975), 18, 691-695

10. Barrett, J.S.: Optimalization of Conductor Design. IEEE Transactions on Power Delivery, Vol. 4, No. 1 (January 1989)

11. Bablena, L., Marton, S., Güntner, O., Tóth, T.: Manufacture and testing of operational properties of energy and material saving steel-cored aluminium (Ental) stranded conductors. Magyar Aluminium 3-4 (1983) (in Hungarian)

12. Güntner, O., Tóth, T., Bablena, L., Marton, S.: Eigenschaften der nach einem neuen ungarischen Patent erzeugten energie- und materialeinsparenden ENTAL Freileitungsseile. Qualität und Zuverlässigkeit, Sonderausgabe 1984

13. Güntner, O., Orgoványi, Gy., Varga, L.: Testing of the mechanical properties of stranded overhead conductors. Manuscript. Part 1 (in Hungarian)

14. Güntner, O., Orgoványi, Gy., Varga, L.: Testing of the mechanical properties of stranded overhead conductors. Manuscript. Part 2 (in Hungarian)

15. DIN 48204: Aluminium-Stahl-Seile (Juli 1974)

16. Güntner, O., Danek, Gy.: Rechnergestütztes Berechnungsverfahren zur Bestimmung technischer und wirtschaftlicher Parameter beliebiger Seilkonstruktionen. Presented at the 3rd International Cable Conference, Budapest, October 18-19, 1989

17. Effect of tangential current component in aluminium cladddings of aluminium-steel conductors on losses of the conductor. Essay-competition paper, VEIKI 1975

Acta Technica Acad.Sci.Hung., 105(1-2), pp. 41-52 (1993)

CORRECTIVE MEASURES FOR DECREASING THE DETRIMENTAL ENVIRONMENTAL IMPACTS OF HIGH VOLTAGE LINES

HADRIAN, W.[1] - HOFBAUER, F.[2] - LUGSCHITZ, H.[3] - KROPIK, W.[4] - JERMENDY, L.[5]

(Received: 3 January 1991)

Oily and fatty sediments on the surface of conductors as a result of improper manufacturing in combination with particles from the air like pollen, grain and products of combustion can produce pollution in shape of small drops. Too big quantities of lubracants in the core of steel-reinforced aluminium conductors can especially result in outcoming grease in case of high temperature, and can produce corona effects in audible and visible range, as well as radio noise. In this paper, the principle of a newly developed method of cleaning the conductors is described. Extensive measurements were carried out to show the efficiency of this cleaning method.

1. Introduction

The ever increasing demands on energy transfer systems have resulted, among others, in a constant increase in the voltage of overhead power lines. In the high voltage range, a slight reduction of the insulation distance in the design of overhead lines results in considerable savings. However, this can lead to undesirable environmental effects, such as radio interference and audible noise. These problems can be especially critical in densely populated areas.

On bundled conductors, partial discharge can occur for long periods during the normal operation of the high voltage line. The damage caused on the surface of aluminium conductors may result in further intensely perturbing effects. Though partial discharges occur at different points,

[1]Hadrian, W., Technical University of Vienna, A-1040 Vienna, Gusshausstr. 25, Austria

[2]Hofbauer, F., Austrian Electricity Supply Board Vienna, Austria

[3]Lugschitz, H., Austrian Electricity Supply Board Vienna, Austria

[4]Kropik, W., Siemens AG Vienna, Austria

[5]Jermendy, László, H-1026 Budapest, Pasaréti u. 63, Hungary

Akadémiai Kiadó, Budapest

the nature of lines favours the spreading of interference over considerable distances.

Some damage to an aluminium conductor is inevitable. Damage can normally result in a decrease of about 20% in the test voltage for partial discharge when the overhead transmission line is put into service. During service, the notches burn away, this, in turn, resulting in a slight improvement of partial discharge values .

It is confirmed that the audible noise and radio interference are generated by the same phenomenon, mainly positive polarity streamers.

The losses are rapidly increased by the corona caused by surface irregularities. In one case very large corona losses were reported on a 220 kV line. 57.4 kW/km losses were measured on three phases because of the severe deterioration of conductor surface as a result of applying a kind of fat not corresponding to specifications .

2. The specific situation of the Austrian network

Since 1981, the Austrian Electricity Supply Board has been installing a supra-regional 380 kV high voltage grid having a length of 1025 km at the moment.In 1977, a power line for two systems with a length of 72 km was constructed in the south of Austria. This line was designed for a maximum operation voltage of 420 kV.

The bundle of two conductors of the type ACSR (2x680/85; bundle: 36 mm; vertical distance: 400 mm) is dimensioned for a permanent current of 2300 A. The most part of this power line runs in a rural and populated area.

Since the 380 kV high voltage grid had not yet been developed in this part of Austria, this power line was integrated into the 220 kV grid and was operated with a maximum voltage of 245 kV during the first few years. The integration into the 380 kV grid took place in 1987. At this voltage and at the maximum operation voltage of 420 kV, the corona discharge of the conductors caused a considerable audible noise within the neighbourhood of the power line. The corona discharges on a section of the power line (voltage: 420 kV) can be seen in Fig. 1. The first analysis showed that the contamination has outcome in form of drops on the surface of the conductors. The reason for this pollution was a too large quantity of grease in the core of the ACSR-conductor, coming out at increased temperatures of the conductor.

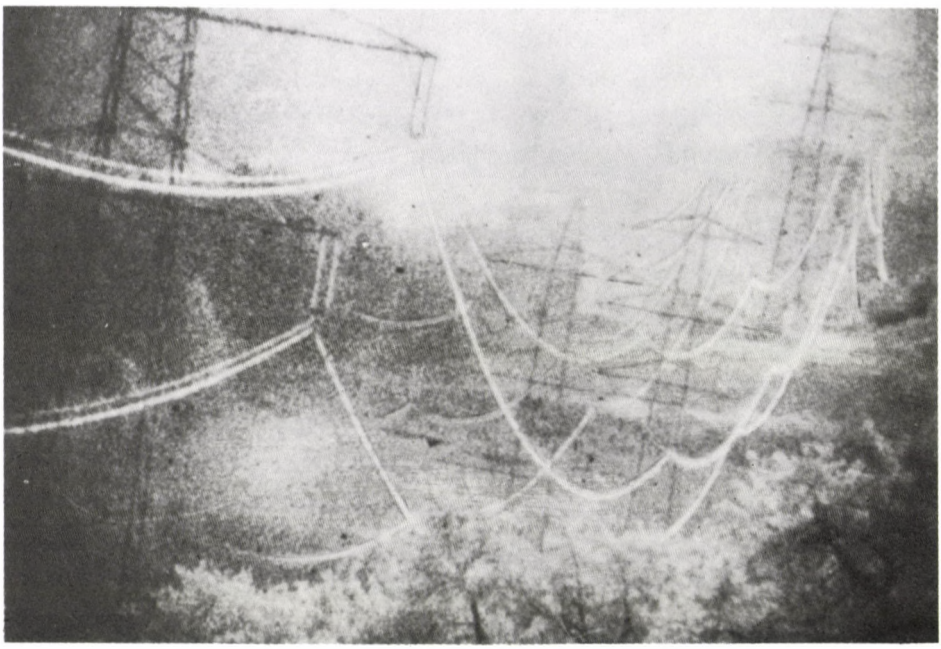

Fig. 1. Corona discharges on a section of the power line (voltage: 420 kV)

The level of audible noise caused by this corona discharge was about 50 dB(A) at an operation voltage of 420 kV at a distance of 20 m from the outer phase of the line. This value exceeds the maximum critical value of audible noise both in rural and in populated areas.

Therefore, corrective measures were indispensable to reduce the audible noise along the power line. Consequently, a method for cleaning the conductors had to be developed, by which, on the one hand, the contamination on the surface of the conductor and, on the other hand, the surplus grease in the core had to be removed so that in the future an undisturbed operation of the 380 kV power line could be achieved. In addition, the ground should not be contaminated by any greasy water.

In the following, the principle of this newly developed method of cleaning the conductors is described. Extensive measurements were carried out to show the efficiency of this cleaning method. Additional tests with contaminated and cleaned conductors were carried out in the laboratory of the Institute for Electrical Power Research (VEIKI) in Budapest.

3. Cleaning of conductors

A method of cleaning the conductor surface and washing out the surplus of grease from the steel core at the same time was elaborated at the Institute mentioned above. Accordingly, a fixed quantity of the protective material had to be retained in the core. In cooperation with several companies, a cleaning system was developed, presented briefly here.

3.1 Principle of cleaning

The conductors are heated and cleaned by steam without solvent at a temperature of 110 degrees Centigrade and a steam pressure of 130 bar. In case of very severe pollution certain chemical additives can be used. The system is built as a self-contained unit, so there is no impairment to the environment and no need for any additional protective measures. Merely leakages at the gaskets let little steam escape. The cleaning work can be done both in agricultural and in populated areas, and these are the regions where annoyances by defect conductors are most disturbing.

The line must be put out of service during the cleaning work. The cleaning system consists of two main parts (see Figs 2, 3, 4):

- cleaning unit at the conductor
- supply unit on the ground.

3.2 Cleaning unit

The cleaning unit enclosing the conductor is a tightened steel cell, hanging with rubber reels on the line, covering the jets and heating up the conductor. This cell also collects the emulsion washed out. Flexible high-pressure tubes bring the waste water down and deliver steam up.

As a result of heating, most part of the surplus grease comes out on the conductor surface, and the jets mounted on it in circumferential direction clean the surface and wash out the pollution. Several washing units can be moved by one line car, so it is possible to clean bundle conductors simultaneously, after the spacers have been dismounted.

The car is moved by an electric winch to guarantee a constant speed. Pilot tests resulted in an optimal speed of 1.5 meter/min. This makes sure that, on the one hand, a necessary remainder of the lubricant will be left behind in the core, and on the other hand, no grease will come out and produce corona effects in the future, so that only the detrimental surplus may be washed out.

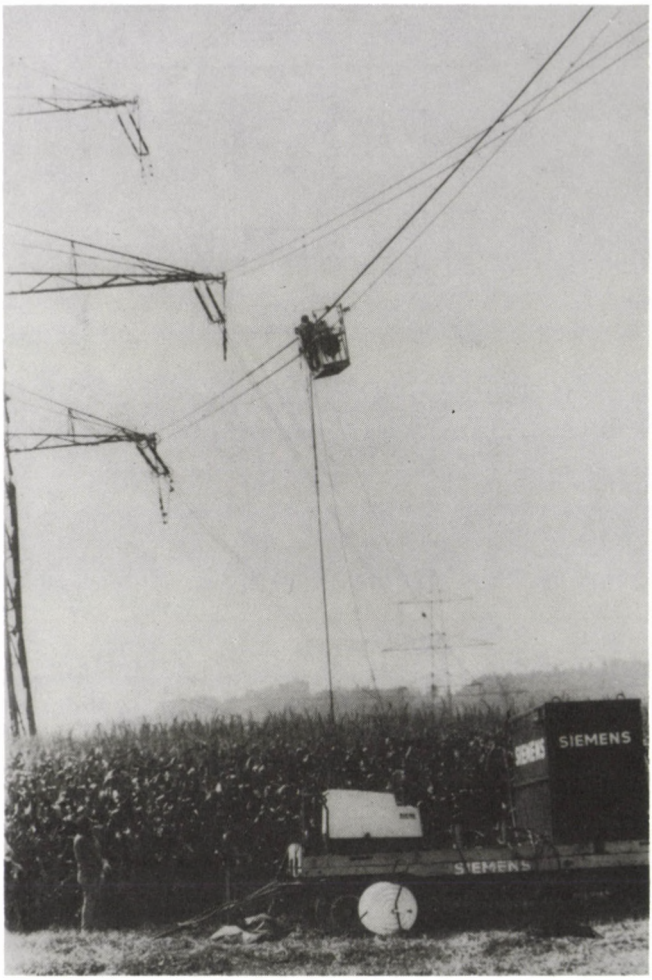

Fig. 2. Line car with the cleaning unit, connected by high-pressure tubes to the supply unit on a trailer

The speed also depends on the ratio of steel and aluminium and their different heat absorption. The cleaning of jumpers and fittings if necessary is done by hand with the same method applied.

3.3 Supply unit

Every cleaning unit needs an own steam generator. In our test, standard high-pressure generators are used which allow continuous operation over several hours. The aggregates can supply the cleaning units to a distance of 200 m through coupled high-pressure tubes. The units need 3x380 V which is produced by diesel aggregates.

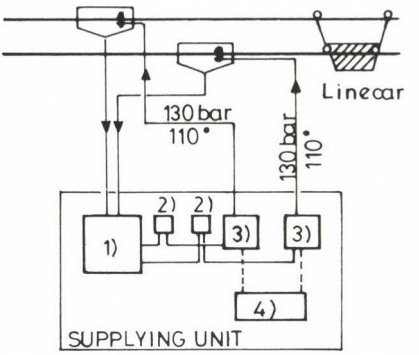

Fig. 3. Cleaning system
1) tank and filter, 2) filter, 3) steam generator, 4) diesel aggregate of 3x380 V

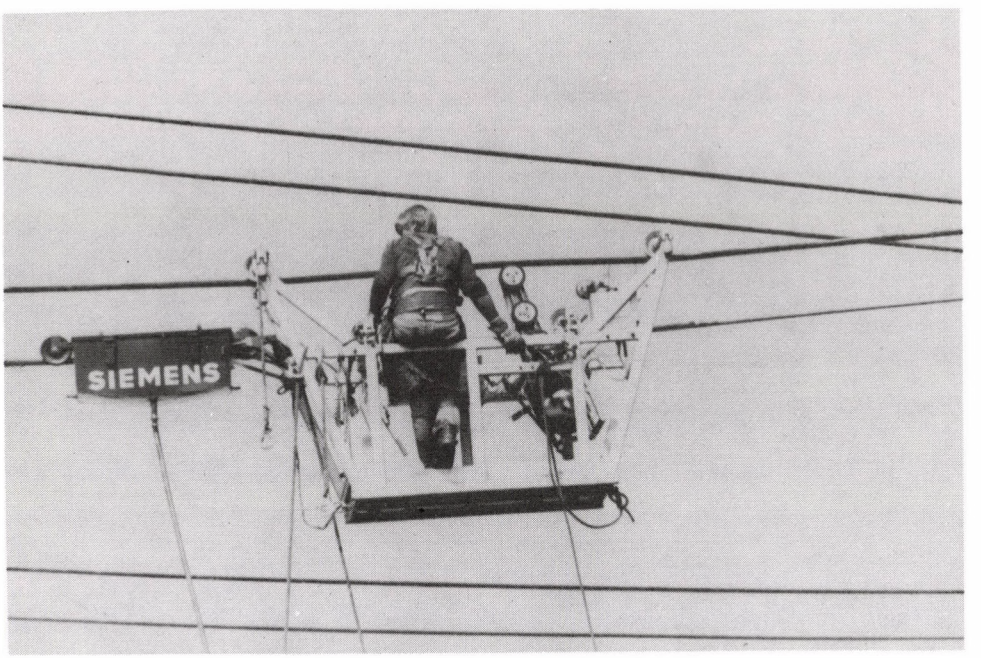

Fig. 4. Line car with a cleaning unit

Water for the steam generator is provided from a tank, so the plant is independent from the water mains. The filters in the tank clean and cool the emulsion coming from the units at the line, so water can be recirculated through the system several times, and operation for days is possible without changing the circulating water and without depositing the waste too often.

4. Measurement of radio noise and audible noise

The detrimental environmental impact of the polluted conductors should be controlled in the vicinity of the transmission line. For the sake of a better comparison between the measures developed for cleaning the bundle, also laboratory radio interference and audible noise measurements were carried out.

Radio interference is caused mainly by partial discharge taking place during the positive half-cycle. The measurements are carried out under normal working conditions after the determination of the interference field strength. A special amplitude-modulated receiver was used for this purpose. The intensity of the electromagnetic field is determined by means of corresponding coupling and antenna.

The actual procedure for determining radio interference is well established.

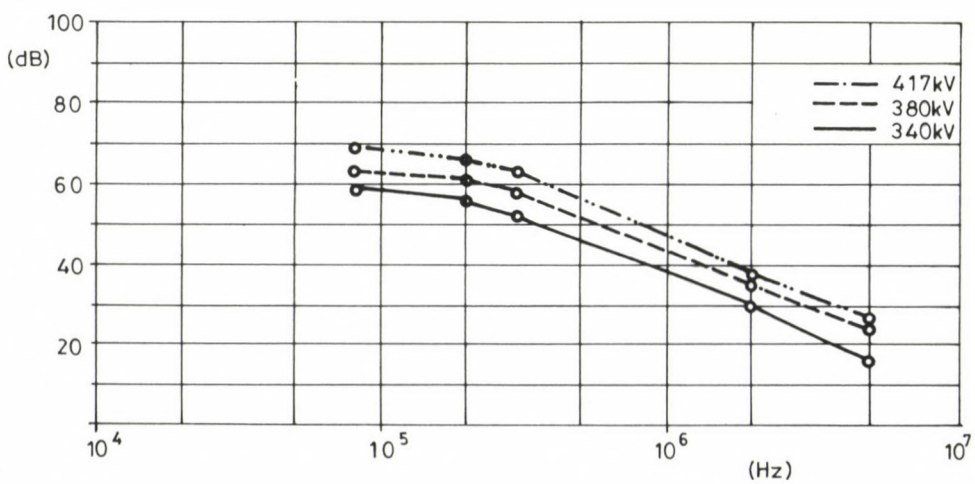

Fig. 5. Frequency characteristics of radio interference of a 400 kV transmission line at a direct distance of 50 m from the conductor with fat drops on the conductor surface

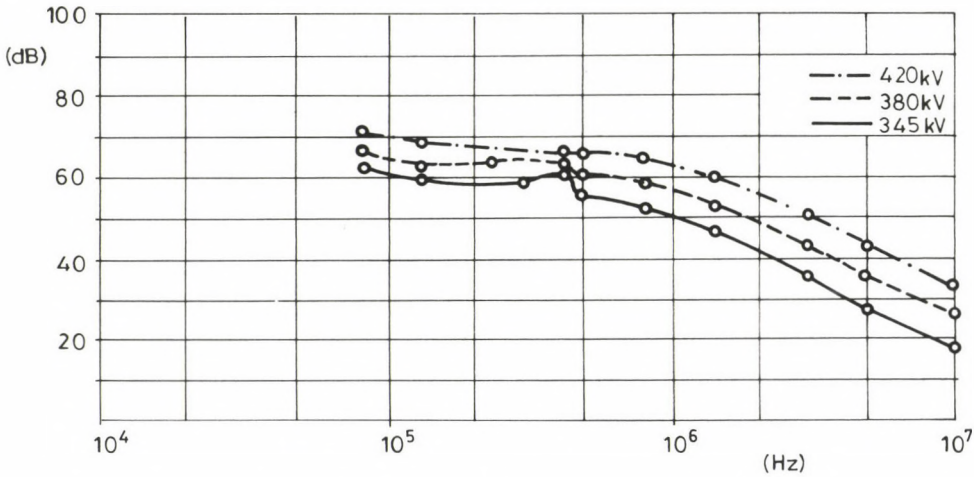

Fig. 6. Frequency characteristics of radio interference of a 400 kV transmission line at a direct distance of 20 m from the conductor with fat drops on the conductor surface

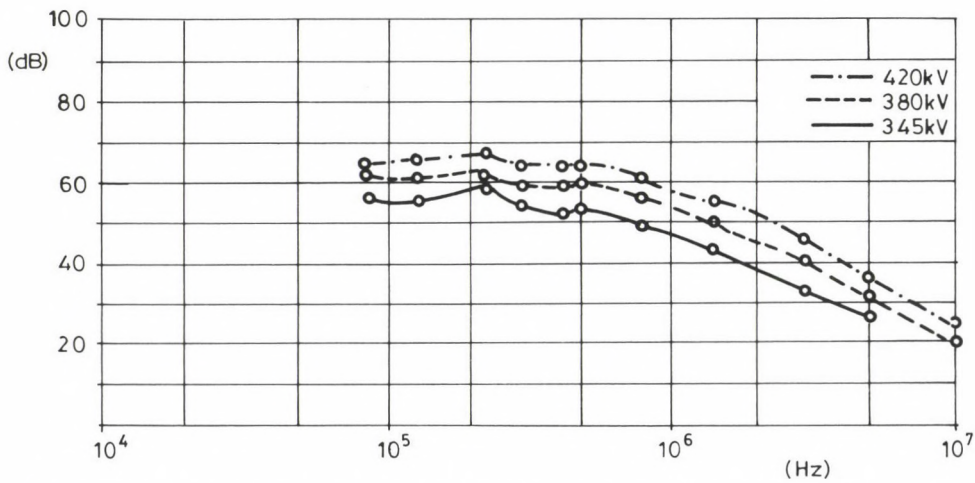

Fig. 7. Frequency characteristics of radio interference of a 400 kV transmission line at a direct distance of 20 m from the conductor without fat drops on the bundle conductor

The measurements show the results gained at different voltage levels of the transmission line for the conductor before cleaning as in Figs 5 and 6, and on the same line over a section where no fatting problem occurred as seen in Fig. 7.

The radio interference is the function of the frequency decrease. The increase of the RI with higher voltages and shorter distance to the conductor follows with relatively good agreement the values computed by formula:

$$Y = 29.3 + 3.8\, E_{max} - 34 \log D$$

where

Y - interference field strength in dB

E_{max} - maximum gradient of the conductor in kV/cm

D - distance between the outer phase and the antenna.

According to this formula, the maximum gradient of the bundle with fat drops on its surface can be determined. In this way, it is evident that the irregularities on 220 kV do not cause any problems to the environment because corona appears only at 420 kV system voltage. In this latter case, the maximum gradient is estimated to be higher than the gradient belonging to the initial voltage of the corona. The influence of fat drops on RI at 0.5 MHz was about 3 dB.

Table 1

Audible noise at a distance of 20 m from the outer phase of the power line

Voltage	345 kV	380 kV	420 kV
Audible noise			
polluted conductors	40 dB(A)	44 dB(A)	50 dB(A)
cleaned conductors	non-measurable		35 dB(A)

The level of audible noise caused by the corona discharges was about 50 dB(A) at an operation voltage of 420 kV at a distance of 20 m from the outer phase of the line. After cleaning the conductors, this level could be reduced to 35 dB(A) (see Table 1).

For comparison, a 12 m long bundle conductor was tested 3 m above the ground in the high voltage laboratory. At the same voltage levels, the radio interference (see Figs 8a and 8b) and the acoustic noise were determined in both cases, i.e. for the polluted and for the cleaned

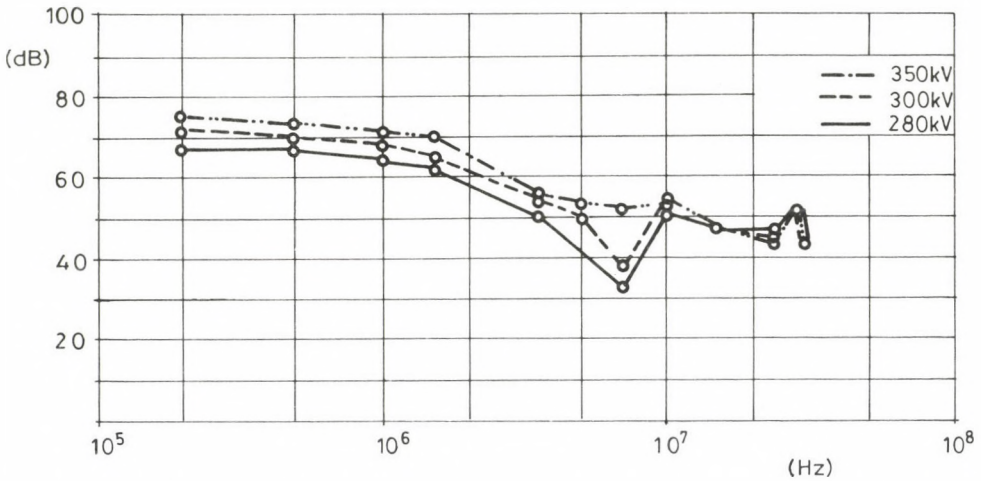

Fig. 8a. Radio interference of a 12 m long bundle conductor measured in the laboratory (polluted conductor)

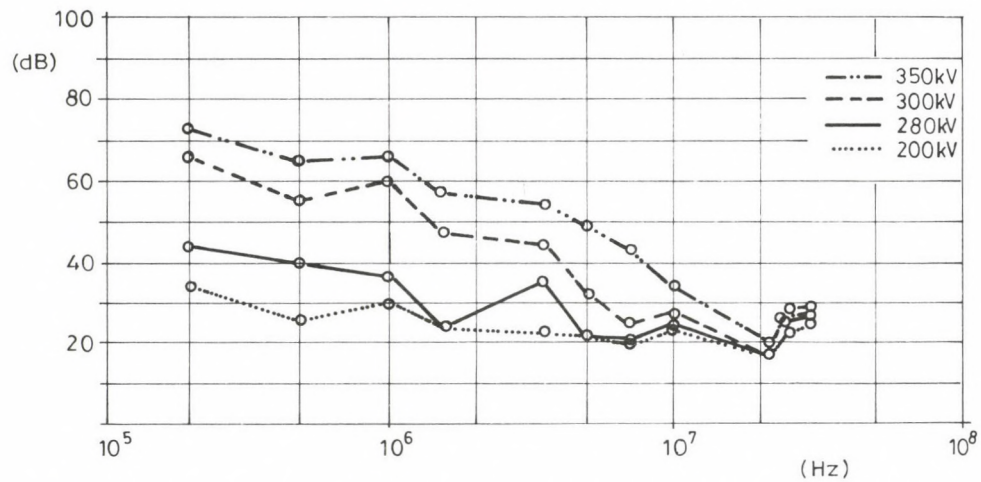

Fig. 8b. Radio interference of a 12 m long bundle conductor measured in the laboratory (cleaned conductor)

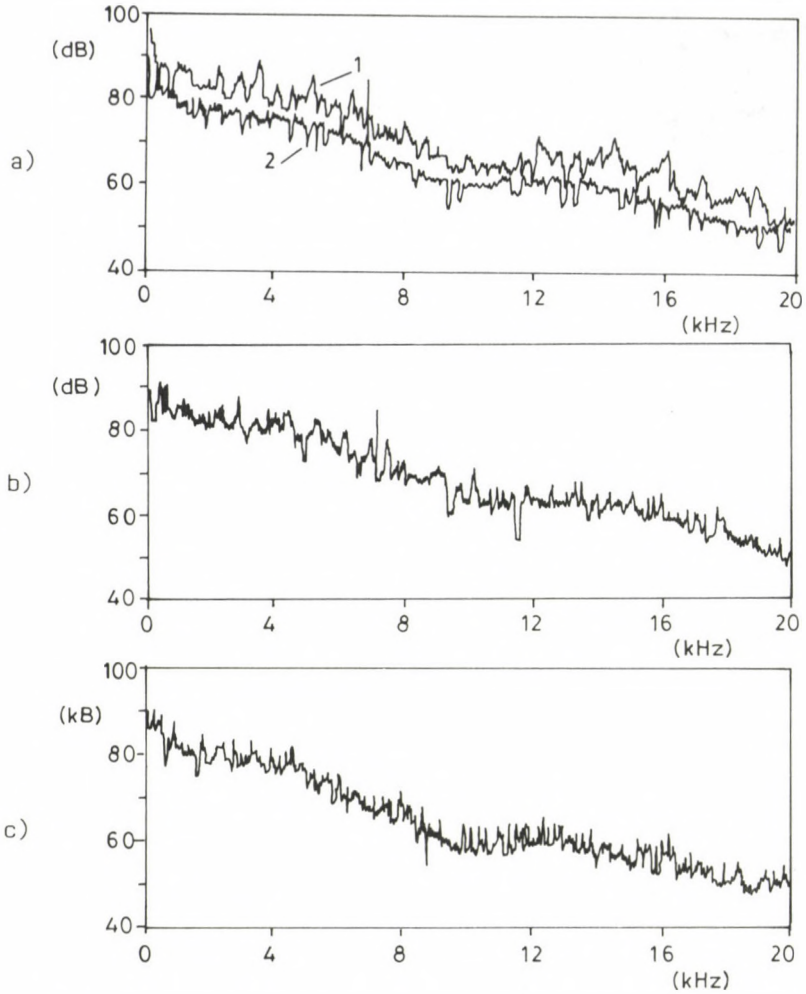

Fig. 9. Audible noise of a 12 m long bundle conductor measured in the laboratory
a) polluted (curve 1) and cleaned (curve 2) conductors at 350 kV,
b) polluted conductors at 350 kV, c) cleaned conductors at 350 kV

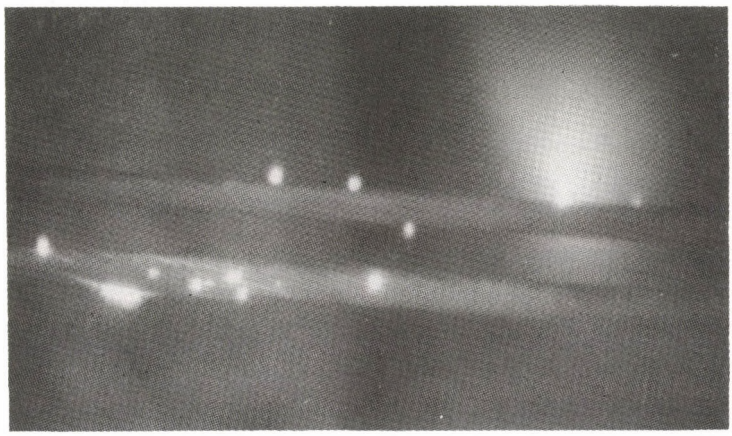

Fig. 10. Corona discharges shown by a night vision system (polluted conductors at 300 kV)

conductor. During the audible measurements the Fourier analyzer recorded the spectrum at four hundred different frequencies. The difference can be evaluated at each frequency for the different voltages as shown in Fig. 9a, b, c.

The same influence made on radio interference and audible noise can be determined as on the actual line. Especially, a drastic increase can be measured for these characteristics at the voltage where the intensive corona appeared over the drops of the polluted conductor. This phenomenon is shown in the picture transmitted by a night vision system (see Fig. 10).

The laboratory results were in good agreement with the field test results and proved that the corrective measures were suitable for decreasing the environmental influence of the high voltage line below the limit.

5. Conclusion

About 130 km single conductor length in the Austrian 380 kV network have been cleaned with the system described above in the mountainous and agricultural area. The results of the measurements performed on the 380 kV power line and in a high voltage laboratory show the applicability of this method.

Acta Technica Acad.Sci.Hung., 105(1-2), pp. 53-67 (1993)

A STUDY OF TRANSMISSION LINE INTERFERENCE CAUSED BY SPACERS

JERMENDY, L.* - KRYLOV, S.V.** - TIMASHOVA, L.V.***

(Received: 7 March 1991)

With increasing the number of subconductors in phase bundles of EHV and UHV transmission lines, the number of spacers in spans also increases. Unstable contacts in hinge joints under conductor oscillations give rise to gap discharges and an increase of overall transmission line interference level. In the development of new spacer designs measures should be taken in order to rule out gap discharges.

Interference on transmission lines can occur both as a result of corona on conductors and due to partial discharges and corona on insulators, breakdown and spark-over of defective insulators, corona on line fittings, as well as due to sparking in bad contacts of line fittings and insulators in strings.

Measurements on transmission lines have shown that in a number of cases line fittings and insulator strings are interference sources in the presence of gaps and sharpened elements.

Discharges occur between metal parts with bad contacts. These bad contacts may be caused by corrosion, dirt and dry pollution.

Dry weather improves insulation of contacting metal parts and favours the appearance of sparks. Rain and snow short out a gap, creating a conducting chain between charged parts.

Measurements of interference caused by gap discharges at different relative humidity have shown /1/ that with a 10% increase of humidity in the range of 70-95% interference decrease was about 20 dB, and at humidity

*Jermendy, László, H-1026 Budapest, Pasaréti út 63, Hungary

**Krylov, S.V., VNIIE Moscow, Kashirskoe chaussee, Russia

***Timashova, L.V., VNIIE Moscow, Kashirskoe chaussee, Russia

Akadémiai Kiadó, Budapest

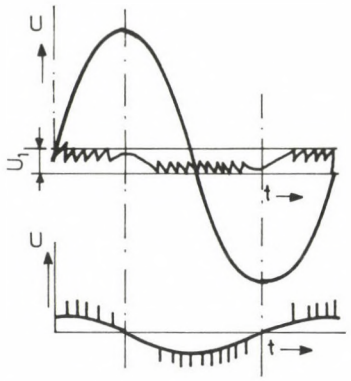

Fig. 1. Voltage change and current impulses in the process of gap discharge

higher than 95% interference was comparable with inherent meter noise. Thus, interference, caused by gap discharges takes place in dry weather.

Interference generated by corona on conductors is maximal at precipitation. With gap discharges the highest interference occurs in fair weather which amounts to about 75% of the year for the central part of the USSR.

With increasing and decreasing voltage U (Fig. 1) /2/ during each half-cycle capacitive discharges occur in gaps of fitting joint, having bad electric contact. Such break-down happens at voltage U_1 and results in decreasing the potential difference of two parts joint up to zero. Electric strength of the non-conducting film in the joint (or the air gap in it) is restored and voltage applied to the capacitor electrodes rises again up to the break-down voltage and then the capacitive discharge occurs again. At the voltage amplitude value during a half-cycle a small arc may be initiated for a short time. The arc goes out at voltage drop during the half-cycle in which capacitor break-down occurs again with a high pulse repetition rate at voltage U_1. Such capacitive discharges take place both at the positive polarity and at the negative polarity of voltage having an estimated value of 100-300 V /2/. The capacitive discharges result in the appearance of current impulses, as shown in a current oscillogram (Fig. 1). Each current impulse is accompanied by the change of electromagnetic field and is a source of high frequency interference.

Gap discharges generate interference in a wide frequency range /2, 3, 4/. Investigations carried out have shown that gap discharge frequency

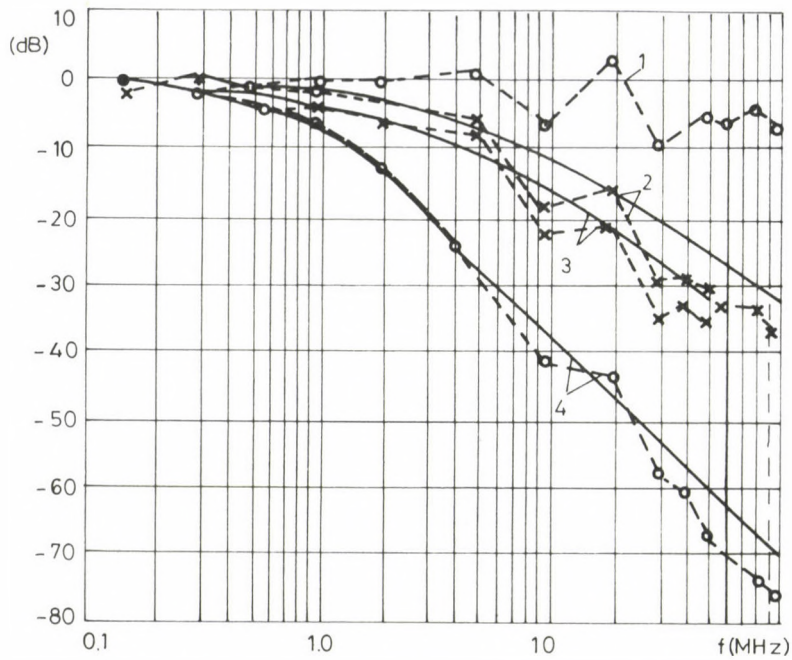

Fig. 2. Frequency spectra of interference from electric discharges and corona (1 - gap discharge, 2 - negative streamer, 3 - negative glow, 4 - positive streamer)

spectrum was sloping and in this case interference intensity decreases with increasing frequency more slowly (see Fig. 2, curve 1) than with corona on conductors (see Fig. 2, curves 2, 3, 4).

Most of hinge joints of insulators and fittings in strings carry considerable static load and have stable electric contact.

Unstable electric contact occurs inslightly loaded joints or hinge joints, subjected to alternating loads.

On transmission lines with bundle conductors most commonly used fittings are spacers, having movable hinge joints, subjected to loads varying their value and direction. It promotes the appearance of additional interference sources on transmission lines with bundle conductors. Tests on 400 kV lines with defective spacers /1/ have shown that interference was generated in a wide frequency range and slowly attenuated with a distance from the transmission line (Fig. 3). Figure 4 shows, for comparison, frequency spectra of interference caused by double circuit 400 kV lines with delta phase arrangement. Curve 1 (Fig. 4a) is related

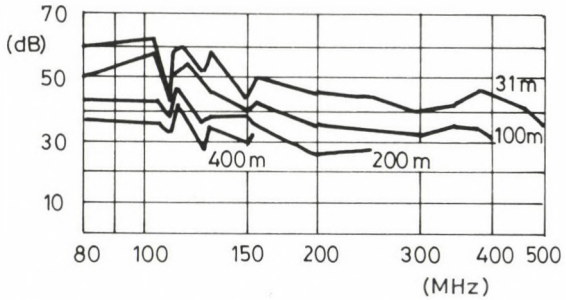

Fig. 3. Frequency spectra of TVI generated by gap discharges on the 400 kV transmission line

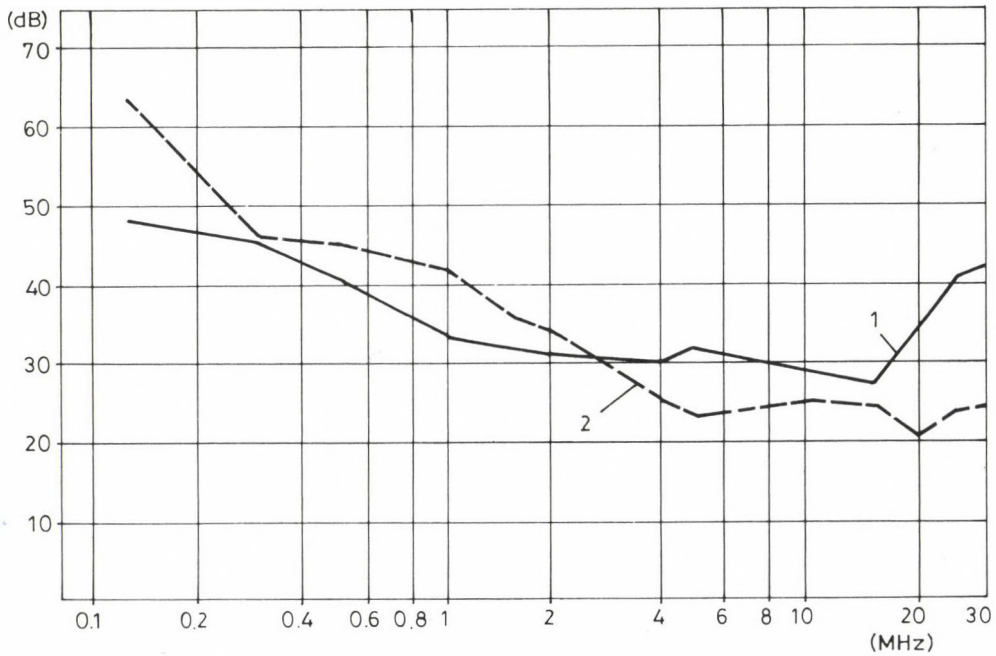

Fig. 4a. Frequency spectra of interference caused by 400 kV lines in the frequency range of 0.1 - 30 MHz
(1 - for lines with discharge in gaps of defective spacers, 2 - for lines with corona on conductors)

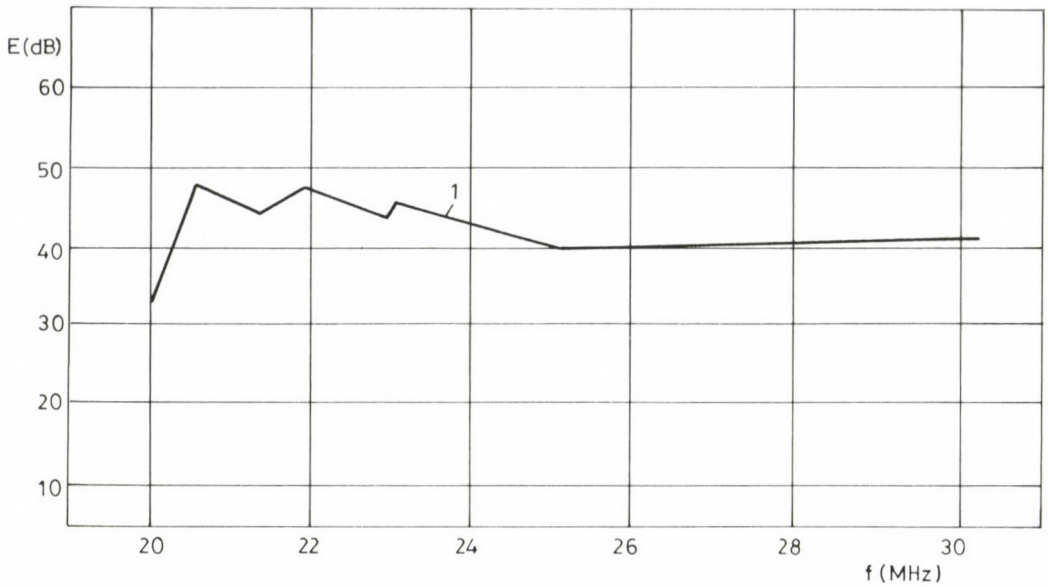

Fig. 4b. Frequency spectra of interference caused by 400 kV lines in the frequency range of 20 - 30 MHz
(1 - for lines with discharge in gaps of defective spacers)

to a transmission line with defective spacers. For the same line a spectrum in the 20-30 MHz frequency range was obtained (Fig. 4b). It shows that interference intensity is not influenced by the frequency practically.

Measurements on 1150 kV lines have shown that in fair weather interference intensity is determined to a considerable extent by discharges in gaps of line fittings because of fitting complication in comparison with 400 - 750 kV transmission lines. Gap discharges in a strongly non-uniform field are generated at low line voltages. So, on a 1150 kV line considerable interference (48 - 58 dB) under the nearest phase was detected at 500 kV, when electric field strength on the conductor surface was smaller by a factor of 2.5 than the corona onset voltage (12.3 kV/cm). In this case interference sources were discharges in spacer gaps. To estimate interference from spacers, having hinge joints with gaps, special experimental investigations were carried out in a HV room on a model of a bundle conductor together with a spacer design, having movable hinge joint of increased resistance. The model of the bundle conductor of 6 m length had end screens to eliminate corona sources.

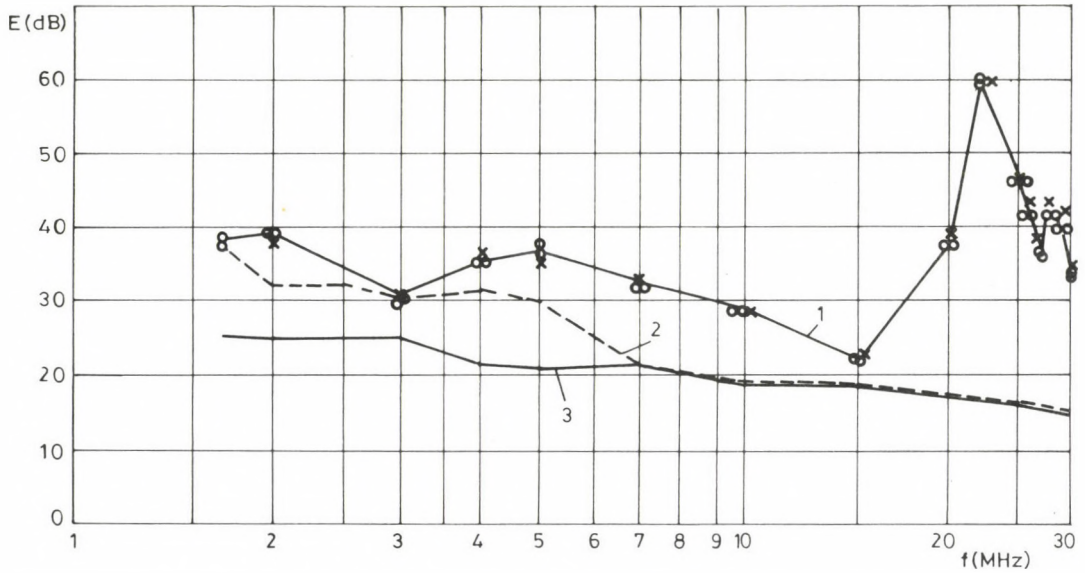

Fig. 5. Frequency spectra for the bundle conductor model
(1 - with a spacer, having an artificial gap at voltages of 150, 200 and 250 kV,
2 - without spacer at U = 250 kV, 3 - testing room background)

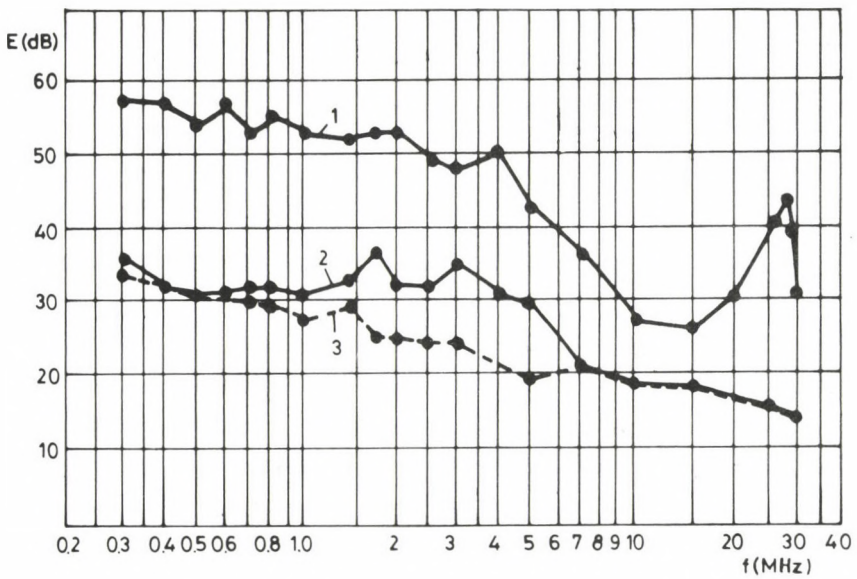

Fig. 6. Frequency spectra for the bundle conductor model in the frequency range of 0.3 - 30 = MHz
(1 - with a spacer in gap discharge at voltage of 250 kV, 2 - without spacer, U = 250 kV,
3 - testing room background)

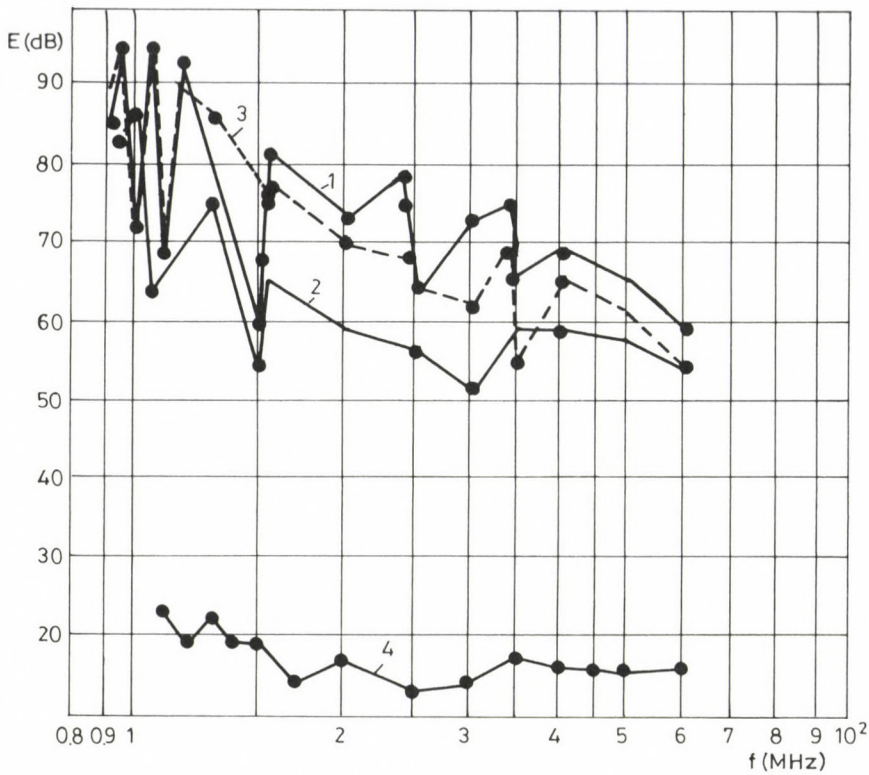

Fig. 7. Frequency spectra of spacers on the bundle conductor model (1, 2, 3 - in hinge joint gaps of 0.3 mm, 0.09 mm and 1 mm, respectively, 4 - testing room background)

Measurements of frequency spectra from spacers mounted on the bundle conductor model (curve 1, Fig. 5) were made without streamer corona. Measurements of the model frequency spectrum at 250 kV without spacer (curve 2, Fig. 5) were also carried out and the testing room background noise was measured (curve 3, Fig. 5). When a spacer with an artificially made gap was installed on the bundle conductor model, measurements of frequency spectra were carried out at voltages of 150, 200 and 250 kV (curve 1). The measurements showed that interference levels were independent of voltage applied to the bundle conductor model. Figure 6 (curve 1) shows a frequency spectrum of the model with a spacer at 250 kV in the 0.3-30 MHz frequency range. Also investigations of frequency spectra were carried out in the HV testing room in the range of 90-600 MHz with installation of spacers, having artificial gaps of 0.09, 0.3 and 1 mm, on the bundle conductor model. Results of these investigations are presented in Fig. 7. The

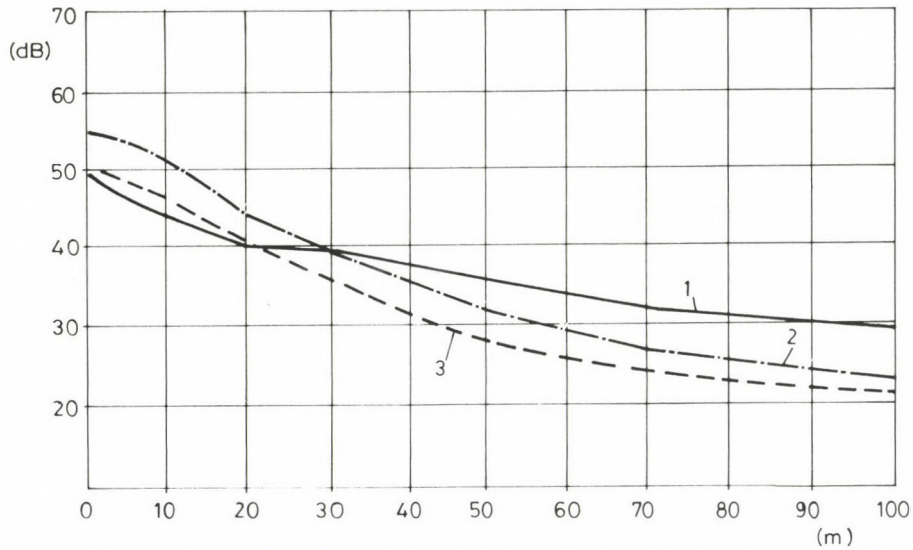

Fig. 8. Lateral profiles of interference from 400 kV transmission lines at 0.5 MHz (1 - for lines with defective spacers, 2 - for lines with corona on conductors, 3 - calculated characteristics taking account of corona on conductors; see formula (1))

results presented in Figs 5 to 7 show capacitive discharge in a gap of a spacer hinge joint to be an interference source in a wide frequency range.

The gap discharge generates interference which holds a considerable level at a great distance from the line. Values obtained from measurements on operating lines are a sum of interference from various sources. Figure 8 shows lateral profiles of interference from double-circuit 400 kV lines with delta-phase arrangement at 0.5 MHz. Curve 1 (Fig. 8) was obtained for a line with defective spacers. Curve 3 was plotted on the basis of calculations according to the well-known formula:

$$E''_n = E'_n + 20\ k \log \frac{R'}{R''} \qquad (1)$$

where

E'_n, E''_n - interference level,

R', R'' - distances from the nearest phase of the line,

k - the lateral attenuation factor.

Based on the measurement results obtained on 400 kV transmission lines with delta-phase configuration the lateral attenuation factor k is equal to 1.7. When an interference source on the line is only corona on con-

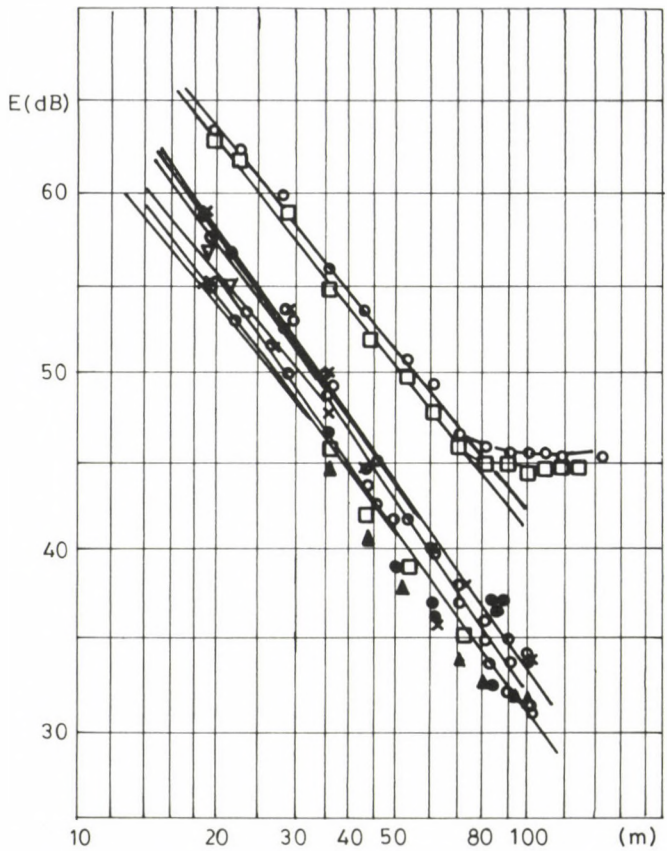

Fig. 9. Lateral profiles of radio interference on the Ekibustuz-Kokchetav 1150 kV line in the spans between towers
(1 - No 1314 - 1315, No 1229 - 1230, 3 - No 1254 - 1255, 4 - No 1314 - 1315, 5 - No 1263 - 1264)

ductor (curve 2, Fig. 8), an attenuation character coincides with the wide spread dependence (curve 3).

Figure 9 presents lateral profiles of radio interference at 0.5 MHz from the Ekibustuz-Kokchetav line on a semi-log arithmetic scale that well represents the physical law of interference variation with a distance. The straight lines in the figure were obtained by the method of least squares /5/. As seen from the figure, an attenuation character for most of the spans follows equation (1). However, on a number of spans interference at distances of 60-80 m from the line is almost unchanged. It is caused by interference due to discharges in spacer gaps that was determined by direct measurements with a directional antenna. Spacers for sub-

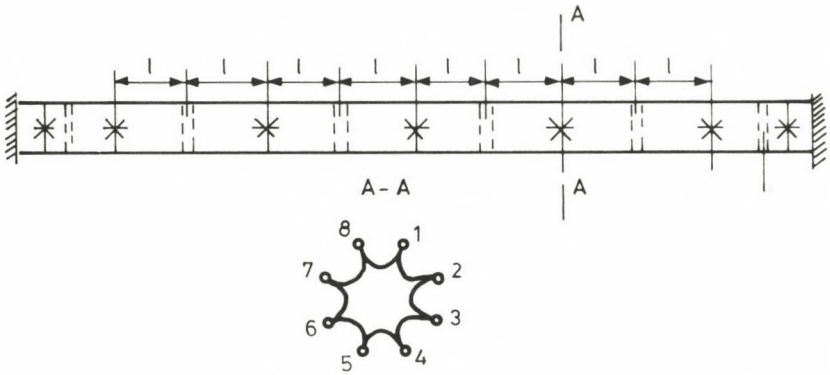

Fig. 10. Scheme of spacer installation on the bundle conductor of the Kustanay - Chelyabinsk 1150 kV line. Distance l is no longer than 40 m

conductor fixing on a given contour contain clamps locked on the subconductors. The clamps are usually demountable threading die ones, movably jointed to the spacer (arm) body.

Spacers may be made as twin-spacers (for jointing two subconductors) or "fixed" ones with clamps attached to the common body-arm configuration or in the form of a frame.

Subconductor fixing in spans is effected by spacers of various designs. The simplest designs are the spacers intended for two conductors fixing at a given distance.

On initial sections of a 1150 kV line for subconductor fixing 8RGSh - 4-400 type spacers with RGSh threading clamps are used. Different spacer configurations (twin or arm) were tested on different sections of the 1150 kV line, proceeding from subconductor oscillation control and for the future it is recommended to use spacers with RGN type threading die clamps (instead of RGSh clamps) on new line sections.

Figure 10 shows a scheme of installation of twin-spacers and fixed (arm) ones on the Kustanay-Chelyabinsk 1150 kV transmission line conductors. In this scheme, side with fixed spacers (similar to arm spacers for functions), fixing units, made on the basis of RGN twin-spacers, are used.

Spacer threading die clamps, locked on line conductors and being at high conductor potential in the strong electric field may be a source of corona interference.

The appearance of streamer corona sources on spacer threading dies may be related to a design defect of spacer parts (protrusions, sharp edges) or technical defects on surfaces of spacer parts (burns, protruding sur-

face defects, marks,etc.). Spacer damages in mounting (traces of strokes, scratches and hang-nails from mounting tools) are possible. Protruding parts of bolted joints (the protruding bolt end and the nut head) may be streamer corona sources as a result of incorrect clamp assembly or an incorrect choice of the spacer bolt.

Electrical potential values of bundle subconductors are somewhat different from one another, and a change of voltage for two subconductors varies from 0 to 1000 V. In such conditions a spacer is an electric circuit, characterized by contact resistances in successive contact joints and by conductance of spacer parts which carry currents.

Spacer parts are made massive and their resistance does not vary practically all through transmission line operation. The contact resistance of "conductor-threading die clamp" contacts is relatively stable. The ring joint of the threading die clamp to the spacer arm is movable and electric contact break in such joints gives rise to gap discharges.

RGN spacers have been used on 330 kV lines in different climatic conditions of Russia for a long time. The RNG spacer consists of two threading die clamps and a steel arm, jointed by hinges at its ends to the above mentioned threading die clamps. Each clamp (Fig. 11a) consists of two aluminium threading dies and a coupling bolt, ensuring reliable fixing of the threading dies on bundle subconductors. With normal fixing of the spacer clamps on the conductors sufficiently stable electric contact is secured.

Figure 12 shows equivalent circuits of spacers with clamps of RGN and RGS types. The contact resistances of the "threading die-conductor" contacts are denoted R_{11} - R_{1n} as unchanged values. The threading die clamp joints to the arm of the RGN type spacer is made movable by means of the "finger-lug" hinges. The electrical contacts of "finger-lug" parts, shown as resistances R_{21} - R_{2n} (Fig. 12a), are unstable. In conductor oscillations these contacts may be interrupted completely, in which case these connections can be represented by capacitors C_{21} - C_{2n} with air dielectric between the parts (see Fig. 12c).

An air gap value of hinge conjugated parts of RGN spacers is a random variable and even under the greatest difference of subconductor potentials U_1 and U_2 air gap break down occurs in the "2-finger-lug" hinge gap with high probability. Electric discharges arising in hinge gaps, as experimental investigations have shown /1, 4/, are interference sources both in the radio frequency range and the television frequency range. The RGS

a)

b)

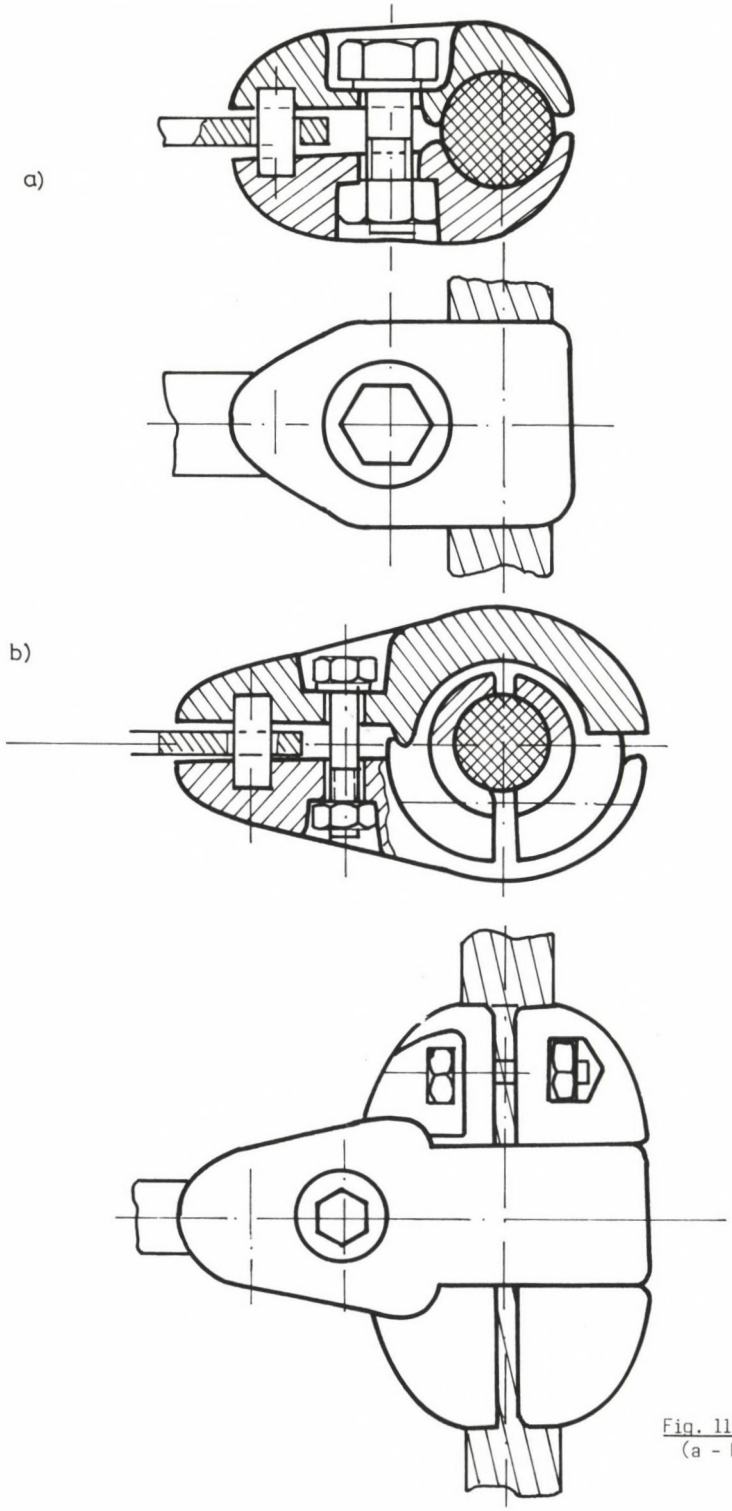

Fig. 11. Design of spacer clamps
(a - RGN type, b - RGS type)

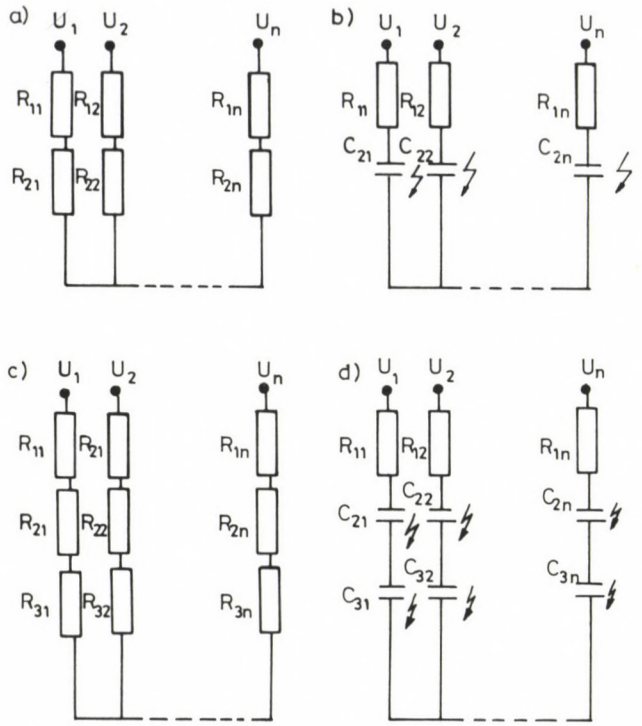

Fig. 12. Equivalent circuits of arm spacers of RGN type (a, b) and RGS type (c, d) for a phase bundle conductor of n subconductors
(a, c - under stable contacts in joints, b - under unstable electric contacts in hinge joints)

spacer is equipped with additional hinge joints between the arm and the threading die clamps fixed on bundle subconductors.

Equivalent circuits of such spacer are presented in Fig. 12c, d. The contact resistances of electrical contacts of the threading die clamps, mounted on bundle subconductors, are denoted R_{11} - R_{1n} in accordance with subconductor ordinal number, the resistances of the movable "threading die clamp enclosing threading dies" hinges are denoted R_{21} - R_{2n}, respectively and the resistances in the movable joints of the enclosing threading dies to the arms on the spacer body are denoted R_{31} - R_{3n}, respectively.

As shown in Fig. 12a, c, the hinge connection resistances (R_{21} - R_{2n}) and R_{31} - R_{3n}) as air gaps in the hinges are formed, can be converted (see Fig. 12b, d) into capacitors with air dielectric denoted as C_{21} - C_{2n} and C_{31} - C_{3n}, interference occurring in their breakdown. As it follows from the spacer equivalent circuits, the number of hinge joints in the 8RGN spacer design decrease twice as compared to the 8RGS spacer and according-

ly a probability of electric discharge occurrence in gaps of spacer hinge joints decreases.

Calculations have shown that in the use of the spacer installation scheme, shown in Fig. 10, on transmission lines the number of hinge joints with unstable electric contact reaches 1140 per 1 km of a line. As compared to 330 kV transmission lines with twin bundle, where there are 150 contact joints with unstable electric contact per 1 km, the number of such contacts on 1150 kV lines increases 7.6 times in 4 times increasing the number of subconductors in all. Such estimations point out a probability of interference occurrence due to discharges in spacer gaps on UHV transmission lines to be nearly by an order of magnitude greater than for 330 kV lines and twice as much as for 750 kV lines.

Designs of movable spacer part joints without gaps, realized at the cost of application of elastic damping elements /6, 7/ are used. In this case, elastic polymer materials (rubber), having dielectric properties along with properties of elasticity, are used as damping elements in hinges. Such hinge joints become capacitors in a spacer equivalent circuit. In addition, air gaps in hinge joints of spacer parts are made large enough in order for break-down of air gaps in joints of insulated spacer parts not to take under voltages less than 1.5 kV.

Conclusions

Many psacers mounted on EHV transmission line bundle conductor can be sources of interference at the transmission lines in a wide frequency range caused by both gap discharges and the presence of streamer corona.

Spacers are subjected to alternating loads under which the probability of gap occurrence is high.

Gap discharges are local interference sources, which do not attenuate at considerable distances from the lines and propagate along the conductors far away. Taking account of that, either reliable electric contact of conjugated parts under all spacer operating conditions or reliable insulation at voltage of 1.5-2.0 kV should be secured in hinge joints.

A design of spacers with elastic hinge joints, providing reliable insolution, meets also high service requirements to reliability under phase conductor dynamic oscillations.

New spacer designs should be subjected to thorough tests for interference absence.

REFERENCES

1. Jermendy, L., Timashova, L.V.: Television interference and audible noise caused by lines. Laboratory and field test results. R89N7 Electromagnetic compatibility 1989. 8th International Zurich Symposium and Technical Exhibition on Electromagnetic Compatibility, 7-9 March, 1989

2. Kohutova, D., Vokalek, F.: Hochfrequente elektromagnetische Störungen des Rundfunk- und Fernsehempfangs durch Hochspannungs-Energieübertragung. Fernmeldetechnik 20 (1980) H5, 188-190.

3. Janischewskij, W., Hussein, A.M., Santiago, N.H.C.: Performance and analysis of a micro-gap discharge circuit. IEEE Transactions on Power Delivery. Vol. 3, No. 2, April 1988, 694-706

4. Jutte, G.W.: Evaluation of television interference from high-voltage transmission lines. IEEE Trans. PAS 1972. Vol. 91, No. 3, pp 3 and 865-873

5. Gurskij, K.I.: The theory of probability with elements of mathematical statistics. - M. Vischaya Shkola, 1971

6. Morsetteria hardware. Electromeccanica Sud. (NES) Catalogue Italia, 1974

7. Hochspannungsarmaturen HA'74. Karl Pfisterer Catalogue (Germany), 1974

Acta Technica Acad.Sci.Hung., 105(1-2), pp. 69-81 (1993)

EXPECTED CREEP OF THE STEEL-ALUMINIUM TRANSMISSION CONDUCTORS IN OPERATION

NÁDOR, L.* - KRÓMER, I.** - VÖŐ, L.***

(Received: 14 April 1992)

Due to the effect of lasting mechanical loading the transmission line conductors of aluminium show permanent elongation, that is why the expected load and sag conditions for their lifetime can only be determined with consideration to creep developing in operation. The purpose of our examinations referred in the article is to determine the relations describing permanent elongation of the conductors in the function of the condition parameters by means of measurements, and to calculate the expected creep for the total lifetime.

For this purpose we have elaborated a measuring and evaluation method that would ensure reproducibility of the experimental results. Having added the measuring results to those of foreign studies we have determined the empiric creep equations characterizing the steel-aluminium conductors. Having made the generally used condition equation of the transmission line conductors suitable for paying attention to permanent elongation we obtained a time-dependent condition equation which can be numerically solved. The lasting control examinations performed with transmission lines of 400 kV proved that the results calculated this way show good compliance with the measurement.

Introduction

Overhead lines will remain the most important means of electric power transmission and distribution for a long run. In addition to their other advantages and relative cheapness, their key strength is that they can be envisaged for a long lifetime with relatively low demand for maintenance. In compliance with the traditional method of designing, the height of live conductors above the ground or another establishment has to be determined on the basis of sag resulted from external mechanical load developing in the conductor or as a result of the permitted current loading. If we fail

*Nádor, Tamás, H-1055 Budapest, Balassi Bálint u. 25, Hungary

**Krómer, István, H-1118 Budapest, Sasadi u. 14, Hungary

***Vöő, László, H-2310 Szigetszentmiklós, Miklós tér 10, Hungary

Akadémiai Kiadó, Budapest

to consider creep expected in course of the lifetime of the conductor in our calculations, or do not provide, in any other way, for compensation of growing sag caused by permanent elongation, then we have to take the hazard of reducing the free height below the minimum permitted value.

However, on the other hand, if we wish to compensate the effect of creep by means of overregulation of the conductors (being in the present domestic practice 5% in case of ACSR wire of 500/65 mm^2) and adjustment is performed in the winter period, then it may happen that we not only achieve the greatest standard tower loading resulting from pulling of the conductor, but can even exceed it.

It can be seen from the above that knowledge of creep of the conductors is needed already in the phase of designing. The fact that the consumers require from the manufacturer announcing of the value of creep determined by means of measurements refers to the same fact.

As it has already been revealed by earlier examination, permanent elongation of the aluminium conductors is developing as a resultant of components being dependent on the period of load and of components being in fact independent of the same. The first one is creep of metallurgical origin, while the second group is made of permanent elongation resulting from the geometrical layout of the elementary wires and from the pressure developing at the crossing of the elementary wires.

The method of laboratory testing has to be developed, in compliance with the above, so that it would provide well assessable measures of permanent elongation occurring during long time period in the range of the expected mechanical stresses as well as conductor temperatures.

We shall describe in this article the method of laboratory procedure developed for determination of creep of aluminium conductors as well as the method of assessment of the measured values by means of which reproducibility of the empirical results is granted.

In addition to the tests performed in the laboratory ERŐTERV (Power Station and Network Engineering Co.) we carried out regular measurements of sag and temperature from the moment of adjustment of the conductors in a span of the 400 kV transmission line Toponár-Héviz with the target of obtaining direct results as to the permanent elongation of conductors subjected to real mounting and weather conditions.

For the sake of comparing the results of laboratory and field tests a method has been elaborated, by which the increase in sag of the conductors operating under different loading conditions can be reliably calculated.

1. Laboratory method for the measurement of creep of conductors

The method of laboratory measurement of permanent elongation of the conductors had to be developed so that the external factors that may affect the creep following its production, could be kept at a constant value in course of the examination.

The measure of creep is affected by mechanical load and temperature of the conductor and accordingly these two parameters have to be maintained as constant as possible /1/. That is why the measurements were performed on 6 m long conductor pieces spanned on an 8.5 m long stand located in a chamber with heat insulation and conditioning. Pulling force was developed by means of a weight hanged in the middle of the test samples. Application of the loading was solved by means of quick removal of the supports of the weight. The exact value of the required pulling force could be adjusted by means of pulling spindles. Elongation measurement was made on each sample at two points, on 1 meter long sections, with 2 extensometers each. Accuracy of the readings was 0.002 mm.

Following application of the loading the extensometers were read first every 2 minutes, then after an hour, every two hours, and beginning from the next day once a day. The first 5 points of measurement have been drawn in a coordinate system of linear scales and we drew the curve from which the strain which occurs during the first 6 minutes was determined. This value is considered as the one belonging to time 0.

Further on we have plotted the points on logarithmic (log-log) scales where the temperature must not differ from the set value by more than $\pm 1\ ^{o}C$. Temperature correction of the creep values was carried out on the basis of the remained readings. Every measurement result was converted by means of a temperature correction factor determined empirically. Then by means of linear regression we have determined the equation of creep curve and then neglecting the points where the measured creep values differed from the calculated one by more than 2% we have calculated the creep equation again. Creep-time functions measured on CARDINAL 483/63 mm^2 conductor indicated in Fig. 1.

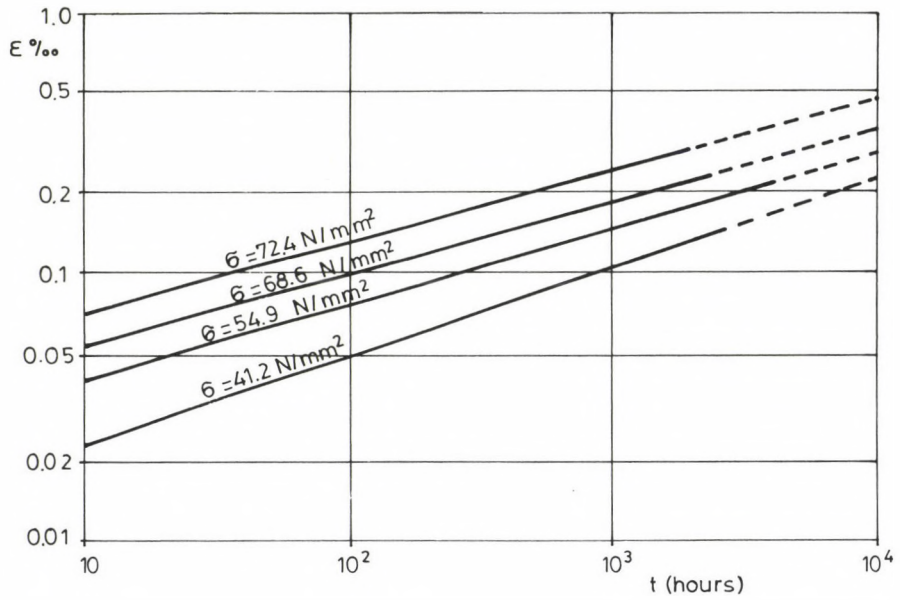

Fig. 1. Creep functions of ENTAL "CARDINAL" 483/63 mm^2 (τ = 28 ^oC)

2. General expression for determination of creep

Creep equation considering changes in both the temperature and the pulling stress may be written according to experience in the following form:

$$\varepsilon = K' \cdot e^{\phi \tau} \cdot \sigma^{\alpha} \cdot t^{\mu/\sigma^{\delta}} \qquad (1)$$

where

σ is pulling stress (N/mm^2)

τ is temperature (^oC)

K', ϕ, α, μ, δ are constants depending on the conductor.

At constant τ the creep equation can be rewritten in the following form:

$$\varepsilon = K'' \cdot \sigma^{\alpha} \cdot t^{\mu/\sigma^{\delta}} \qquad (2)$$

where

$K'' = K' e^{\phi \tau}$

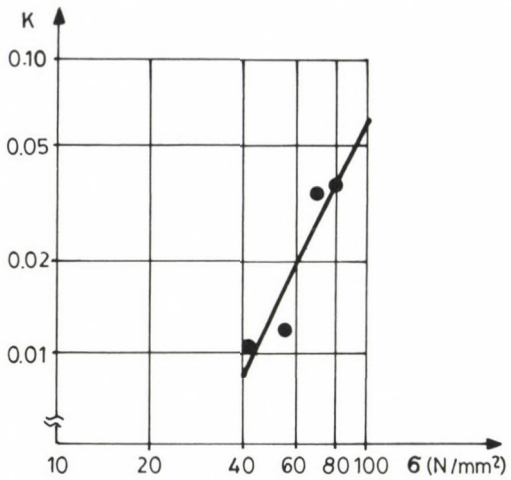

Fig. 2. Parameter "K" in the function of mechanical stress (τ = 28 ^{o}C)

Plotting the product of K" $.\sigma^{\alpha}$ - multiplication factors of the creeping equation - in log-log scales we obtain a straight line (Fig. 2) since:

$$\lg K = \lg K'' + \alpha \, . \, \lg\sigma \tag{3}$$

Parameters K" and α as well as $K' = K''/e^{\phi\tau}$ can be calculated from the points of measurements by means of linear regression.

Exponent μ/σ^{δ} from equation (1) can be written in the following form:

$$\mu_i = \mu/\sigma^{\delta}{}_i \tag{4}$$

where

μ_i is the exponent measured at σ_i stress and

μ, δ are the constants depending on the conductor.

Deriving logarithm of both sides:

$$\lg\mu_i = \lg\mu - \delta \, . \, \lg\sigma_i$$

we can see that in logarithmic scales it is straight, too (Fig. 3), thus the value of μ and δ can be determined by means of linear regression.

Knowing the parameters we can write the equation of creep, which takes into account the change in pulling force and in temperature, too. In case of the CARDINAL 483/63 mm^2 wire the following empirical relation is obtained /4/:

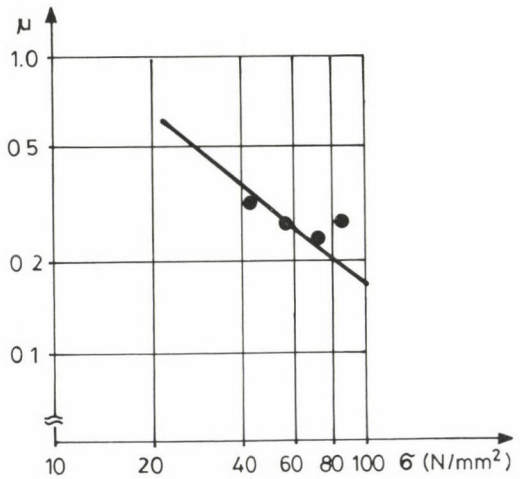

Fig. 3. Parameter "μ" in the function of mechanical stress

$$\varepsilon = 9.933 \cdot 10^{-6} \cdot e^{0.01824 \cdot \tau} \cdot \sigma^{1.7756} \cdot t^{0.0132/\sigma^{0.26451}} \qquad (5)$$

where

t time (hours),

σ stress (N/mm^2),

τ temperature (^{o}C).

In view of that fact that the wire manufacturer often needs creep parameters of conductors that have never been subjected to measurements and has no possibilities for long-lasting tests, we have tried to elaborate a generally usable empirical expression.

For this purpose we have proceeded from the fact that in addition to the loading of the aluminium elementary wires the conditions of twisting exert the greatest effect. This effect, according to the experience of ALCOA, can compensate the effect of steel-aluminium ratio. Only steel wires with cross section below 7.5% are the exceptions /2/.

As a result of the above the deviation between the creep of ACSR conductors of different sizes, made under the same twisting conditions is of similar magnitude as the deviation of creep of conductors of the same size but made under different twisting conditions. That is why it is most practical to give the creep of steel-aluminium conductors with a relation expressing an average value. For the purpose of determining this general relation we used the measurement results obtained in 20 ^{o}C environ-

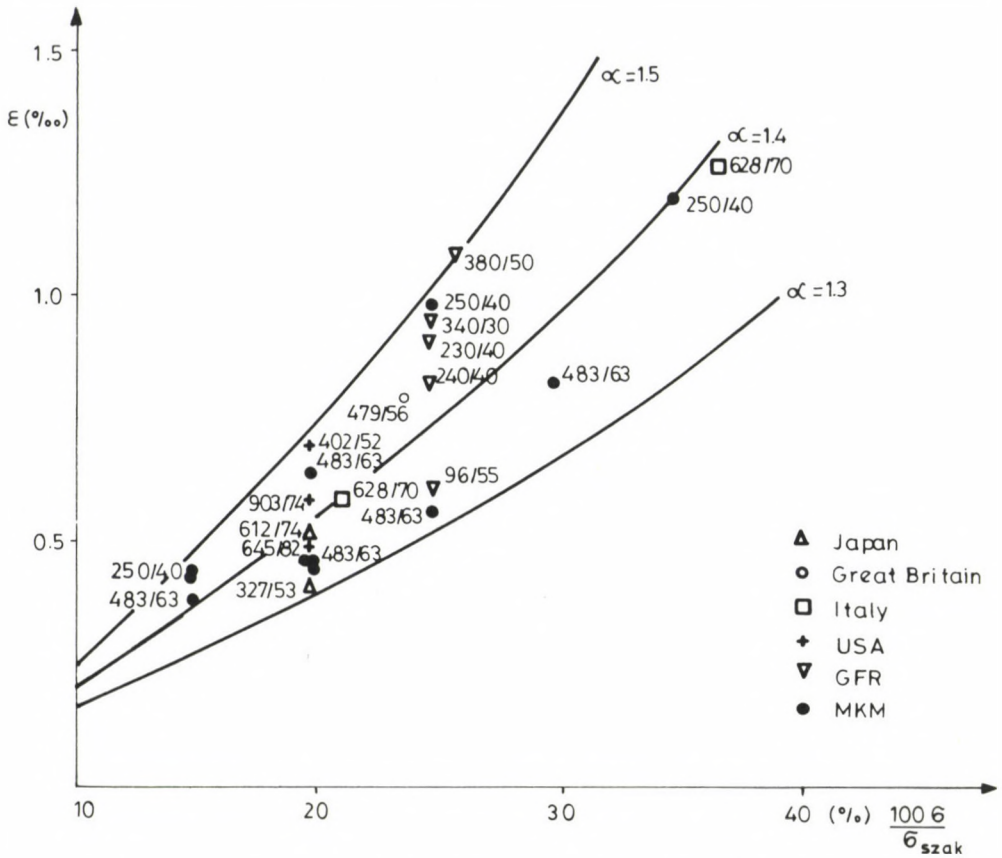

Fig. 4. Change in creep calculated for 37600 hours in the function of specific tensile forces, according to different measurements

ment of other laboratories, which were plotted in the function of the relative tensile strength in Fig. 4 /3/.

The figure shows the size of creep for a period of 10 years. We have used the following equation for summing up the measurement results:

$$\varepsilon = K'' \left(\frac{100}{\sigma_{ult}} \right)^{\alpha} t^{\mu} \qquad (6)$$

where the value of μ was taken for 0.3 - average of the measurement conducted with the domestic conductors and elementary wires for more than a decade, and we have determined the equation of the covering curves. The value of K" is $0.27 \cdot 10^{-3}$, and the extreme values of α are 1.3 and 1.5.

We have to remark that for reasons of simplicity we have omitted the exponential member expressing change in the temperature in equation (6), the exponent of which was in the average of our measurements so far 0.018. This member can be introduced as the effect of change in temperature, if required. We have to note that although the general creep equation of the steel-aluminium conductors is suitable for giving quick information, still the creep parameters of a given conductor with consideration to the large number of the affecting factors and the lack of knowledge of their quantitative influence can be exactly determined only by means of measurements.

3. Calculation method for the determination of creep expected in operation

The equation used for determination of the change in the condition of a conductor suspended between two points describes the joint effect of changes in temperature and load starting from an optional initial condition.

However, permanent elongation is not only the function of load and of temperature of the conductor but also that of time. This way the equation of state becomes the function of time, too, with consideration to the permanent elongation.

The time dependent equation of state can be relatively simply solved numerically, if we divide the total time interval to be examined to subintervals within which the temperature of the conductor is constant or can be considered constant with good approximation.

Within the intervals of constant temperature we can form such subintervals in which load can be considered constant. By means of making the division more precise we can obtain creep-time relation that can be expected under the real conditions. The temperature of the conductors depends, in addition to the ambient temperature, solar radiation and wind conditions, on loading current. That is why the temperature of the conductor in the examined time interval was calculated with consideration to the environmental data on statistical bases, as well as by means of estimation of the expected loading current values of the given period as described below.

From the medium-term network development plans we can determine for a given network the loading of a conductor of a given cross-section.

a)

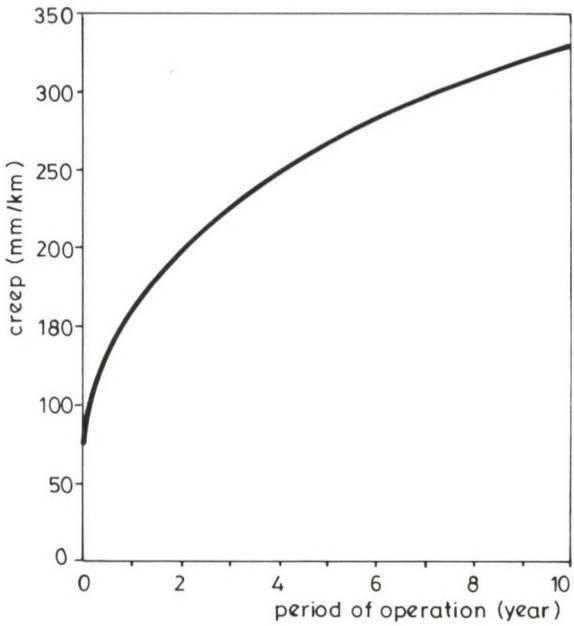

b)

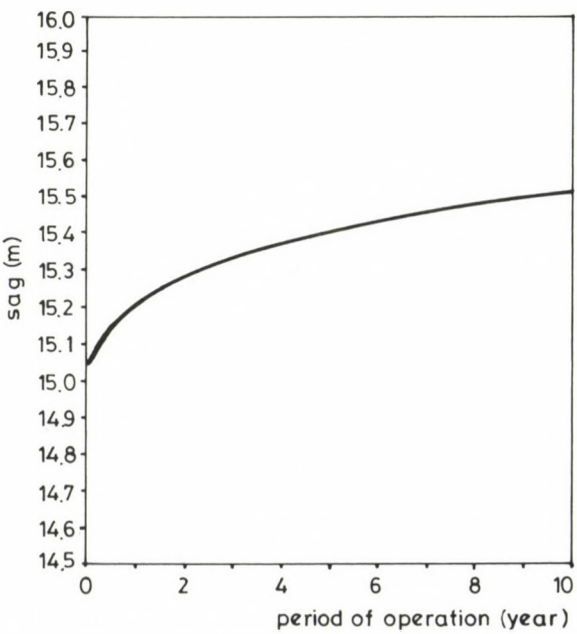

Fig. 5. Functions of CARDINAL ACSR conductor. (a) Creep, (b) sag

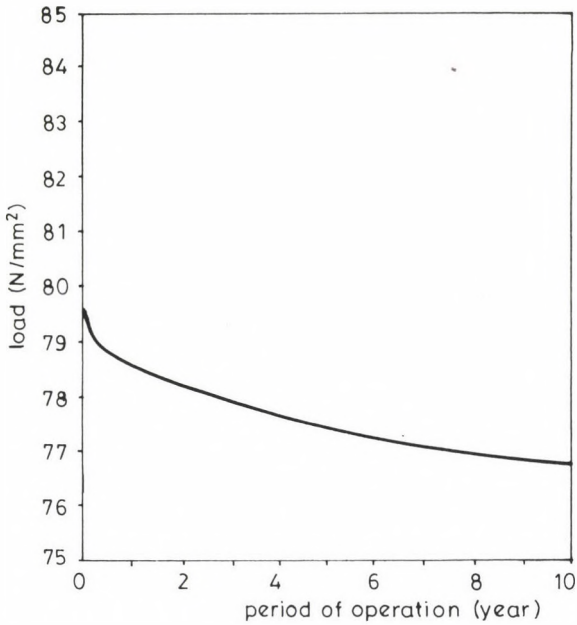

Fig. 5c. Load time

Taking it as an initial basis we can estimate the current with sufficient accuracy for this examination from the daily, monthly and yearly load distribution curves which can be considered as the expectedly most characteristic monthly average value.

The rate of increase in electric energy demands was taken for 3% per annum for the examined period. We have developed a computer program for performing the calculations, which includes the simplified calculation method of temperature change caused by the loading current, the solution of the time-dependent equation of state, and numerical determination of the time functions of creep, sag and load. In the present study the values of sag of the conductor calculated at 60 ^{o}C are considered. Characteristic loading for the tower, however, is determined from the pulling strength of the conductor loaded with an ice burden of -5 ^{o}C.

The functions calculated for 500/65 ENTAL conductor (similar in construction to the Cardinal conductor) and for the domestic meteorological conditions can be seen in Figs 5a, b and c. (Span: 400 m, basic load in mounting: 80 N/mm^2.) Comparing the diagrams with the publications dealing with this subject in the foreign literature we could state that considering the tendency of the change we achieved similar results. The parameters of the creep equation may show differences, mainly due to the

different construction of the conductors. Similarly the load and sag curves may also show deviation, in which the environmental conditions and the loading current patterns play some role, too.

4. Checking of the measurements performed on the 400 kV transmission line Toponár-Héviz

In 1984-85 we performed regular measurements of sag on the 400 kV overhead line Toponár-Héviz, based on a preliminary elaboratored measuring program made on the basis of charge from OVIT (National Overhead Line Co.). In order to get precise picture on permanent elongation of the conductor we measured two related value pairs in every case: namely sag and temperature of the conductor. The possibility for temperature measurement was ensured by the use of thermocouple built into the conductor. The measurements of sag were performed from instrument positions placed at two preliminary set points, by geodetic way. With the help of this method inaccuracies in measurement caused by swinging of the wire due to the wind could be eliminated.

In order to follow the changes in the conditions in the function of time, we had to recalculate every pair of the measured temperature and sag value to the sag occurring at 60 ^{o}C, and to load and change in curve length belonging to -5 ^{o}C + ice load.

The resultant points are seen in Figs 6a and b, where the calculation result that was obtained through insertion of the creep equation measured in the laboratory into the equation of state is represented by the solid lines. The data of the ambient temperature - as monthly average values - were taken into account as per Fig. 7, with consideration to the fact that adjustment of the conductor was performed at the end of July.

The conclusions drawn from comparison of the measured and calculated values are summarized below:

- The performed field measurements and the calculation method based on the laboratory measurements show the same result with good approximation.

It means at the same time that the creep function taken in the laboratory in 2000 hours well covers the approx. 6500 hours' duration of the field measurement. Namely extrapolation for this period is permitted.

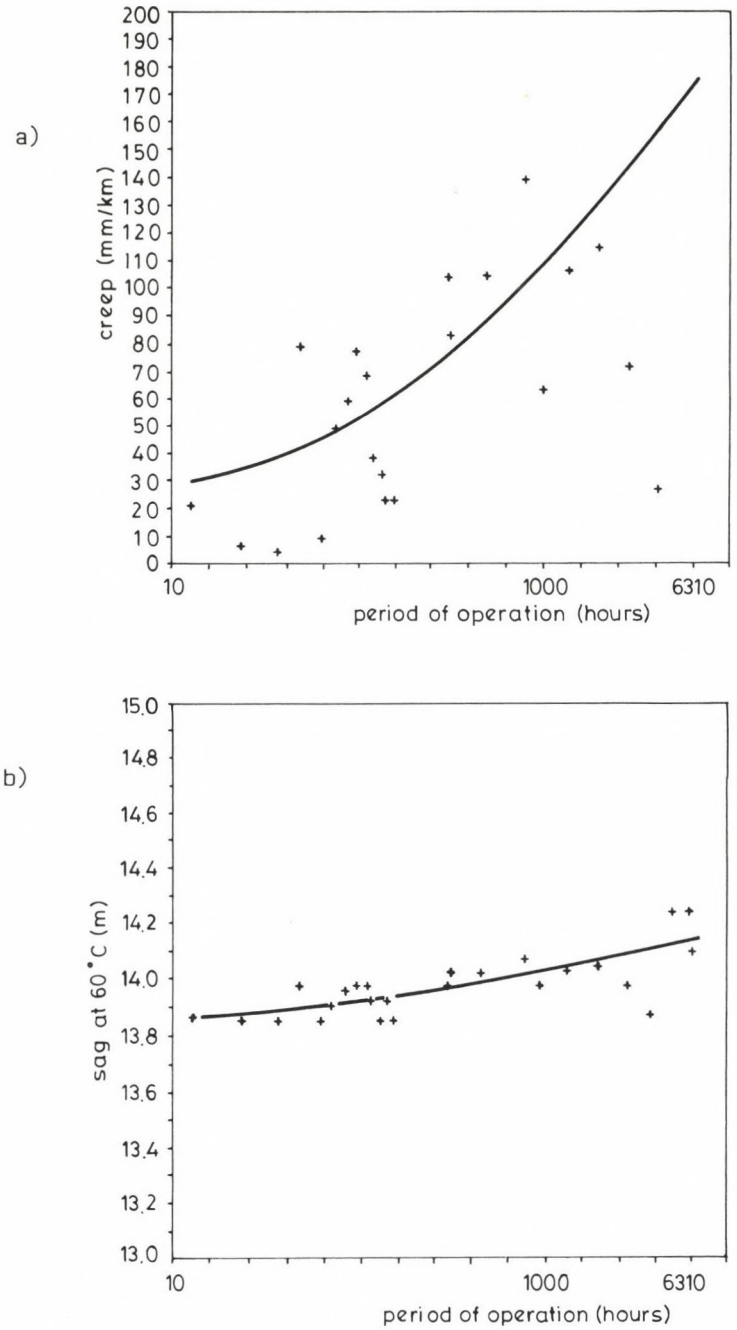

Fig. 6. Function of creep (a) and sag (b) measured and calculated for Toponár-Héviz ACSR transmission line of 500/65 mm^2

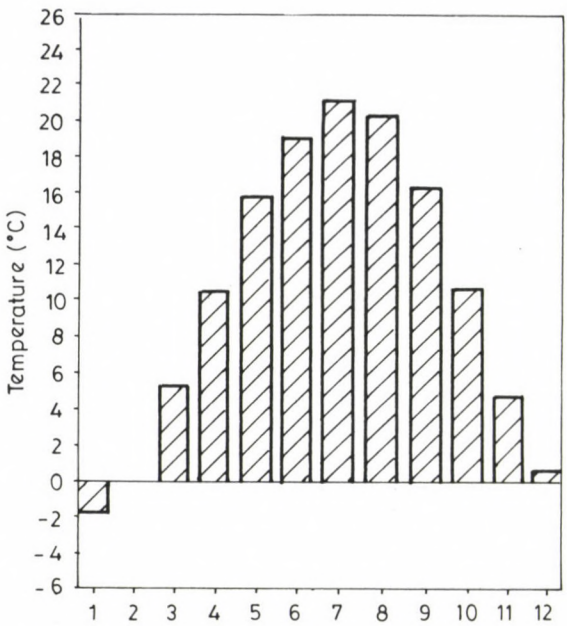

Fig. 7. Monthly average temperature distribution considered in the calculations

- Important differences occur in creep to the relatively low deviation of the measured sag values. It results from the same that the creep time function itself should not be practically determined by means of field measurement. However, this method provides appropriate accuracy for the examination of the development of sag and loading conditions in time. Should we have to know the expected change in sag in the period of planning, then we can determine the expected change in time in the sag and loading conditions of the conductor means of the calculation method applying the empirical general creep expression.

REFERENCES

1. Permanent elongation of conductors: Predictor equation and evaluation methods. ELECTRA No. 75, 64-98

2. Harvey, J.R., Larson, R.E.: Creep equations of conductors for sag-tension calculations. C 72 190-2 IEEE WPM 1972

3. Brandt, E., Thomas, R.: Der Einfluss der bleibenden Seildehnung auf das Durchhangverhalten von Freileitungen. Elektrizitätswirtschaft, 1979. H. 8, 262-268

4. Dániel, I., Krómer, I., Vöő, L.: Examination of the operating behaviour of aerial wires. 3rd International Conference of the Cable Industry, Budapest, 1989

Acta Technica Acad.Sci.Hung., 105(1-2), pp. 83-95 (1993)

MEASUREMENT OF 50 Hz MAGNETIC INDUCTION DEVELOPING IN THE ENVIRONMENT OF 120-750 kV TRANSMISSION LINES

PAULUSZ, M.*

(Received: 3 January 1991)

50 Hz magnetic fields are developing in the environment of transmission lines. To get know the values of these fields measurements have been carried out. The maximum values of magnetic induction were 7.47-35.89 μT. These are lower compared with the 100 μT permissible value of continuous exposure of the populations by IRPA.

There is little experimental evidence to suggest that 50 Hz magnetic fields can affect human physiology at the intensities mentioned.

In the course of transport and utilization of electric energy, 50 Hz magnetic fields are developing in the environment of transmission lines and electrical equipment. Magnetic induction develops in the neighbourhood of magnetic fields or in the body of persons staying there, the magnitude of which being identical with that brought about outside the body, because the relative permeability of biological substances is approximately 1 ($\mu_r \approx 1$). Current is induced in the human body by the alternating magnetic induction. The normal biological functions of the organism are less affected, if at all, by currents of a density below the endogenous current.

The assumed biological effect of magnetic fields is studied by a large number of research institutes and universities all over the world.

As a result of a retrospective epidemiological analysis including children younger than 19, of whom 344 had died of cancer while another 344 belonged to the control group. Wertheimer and Leeper /1/ found that the risk of contracting cancer was higher in case of children living in the environment of transmission lines of high current. The risk increased two to threefold according to the authors' 1979 publication.

---

*Paulusz, Mihály, H-1035 Budapest, Szentendrei út 24, Hungary

Akadémiai Kiadó, Budapest

A second work of the same authors published in 1982 /2/ reported on an epidemiological analysis including adults. As a result, the authors found a relationship between cancer of adult population and the magnetic field of transmission lines of high current near the place where cancer patients lived.

According to the epidemiological analysis of Savitz /3/ including children of 0 to 14 years, little relationship can be found between the frequency of cancer and magnetic fields developing in the environment of transmission lines of low current.

Other authors /4-9/ found no relationship between cancer and 50 Hz magnetic fields according to the result of their epidemiological analysis.

The analyses described are not free from the well-known deficiencies inherent in epidemiological analysis in general. Firts of all, the sample number was small in each case. At the same time, the increase of the risk was insignificant. The control group was selected at random and therefore the age, occupation, sex and social position of persons in the control group differed from those of the group analyzed. The causality between the frequency of cancer and magnetic fields is still a hypothesis only.

Epidemiological analyses are still going on to find a reliable answer to the problem. A joint Canadian-French investigation includes 6000 employees of the electricity industry who have contracted cancer and 24 000 persons in the control group. Another investigation in the United States includes 50 000 persons. Evaluation of the results is expectable in 1992.

Note that Wertheimer and Leeper determined the magnitude of magnetic fields developed in the environment investigated by measurement and calculation.

Maximum values of 0.4, 0.5, 0.8, 2.0, 3.5 μT while mean values of 0.09, 0.17, 0.22, 0.7 μT have been obtained for magnetic induction at a height of 75 cm above earth surface in the environment of transmission lines of different current.

Savitz measured magnetic fields developed at a height of 1 m at the entrance of living-rooms. In this case, values of 0.065, 0.1, 0.25 μT were obtained for magnetic induction.

On the basis of evaluation of these field measurements, it can be seen that magnetic fields of a relatively low strength, 0.065 to 3.5 μT only, have developed in the dwelling units tested.

Due to deficiencies of quite a number in epidemiological analyses, a

conclusion that there is a relationship between 50 Hz magnetic field and the frequency of cancer cannot be definitely drawn.

According to the measurements published, the magnetic induction to which the population is exposed is small and it is therefore difficult to assume a mechanism explaining the contribution of this small magnetic induction to the development of cancer.

Utilization of electric energy is of vital importance for both industry and population. It is very important to detect any risk to health inherent in the utilization of electric energy. To our present knowledge, objections against 50 Hz magnetic fields are unfounded. However, research must be continued as long as there exists any doubt in relation to the effect of magnetic fields.

1. 50 Hz magnetic induction developing in the environment of transmission lines

50 Hz magnetic induction developing as a result of current of intensity $\bar{I}_i$ at point $p(y_p, x_p)$ above earth surface in the vicinity of transmission lines (Fig. 1.1):

$$\bar{B}_i = \frac{\mu_o}{2\pi} \cdot \frac{\bar{I}_i}{\sqrt{(x_i - x_p)^2 + (z_i - z_p)^2}} , \qquad (1)$$

where $\mu_o = 4\pi \cdot 10^{-7} \frac{\text{ohm.s}}{\text{m}}$, permeability of vacuum.

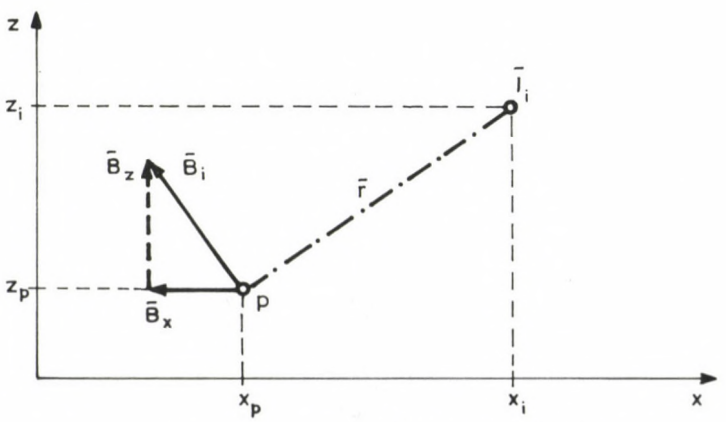

Fig. 1.1. Components of magnetic induction

2. Measurement of 50 Hz magnetic induction

The following relationship can be used to calculate the voltage induced in a single-turn coil placed in an alternating magnetic field of homogeneous magnetic induction $\overline{B}$:

$$U = \oint_L \overline{E} \cdot \overline{dl} = - \int_A \frac{\partial \overline{B}}{\partial t} \cdot d\overline{A} \quad . \tag{2}$$

After integration over a circular surface of radius r normal to induction $\overline{B}$:

$$U = \omega \cdot B \cdot r^2 \cdot \pi \quad . \tag{3}$$

As shown by this equation, measured induced voltage U is proportional to magnetic induction B.

With the principles mentioned taken into consideration, an instrument suited for the measurement of 50 Hz magnetic induction in the range of 0.01 to 1000 μT has been developed by the staff of the Department of Electrical Equipment, Institute for Electrical Power Research VEIKI.

3. Measurement of 50 Hz magnetic field of 120-750 kV transmission lines

Magnetic induction developing as a function of distance x measured from the axis of the central current conductor projected to earth has been measured at points normal to the axis of the line, at a height of 1.5 m above earth surface where the sag of the conductor is maximum, between the supports of the transmission line.

Change of the magnetic induction as a function of distance x can be seen in Figs 3.1 thru 3.4.

These functions reach maximum at the axis of the line (x=0) to reduce then considerably.

4. Evaluation of the results of measurements

The maximum values of magnetic inductions developing at a height of 1.5 m above earth surface in the environment of 120-750 kV transmission lines are complied in Table 4.1.

Table 4.1

Maximum values of magnetic induction in the environment of 120-750 kV transmission lines

Transmission lines	Maximum magnetic induction μT
Angyalföld I, II - Zugló 120 kV	11.13
Dunamenti - Zugló 220 kV	35.89
Zugló - Göd 220 kV	9.22
Albertirsa - Göd 400 kV	29.53
Sándorfalva - Szabadka 400 kV	7.47
National boundary - Albertirsa 750 kV	31.00

The values of magnetic induction measured at the edge of the safety zone around transmission lines are complied in Table 4.2.

Table 4.2

Values of magnetic induction measured at the edge of the safety zone around transmission lines

Transmission lines	Safety zone	Phase distance	Edge of safety zone	Magnetic induction at edge of safety zone
	m	m	m	μT
Angyalföld I-II - Zugló 120 kV	13	5	18	4.35
Dunamenti - Zugló 220 kV	18	7	25	9.02
Zugló - Göd 220 kV	18	7	25	2.66
Albertirsa - Göd 400 kV	28	14	42	3.07
Sándorfalva - Szabadka 400 kV	28	11	39	0.975
National boundary - Albertirsa 750 kV	40	17.5	57.5	3.87

5. Magnetic fields in dwelling houses near transmission lines

The values of magnetic induction developing at a height of 1.5 m above floor in dwelling houses in the vicinity of 120-750 kV transmission lines are compiled in Table 5.1.

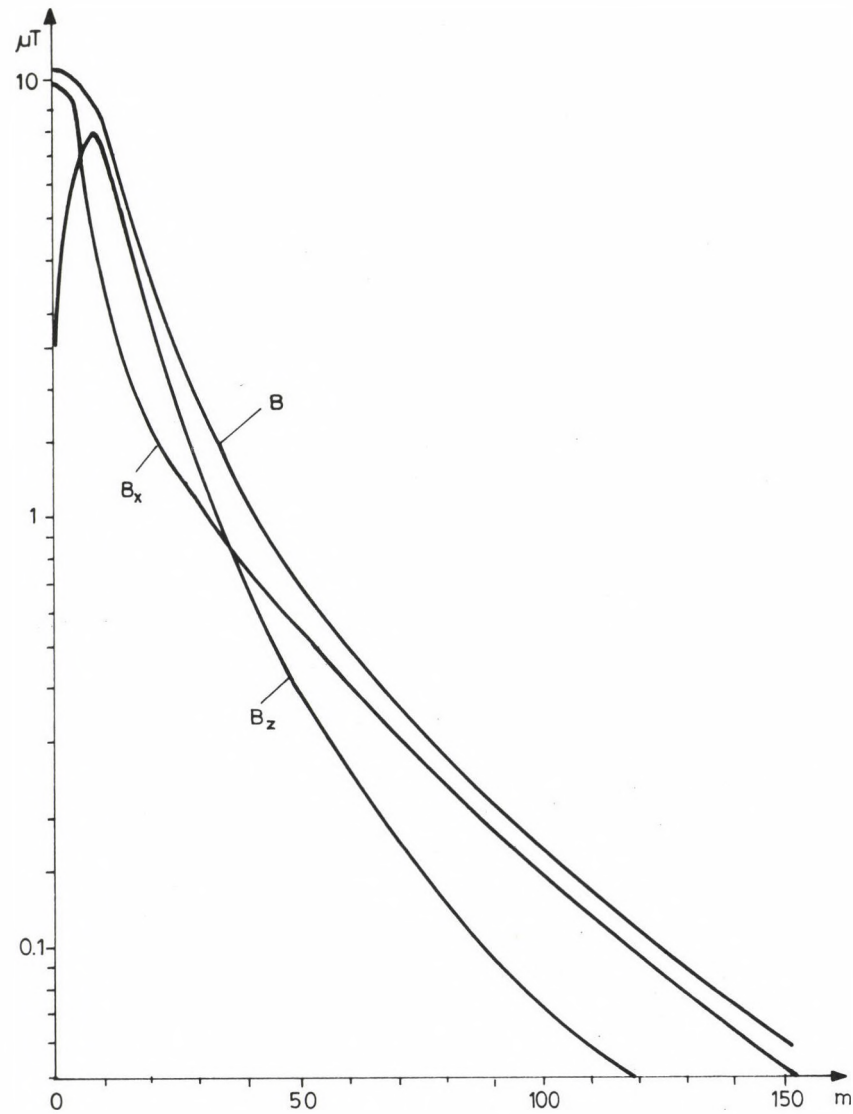

Fig. 3.1. 50 Hz magnetic induction developing as a function of the distance measured at right angles to the route at a height of 1.5 m above earth surface in the environment of Angyalföld I-II - Zugló two-system 120 kV transmission line

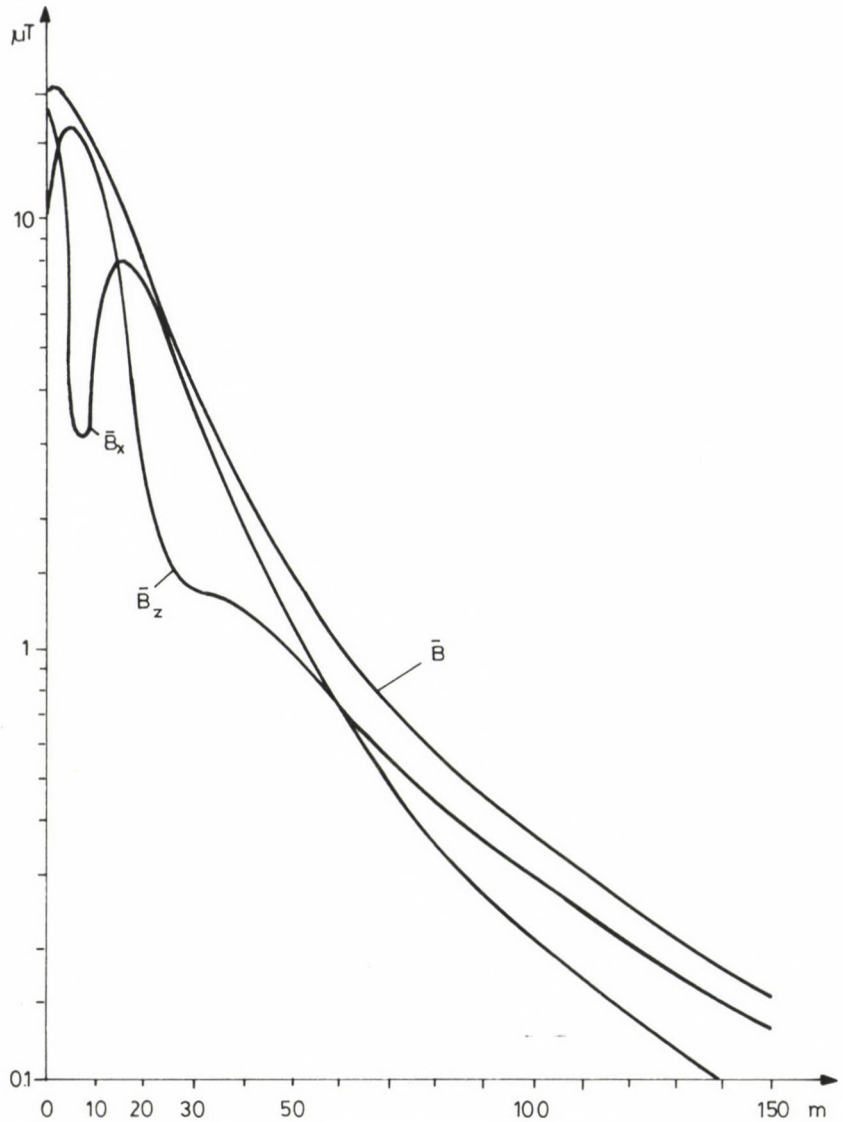

Fig. 3.2. 50 Hz magnetic induction developing as a function of the distance measured at right angles to the route at a height of 1.5 m above earth surface in the environment of Dunamenti - Zugló 220 kV transmission line

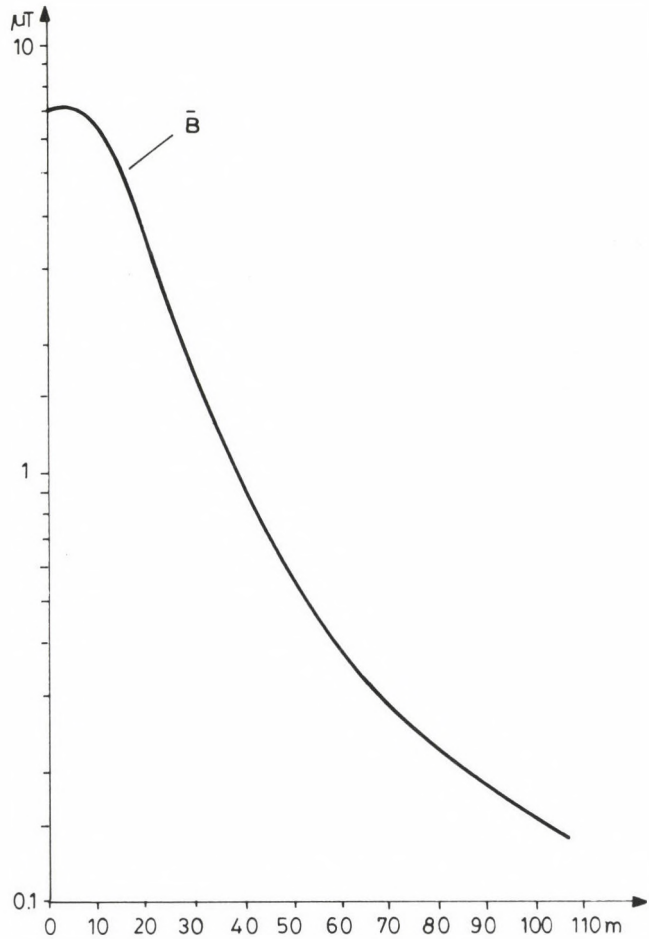

Fig. 3.3. 50 Hz magnetic induction developing as a function of the distance measured at right angles to the route at a height of 1.5 m above earth surface between supports No. 35 and 36 of Sándorfalva - Szabadka 400 kV transmission line

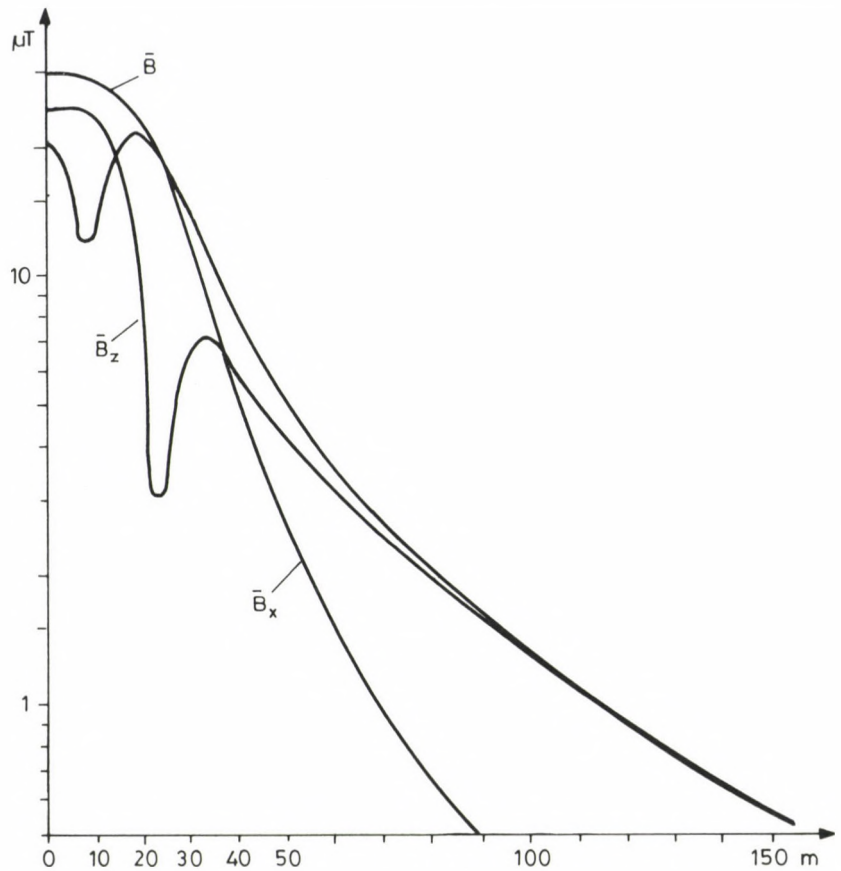

Fig. 3.4. 50 Hz magnetic induction developing as a function of the distance measured at right angles to the route at a height of 1.5 m above earth surface in the environment of national boundary - Albertirsa 750 kV transmission line

There is practically no difference between the values of magnetic induction measured inside and outside of the buildings. The magnetic induction was practically not reduced by the walls of the buildings.

6. Permissible values of exposure of the population to magnetic induction

Electric and magnetic fields developing in the environment of transmission lines result in different environmental impacts due to their different physical characteristics.

Table 5.1

Magnetic induction in the interior of dwelling houses near transmission lines

Location	Maximum magnetic induction /μT
Bedroom (house No. 187)	0.93
Kitchen (house No. 187)	1.30
Bedroom (house No. 186)	3.21
Kitchen (house No. 186)	2.53
Bedroom (house No. 235)	3.15
Kitchen (house No. 235)	2.95
Porter's lodge	0.93
Corridor	0.98
Snack-bar	0.87
Restaurant	1.39
School room	2.29
Corridor I	0.59
School room I	1.63
Corridor II	0.77
School room II	1.22
Corridor III	0.37
Ballet training room II	0.39
Dining room	1.03
Children's room	0.96
Bedroom	1.26
Hall	1.28
Attic	1.54
Bedroom	0.59
Living room	0.52

Current develops between the body of persons staying in the electric field and earth while circular currents are brought about in the body of persons staying in the magnetic field.

No generally accepted values are available for the permissible exposure of persons to magnetic induction in the present international practice.

Opinions are divergent. One group suggests permissible exposure levels on the basis of the results of medical examination of living tissues, animals and volunteer persons.

Another group prefers permissible values of magnetic induction based on the results of epidemiological analysis.

In some epidemiological analyses, the risk of cancer was assumed to increase as a result of a maximum and a mean magnetic induction of 3.5 /μT and 0.25 /μT, respectively. On the basis of this hypothesis, the values of magnetic induction developing in the environment of the transmission lines investigated are higher than 3.5 /μT, the maximum magnetic induction being assumed to result in increasing risk.

7. Temporary directives of the International Committee of Non-ionizing Radiation (IRPA)

The International Committee of Non-ionizing Radiation worked out temporary directives for the permissible exposure of population to magnetic fields in 1990 /10/.

The minimum requirement is that the value of current density induced in the head and heart of man as a result of continuously acting 50 Hz magnetic field be max. 1 $\mu A/cm^2$.

Maximum permissible value of continuous exposure of the population to magnetic induction for 24 hours is 100 μT.

8. Measured values and permissible values of exposure of the population to magnetic induction according to IRPA

The values of magnetic induction measured in the environment of the transmission lines investigated lie below the permissible values of exposure of the population to magnetic induction according to IRPA.

The maximum values of magnetic induction measured in the environment of 120-750 kV transmission lines lies at 7.47 to 35.89% of the permissible values of exposure.

As compared with the permissible values, the value of magnetic induction at the edge of the safety zone is only 0.975 to 9.02%, while the value of magnetic induction in the interior of dwelling houses in the vicinity of transmission lines is 0.23 to 3.21%.

REFERENCES

1. Wertheimer, N., Leeper, E.: Electrical wiring configurations and childhood cancer. American Journal of Epidemiology, 109, No. 3 (1979)

2. Wertheimer, N., Leeper, E.: Adult cancer related to electrical wires near the home. International Journal of Epidemiology, 11, No. 4 (1982)

3. Savitz, D.A.: Case-control study of childhood cancer and exposure to 60 Hz magnetic fields. American Journal of Epidemiology, 128, No. 1 (1988)

4. McDowall, M.E.: Mortality of persons resident in the vicinity of electricity transmission facilities. Br. J. Cancer, 63 (1986)

5. Myers, A.: Overhead lines and childhood cancer. IEE Conference Publication, No. 257 (1985)

6. Fulton, J.O.: Electric wiring configurations and childhood leukemia in Rhode Island. American Journal of Epidemiology 3 (1980)

7. Tomenius, L.: 50 Hz Electromagnetic environment and the incidence of childhood tumors in Stockholm County. Biomagnetics 7 (1986)

8. Severson, R.K.: Acute nonlymphocytic leukemia and residential exposure to power frequency magnetic fields. American Journal of Epidemiology 128, No. 1 (1988)

9. Rodvall, Y.: En utredning av cancersjukligheten i alftaområdet. Statens Miljömedicinska Laboratorium Epidemiologiska enheten. Sapport Nr. 10/85, Stockholm (1985)

10. Interim guidelines on limits of exposure to 50/60 Hz electric and magnetic fields. International Non-ionizing Radiation Committee. Health Physics 58, No. 1 (1990)

11. Polk, C.: CRC handbook of biological effects of electromagnetic fields. CRC Press, Inc., Boca Raton, Florida 1986.

12. Environmental Health Criteria 69, 1987. Magnetic fields. World Health Organization, International Radiation Protection Association, Geneva

13. Non-ionizing radiations: physical characteristics, biological effects and health hazard assessment. Proceedings of the International Non-ionizing Radiation Workshop, Melbourne, 5-9 April, 1988

14. Dennis, I.A.: Towards the development of exposure limits for low frequency electromagnetic fields. IEE International Conference on Electric and Magnetic Fields in Medicine and Biology. Conference Publication No. 257, London, 1985

15. Loustrand, K.G.: Exposure of persons to electric fields in Swedish extra-high-voltage substations: field strength and dose measurements. Proc. of 18th Ann. Hanford Life Sc. Symp. at Richland, Washington, 1978

16. Maddock, B.J.: 50 Hz electric and magnetic field near power transmission circuits and some associated exposure and health studies. IEE Conference Publication No. 257 (1985)

17. Caola, R.J.: Measurements of electric and magnetic field in and around homes near a 500 kV transmission line. IEEE Transactions on Power App. and Syst. PAS-102, No. 10 (October 1983)

18. Jacobs, P.D.: Measurements of transmission line electric fields in a residential environment. IEEE Transactions on Power App. and Syst. PAS-103, No. 8 (August 1984)

19. Grandolfo, M.: Biological effect and dosimetry of static and LLF electromagnetic fields. Plenum Press, New York and London 1983

20. Graham, C.: A double-blind evaluation of 60 Hz field effects on human performance, physiology and subjective state. Report presented at the 23rd Annual M. Life Science Symposium on Interaction of Biological System with static and ELF Electric and Magnetic Fields

21. Stimmer, H.: Krebs durch Strom. Elektrotechnik und Informationstechnik, Jg. 106, Heft 3 (1989)

22. Elektromagnetische Felder und unsere Gesundheit. 16 März, 1989, Wien.

23. Some aspects of the electromagnetic compatibility of biological systems. 5th International Symposium on High Voltage Engineering. Tech. Univ. Braunschweig, 1987

24. Schutz vor nichtionisierender elektromagnetischer Strahlung. Teil 1: Statische und Niederfrequenzfelder bis 10 kHz. Österreichisches Forschungszentrum, Seibersdorf, 1988

25. Silva, M.: Power frequency magnetic fields in the home. IEEE Transactions on Power App. and Syst. 4, No. 1 (1988)

26. Magnetic fields from electric power lines. IEEE Transactions on Power Delivery 3, No. 4 (October 1988)

27. Shore, R.E.: Electromagnetic radiation and cancer. Cancer, (October 1988)

28. Wolpaw, J.R.: Chronic exposure of primates to 60 Hz electric and magnetic fields: I. Exposure system and measurements of general health and performance. Bioelectromagnetics 10 (1989)

29. Seegal, R.F.: Chronic exposure of primates to 60 Hz electric and magnetic fields: II: Neurochemical effects. Bioelectromagnetics 10 (1989)

30. Dowman, R.: Chronic exposure of primates to 60 Hz electric and magnetic fields: III. Neurophysiologic effects. Bioelectromagnetics 10 (1989)

31. Clairmont, B.A.: The effect of HVAX-HVDC line separation in a hybrid corridor. IEEE Transactions on Power Delivery 4, No. 2 (1989)

32. Dlugosz, L.J.: Ambient 50 Hz magnetic flux density in an urban neighbourhood. Bioelectromagnetics 10 (1989)

Acta Technica Acad.Sci.Hung., 105(1-2), pp. 97-116 (1993)

A STUDY OF FLUIDIZED BED SOLIDS AND FLY ASH SAMPLES TO BETTER UNDERSTAND THE TRANSFORMATIONS OF THE COAL ASH

REMÉNYI, K.* - HORVÁTH, F.**

(Received: 6 April 1992)

A special type of fuidized bed combustion technology, the Hybrid-fluid combustion system, was developed in the Institute for Electric Power Research, Hungary. The technology is patented for a number of countries. The possibility for the development was given by the Ajka Power Plant, Hungary, where the new fluidized bed combustion technology is introduced and also, where the CaO content of the ash in the local coal is high.

A thermogravimetric (TG) balance supplied with mass spectrometry (TG-MS) was used to study the bed solids and fly ash samples from the Hybrid-fluid boiler. Our main interest was to study the interconnections between the sulphur, lime and carbon compounds, to study the main possible reaction pathways characteristic at different temperature levels in the boiler.

It is the main conclusion that the decomposition of sulfates in the TG balance can start at 800 ^{o}C in the presence of carbon, and if the atmosphere is inert. There is no decomposition in an oxidizing atmosphere.

LABELS ON FIGURES

GO	initial sample mass, mg
G	sample mass as a function of temperature
FS: 25%	the number is the scale of vertical axis in the percentage of the initial sample mass (10 or 25%)
DTG	the rate of mass variation, the numeric derivaties of mass
FS: 0.09%/s	the scale factor is generally the maximum of the actual DTG curve
H_2O	the intensity of water (m/z 18 ion)
FS: 1.5E-07 A/mg	the scale factor is the maximum of the intensity
CO_2	m/z 44 ion
SO_2	m/z 64 ion
CO	m/z 28 ion (the intensity of the 28 ion of CO_2 is suppressed)
NO	m/z 30 ion (the same as the main ion of the NO_2)

*Reményi, Károly, H-1014 Budapest, Úri u. 38, Hungary

**Horváth, Ferenc, H-1074 Budapest, Dohány u. 84, Hungary

Akadémiai Kiadó, Budapest

Introduction

A special type of fluidized bed combustion technology was developed in the Institute for Electric Power Research. The technology is properly applicable for the retrofit of existing boilers with pulverized coal combustion system. The new fluidized bed combustion technology preserves most of the key elements of the pc system, that is the cause why it is named Hybrid-fluid combustion system. The technology is patented for a number of countries (for example it is protected also by the US Patent 4,993,332). Figure 1 shows the scheme of the technology. As it is shown the dried coal streams of different size distributions are introduced in the combustion chamber at separate heights. By the special arrangements of the air distributor an internal solids circulation is maintained in the furnace. The

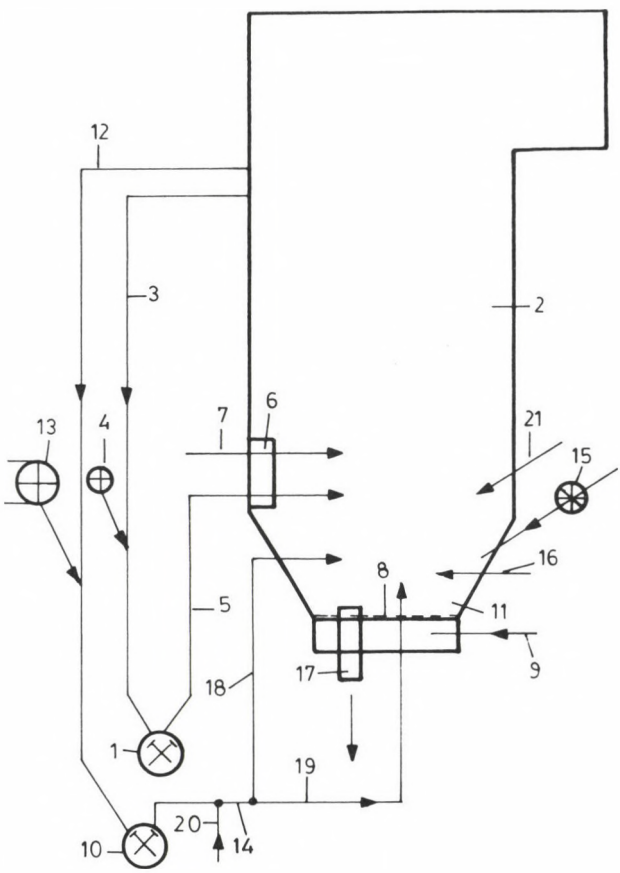

Fig. 1. U.S. Patent 4,993,332 (Feb.19.1991, Sheet 1 of 5)

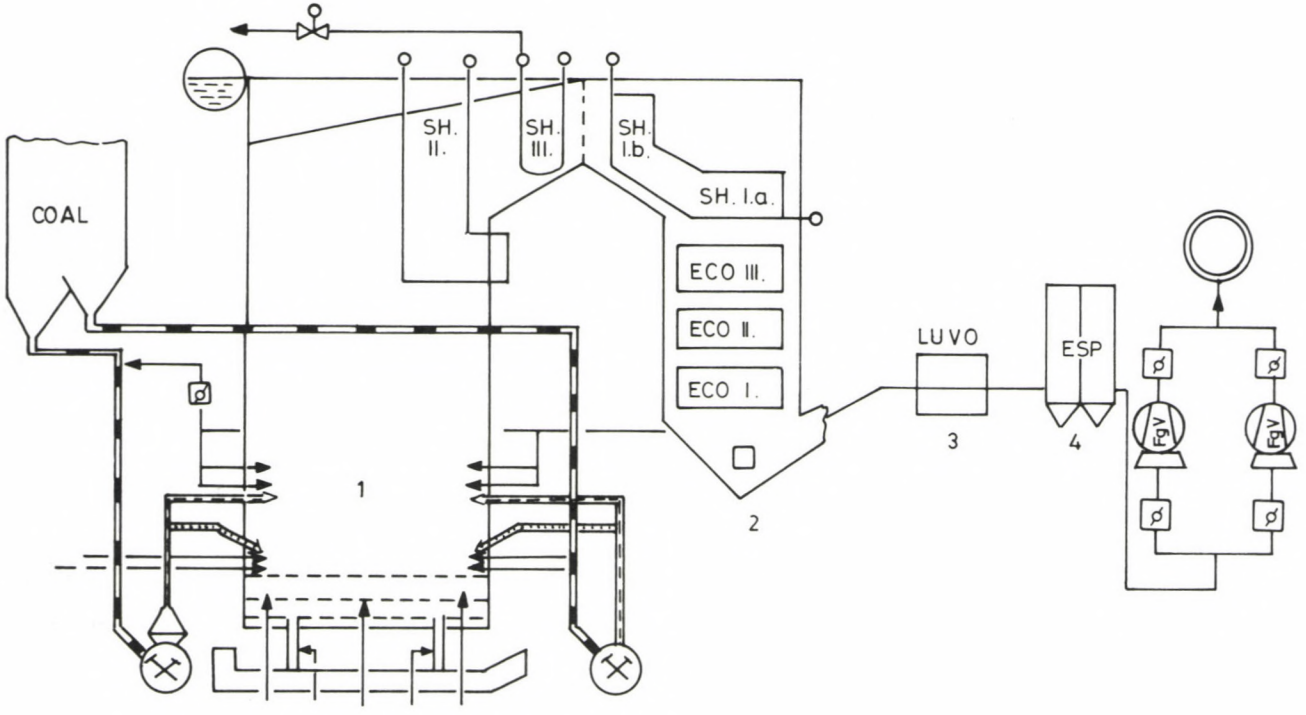

Fig. 2. Ajka II. 100 M Steam generator

main aim of the development was to utilize low calorific value coals in an environmentally accepted way. It was an additional aim to be achieved that for coals with high CaO content the degree of sulphur retention must be increased without any limestone additives. The possibility for the development was given by the Ajka Power Plant, Hungary, where the new fluidized bed combustion technology is introduced and also, where the CaO content of the ash in the local coal is high.

Industrial experimental apparatus

The physical-chemical transformations of the samples of the combustion residues taken were experimented. A thermogravimetric balance supplied with mass spectrometry (TG-MS) was used to study these solid samples from the Hybrid-fluid boiler. The origins of the samples are labelled on Fig. 2. The combustion tests were made at 60 and 100 t/h load of the 100 t/h capacity boiler.

The coal chemical characteristics are the following:

Chemical characteristics of the raw coal

Load	t/h	60	100
W_t	wt%	22.7	22.7
A	wt%	30.5	30.2
Q_s	MJ/kg	11.27	10.79
Q_h	MJ/kg	10.32	9.86
C_t	wt%	31.1	30.5
H_t	wt%	1.8	1.7
S_t	wt%	3.1	3.0
N	wt%	0.6	0.6
O_d	wt%	10.2	11.3
$[CO_2]_M$	wt%	10.1	11.6

Chemical characteristics of the coal ash

CaO	wt%	49.6	54.2
MgO	wt%	4.0	4.3

Mass balance of the ash withdrawn from the boiler

Legend on Fig. 2		Ash ratio
1	bed solids	2 wt%
2	ash hopper below the economizer	15 wt%
3	ash hopper below the air heater	5 wt%
4	electric precipitator	78 wt%

Chemical characteristics of the bed solids and fly ashes

The figures below are given in XX/YY form, where XX and YY are the data for 60 and 100 t/h boiler load, respectively.

C_t	wt%	1.3/0.6	2.3/2.5	2.7/2.3	1.4/0.6
H_t	wt%	0.4/0.5	0.1/0.2	0.2/0.1	0.2/ < 0.1
S_t	wt%	9.5/11.3	4.5/4.3	4.1/3.6	4.5/4.3
$[CO_2]_M$	wt%	1.9/2.4	2.5/1.4	1.8/1.3	0.6/0.4
CaO	wt%	41.8/57.1	54.4/62.5	63.0/60.0	64.0/60.2
MgO	wt%	2.4/2.4	3.6/3.2	3.2/3.6	4.8/4.4
Q_s	MJ/kg	-1.9/-2.3	-0.3/-0.2	0.1/0.1	-0.3/-0.3
Q_h	MJ/kg	-1.9/-2.4	-0.3/-0.3	0.1/0.1	-0.4/-0.3

The TG-MS technics used

The solid samples of the combustion residues were analyzed in the Anorganic Chemical Laboratory of the Hungarian Academy of Science by a Perkin-Elmer TGS-2 thermobalance supplied with a Blazers QMG 511 quadruple mass spectrometer (Fig. 3). The sample mass was in the range of 12-15 mg. The heating of the samples was carried out at a rate of 20 ^{o}C/min in the range of 30-1000 ^{o}C in inert (argon) and oxidative (oxygen/argon: 30/70%) atmospheres.

Conclusions from the experiments

The transformations of the mineral compounds of the coal ash are depending on the local physical-chemical circumstances in the combustion chamber and in the flue gas stream of the boiler. Our main interest was to study the interconnections between the sulphur, lime and carbon compounds,

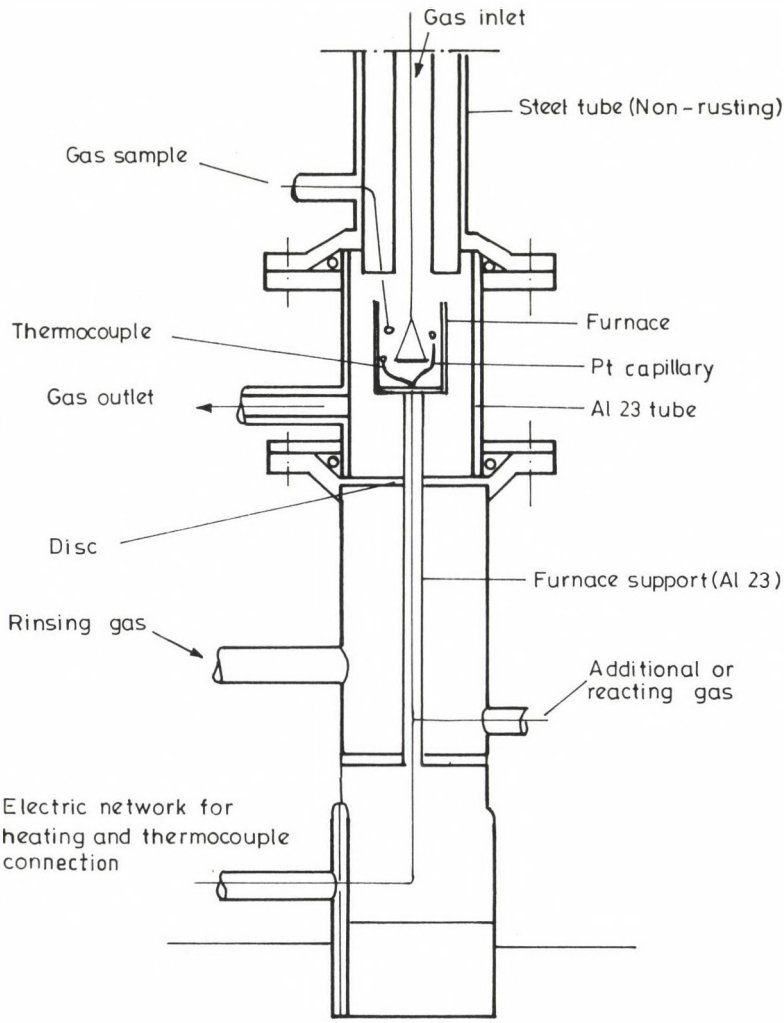

Fig. 3.

to study the main possible reaction pathways characteristic at different temperature levels in the boiler.

In the combustion chamber the reaction pathways with lime are

$$CaCO_3 = CaO + CO_2$$
$$CaO + SO_2 + 1/2\ O_2 = CaSO_4$$

and the reaction as the task of the present work is

$$2\ CaSO_4 + C = 2\ CaO + 2\ SO_2 + CO_2$$

as a possible sulfate decomposition pathway in the presence of carbon.

At lower temperatures the following reaction pathways are also possible as water steam is always present in the flue gas:

$$CaO + H_2O = Ca(OH)_2$$
$$Ca(OH)_2 + SO_2 = CaSO_3 + H_2O$$
$$CaSO_3 + 1/2\ O_2 = CaSO_4$$

or

$SO_2 + H_2O = H_2SO_3$	absorption
$CaCO_3 + H_2SO_3 = CaSO_3 + CO_2 + H_2O$	neutralization
$CaSO_3 + 1/2\ O_2 = CaSO_4$	oxidation
$CaSO_4 + 2\ H_2O = CaSO_4 \cdot 2H_2O$	crystallization

The nitrogen residues in the samples are transforming in the thermobalance to nitrogen oxides in a similar way as the fuel nitrogen does. The organic nitrogen compounds are transforming to hydrogen-cyanide, for example by pyrolysis, and later it disappears depending on the local circumstances:

$$CN + H_2O = HCN + OH$$
$$2\ HCN + 2\ O_2 = 2\ NO + H_2O + CO$$

Processes in inert atmosphere

Figures 4-7 present the TG-MS results for the combustion residue samples taken at 100 t/h boiler load. Figure 8 is for the fly ash sample when dry additive was used in the boiler. Figure 9 is for pure $CaSO_4$. Figures 10 and 11 show the variations in the sample when $CaSO_4$ and carbon mixture was tested in inert and oxidative atmosphere.

The following characteristic temperature ranges occurred.

- 50-300 ^{o}C, liberation of the absorbed water,
- 600-700 ^{o}C, thermic decomposition of $CaCO_3$; CO_2 production,
- 800-(1000) ^{o}C, in the presence of carbon the sulfates decompose; production of CO_2 and SO_2.

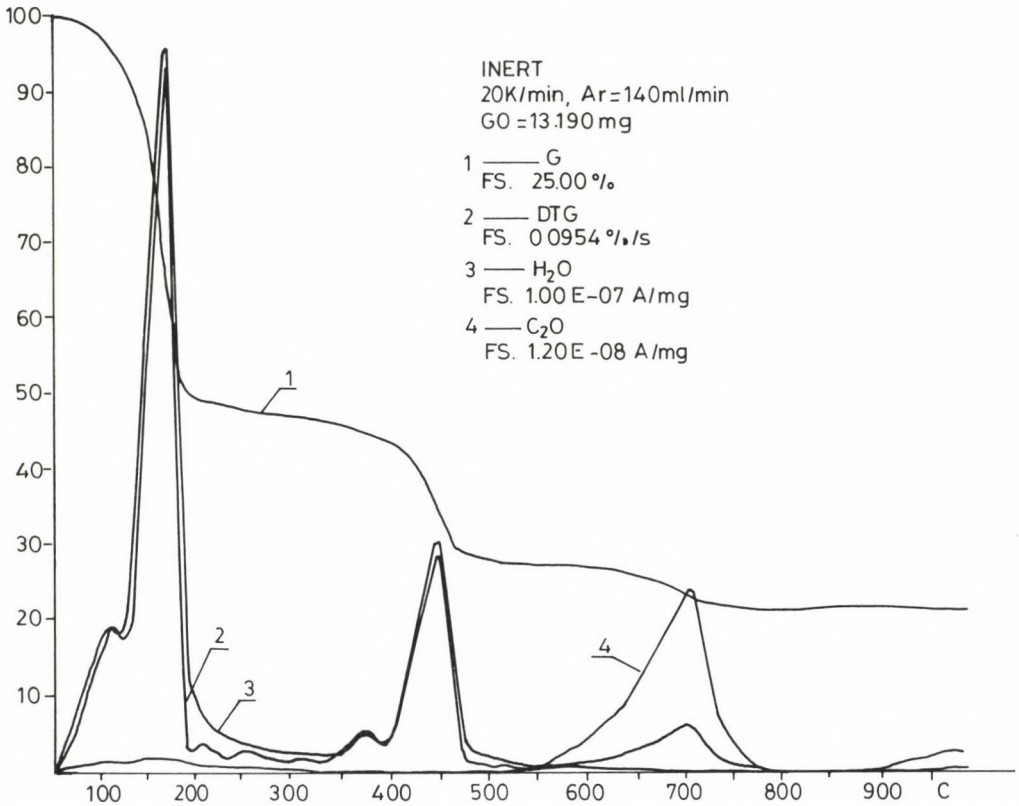

Fig. 4. A.H.V. 12. Boiler. Slag from combustion chamber

Except for the fly ash sample of the combustion test with additives used, the $CaSO_4$ decomposition peak occurred below 1000 ^{o}C. The CO_2 and SO_2 peaks do not coincide, they can develop at different temperatures. This may underline a two step decomposition process of the carbon-sulfate mixture.

There is no $CaSO_4$ decomposition in the absence of carbon below 1000 ^{o}C, as it is shown in Fig. 9, but the decomposition of the sulphate is significant below 1000 ^{o}C when mixed in and the atmosphere is inert (Fig. 10).

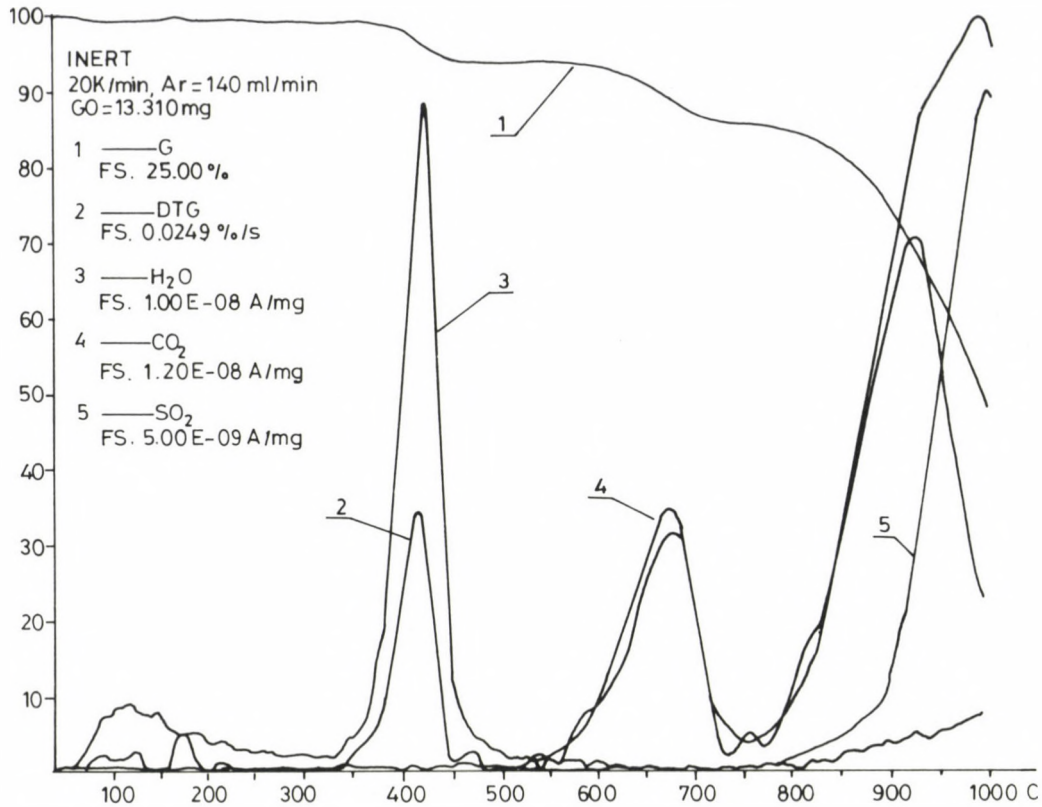

Fig. 5. A.H.V. 12. Boiler. ECO fly ash

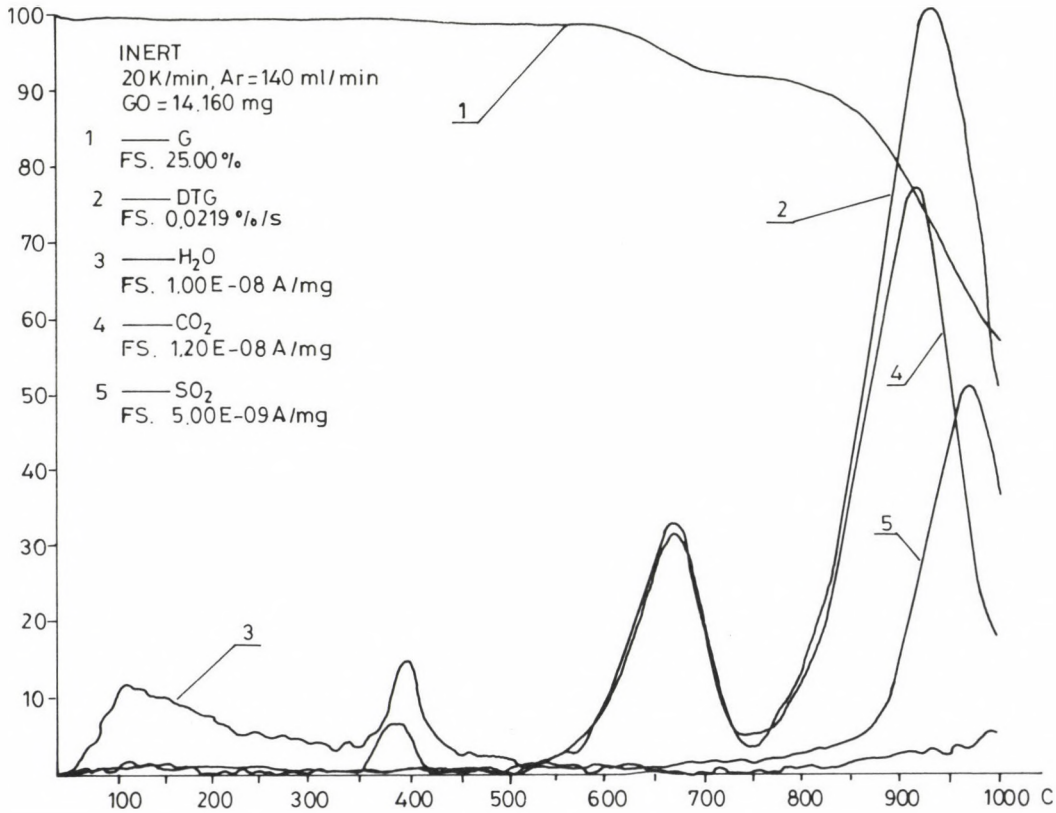

Fig. 6. A.H.V. 12. Boiler. Ljungstrom fly ash

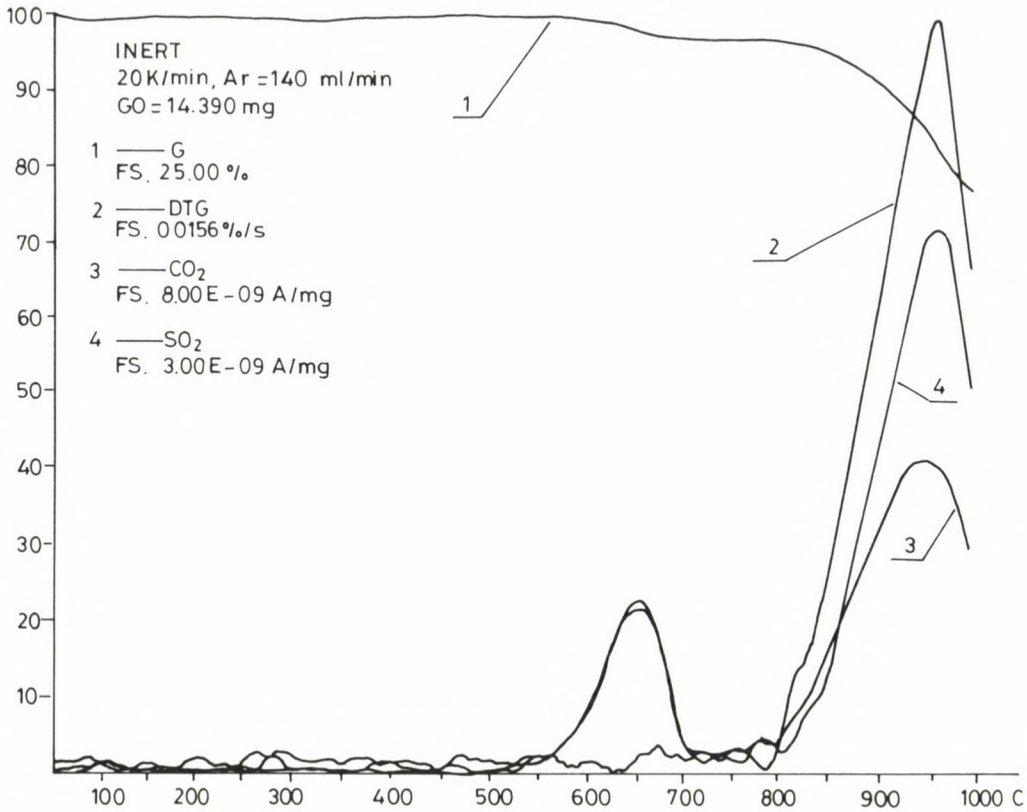

Fig. 7. A.H.V. 12. Boiler. EPS fly ash

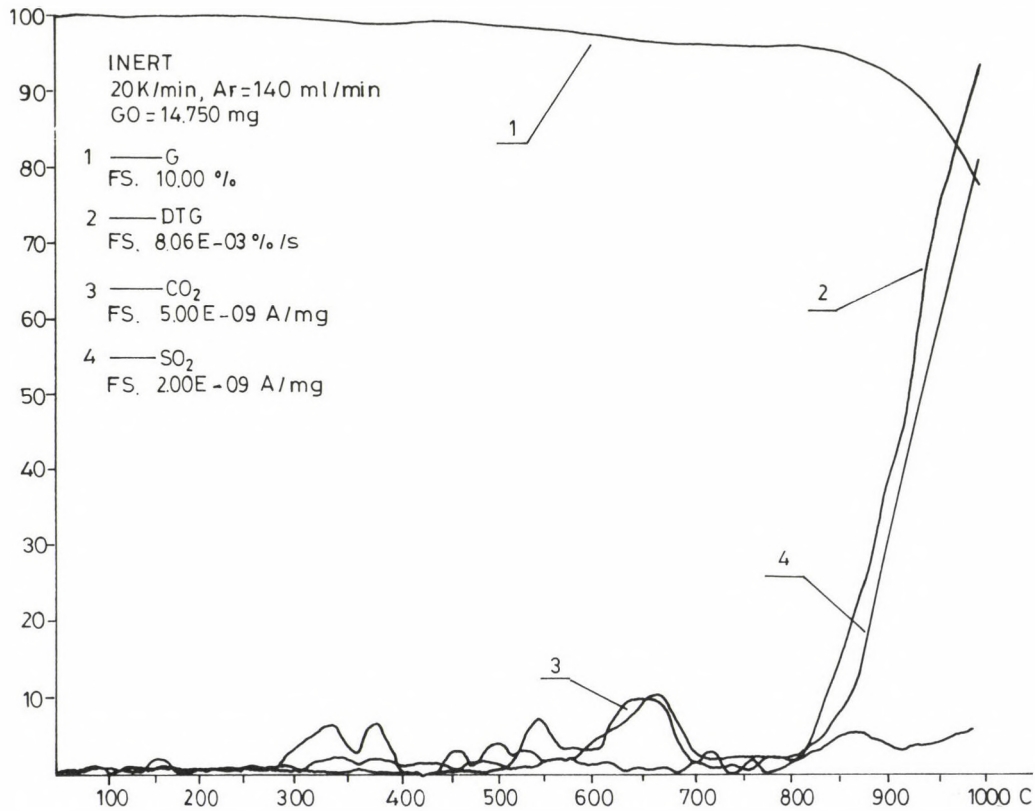

Fig. 8. DZO 1/A EPS fly ash + additive

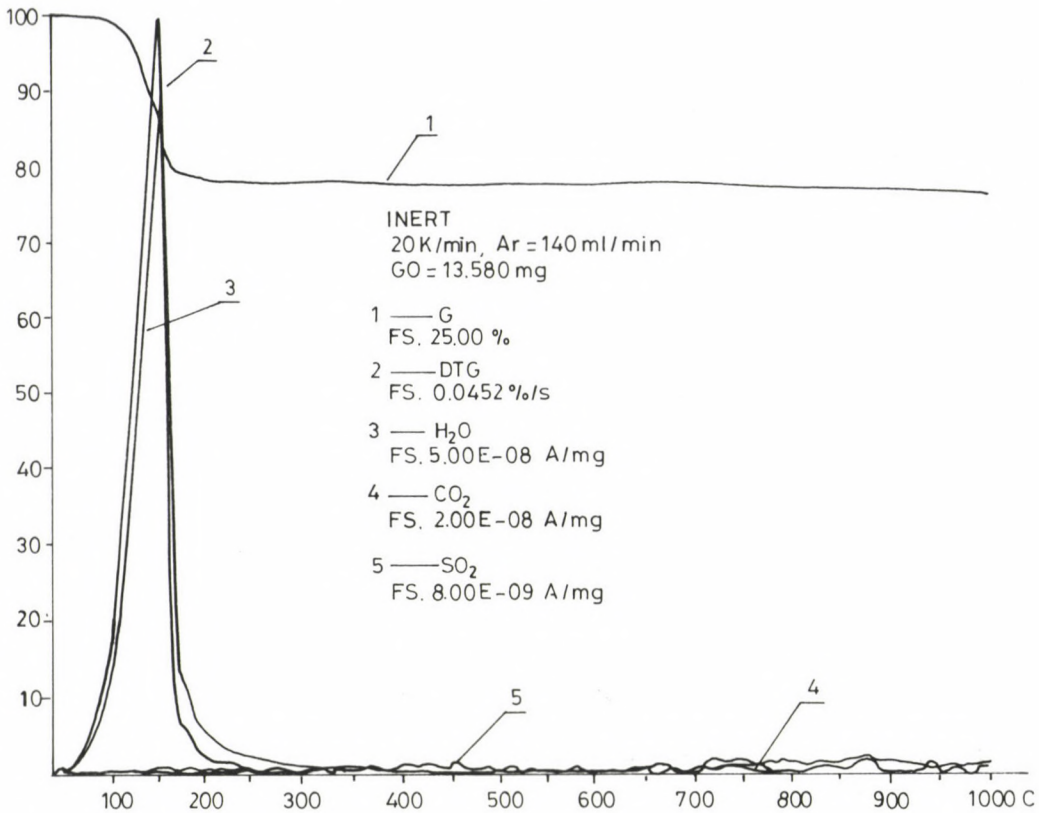
100
90
80
70
60
50
40
30
20
10
100
200
300
400
500
600
700
800
900
1000 C
1
2
3
4
5
INERT
20K/min, Ar = 140 ml/min
GO = 13.580 mg
1 —— G
FS. 25.00 %
2 —— DTG
FS. 0.0452 %/s
3 —— H_2O
FS. 5.00E-08 A/mg
4 —— CO_2
FS. 2.00E-08 A/mg
5 —— SO_2
FS. 8.00E-09 A/mg

Fig. 9. $CaSO_4$

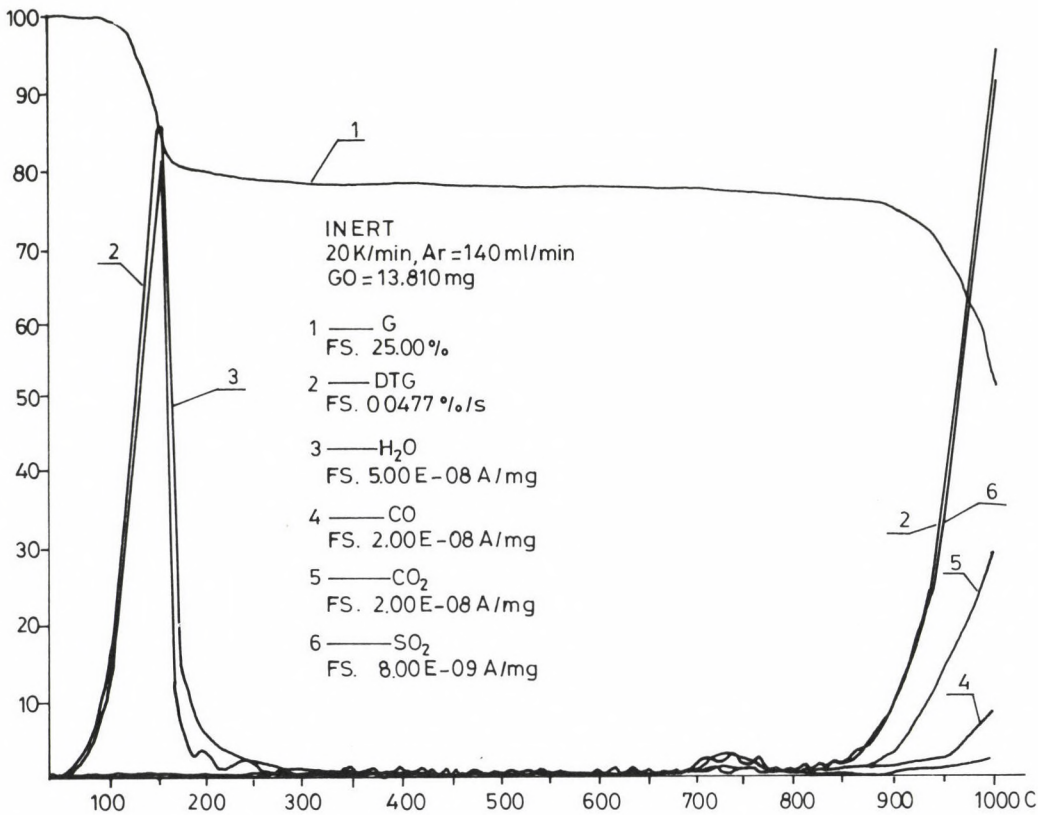

Fig. 10. $CaSO_4$ + 4% carbon

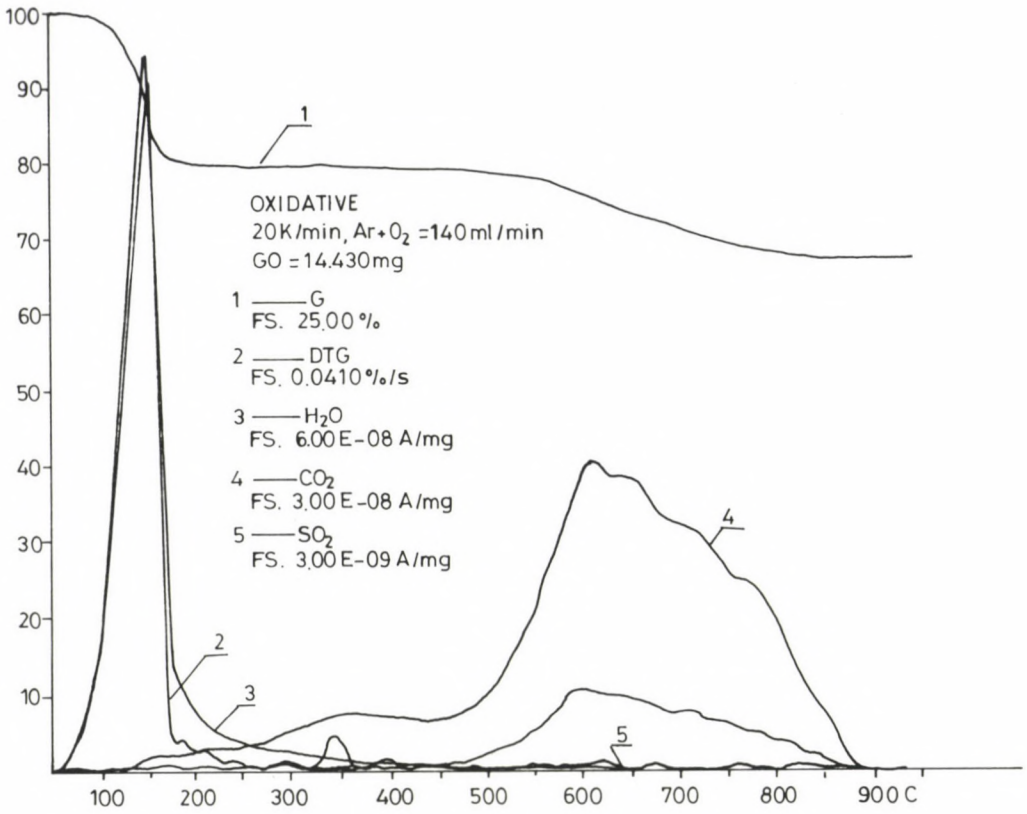

Fig. 11. $CaSO_4$ + 4% carbon

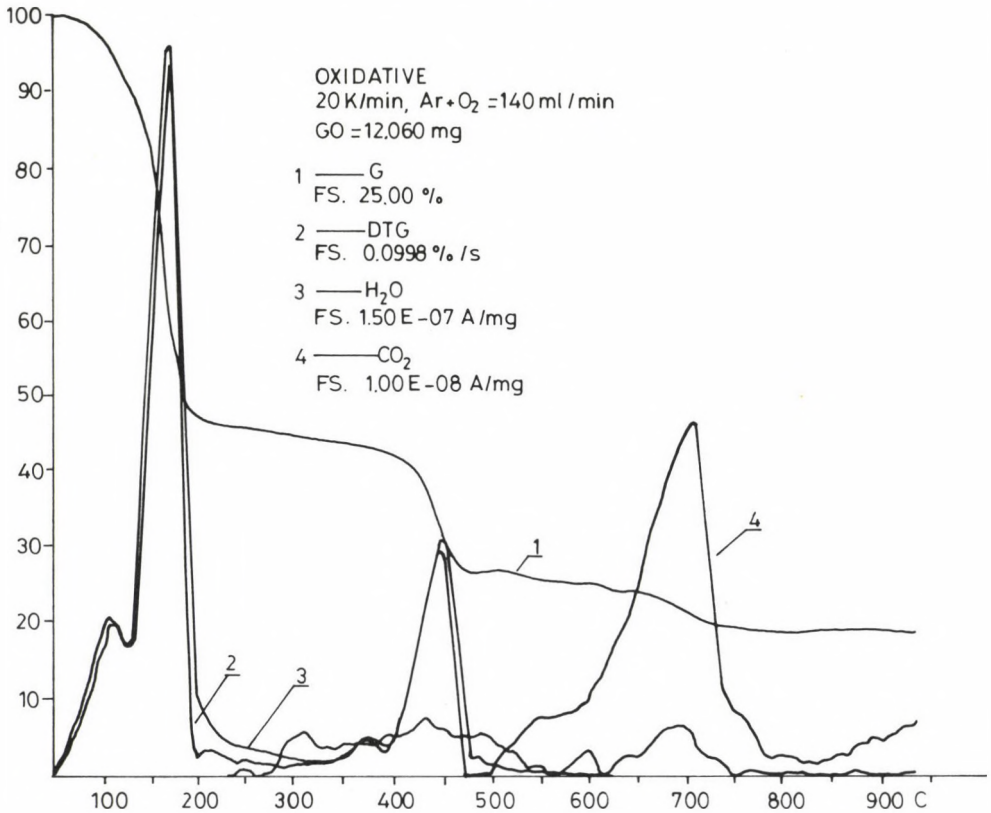

Fig. 12. A.H.V. 12. Boiler. Slag from combustion chamber

Processes in oxidative atmosphere

The TG results are presented in Figs 11-16. The liberation of the adsorptive and structural water is in the similar temperature range as in inert atmosphere.

There is no sulfate decomposition at all. The carbon content of the solid samples disappears between 450-600 ^{o}C producing CO_2.

There is also some NO production for the fly ash samples taken from below the water and air preheaters.

There is some increase in mass for the samples with higher carbon content in oxidative atmosphere. It is due to the adsorption of the CO_2 produced by the oxidation of the carbon forming carbonates by the reversible reaction pathway: $CaCO_3 = CaO + CO_2$.

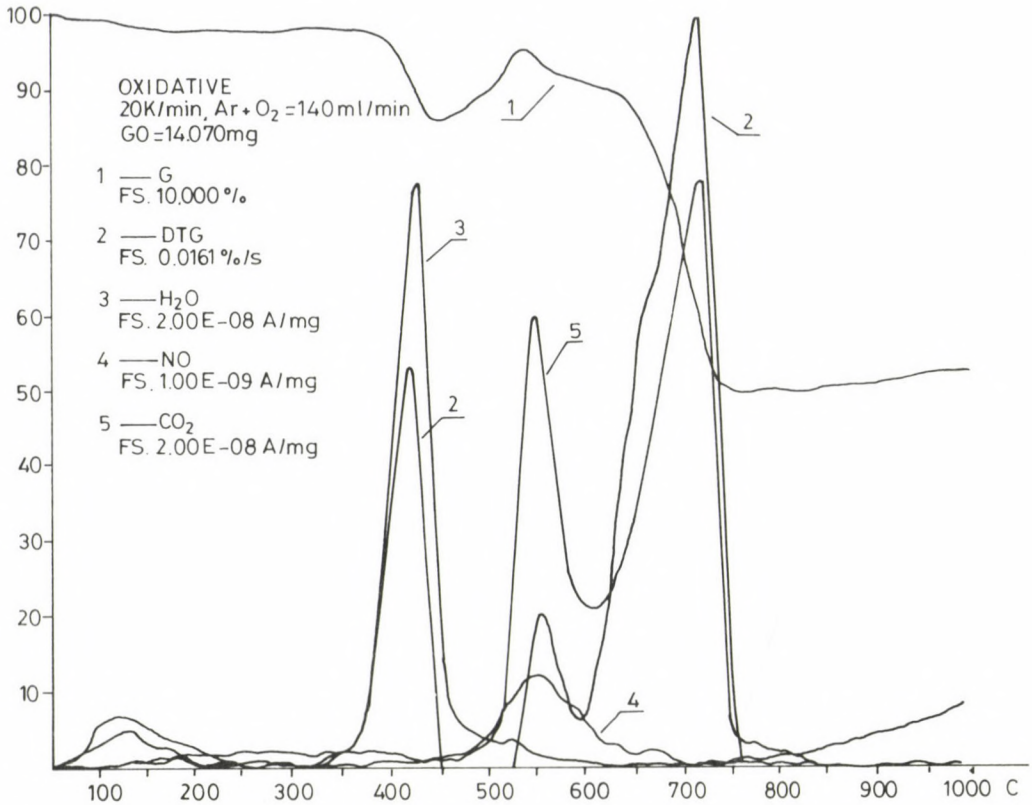

Fig. 13. A.H.V. 12. Boiler. ECO fly ash

The main conclusion from the above results is that the decomposition of sulfates in the TG balance can start at 800 ^{o}C in the presence of carbon, and if the atmosphere is inert.

The main specification of the TG-MS

Thermobalance: modified PE TGS-2/syst. 4
measuring range: (max. load) 5 g,
sensitivity: 0.5 µg,
noise: 1 µg (in the measuring range of 1 mg/10 V),
gas atmosphere: dynamic, neutral or reactive, 50-350 ml/min

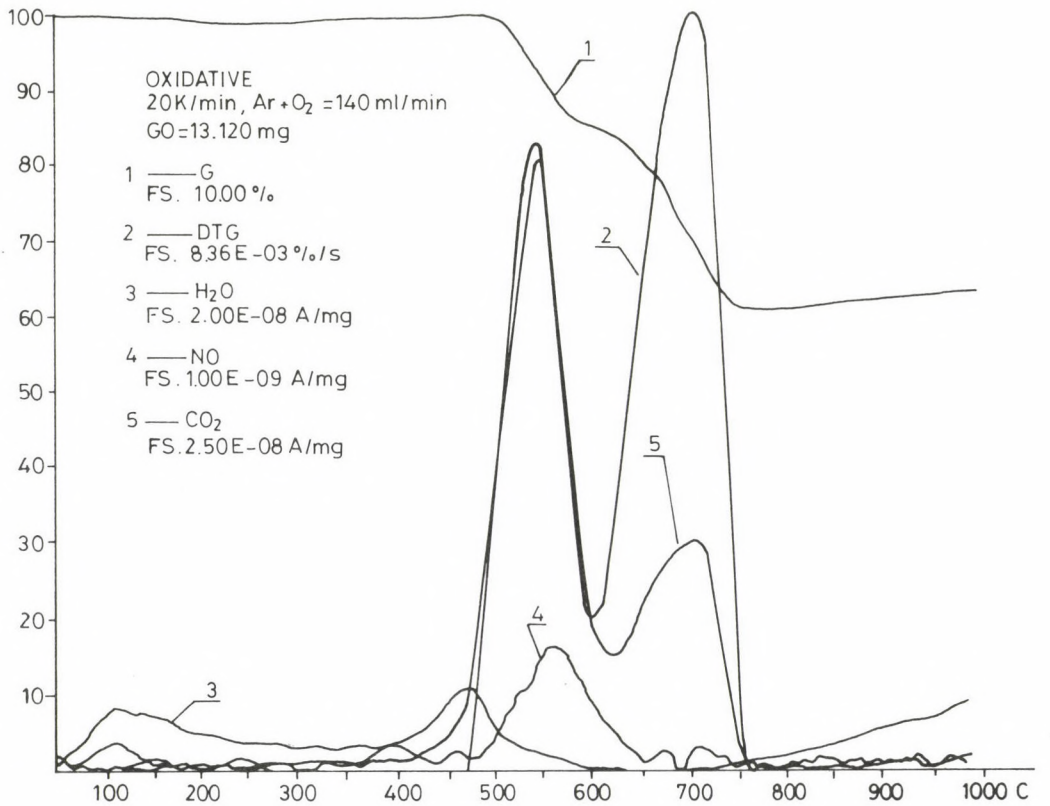

Fig. 14. A.H.V. 12. Boiler. Ljungstrom fly ash

Temperature control: PE syst. 4
temperature range: 20-1000 °C,
linear heating rate: 0.3-200 °C/min in steps of 0.1 °C,
tolerance in heating rate: max 5 °C for the whole temperature range,
tolerance in temperature measurement: max 5 °C for the whole temperature range (with calibration),
number of linear heating rates in the program: max 3

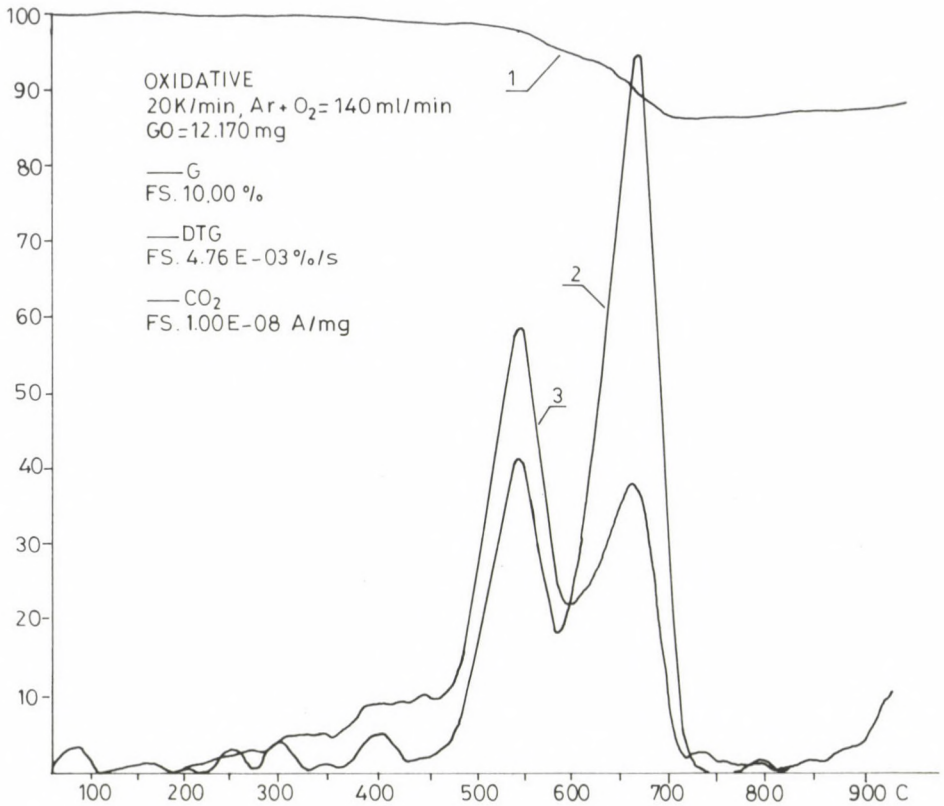

Fig. 15. A.H.V. 12. Boiler. EPS fly ash

Mass spectrometer: Blasers QMG 511
range of mass numbers: 1-511,
selectivity: max 2000 for M = 500 (FWHM), tunable,
sensitivity: 10^{3} A/mbar (multiplier included),
sensitivity in partial pressure: 10^{-14} mbar,
range of ion current: 10^{-5} - 10^{-13} A,
time constant: 40 µsec - 60 msec depending on the measuring range,
Ion source: "cross beam"
sensitivity: 2.5E-04 A/mbar,
measuring rate: 0.1 ms - 10 s/unit mass

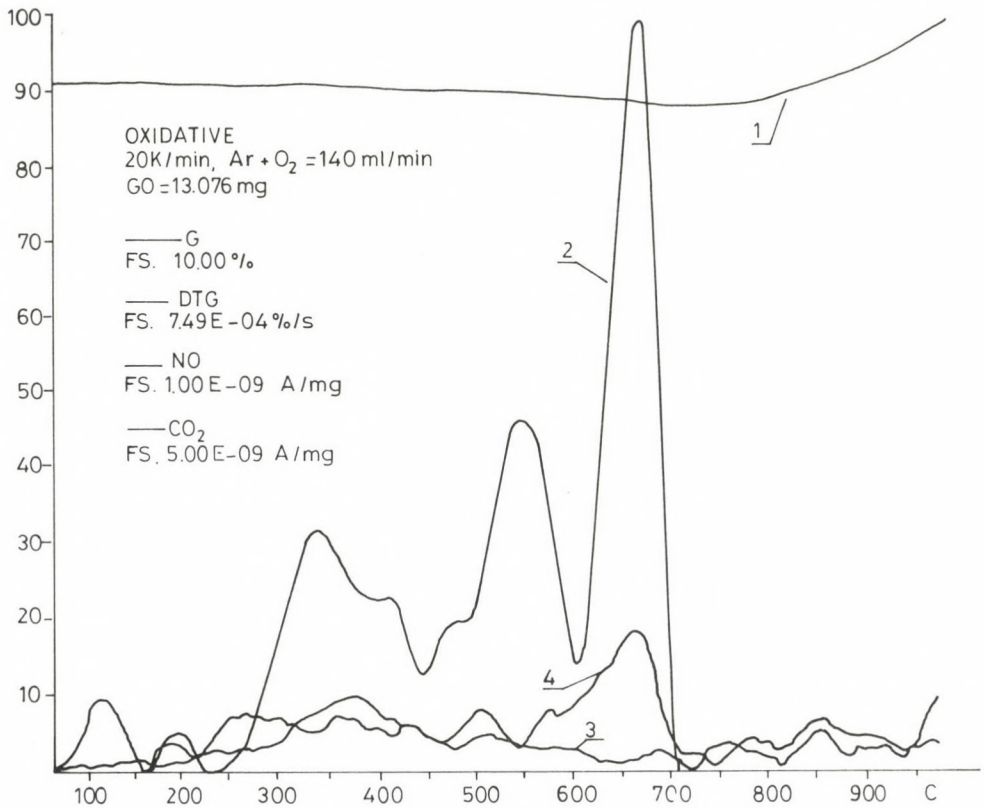

Fig. 16. DZO 1/A EPS fly ash + additive

REFERENCES

1. Till, F., Jakab, E., Mrs. Nemes, S.: VEIKI tüzeléstechnikai kísérletei kapcsán keletkező maradékok (salak, pernye) termoanalitikai vizsgálata. Report of Hungarian Academy of Sciences, Budapest, 1991

2. Horváth, F.: Ajkai Hőerőmű hibrid tüzelésű 12. hsz. kazán szavatossági vizsgálatai. VEIKI Report, Budapest, January 1991

Acta Technica Acad.Sci.Hung., 105(1-2), pp. 117-128 (1993)

DETERMINATION OF THE CURRENT DISTRIBUTION AND CURRENT LOAD OF OVERHEAD LINE CONDUCTORS

VARGA, L.*

(Received: 3 January 1991)

The author describes a new method for calculation of the loading current of aluminium-steel stranded conductors based on determination of the temperature of each layer in the conductor. Presented are a measurement method developed for determination of the temperature and current distribution within the stranded conductor and the thermal model based on decomposition of the conductor into layers.

On the basis of the results of measurements, it can be seen that a change of temperature in radial direction within multilayer conductors and a different current density of each layer of aluminium-steel conductors shall be reckoned with.

As a result of measurement made in a wind tunnel, a difference of 1-4% was found between the measured and calculated values of loading current in case of the new method based on decomposition of the conductor into layers as compared with 10% in case of the conventional method where the conductor is considered to be homogeneous.

The new method taking the radial temperature changes and current distribution into consideration results in increased accuracy of loading current calculations and thus in a more reliable calculating of overload on breakdown.

Limits are set to the current load of overhead lines among others by the rating of the line, voltage drop, optimum choice of losses and value of thermally permissible loading current. In case of short overhead lines with the number of junctions increased, the thermal rating is often determined by the thermally permissible loading current of the conductor.

The permissible loading current is determined by the maximum permissible temperature for the material of the conductor, the heat absorption depending on the meteorological parameters and by the heat output. Loading currents of a value determined on the basis of permissible aluminium and alloy aluminium conductor temperatures by metallurgical tests result in no reduction of the mechanical strength affecting the safety of operation unfavourably during the expected service life of the conductor. Methods widely used for calculation of the current load of stranded conductors ac-

*Varga, László, H-2145 Kerepestarcsa, Bajcsy Zs. u. 92, Hungary

Akadémiai Kiadó, Budapest

cording to the literature consider the conductor to be a homogeneous heat source from a thermal point of view.

In these methods, the formula of thermal equilibrium applicable to a homogeneous heat source is written for the surface of the conductor /1, 2, 3, 4, 5, 6/ and the current density of the conductor is assumed to be constant. In the course of research, we determined the current for each layer of the conductor. It was found that in case of conductors of a large cross section and aluminium-steel conductors, the calculation method described in the literature results in an error of 10% in the calculated value of loading current.

This error can be reduced by use of a calculation model developed for the temperature rise of the conductor, taking also the layer currents and layer temperatures into consideration.

Temperature distribution in the conductor

In the course of investigations to determine the thermal rating of the conductor, the currrent distribution in the conductor was found to be uneven and temperature differences were measurable in radial direction in the conductor.

To measure changes in the conductor temperature in radial direction, thermocouples have been placed into the strands of each aluminium cladding (T_1, T_2, T_3), into the steel core (T_4) and in between the outer aluminium cladding and that under it (T_5) (Fig. 1).

For measurement of temperatures T_1-T_4, the thermocouples have been placed in holes prepared in the strands while the thermocouple for measurement of temperature T_5 has been fastened on a small flexible metal plate and placed in between the claddings to measure the average of the temperatures of both aluminium claddings.

Figure 1 shows the change of temperature of a 500/65 mm^2 ACSR conductor as a function of current density, indicating also the average temperatures.

In calculating for average temperature, the weighted average (1) of the aluminium strands has been taken into consideration, assuming that the temperature of the steel core is independent of the strand temperatures.

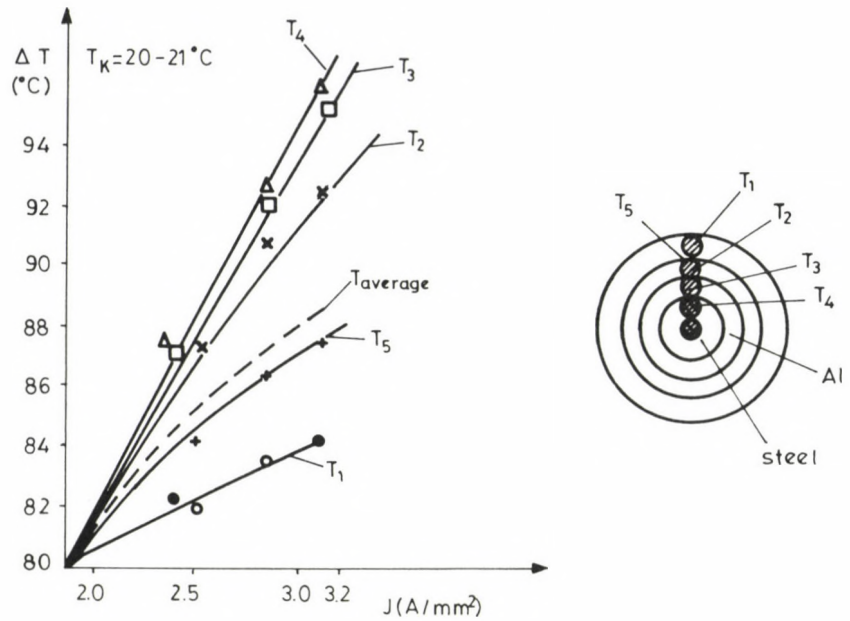

Fig. 1. Change of ACSR 500/65 conductor temperature as a function of current density

$$T_{average} = \frac{\sum_{i=1}^{K} n_i T_i}{\sum_{i=1}^{K} n_i} \qquad (1)$$

where

n_i - number of strands in the i-th aluminium cladding,

T_i - average cladding temperature,

K - number of claddings, K = 3 in case of ACSR 500/65.

In the range of wind speed investigated, the value of weighted average temperature ($T_{average}$) agrees with the value of average temperature measurable betwen the other and middle cladding within 1-2 ^{o}C. The results of Black, W.Z. and Collins, S.S. confirm the results of measurement obtained /7/.

Thermal model of the conductor

On the basis of the results of measurement, the conductor cannot be considered to be homogeneous. Therefore, the conductor has been split into layers or claddings for the purposes of calculation.

The stationary model of the conductor split into claddings is illustrated in Fig. 2.

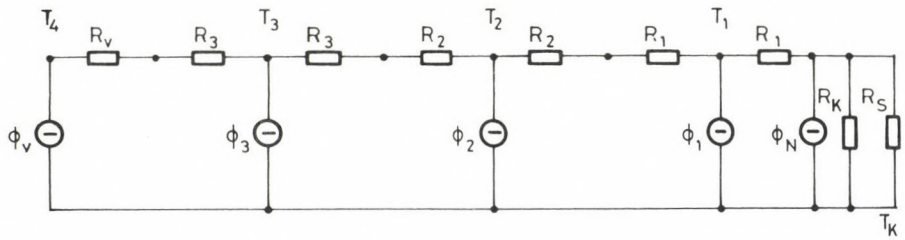

Fig. 2. Thermal model of a steel-cored conductor with three aluminium claddings

In the model,

ϕ_N - heat input as a result of solar radiation (W/m),

ϕ_v - losses in the steel core (W/m),

ϕ_i - losses in the different claddings, i = 1, 2, 3 (W/m),

R_i - half of the heat conduction resistance of the claddings, i = 1, 2, 3 (K/W),

R_K, R_S - thermal resistance characteristic of convective and radiant heat output, respectively (K/W).

On the analogy of Ohm's law, the equation of thermal conduction can be written /8/:

$$\phi_h = -\lambda A \frac{dT}{dx} \quad , \tag{2}$$

$$I = -\frac{1}{R} \frac{dU}{dx} \quad , \tag{3}$$

where

ϕ_h - heat flux (W/m)

λ - coefficient of thermal conductivity (W/mK),

A - surface (m^2),

dT - change of temperature along section dx (K),

I - current (A),

R - resistance (Ω),

dU - change of voltage along section dx (V).

In case of a cylindrically symmetric arrangement, equation

$$T_i - T_{i-1} = - \frac{\phi_r}{2\pi\lambda} \ln \frac{r_i}{r_{i-1}} \qquad (4)$$

can be written for the temperature difference between two and another two surfaces /8, 9/,

where

T_i and T_{i-1} are the temperatures of cylindric surfaces of radius r_i and r_{i-1}, respectively, (K),

r_i and r_{i-1} are the radii of the cylindric surfaces (m),

λ is the coefficient of thermal conductivity of the material (W/mK),

ϕ_r the loss occurring in the interior of the cylinder of radius r_{i-1} (W/m).

With the equations of the thermal model written for each surface, the temperatures of the different points of the conductor can be determined. For the calculation, it is necessary that the losses occurring in the different layers and the coefficient of thermal conductivity be known.

The coefficient of thermal conductivity is the resultant of the coefficients of thermal conductivity characteristic of the contact resistance occurring upon contact between aluminium strands /10/.

Loss ϕ_r in cylinders of radius r_i can be calculated on the basis of losses of the different layers:

$$\phi_r = \sum_{i=0}^{K} \phi_i \qquad (5)$$

where

ϕ_i - loss of the different layers within which $\phi_o = \phi_v$ is the loss of the steel core.

Loss ϕ_i can be calculated on the basis of current and resistance, measurable at given temperature, of the cladding:

$$\phi_i = I_i^2 R_i(T_i) = (J_i A_i)^2 \cdot R_i(T_i) \text{ (W/m)} \qquad (6)$$

where

I_i - current of the cladding (A),

J_i - current density of the cladding (A/mm^2),

A_i - cross section of the cladding (mm^2),

$R_i(T_i)$ - resistance of the cladding (Ω/m).

The current density per layer of aluminium-steel conductors depends on excitation of the steel core and on the stranding geometry /6, 11/.

The difference in current density is smaller in case of an even number of claddings while greater in case of an odd number of claddings, depending on the magnetic balance. The layer currents depend rather on excitation of the steel core than on layer temperature.

For thermal rating calculations, the current density of ACSR conductors with two and three claddings has been determined by measurement.

Methods of layer current measurement

Layer currents have been measured in the course of thermal rating measurements in wind tunnel. Pressed fittings have been applied to both ends of the conductor in order to avoid errors in measurement due to contact resistance of the fittings. Tensile stress σ of the conductor was 30-40 N/mm^2 during the measurement.

The cross section of the wind tunnel with the stranded conductor placed in it is illustrated in Fig. 3.

The direction of wind has been normal to the conductor (v). The place of the measuring coils is denoted by A while the place of the thermocouples by B.

Coils without iron core, placed in between the claddings of the conductor, have been used for layer current measurement. The voltage induced in the coil is proportional to the current flowing in the coil. Thus the ratio of voltage induced in the different coils can be used to calculate the layer currents (Fig. 4).

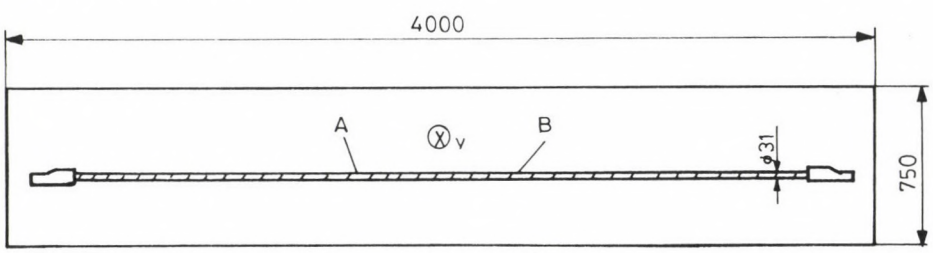

Fig. 3. Cross section of the wind tunnel with the conductor in it

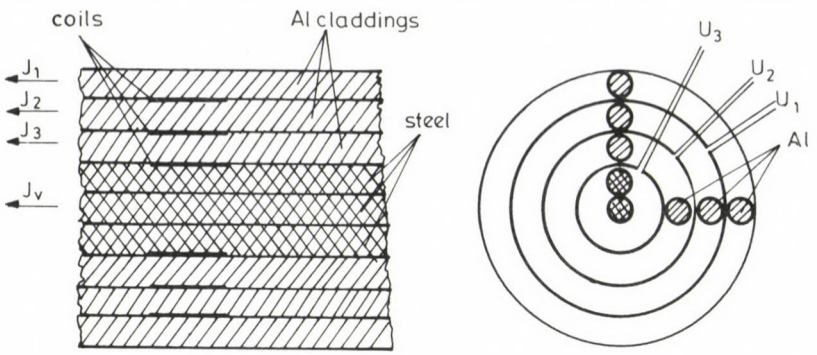

Fig. 4. Measurement setup with measuring coils for current distribution measurements in case of an ACSR 500/65 conductor

A current transformer connected in series with the conductor has been used for calibration of the coils after measurements in wind tunnel, with the layers outside of the coil removed.

In case of given resultant currents, the layer currents can be calculated by means of diagrams $U_i = f(I_i)$:

$$I_v = f(U_3), \tag{7}$$
$$I_3 = f(U_2) - f(U_3), \tag{8}$$
$$I_2 = f(U_1) - f(U_2), \tag{9}$$
$$I_1 = I_{resultant} - f(U_1) \quad . \tag{10}$$

The effect of the steel core, resulting in distortion of the current density, can be characterized by deviation of the current density of the layers from homogeneous current density, described by the slope of functions $J_i = f(J_h)$ of shape $y = mX$:

$$J_i = m_i J_h \tag{11}$$

where

J_i - current density of the i-th layer (A/mm^2),

J_h - current density calculated for homogeneous current distribution (A/mm^2).

Slopes m_i determining the current distribution in calculation of the loading current can be calculated by plotting the current density of the different claddings as a function of homogeneous current density.

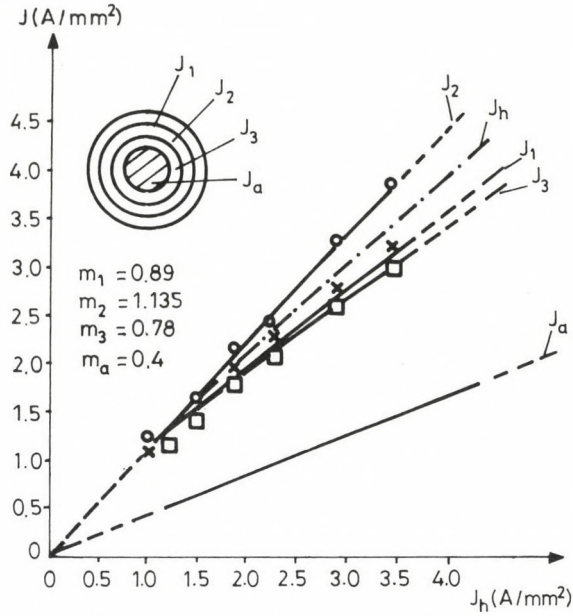

Fig. 5. Change of the current density of the layers of a conductor with three claddings as a function of average current density

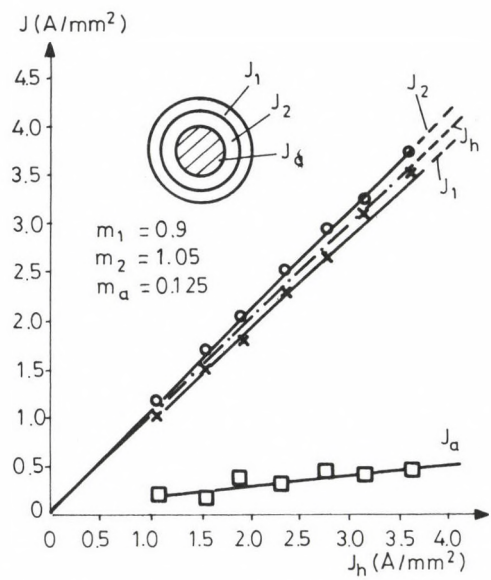

Fig. 6. Change of the current density of the layers of a conductor with two claddings as a function of average current density

Table 1

Slope of current density functions

Serial number of cladding i		Odd cladding number	Even cladding number
Al	1	0.89	0.9
	2	1.135	1.05
	3	0.78	-
Steel		0.4	0.125

Illustrated as a function of homogeneous current density, Figs 5 and 6 show the current densities of a conductor with 3 and 2 aluminium claddings, respectively, the slope of the current density functions being given in Table 1. In the diagrams, the domain not investigated is indicated by broken line.

On the basis of the slope of the current density functions, the power lost can be calculated for the different claddings in case of given homogeneous current density (J_h):

$$\phi_i = (m_i \cdot A_i \cdot J_h)^2 \cdot R_i(T_i) \qquad (W/m) \qquad (12)$$

where

m_i - slope of the current density curve of the i-th cladding (Table 1),

A_i - cross section of the i-th cladding (mm^2),

J_h - current density of homogeneous current distribution (A/mm^2),

$R_i(T_i)$ - resistance of the i-th cladding of the conductor at temperature T_i (Ω/m).

Calculation of permissible loading current

The current density of the loading current determined for the conductor considered to be homogeneous in the calculation can be determined by means of the following relationship:

$$J_h = \frac{1}{A_{Al}} \sqrt{\frac{\phi_K(T_f) + \phi_S(T_f) - \phi_N}{R(T_f)}} \quad (A/mm^2) \qquad (13)$$

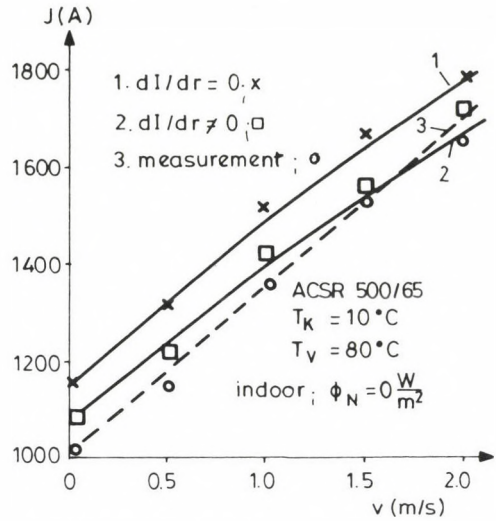

Fig. 7. Change of the measured and calculated values of loading current as a function of wind speed at an ambient temperature of T_K = 10 °C

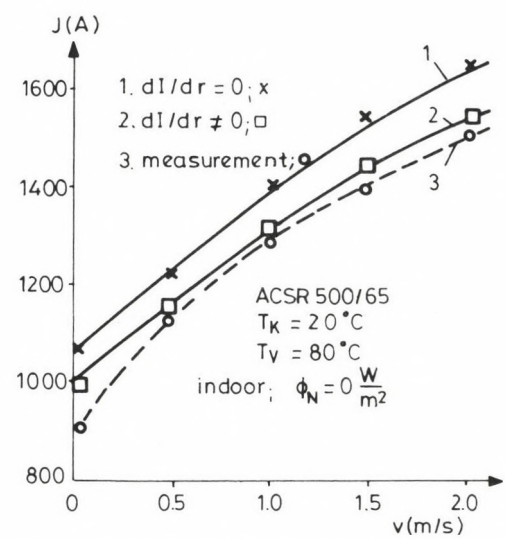

Fig. 8. Change of the measured and calculated values of loading current as a function of wind speed at an ambient temperature of T_K = 20 °C

where

ϕ_K and ϕ_S - heat output by convection and radiation of the conductor of surface temperature T_f (W/m),

ϕ_N - radiant heat absorption (W/m),

$R(T_f)$ - resistance of the conductor (Ω/m),

T_f - surface temperature of the conductor (K).

Losses ϕ_i determined by relationship (12) can be used to determine the layer temperatures, losses and the permissible loading current by iteration on the basis of the model according to Fig. 2.

The values of loading current determined by calculation, taking also the inhomogeneous current density of the conductor into consideration, as well as the measured values of loading current for an ACSR 500/65 mm^2 conductor are given in Fig. 7 at an ambient temperature of T_K = 10 ^oC while in Fig. 8 at an ambient temperature of T_K = 20 ^oC.

With the current distribution taken into consideration, the difference between the calculated and measured values of loading current is less than in case the current distribution is assumed to be homogeneous. In the calculation assuming homogeneous current distribution at a wind speed of 1 m/s, the error is 7-10% while in case the change of current density is taken into consideration, the error of the calculation is only 1-4%.

Use of the method taking the radial temperature changes and current distribution of the conductor into consideration results in increased accuracy of loading current calculations and thus in an increasingly reliable calculation of overload upon breakdown.

REFERENCES

1. Zarebski, W.: Obciaualnosc pradoeva prezewodow linij napowietrznich. Biuletin Institut Energetiyki 1968, 3/4, (Warsaw), 24-47

2. Nicholson, I.: Influence of conductor designs and operating temperature on the economy of overhead lines. Proc. IEE, 118, No. 3/4 (1971)

3. Vajta, M.: Maximum permissible current load for overhead line conductors II. VEIKI Publications No. 21, Budapest 1964 (in Hungarian)

4. Webs, A.: Dauerstrombelastbarkeit von nach DIN 48201 gefertigten Freileitungsseilen aus Kupfer, Aluminium und Aldrey. Elektrizitätswirtschaft 23 (1963), 861-872

5. Morgan, V.T.: The thermal rating of overhead line conductors. Part II. Elect. Power Syst., 6 (1983), 287-300

6. Morgan, V.T.: Some factors which influence the continuous and dynamic thermal rating of overhead line conductors. Cigre Symposion 06-85, Brussels 1985, 1-6

7. Black, W.Z., Collins, S.S.: Theoretical model for temperature gradients within bare overhead conductors. IEEE Trans. on Pow. Det. 3, No. 2 (1988), 707-715

8. Imre, L.: Applied Thermodynamics and Fluid Mechanics. Tankönyvkiadó, Budapest 1971 (in Hungarian)

9. Varga, L.: Current load tests of insulated conductors. Elektrotechnika, 80, No. 11 (1986), 420-424 (in Hungarian)

10. Varga, L.: Measurement of radial thermal conductivity coefficient of overhead line conductors. Elektrotechnika 83, No. 2 (1990), 68-71 (in Hungarian)

11. Güntner, O.: Auswirkung der innerhalb der Aluminium-Lagen auftretenden ungleichmässigen Stromverteilung auf die Energieübertragungsverluste von Stahl-Aluminium-Freileitungsseilen. Dissertation 1989, TU-Wien, Fakultät für Elektrotechnik

Acta Technica Acad.Sci.Hung., 105(1-2), pp. 129 (1993)

BOOK REVIEW

Tarnay, K.: Protocol specification and testing, Technical Sciences, Advances in Electronics, Vol. 5. Series Editor: László Papp Akadémiai Kiadó, Budapest, Hungary, Plenum Press, New York, USA, 1991. HU ISSN 0236-6312, pages 368

Our world is moving towards what we might call the information society. In this information society everybody should have an up-to-date computing environment with an easy-to-achieve communication background. The principal means of integrating the computer environment and the communication tools is computer communication. Computer communication is responsible for the data message exchange between the computerized source station and the destination station.

The book deals with the communication protocols. First the reference model and its layers are discussed, then the seven layers and their protocols are described. There are specifications of BSC, HDLC and X. 25 protocols. The author defines the abstract model of testing.

In the second part, the reader can find the formal description techniques: state-transition based models, graph models, algebras and formal languages, specification languages: SDL, ESTELLE, LOTOS.

The third part deals with applications. The protocols introduced in the first part are specified using the methods of the second part.

For applications the user can read the alternating-bit protocol specification with state-transition graph, Petri net and with ESTELLE. There is a formal description of HDLC and the LAPB with SDL/GR. For the transport protocols there are case studies in SDL-graph, numerical Petri nets, data flow graph and LOTOS specification.

In connection with conformance testers and test sequences, we can read about the test sequence generation, w-method, Gönenc method, the automatic test sequence generation and about case studies for testing the NATHAN application protocol, and about Conformance Test Centre in the National Bureau of Standards.

The reader will be familiarized in computer communication, protocol specification with formal description techniques and protocol testing.

The chapters contain examples and the most important international data communication standards, literature and abbreviations are summarized at the end of the book.

The book is highly recommended for self-study and as a university course book. This is one of the first books that summarize the protocol engineering, protocol specification and protocol testing topics.

In the series of Technical Sciences, Advances in Electronics, this book was the fifth in sequence, but the first one published in English.

Gy. Csopaki

Akadémiai Kiadó, Budapest

PRINTED IN HUNGARY

Akadémiai Kiadó és Nyomda Vállalat, Budapest

NOTICE TO CONTRIBUTORS

Papers in English* are accepted on condition that they have not been previously published or accepted for publication.

Manuscripts in two copies (the original type-written copy plus a clear duplicate one) complete with figures, tables, and references should be sent to

Acta Technica
Nádor u. 7. I. 118
Budapest, Hungary
H-1051

Although every effort will be made to guard against loss, it is advised that authors retain copies of all material which they submit. The editorial board reserves the right to make editorial changes.

Manuscripts should be typed double-spaced on one side of good quality paper with proper margins and bear the title of the paper and the name(s) of the author(s). The full postal address(es) of the author(s) should be given in a footnote on the first page. An abstract of 50 to 100 words should precede the text of the paper. The approximate locations of the tables and figures should be indicated on the margin. An additional copy of the abstract is needed. Russian words and names should be transliterated into English.

References. Only papers closely related to the author's work should be referred to. The citations should include the name of the author and/or the reference number in brackets. A list of numbered references should follow the end of the manuscript.

References to periodicals should mention: (1) name(s) and initials of the author(s); (2) title of the paper; (3) name of the periodical; (4) volume; (5) year of publication in parentheses; (6) numbers of the first and last pages. Thus: 5. Winokur, A.—Gluck, J.: Ultimate strength analysis of coupled shear walls. American Concrete Institute Journal 65 (1968) 1029-1035

References to books should include: (1) author(s)' name; (2) title; (3) publisher; (4) place and year of publication. Thus: Timoshenko, S.—Gere, J.: Theory of Elastic Stability. McGraw-Hill Company. New York, London 1961

Illustrations should be selected carefully and only up to the necessary quantity. Black-and-white photographs should be in the form of glossy prints. The author's name and the title of the paper together with the serial number of the figure should be written on the back of each print. Legends should be brief and attached on a separate sheet. Tables, each bearing a title, should be self-explanatory and numbered consecutively.

Authors will receive proofs which must be sent back by return mail.

Authors will receive 50 reprints free of charge.

*Hungarian authors can submit their papers also in Hungarian.

HU ISSN 0865-7459

ACTA TECHNICA

ACADEMIAE SCIENTIARUM HUNGARICAE

EDITOR-IN-CHIEF: P. MICHELBERGER

VOLUME 105
NUMBER 3

MATERIAL SCIENCES AND TECHNOLOGY–T/3

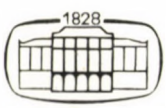

AKADÉMIAI KIADÓ, BUDAPEST 1993

ACTA TECHNICA

A JOURNAL OF THE HUNGARIAN ACADEMY OF SCIENCES

Acta Technica publishes original papers, preliminary reports and reviews in English, which contribute to the advancement of engineering sciences.

Acta Technica is published by

AKADÉMIAI KIADÓ
Publishing House of the Hungarian Academy of Sciences
H-1117 Budapest, Prielle K. u. 19—35

Subscription information

Orders should be addressed to

AKADÉMIAI KIADÓ
H-1519 Budapest, P.O. Box 245

Subscription price for Volume 105 (1993) in 4 issues US$ 80.00, including normal postage, airmail delivery US$ 20.00.

Acta Technica is abstracted/indexed in Applied Mechanics Reviews, Current Contents–Engineering, Technology and Applied Sciences, GeoRef Information System, Science Abstracts.

CONTENTS

PRINTED IN HUNGARY

Akadémiai Kiadó és Nyomda Vállalat, Budapest

Acta Technica Acad. Sci. Hung., 105 (3), pp. 131—152 (1993)

REDUCTION OF NO_x EMISSION FROM NATURAL GAS FIRED INDUSTRIAL FURNACES

BÍRÓ, A.*

(Received: 22 November 1991)

The accuracy of calculation of NO_x formation in industrial furnaces can be increased on the basis of the results of practical measurements.

Research by the Department of Fuel Engineering of the University of Miskolc included investigation of the effect of flue gas recirculation, air factor, two-step air feed and water injection on NO_x formation as a function of furnace temperature.

Since the rate of NO_x formation depends also on the construction of the burner, it is necessary that the value of NO_x emission by the burner, measured at a temperature falling within the range of furnace temperature (basic value, B), be known. In the knowledge of the basic value and the temperature associated with it, NO_x emission from industrial furnaces can be calculated.

EXPLANATION OF THE NOTATION USED

R	— gas constant	8.31 J/mol, K
T	— absolute temperature	K
ϑ	— temperature, swirl parameter	^oC, 1
E	— normal formation potential	cal/mol, J/mol
A	— surface	m^2
ρ	— density	kg/m^3
w	— flow rate	m/s
τ	— direction parameter	1
d	— nozzle diameter	m
Re	— Reynolds number	1
B	— working point of the burner	ppm_V
V	— volume, volume ratio, volume flow rate	m^3, ppm, m^3/h
k	— equilibrium constant	$cm^3/mol/s$
I	— pulse power	N

*Bíró, Attila, H-1016 Budapest, Gellérthegy u. 34, Hungary

Akadémiai Kiadó, Budapest

It	— axial component of pulse power	N
Itm	— pulse power component normal to the axis of the burner	N
Y	— burner working point factor	1
B	— basic value of NO_x production	ppm
V_{CO_2}	— CO_2 content of air	%
$V_{sec.air}$	— secondary air in % of comb. air	%
n	— air factor	1
m_{water}	— mass of injected water	kg/m^3 CH_4

1. Introduction

Much research work has been devoted to investigation of the mechanism of NO_x formation in the recent fourty years and results of quite a number have been published. All this research permits the processes taking place during oxidation of the fuel, among them the volume ratio of NO_x expected to develop, to be determined for the ideal case by approximate calculation.

The reaction constants by means of which the equilibrium constants can be calculated for different reaction temperatures and partial pressures (see Section 2) are available in different publications. However, the use of these constants results in values much (three to ten times) lower than the actual values. Another problem is that within the furnace, neither the axial distance of the reaction zone from the burner nor the combustion process as a function of time, nor the reaction temperature can be determined because the furnace temperature varies from point to point and with time, e.g. it may decrease considerably as a result of the cooling effect of cold material put into the furnace even within a charge (melting) period.

Empirical methods have also been used to study NO_x formation in hot furnaces. Most of these data published in the literature, based on practical (experimental) measurements, cannot be used to determine NO_x formation because more than one factor had been changed during the measurements and the results have been given as simple ratios. These ratios (curves) show tendencies on the effect of NO_x reduction due to some control action on the flame. (E.g. what will be the rate of NO_x formation if the value of air factor is increased whereas the furnace temperature decreases as a result of the cooling effect of the excess of air.)

In case of industrial furnaces, the final furnace temperature must not change as otherwise the normal operation of the furnace would be endangered.

Therefore, the effect of any control action can be investigated only if the furnace temperature remains constant or the results can be recalculated for constant furnace temperature.

In calculation of NO_x formation, the furnace temperature shall be taken as a starting point in every case because NO_x formation is also influenced by reduction of the maximum flame temperature, depending also on the furnace temperature, in case of most control actions. E.g. flue gas recirculation or increase of the air factor or water injection results not only in a change of the partial pressure conditions of oxidation but also in a reduction of the furnace temperature to an extent depending on the mass flow and heat capacity of the media introduced.

Research by the Department of Fuel Engineering of the University of Miskolc has been designed to find relationships permitting the expectable NO_x formation in natural gas fired furnaces of a temperature of 900 ... 1300 ^oC to be determined and controlled on the basis of data continuously supplied by the measurement and recording system of the furnaces.

2. Reduction of NO_x emission from industrial plants

If efforts to determine NO_x formation by calculation are not given up in spite of the difficulties mentioned, two methods can be used in case of natural gas fired furnaces, such as

(a) use of CH_4 oxidation equations,

(b) use of a simpler method based on Zeldovits' research, taking only the most important reactions (2 ... 3) determining NO formation into consideration (this method can be improved by use of additional equations).

Reaction constants determined and collected by Bowman et al. /6--13/ are tabulated in Table 1. The process of CH_4 oxidation, NO_x formation and NO_x reduction is rather complicated, the number of reactions involved in the processes is large and the values of reaction constants found in the literature are different even for the same reaction. Therefore, the method recommended for turbulent diffusion flames by Zeldovits is used in general to investigate the effect of the different gas components and temperature on NO_x formation. According to Zeldovits' chain-reaction mechanism, NO_x formation (predominantly NO) takes place in the furnaces, as follows /3/:

Table 1

	$k = A.\ T^{y}.\exp(-E/RT)$, $cm^3/mol,s$
According to C.T. Bowman (cm^3,J,K,mol,s)	
$H_2 + M = 2H + M$, if M = Ar,O_2	$k = 2.33 \times 10^{12} T^{1/2} \exp(-387.000/RT)$
$H + O_2 = OH + O$	$k = 4.1 \times 10^{13} \exp(-51.500/RT)$
$H_2 + HO_2 = H_2O + OH$	$k = 3.14 \times 10^{11} \exp(-157.400/RT)$
$H_2 + O_2 = OH + OH$	$k = 1.6 \times 10^{14} \exp(-56.500/RT)$
$H + OH = H_2O + H$	$k = 5.2 \times 10^{13} \exp(-27.200/RT)$
$H + H_2O = 2OH$	$k = 6 \times 10^{13}$
$CO + O_2 = CO_2 + O$	$k = 3.14 \times 10^{11} \exp(-157.400/RT)$
$CO + OH = CO_2 + H$	$k = 4.0 \times 10^{12} \exp(-33.500/RT)$
$OH + OH = H_2O + O$	$k = 5.5 \times 10^{13} \exp(-29.300/RT)$
$CH_4 + OH = CH_3 + H_2O$	$k = 2.0 \times 10^{17} \exp(-10500/T)$
$CH_4 + O = CH_3 + OH$	$k = 2.0 \times 10^{13} \exp(-19.400/T)$
$CH_4 + H = CH_3 + H_2$	$k = 6.9 \times 10^{13} \exp(-25.000/T)$
$CH_3 + O_2 = HCO + H_2O$	$k = 2.0 \times 10^{10}$
$CH_3 + O = HCO + H_2$	$k = 1.0 \times 10^{14}$
According to Y. Zeldovits	
$O + N_2 = NO + N$	$k = 1.4 \times 10^{14} \exp(-158.700/T)$
$N + O_2 = NO + O$	$k = 6.4 \times 10^{9} \exp(-13.150/T)$
$N + OH = NO + H$	$k = 4.0 \times 10^{13}$
According to N.P. Cernansky, R.F. Sawyer	
$NO + O_2 = NO_2 + O$	$k = 10^{12.5} \exp(-198.500/RT)$
$NO + OH = NO_2 + H$	$k = 10^{12.5} \exp(-125.600/RT)$
$NO + CO_2 = NO_2 + CO$	$k = 10^{12.3} \exp(-341.650/RT)$
$NO + O_3 = NO_2 + O_2$	$k = 10^{11.73} \exp(-10.000/RT)$
According to M. Gehring, K. Hoyermann, H. Sacke and J. Wolfrum	
$O + NH_2 = HNO + H$ or $NH + OH$	$k = 2.1 \times 10^{12}$
$O + N_2H_4 = N_2H_2 + H_2O$	$k = 10^{13.8} \exp(-5025/RT)$
$H + N_2H_4 = N_2H_3 + H_2$	$k = 1.6 \times 10^{11}$
$NO + NH = N_2 + O$ linear	$k = 1.5 \times 10^{9} \exp(-161.800/RT)$
inverse	$k = 6.4 \times 10^{9} T.\exp(-26.170/RT)$
$O_2 + N_2 = 2O + N_2$ linear	$k = 6.3 \times 10^{13} \exp(-118.000/RT)$
inverse	$k = 1.0 \times 10^{14}$
According to M. Koshi, H. Ando, M. Oya and T. Osaba	
$H + NO = OH + H$	$k = 10^{13.5} \exp(-201.000/RT)$
$H_2 + NO = HNO + H$	$k = 10^{13.6} \exp(-241.600/RT)$
According to E.A. Albers, H. Hoyermann, H. Sacke, K.J. Schamatjko and Wagner	
$H + N_2O = N_2 + OH$	$k = 2.2 \times 10^{14} \exp(-72.500/RT)$
$CN + H_2 = HCN + H$	$k = 6.0 \times 10^{13} \exp(-22.200/RT)$
$CN + O = CO + N$	$k = 1.2 \times 10^{13} \exp(-4200/RT)$
According to L. Fower, R.K. Hanson and C.H. Kruger	
$NO + H_2 = H + HNO$	$k = 3.0 \times 10^{11} T^{1/2} \exp(-10.000/RT)$
$H + NO = N + OH$	$k = 1.34 \times 10^{14} \exp(-206.000/RT)$
$NO + NO = N_2O + O$	$k = 5.7 \times 10^{12} \exp(-267.130/RT)$

$$N_2 + O = NO + N \quad (1)$$

$$O_2 + N = NO + O \quad (2)$$

where reaction (1) takes place at a much slower rate than reaction (2) and therefore the rate of NO formation depends on (1). At the same time, the slower reaction is accompanied with N-atom formation resulting in production of a new NO molecule according to (2). Equation (1) is a mechanism to start while equation (2) a mechanism to stop the chain reaction. If the partial pressure of NO is low in the furnace, the rate of reaction will be determined by straightline development of the reactions. Therefore, we can write that

$$d(NO)dt = 2\, k_1 \cdot [N_2] \cdot [O]^{0.5} \quad (3)$$

Reaction constant:

$$k_1 = 7 \cdot 10^{13} \exp(-75\,500/RT), \qquad cm^3/mole, s.$$

Partial pressure of oxygen:

$$O / O_2^{0.5} = 4.1 \exp(-58\,300/RT), \qquad (mole/cm^3). \quad (4)$$

With equations (3) and (4) lumped:

$$D(NO)/dt = 5.74 \cdot 10^{14} \cdot [N_2] \cdot [O_2]^{0.5} \exp(-133\,800/RT). \quad (5)$$

After calculations and measurements made simultaneously, the following conclusions can be drawn from the results:

1. Depending on the pressure (0.3 ... 1.0 bar), the calculated values are 10 ... 3 times lower than the measured values /5/.
2. The rate of NO formation is highest in the flame front but maximum NO concentration takes place in the section after the flame where fuel is still present.
3. The effect of temperature on the mass of NO developed is decisive. Increase of the combustion temperature by increase or reduction of the oxidant temperature or changing of the air factor or specific heat affects the rate of reactions decisively. With increasing temperature, the mass of NO (NO_x) developed and this the NO_x content of the flue gas increases.

According to what has been said under par. 3, NO_x formation can be reduced by any control action resulting in a reduction of the maximum flame temperature. Included among control actions of this type are, e.g.

(a) reduction of the combustion chamber temperature,

(b) reduction of the partial oxygen pressure in the oxidant,

(c) multistep mixing of fuel and oxidant to increase the combustion time,

(d) increase of the air factor,

(e) introduction of some coolant (water or steam) before the combustion zone,

(f) combinations of control actions (a)--(e).

In respect of NO_x formation, the efficiency of the methods used is different and also the furnace efficiency is affected in a different way by each method. Therefore, an effort was made to measure also the effect of control actions made to reduce NO_x formation on the efficiency of the furnace.

3. Description of the experimental set-up

The vertical section of the experimental furnace constructed for investigation of NO_x formation is shown in Fig. 1. Natural gas of a pressure

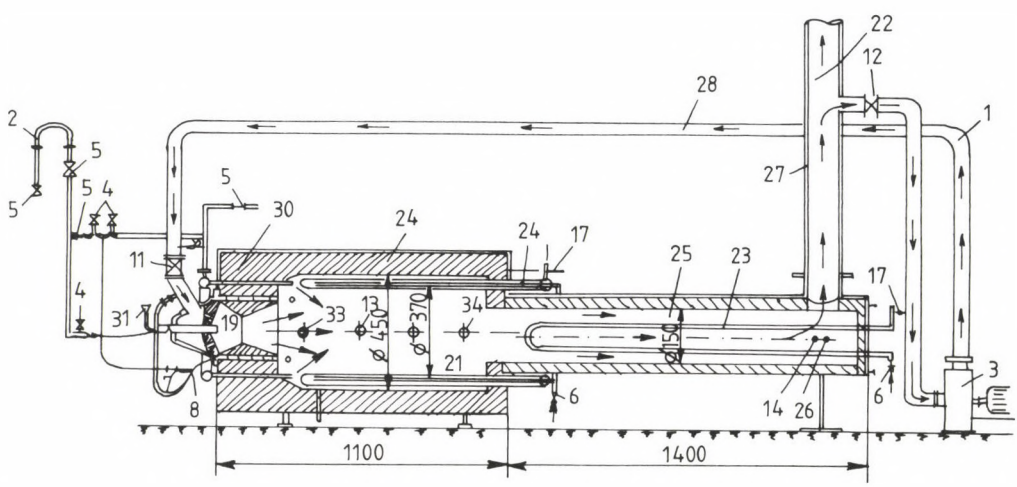

Fig. 1

of 1.5 bar is fed to the burner at a volume flow rate adjustable by means of fittings 5. In compliance with the relevant safety regulations, burner 19 has been equipped with ignition burner, ignition transformer and flame failure alarm. The volume flow rate of gas has been measured by means of turbo-flowmeter 2. Around the brick supporting burner 19, probes 30 protrude into chamber 21 of the experimental furnace, through which secondary gas or compressed air (secondary air) can be introduced into the chamber. The nozzle at the outlet of the six probes includes a 45-degree angle with the axis of the probe, the axis of the probes being parallel to the vertical axis of the furnace.

Air for combustion gets to the burner through rotameter 1, air duct 28 and regulating fitting 11 from ventilator 3. The inlet stub of the ventilator has been connected to flue gas outlet pipe 27 by means of a pipeline. Thus flue gas of a volume flow rate adjustable by means of valve 12 could be admixed with air for combustion to reduce the oxygen content of air. To control the volume of flue gas admixed with air, the carbon dioxide content of combustion air in air duct 28 has been analyzed continuously. The output of ventilator 3 has been adjusted so as to permit the air factor to be varied in the range of $n = 1.0 \ldots 2.0$.

Lining 20 of furnace chamber 21 has been made of fibrous refractory material with a gas-proof refractory layer of a thickness of 3 ... 5 mm applied to the internal surface. This construction of the lining results in a low thermal inertia of the furnace which contributed to stabilization of the measurement temperature within a short time. A gas-proof sheathing has been provided for the furnace. In the sidewalls, holes are available for testing and measurement. The furnace (gas) temperature has been measured at three points along the length of the furnace /13, 33 and 34 in Fig. 1) by means of Pt-PtRh thermocouples.

Combustion produce leave the furnace for calorimeter 25 arranged coaxially with the chamber. Through the end wall of the calorimeter compartment, water calorimeter 23 protrudes into the calorimeter compartment. The mass flow rate as well as the inlet and outlet temperature of water flowing in the calorimeter can be measured to check the heat absorbed by the calorimeter during the different firing processes. An NiCr-Ni thermocouple has been used to measure the temperature of the calorimeter compartment at point 26.

Materials used for insulation of the furnace have been used also for the lining of the calorimeter compartment. The NO_x content of the combustion

products has been recorded at point 26 at the end of the calorimeter compartment, using an instrument operating on the basis of the principle of chemoluminiscence. Flue gas leaves the calorimeter compartment through flue pipe (stack) 27.

A system of water cooled probes 24 has been built around calorimeter compartment 25. The probes can be moved along the axis of the calorimeter compartment. Six water cooled probes are connected between the annular inlet and outlet pipes, which can be pushed into the furnace through end wall 21 of the furnace chamber. By pushing probes 24 into the furnace chamber to a depth corresponding to 25%, 50%, 75% or 100% of the travel of the probes, the temperature of furnace chamber 21 can be varied in a range corresponding to the lower and upper limit temperatures (900 ... 1300 ^{o}C) of metallurgical heat-treatment and reheating furnaces.

A thin metal pipe 31 has been introduced through the gas nozzle coincidently with the axis of the burner, through which water sprayed by natural gas can be fed to the mixture at a rate controlled by means of an infusion dosing device designed for use in hospital.

4. Description of the experiments

The experimental furnace permits the effect of any control action described under (a)--(f) of Section 2 or any combination of these control actions to be studied.

The effect of one control action has been investigated at once with the other parameters kept constant during the measurement.

For example, to investigate the effect of chamber temperature, furnace chamber 21 has been heated to a temperature of 1300 ^{o}C. After stabilization of the temperature, the mass flow rate of gas and air and the air factor have been stabilized at a constant value. Water has not been injected and no secondary medium (gas, air) has been introduced. The flue gas recirculation pipe has been shut off.

The value of NO_x formation has been recorded at the selected temperature of 1300 ^{o}C. This value is called 'basic value'. Then water-cooled (cold) probes 24 have been pushed into furnace chamber 21 over a length corresponding to 25% of the travel. The temperature of chamber 21 has been allowed to stabilize at a lower value as a result of cooling and the mass of NO_x developed has been recorded. The process has then been repeated with the

probes introduced to 50%, 75% and 100% of the travel. The values measured have been checked by withdrawal of the cold probes over 25% of the travel to see whether the NO_x values measured during the cooling process are restored.

The control action according to paragraph (b) of Section 2 is reduction of the partial oxygen pressure. For this measurement, chamber 21 had been heated to 1300 ^{o}C (basic value), then, with the air factor stabilized at a value of n = 1.05, valve 12 has been opened to admix flue gas with combustion air in an amount resulting in CO_2 = 0.3% in pipe 28. The system had been allowed to stabilize before the values of temperature and NO_x etc. have been recorded. Then flue gas admission has been increased by means of valve 12 to increase the CO_2 content in combustion air pipe to 0.6%. After stabilization of the temperature, the values measured have been recorded again. Increase of the CO_2 content of combustion air has been continued in 0.3% steps to 1.5%. This value proved to be the upper limit of direct feed of flue gas (into the air duct) because of flame stability problems.

The control action according to Section 2, paragraph (c) includes multistage combustion. To test the effect, the experimental furnace had been heated to test temperature and 90% of the gas has been introduced through the burner, while 10% through nozzles 30 with 100% of the combustion air entering the furnace through burner 19.

After the instrument readings had been recorded, the gas admission was distributed among the burner and the nozzles of the probe system to a ratio of 80 to 20%, 70 to 30%, 60 to 40% and 50 to 50%.

The effect of two-step air feed has been measured by introducing 90% of combustion air through the burner while 10% (from the compressed air system) through probes 30 with 100% of the gas of controlled volume flow rate entered the furnace through the burner. Air admission has been distributed among the burner and probes in the ratio used for gas admission.

To investigate the effect of control action according to paragraph (d) of Section 2, the furnace had been heated to test temperature and then the air factor of n = 1.05 has been increased to 1.2, 1.3, 1.4, 1.5 and 1.6. For each adjustment, all the measured data have been recorded.

In testing the control action according to paragraph (e) of Section 2, the experimental furnace has been heated to test temperature with all the parameters left unchanged except for the mass of water injected through the burner which has been varied between gas flow rate limits of 0.3 to 1.2 kg/m^3 (resulting, of course, in a different value of temperature and NO_x for each adjustment).

The method used to measure the effect of combined control actions according to paragraph (f) of Section 2 is shown by describing the investigation of the combined effect of control actions (a) and (b). To measure the combined effect of furnace chamber temperature and flue gas recirculation, the furnace was heated to test temperature and the effect of flue gas recirculation was measured at test temperature for a CO_2 content of 0.3%, 0.6%, 0.9%, 1.2% and 1.5% of combustion air. Then cold probes 24 were pushed into chamber 21 to a depth corresponding to 25% of the travel and the measurements were repeated. With the depth of the probes increased to 50%, 75% and 100% of the travel, the measurements were repeated for each probe depth.

A variation of the parameters to be kept constant permits any two control actions to be investigated in combination.

5. Effect of the burner construction on NO_x formation

A 'starting position' has been taken as a basis for every measurement. As proved by the experiments, for evaluation of the results, it is necessary that the starting position be defined because the results obtained relate to this position.

The parameters of the starting position (furnace temperature, pressure, fuel and air volume flow rate, air factor etc.) can be selected optionally provided the field of measurement resulting from them (furnace temperature, air factor) complies with the range of operating parameters of industrial equipment to be investigated. (E.g. in case of natural gas fired furnaces, an air factor of $n = 1.05$ and a furnace temperature of 900 to 1300 ^{o}C.)

The values of gas and air volume flow rate and NO_x emission associated with the starting position depend on the type of the burner used because the flame temperature is fundamentally affected by

(a) the quality of mixing and

(b) the mixing method used (internal or external mixing, single-stage or multistage mixing, increase of internal recirculation etc.)

depending on the burner type.

The Reynolds number and the burner parameters can be used to describe the shape of the flame and the quality of mixing. Characteristic of the missing conditions for turbulent diffusion flames are the pulse power,

$$I = A \rho w^2, N \tag{6}$$

as well as the swirl and direction parameter,

$$\vartheta = Mp/(It \cdot d/2) \quad \text{and} \quad \tau = It/Itm, \tag{7}$$

respectively. Also the air factor (n) where CO emission lies under the permissible value depends on the burner.

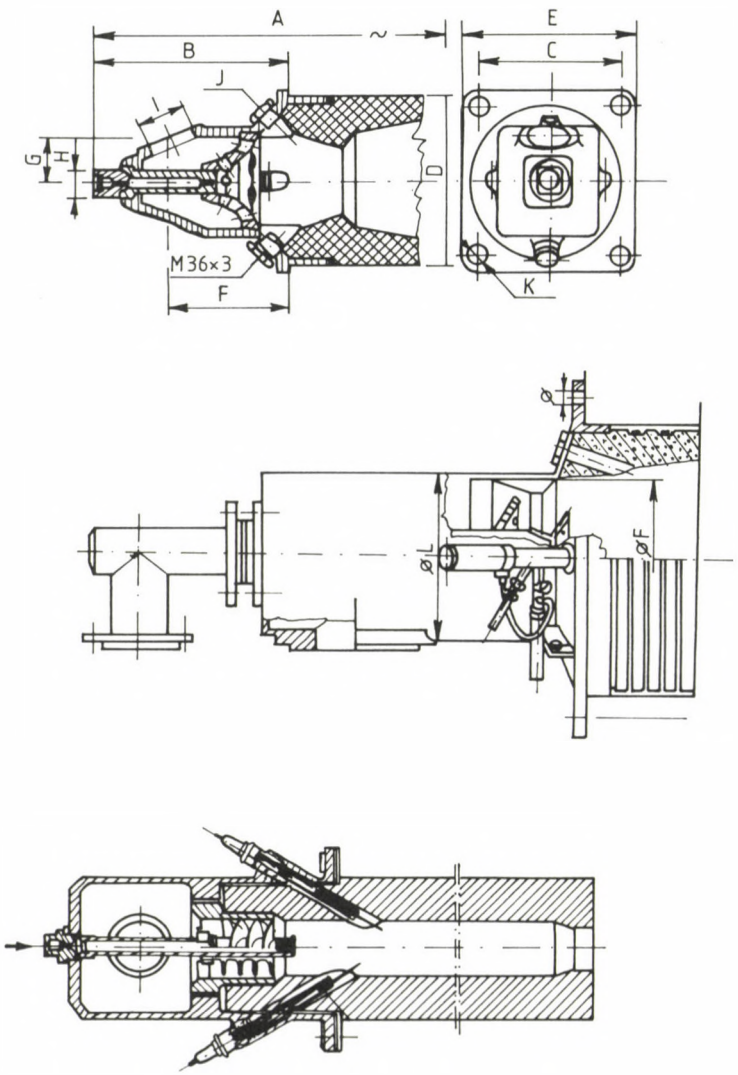

Fig. 2

According to experience, every burner has a 'working point' showing the rate of NO_x emission characteristic of the burner in starting position depending on given temperature. For ABC natural gas burners widely used in Hungary and well known in more European countries (see Fig. 2), a working point of 70 ... 73 ppm is associated with a furnace temperature of 1300 ^{o}C. This means that in case of a natural gas fired furnace of a temperature of 1300 ^{o}C where cold air is used for combustion with an air factor of n = 1.05, the NO_x content of flue gas leaving the furnace will be 70 ... 73 ppm if no control action of any kind is made to reduce NO_x emission:

$$B_{1300} = 70 \ldots 73 \text{ ppm}.$$

Every burner has a working point B. In the knowledge of B, the effect of the different control actions on NO_x emission can be investigated in case of open-flame burners.

In case of other than open-flame burners (e.g. tunnel-type burners), admixture of flue gas with combustion is and water injection through the burner is not possible and operation with the air factor is also difficult. Reduction of the furnace temperature has little effect on NO_x emission because the maximum flame temperature of the mixture burnt in majority in the tunnel is less affected by the furnace temperature as it is determined rather by the partial pressure conditions of combustion taking place in the tunnel.

Curves starting from the working point can be plotted to describe the NO_x emission of a burner of given working point in case of control actions.

6. Effect of different control actions on NO_x emission

The control actions specified earlier affect NO_x emission to a different extent each.

6.1. Effect of furnace temperature

If a burner of a working point of B_{1300} = 73 ppm operated under the conditions of 'starting position' (furnace temperature 1300 ^{o}C, furnace chamber pressure 1 bar, n = 1.05, air and gas temperature 20 ^{o}C) is connected to a furnace of a temperature below 1300 ^{o}C, the NO_x emission will

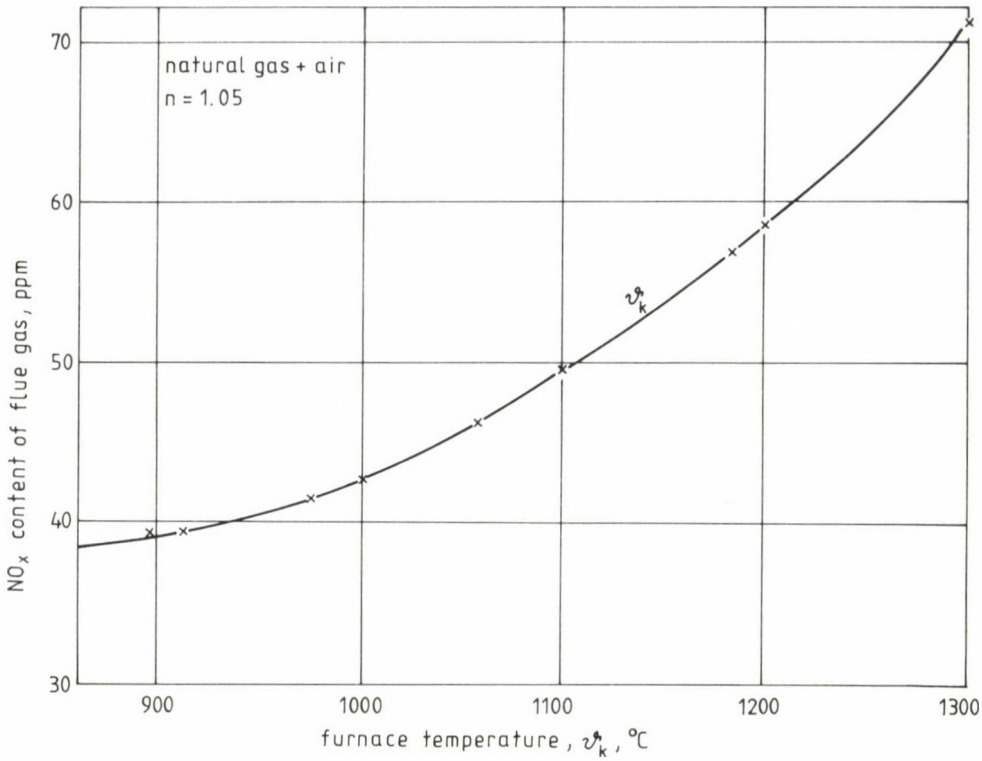

Fig. 3

decrease. Figure 3 shows NO_x emission as a function of temperature in the range of 900 ... 1300 °C.

A highly accurate curve can be plotted by means of a polynomial. In this case, formula

$$V_{NO_x} = Y\,(13.63 \cdot 10^{-5}\,\vartheta^2 - 0.2209\,\vartheta + 126.9), \quad \text{ppm} \tag{8}$$

can be used for calculation of expectable NO_x emission in the above temperature range, where Y is the working point factor of the burner:

$$Y = B_{1300}/(13.63 \cdot 10^{-5}\,\vartheta^2 - 0.2209\,\vartheta + 126.9). \tag{9}$$

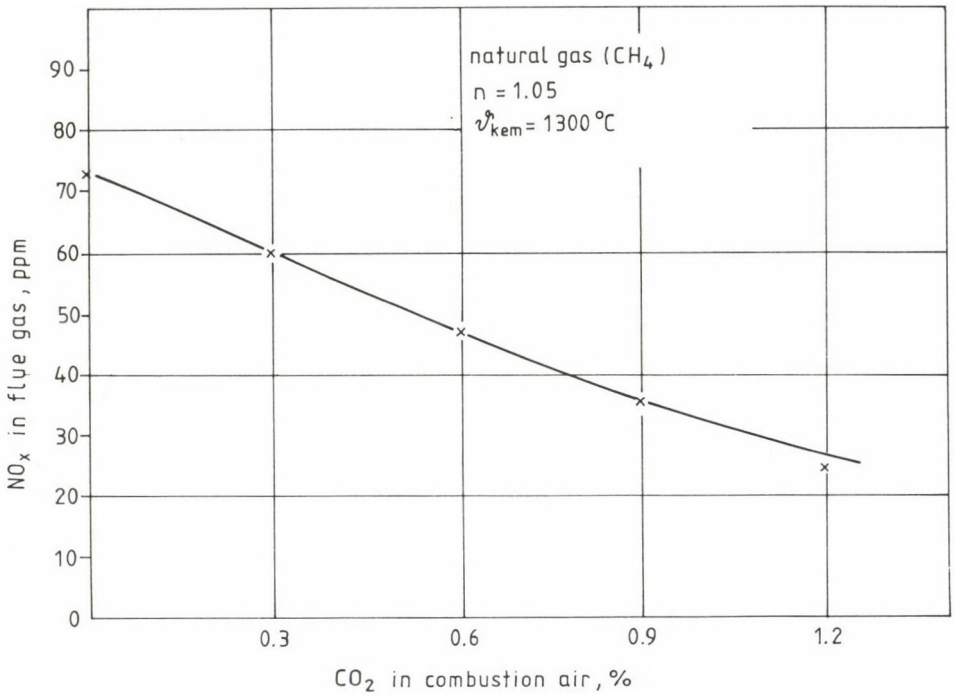

Fig. 4

6.2. Effect of forced flue-gas recirculation

Figure 4 shows the effect of flue-gas recirculation on NO_x emission. As seen, forced flue-gas recirculation is a highly efficient method to reduce NO_x emission. Expectable NO_x emission:

$$V_{NO_x} = Y\ (71.29 - 48.24\ V_{CO_2} + 7.143\ V_{CO_2}^{\ 2})\ \text{ppm}. \qquad (10)$$

6.3. Effect of two-step mixing

Figure 5 is based on the results of two-step air feed. The curve illustrates the effect of 0 ... 30% secondary air feed (for an overall air factor of n = 1.05). Due to introduction of 30% of combustion air through secondary air probes, the furnace temperature decreased (see Fig. 5) and as a result, the mass of NO_x developed decreased by about 30 %. Formula

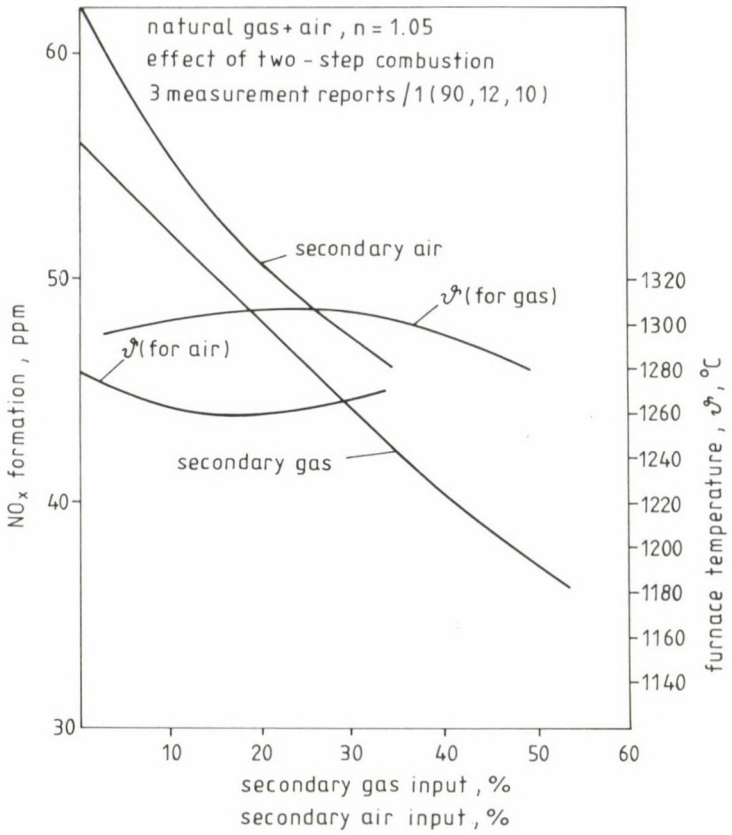

Fig. 5

$$V_{NO_x} = Y\ (0.012\ V^2_{sec.air} + 0.84\ V^2_{sec.air} + 63.06),\ ppm \qquad (11)$$

can be used to calculate the volume of NO_x decreasing as a result of secondary air feed.

6.4. Effect of increase of the air factor

The effect of the air factor is illustrated in Fig. 6. In case of an air factor varied in the range of 1.0 to 1.8, NO_x formation can be calculated by means of formula

$$V_{NO_x} = Y\ (88.08\ n^3 - 412.93\ n^2 + 607.83\ n - 232.38),\ ppm. \qquad (12)$$

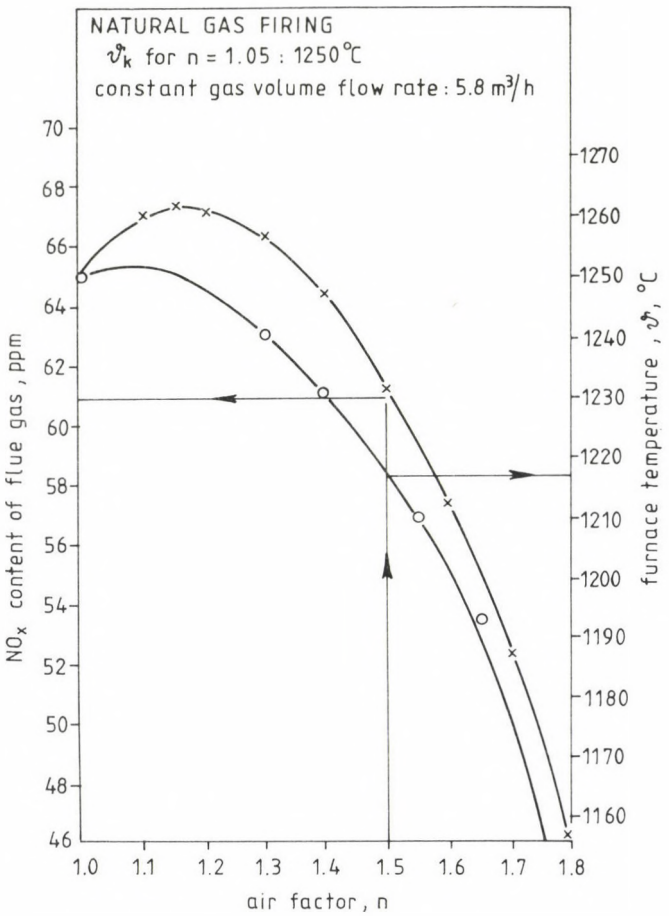

Fig. 6

6.5. Effect of water injection

The results of measurement in relation to the effect of water injection are diagrammatically illustrated in Fig. 7. The relationship between water injection and NO_x emission is not linear either since water injection becomes increasingly inefficient as the mass of water is increased because of the furnace temperature.

Formula

$$V_{NO_x} = (4.92\ m^2_{water} - 19.3\ m_{water} + 63.4),\ ppm \qquad (13)$$

is recommended for calculation of NO_x formation in case of water injection.

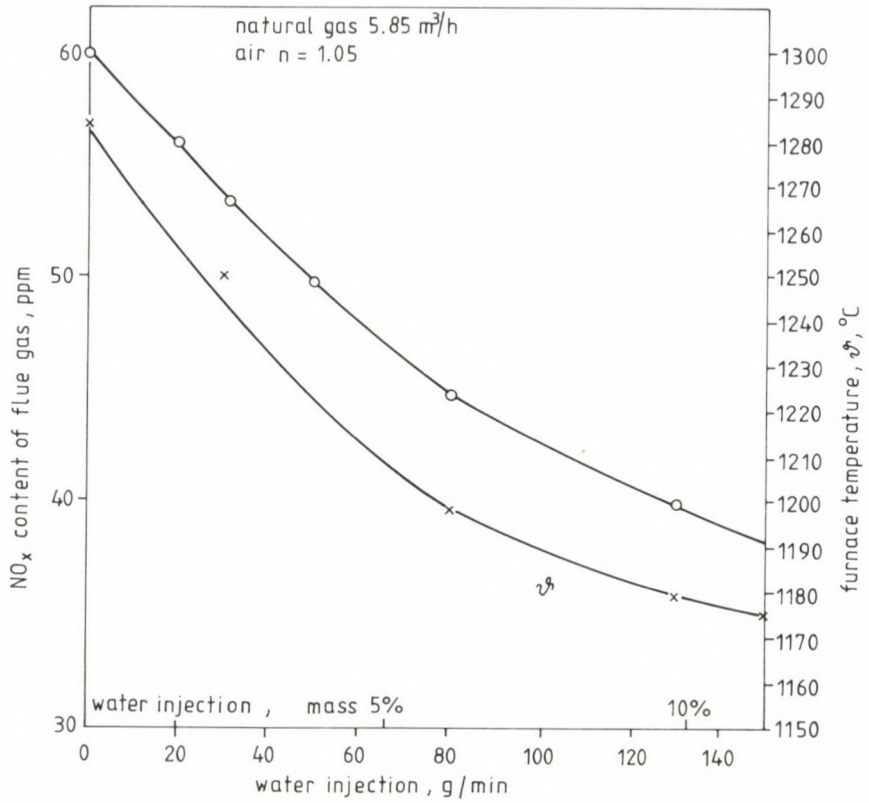

Fig. 7

6.6. Effect of combined control actions

The curves according to Fig. 8 will be obtained if the effect of furnace temperature and flue-gas recirculation is investigated in combination.

The uppermost curve shows the situation without flue-gas recirculation and thus this curve agrees with the curve given in Fig. 4. The following parabolas can be used to plot the curves of NO_x formation as a function of CO_2 content of 0.3 ... 1.2% in combustion air for furnace temperature in range of 900 ... 1300 °C.

At furnace temperature of 900 °C:

$$V_{NO_x} = Y\ (39.34 - 17.29\ V_{CO_2} + 0.7936\ V_{CO_2}{}^2),\ \text{ppm}. \qquad (14)$$

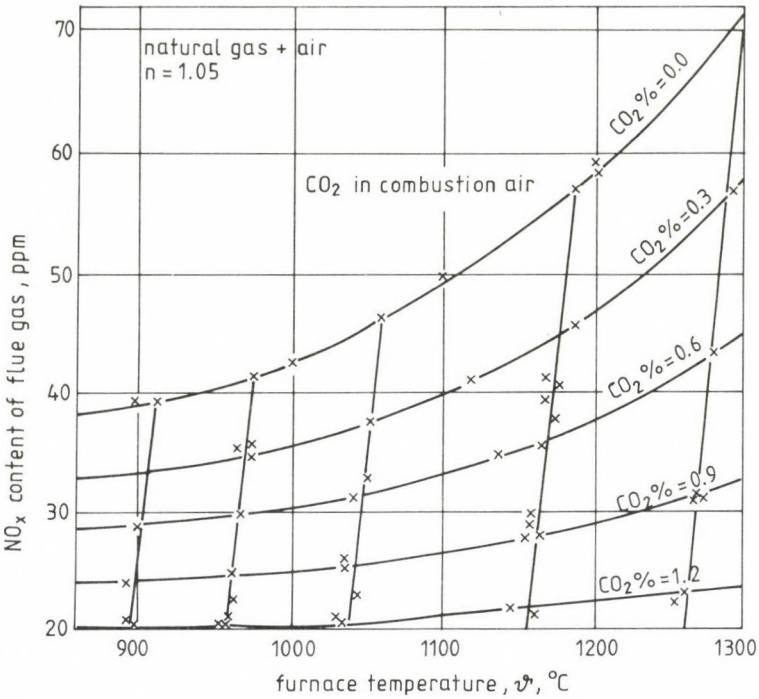

Fig. 8

At furnace temperature of 1000 °C:

$$V_{NO_x} = Y\ (43.17 - 22.47\ V_{CO_2} + 3.1745\ V_{CO_2}{}^2),\ \text{ppm}. \qquad (15)$$

At furnace temperature of 1100 °C:

$$V_{NO_x} = Y\ (49.06 - 28.38\ V_{CO_2} + 4.76\ V_{CO_2}{}^2),\ \text{ppm}. \qquad (16)$$

At furnace temperature of 1200 °C:

$$V_{NO_x} = Y\ (59.34 - 38.3\ V_{CO_2} + 6.35\ V_{CO_2}{}^2),\ \text{ppm}. \qquad (17)$$

At furnace temperature of 1300 °C:

$$V_{NO_x} = Y\ (71.29 - 48.24\ V_{CO_2} + 7.143\ V_{CO_2}{}^2),\ \text{ppm}. \qquad (18)$$

Reduction of partial oxygen pressure as a result of reduced furnace temperature and flue gas recirculation in combination can be read from the

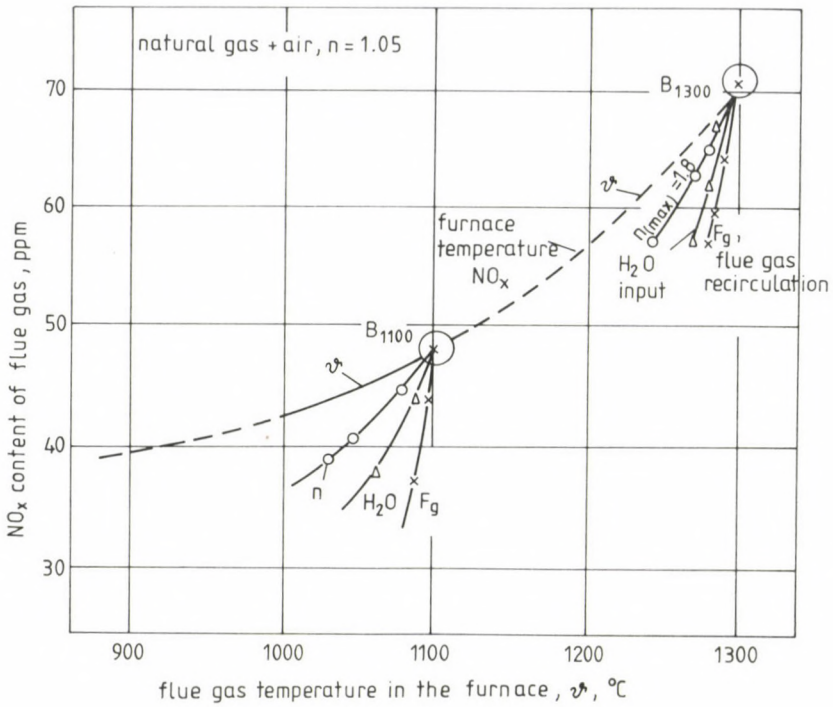

Fig. 9

figure. The mass of NO_x will change along the straights of a significant slope presented in the figure if, simultaneously with flue-gas recirculation, the furnace temperature is reduced. Accordingly, the higher the furnace temperature, the more efficient is the flue-gas recirculation in respect of reduction of NO_x emission.

6.7. Effect of control actions on furnace temperature

Tests made in case of constant fuel volume flow rate of given furnace permit the effect of the different control actions on the furnace temperature to be investigated. Figure 9 is a summary of the effect of reduction of NO_x and change of furnace temperature as a result of different control actions. The curves starting typically from one point (working point of the burner) show the efficiency of the different control actions in respect of NO_x formation and the reduction of furnace temperature with reducing NO_x formation.

It can be seen that the furnace temperature can be best reduced by the cold charge put into the furnace. In this case, the temperature of annealing furnaces can be reduced by several hundred K within a few minutes. As a result of reduction of the furnace temperature from 1300 ^{o}C to 900 ^{o}C due to the cold charge, NO_x formation decreases to half of the earlier value under invariable conditions of firing.

Flue gas recirculation can be most efficiently used to reduce NO_x emission. NO_x emission can be reduced to 1/3 even in case of recirculation of 10% of the flue gas whereas the furnace temperature decreases by 100 K.

Increase of the air factor is a less efficient method in respect to reduction of the furnace temperature. In this case, not only the temperature but also the efficiency of the furnace decrease considerably. NO_x emission can be reduced by 30% at the expense of a reduction of more than 100 K of the furnace temperature (Fig. 8).

In respect of furnace temperature, water injection is a more efficient method than increase of the air factor because the water, introduced through the burner, results also in reduction of the partial oxygen pressure in the flame in addition to its physical cooling effect. NO_x emission is reduced by 50% as a result of 1.2 kg of water injected, the furnace temperature being reduced simultaneously by 100 K.

The temperature of industrial furnaces is determined by the purpose of the technology used. Accordingly, in case of given furnace temperature, only that component of the mechanism of NO_x reduction can be utilized which resulted rather from a change of the partial gas pressure or increase of the number of oxidation steps than from reduction of the furnace temperature. In case of furnaces of a specified temperature, additional fuel shall be introduced to the furnace to compensate for reduction of the temperature as a result of the control action (provided the reduction in temperature takes place in a part of the furnace decisive in respect of the technology), resulting in a reduction of the efficiency of the furnace.

7. Conclusions, summary

1. In case of reheating and heat-treatment furnaces, the expectable effect of the different methods to reduce NO_x emission (such as reduction of the furnace temperature, forced flue-gas recirculation, two-step mixing, increase of the air factor, water injection or combinations of these meth-

ods) can be calculated to an accuracy sufficient for practice if the basic value, 'B', of NO_x emission of the burner used is known at least at one temperature falling within the furnace temperature range of 900 ... 1300 ^{o}C.

2. Accurate measurement of maximum flame temperature is not necessary for practical calculations. It is enough to measure maximum furnace temperature before the burner, coincidently with the centreline of the burner, a measurement feasible in most cases after some modification of the instrumentation of the furnace.

3. Formula

$$V_{NO_x} = B_{\text{furnace temp.}} - \Delta NO_{x_T} - \Delta NO_{x_b}, \text{ ppm} \qquad (19)$$

can be used to calculate the expectable NO_x formation in the furnace with the value corresponding to the effect of possible temperature reduction as well as to the effect of the control action, resulting in reduction of temperature and partial pressure, subtracted from basic value B corresponding to the furnace temperature measured along the centreline of the burner, characteristic of the burner and fuel. The factors according to paragraphs 2) and 3) can be calculated to a good approximation by means of the method described.

REFERENCES

1. Kremer, H.: Grundlagen der NO_x-Entstehung und Minderung. GWI 1990, 9
2. Bowman, B.R. - Pratt, D.T. - Crowe, C.T.: Effect of turbulent mixing on nitric oxide production in a jet-stirred reactor. 14th Symp. on Comb. 1973, 819—828
3. Zeldovits, B.Y.: Acta Physico-Chemica, URSS wl. 1946/4
4. Bracco, F.V.: Nitric oxide formation in droplet diffusion flames. 14th Symp. on Comb. 1973, 831—841
5. Quan V. - Marble, F.E. - Kliegel, J.R.: Nitric oxide formation in turbulent diffusion flames. 14th Symp. on Comb. 1973, 851—859
6. Golden, D.M.: Estimation of rate constants of elementary processes. 14th Symp. on Comb. 1973, 121—131
7. Cernansky, N.P. - Sawyer, R.F.: NO and NO_2 formation in a turbulent hydrocarbon/air diffusion flame. 15th Symp. on Comb., 1039—1048
8. Koshi, M. - Ando, H. - Oya, M. - Asaba, T.: Shock tube study of decomposition of nitric oxide at high temperatures. 15th Symp. on Comb. 1975
9. Albers, E.A. - Hoyermann, K. - Schacke, H. - Schatjko, K.J. - Wagner, H.G. - Wolfrum, J.: Absolute rate coefficient for the reactions of CN radicals. 15th Symp. on Comb. 1975
10. Gehring, M. - Hoyermann, K. - Schacke, H. - Wolfrum, J.: Direct studies of some elementary steps for the formation and destruction of nitric oxide in the H-N-O system. 14th Symp. on Comb. 1973, 99—105

11. Bowman, C.T.: Kinetics of nitric oxide formation in combustion processes. 14th Symp. on Comb. 1973, 729—736

12. Gardiner, W.C. Jr. et al.: Elementary reaction rates from post-induction period profiles in shock initiated combustion. 14th Symp. on Comb. 1973, 61—70

13. Flower, W.L. - Hanson, R.K. - Kruger, C.H.: Reaction of nitric oxide with hydrogen. 15th Symp. on Comb. 1975, 823—840

14. Magnussen, B.F.: Prediction of characteristics of enclosed turbulent jet flames. 14th Symp. on Comb. 1973, 553—566

15. Benedek, P. - László, A. - Németh, A. - Váczi, P.: Mathematical model of the partial oxidation flame-reaction of methane. Hung. Journ. of Ind. Chem., Veszprém, 4 (1976), 77—92

16. Bíró, A.: New mathematical method to determine NO_x emission from natural gas fired furnaces (in Hungarian). ETE-TÜKI Industrial Seminar, Miskolc, July 1991

Acta Technica Acad. Sci. Hung., 105 (3), pp. 153—172 (1993)

POLARIZATION TAKING PLACE DURING ELECTROLYTIC REFINING OF COPPER, POSSIBILITIES OF ITS REDUCTION

KÉKESI, T.*

(Received: 21 November 1991)

A significant but undesirable polarization is taking place in the course of electrolytic refining of copper. The properties of the most important overvoltage components have been analyzed first mathematically, then measured using a method and equipment developed for this special purpose, suitable for separation, and measurement under quasi-practical conditions, of the different types of overvoltage. The effect of the basic operating characteristics on anodic and cathodic polarization as well as the nature of the overvoltage and the most important components thereof have been determined. Furthermore, the polarization process in case of the different technologies involving current reversal had been investigated and on the basis of the results, more favourable techniques have been recommended.

1. Introduction

As proved also by operating tests /1/, the contribution of the polarization of electrodes to the voltage demand of electrolysis is considerable and it has also other effects which make it extremely important from the point of view of providing the necessary conditions for an intensive operation of increased current density. Still, from among the components of the cell voltage, polarization, or in particular, its nature and the possible way to control it are a question that has not been cleared up in full yet. According to the theory /2/, polarization (overvoltage) resulting from the change of the equilibrium electrode potentials when current is applied to the electrodes can also be attributed to the necessity to overcome several effects impeding the process.

*Kékesi, Tamás, H-3532 Miskolc, Tátra u. 13, Hungary

Akadémiai Kiadó, Budapest

The fundamental "impediment" is the demand that the activation energy of the electrode process of the desirable direction be reduced allowing an increase of the resultant current intensity to the required extent. Polarization that can be covered by the supply voltage is capable of reducing the activation energy in this way, bringing about at the same time the activation overvoltage. Polarization of this type may be required to reduce the activation energy of the charge transfer process or of the process of incorporation into (or dissolution from) the crystal lattice.

Another important "impediment" of the electrode processes is the slow rate of diffusional material transport, resulting in a decrease along the cathode, while in an increase along the anode, in the copper ion concentration. The electrode potential determined by the kinetic conditions of the electrode reaction is more or less shifted by the diffusion (concentration) overvoltage so developed and thus the deviation from the equilibrium potential, i.e. the polarization is further increased.

Polarization not resulting from diffusion but still of concentration type may take place if the species involved in the electrode process have to be transformed in a slow chemical reaction before or after the step accompanied with a change in the charge. This latter (reaction) overvoltage is not characteristic of copper electrodes submerged in sulphate solutions /2, 3--6/.

A solid layer of high resistance on the electrode surface could cause an apparent (resistance) overvoltage. However, in the given system, such a deposition need to be reckoned with.

At the same time, the voltage drop occurring as a result of current passing through the electrolytic resistance between the reference electrode and the electrode tested can be practically eliminated by a suitable measurement method.

1.1. Activation polarization

The following overall reaction takes place on the copper electrode:

$$Cu^{2} + 2e^{-} \rightleftharpoons Cu.$$

As has been generally accepted and proved experimentally, the overall reaction consists of the following two main steps in case of higher overvoltages /2, 3—11/:

1) $Cu^{2+} + e^- \underset{k_1}{\overset{k_2}{\rightleftharpoons}} Cu^+$ (slow)

2) $Cu^+ + e^- \rightleftharpoons Cu$ (fast).

A first-order relationship can be assumed for the rate of the "slow" step (step 1) while equilibrium conditions for the "fast" one (step 2). In case of operating current densities, the process of charge transfer can be considered determining in respect of the rate of reaction and activation polarization /3--11/. Therefore, on the basis of the reaction rate equation of the slow step for unit electrode surface, it is relatively easy to express the absolute values of the partial current densities, taking the effect of Galvani potential difference $\Delta\psi$ between the electrode and the solution, which modifies the activation energy, into consideration /2, 3--11/. To set up a theory suited for practical application, the effect of the diffuse nature of the double layer (Frumkin effect) shall reasonably be neglected /6/. Thus relationship

$$|i_a| = 2F\, k_a\, a_{Cu} + \exp\left(-\frac{\Delta G_a^{\#} - \alpha_a F \Delta\psi}{RT}\right) \tag{1}$$

can be written for the anodic direction (dissolution) while relationship

$$|i_c| = 2F\, k_c\, a_{Cu^{2+}} \exp\left(-\frac{\Delta G_c^{\#} + \alpha_c F \Delta\psi}{RT}\right) \tag{2}$$

for the cathodic direction (deposition). With the constants in the expressions of the partial current densities lumped and the absolute value of the current density corresponding to the equilibrium potential (exchange current density) denoted by i_o, the relationship between the resultant (Faraday) current density and the activation polarization can be expressed as the sum of anodic and cathodic partial currents with the conventional sign:

$$i = |i_a| - |i_c| = i_o \left\{ \exp\left[\frac{\alpha_a F\, \eta^{act}}{RT}\right] - \exp\left[-\frac{\alpha_c F\, \eta^{act}}{RT}\right] \right\} \tag{3}$$

where

i_a -- anodic (Cu^{2+} ion formation) partial current density of the copper electrode, A dm^{-2};

i_c — cathodic (Cu^{2+} ion deposition) partial current density of the copper electrode, A/dm^{-2};

T — thermodynamic temperature, K;

R — molar gas constant, $J/mol^{-1}K^{-1}$;

$a_{Cu^{2+}}$, $a_{Cu^{+}}$ — activity (or approximate concentration) of copper ions, mol/dm^{-3};

F — Faraday constant, zF = z96 500 As/mol if the numerical value of the change in charge is z;

2 — charge change number (z_{or}) of the overall process (the rate-determining step, if taking place once, means the transition of two electrons in the overall reaction);

$\Delta G_a^{\ddagger}$, $\Delta G_c^{\ddagger}$ — chemical (independent of the electric field) free enthalpy of activation of anodic and cathodic partial processes, respectively, J/mol^{-1};

α_a, α_c — dimensionless transition factors of the anodic and cathodic partial processes of the copper electrode, respectively;

$\Delta\psi$ — Galvani potential difference between the copper electrode and the solution, V;

ε^e — $\{\varepsilon^e = \varepsilon_a^e = \varepsilon_c^e\}$ equilibrium electrode potential of the copper electrode tested, V;

η_{act} — activation overvoltage, V;

i_o — exchange current density, A/dm^{-2};

k_a, k_c — reaction rate constant for the anodic and cathodic partial processes of the electrode reaction, respectively, dm/s^{-1}.

In case of higher resultant current densities ($|i| > 100\ A/m^2$), the partial current density of the anode in the direction of deposition and that of the cathode in the direction of dissolution can be neglected to a good approximation.

In the range of higher current densities, the typical slope of the Tafel lines (polarization curve) is about 110 mV/decade in cathodic direction while about 45 mV/decade in anodic direction. On the basis of these values, the transfer coefficients can also be calculated. Results relatively easy to reproduce, approximately identical with the theoretical values of $\alpha_c = 0.5$ and $\alpha_a = 1.5$, have been obtained in this way by a number of research workers (Table 1). As shown by the values tabulated, the value of the exchange current increases as the copper concentration in the electrolyte increases while the transfer coefficients do not change significantly. At

Table 1. Average values of the most important polarization parameters of experimental copper electrodes produced by electrolysis

Literature	T	Concentration mol/l		i_o, mA/cm^2		α_a	α_k
	K	$CuSO_4$	H_2SO_4	Anodic	Cathodic		
/3/	303	0.5	0.5	5.1	8.3	1.64	0.49
		0.075	0.5	3.0	3.7	1.3	0.49
/4/	303	0.46	0.5	5.2	8.0	1.51	0.42
		0.30	0.5	5.7	9.7	1.44	0.45
		0.096	0.5	3.7	3.3	1.36	0.48
/8/	303	0.05	1.0	3.8	5.4	1.46	0.49
/11/	303	0.05	1.5	0.8	2.1	1.35	0.52
		0.1	1.5	1.1	2.5		
		0.3	1.5	2.3	5.6		
		0.7	1.5	5.0	9.0		
		0.7	0.5	5.2	10.5	1.25	0.58
		0.7	1.0				
		0.7	1.5				
		0.7	2.0				

the same time, the sulfuric acid concentration leaves the kinetics of the electrode processes practically uneffected.

The activation overvoltage develops rapidly (within a few milliseconds, after switching on the current). This transient is described by a relationship containing the capacitive current component expressed as the difference of the total current and the Faraday current as well as the measurable parameter of the double-layer capacitance

$$\frac{dt}{d\left|\eta_t^{act}\right|} = \frac{C}{\left|i\right| - \left|i_o\left\{\exp\left[\frac{\alpha_a F \eta_t^{act}}{RT}\right] - \exp\left[-\frac{\alpha_c F \eta_t^{act}}{RT}\right]\right\}\right|}, \qquad (4)$$

where

i_ϕ -- total current density of the electrode, A/dm^2;

C -- capacitance of the double layer, F/dm^2;

η_t^{act} -- activation overvoltage developed within time t, V.

1.2. Diffusional polarization

Because of the changes of Cu^{2+} ion concentration along the surface of the electrodes in operation, an overvoltage component arising from diffusion, increasing at a slow rate, is superimposed on the rapidly increasing activation overvoltage. The diffusional polarization can be directly attributed to the dependence, of the equilibrium electrode potential on the activation of the ion taking part in the process,

$$\eta^{diff} = \frac{RT}{2F} \ln \frac{a_{Cu^{2+},\,s}}{a_{Cu^{2+},\,b}} \simeq \frac{RT}{2F} \ln \left(1 - \frac{i}{i_{dl}}\right), \qquad (5)$$

where

η^{diff} -- diffusion overvoltage, V;

$a_{Cu^{2+},\,s}$, $a_{Cu^{2+},\,b}$ -- activity of the copper ion along the electrode surface (on the external side of the double layer) and in the bulk of the solution, respectively, mol/dm^{-3};

i_{dl} -- limiting current density of diffusion, A/dm^2.

Theoretically, the voltage term (5) can be described as a function of time in the transient state on the basis of the linear stationary diffusion model according to relationship

$$\eta^{diff}(t) = \frac{RT}{2F} \ln \left(1 + \frac{i}{c_o F} \sqrt{\frac{1}{\pi D_{Cu^{2+}}}} \sqrt{t}\right), \qquad (6)$$

where

c_o -- average copper ion concentration in the electrolyte, considered to be constant, mol/dm^3;

t -- time after the current has been switched on, s;

$D_{Cu^{2+}}$ -- diffusion coefficient of copper ions, dm^2/s^{-1}.

However, the practical conditions are described by relationship (6) for a rather short time only because the effect of the gradually developing, natural electrolyte convention prevents, the increase of diffusional polarization beyond a certain value.

2. Experimental electrolyzing set-up and auxiliary equipment

In the course of laboratory experiments, one of the primary objectives has been to use methods and practices which provide "pure" conditions for the investigation of the polarization characteristics, permitting at the same time the practical requirements to be met. Accordingly, a synthetic $CuSO_4$-H_2SO_4 electrolyte of a temperature as well as copper and sulfuric acid content similar to those under operating conditions (but free from inhibitors and impurities and not circulated forcibly) has been used.

Cathodes and anodes of a surface of 150 x 78 mm cut out of electrolytic copper starter plates from the electrolysis plant of the Csepel Metalworks, have been used for the measurements. On the base plates of metallic purity, the working surface was formed by means of electrodeposition of a current density of 200 A/m^2 for 2 hours. To improve reproducibility, a 15-minute pre-electrolysis of a current density of 100 A/m^2 was carried out after washing and immediately before the measurements.

An insulating coat was applied to the back side of the electrodes in order to expose only one surface to the electrolytic process. By means of a threaded support bar and clamping jaws, the electrode spacing could be adjusted optionally (Fig. 1).

A fresh synthetic sulfuric acid — copper sulphate electrolyte had been prepared for each measurement cycle, using reagent grade chemicals. Adsorption columns filled with activated aluminium oxide and active carbon were used to remove organic impurities possibly present in the electrolyte.

During the measurements, the electrolyte temperature was controlled by means of a thermostatic bath and heating elements. Water was fed into the bath drop by drop continuously, at a rate determined experimentally, to replace the water evaporated. Scavenging by nitrogen before and during the measurements to deaerate and/or homogenize the solution was also possible.

Current for the electrolysis was supplied by TR 9177 and TR 9178 stabilized d.c. supply units connected to the electrodes through a multicontact relay operated by a logic circuit and/or a computer controlled transistor type twin switch, developed specifically for this purpose. These control units permitted the current, adjusted on the current generator type supply units, to be switched on and off as required. Moreover, also periodic current reversal (PCR) operation could be brought about by the co-ordinated control of two counter connected supply units.

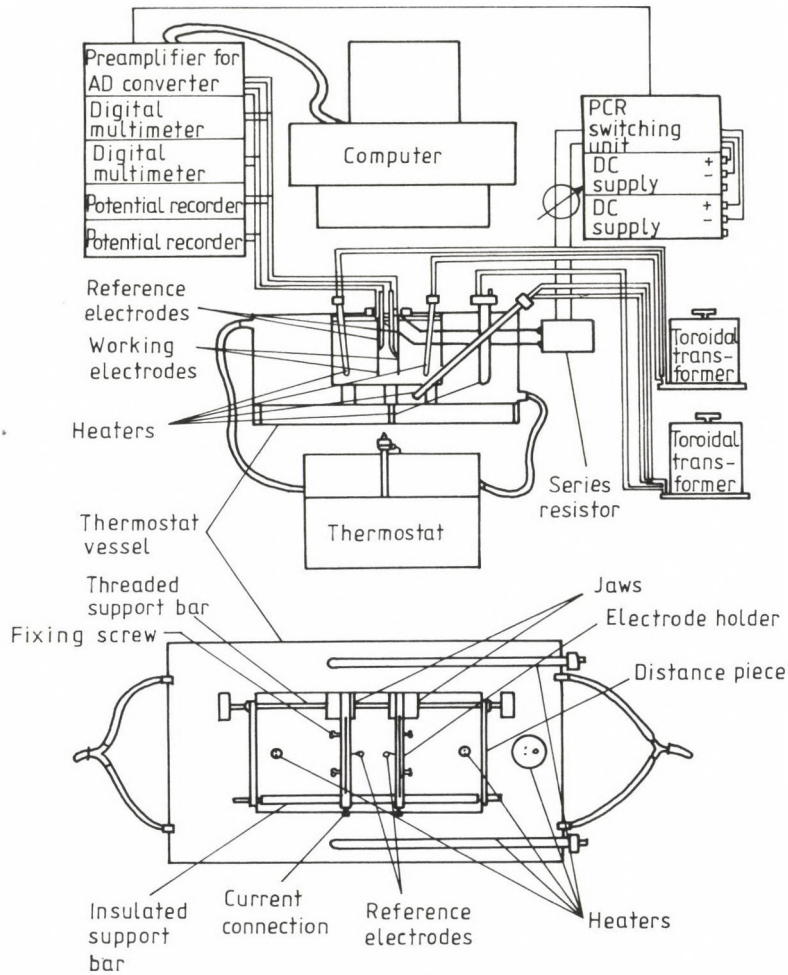

Fig. 1. Experimental equipment (layout)

For the polarization measurements, special small-size copper reference electrodes of controlled stability, causing minimum disturbance, were used.

Voltage data used for evaluation were recorded by a VIDEOTON VT 160 (IBM compatible) computer equipped with a RHS-8 4-channel converter interface card. The measuring channels of variable sensitivity as well as the

differential measuring inputs have been provided by a pre-amplifier unit developed specifically for this purpose.

The software in Turbo Pascal language, required for the operation of the data collection system, has been developed together with the experimental set-up in compliance with the special purposes.

3. Experimental results

Using the measurement system described above, three main series of experiments have been run, such as

-- determination of the mathematical model to describe the steady-state overvoltage of the electrodes as a function of the most important four operating parameters in the selected range of factors,

-- investigation of the most important components of polarization, developing at different rates, based on the transient values recorded after switching-on,

-- investigation of the polarization components in case of different settings of PCR operation by comparative method.

3.1. Effect of the most important operating parameters on the stabilized value of polarization

The values of the four basic operating parameters included in the investigation have not been changed one by one but simultaneously. The iteration of the complete factorial plan of type 2^4 permitted the results to be processed statistically.

Associated with the selected lower and upper level of the factors investigated by designed experiments are transformed values -1 and +1, respectively. The transformation formula applying to the general case is

$$x^* = \frac{x - x_0}{x^{upper} - x_0} = \frac{x - x_0}{x_0 - x^{lower}} = \frac{x - x_0}{I} \qquad (7)$$

where

x^* — transformed value of the given factor;

x — value of the factor according to the original scale;

Table 2. Range of the factors tested in the first series of experiments

Factor level	Factors tested							
	Absolute value of current density		Temperature		Cu concentration		H_2SO_4 concentration	
	j	j^*	T	T^*	c_{Cu}	c^*_{Cu}	$c_{H_2SO_4}$	$c^*_{H_2SO_4}$
	A/m^2	—	°C	—	g/l	—	g/l	—
Upper	300	+1	50	+1	40	+1	180	+1
Base	250	0	40	0	35	0	135	0
Lower	200	-1	30	-1	30	-1	90	-1
Variation interval	50	—	10	—	5	—	45	—

x_o — base level of the factor according to the original scale
$x_o = [x^{upper} + x^{lower}]/2$;
I — variation interval of the given factor.

Transformation is required to make the multivariable regression calculation practically feasible.

The lower and upper factor levels adjusted in the course of the experimentation are tabulated in the original and transformed form in Table 2.

The statistically adequate interpolation polynomial, containing a minimum number of insignificant coefficients, describing the effect of the factors on the absolute value of the steady-state polarization is

$$e_{cp} = 71.656 + 13.594\, j^* - 32.406\, T^* - 12.031\, C^*_{Cu} + 11.344\, C^*_{H_2SO_4} - \\ - 4.719\, j^*T^* - 3.719\, j^*C^*_{Cu} + 2.656\, j^*C^*_{H_2SO_4} + 5.906\, T^*C^*_{Cu} - \\ - 2.719\, T^*C^*_{H_2SO_4} + 2.156\, C^*_{Cu}\, C^*_{H_2SO_4} + 1.969\, j^*T^*C^*_{Cu},\ mV; \quad (8)$$

for the cathode, while

$$e_{ap} = 18.969 + 2.156\, j^* - 6.406\, T^* + 2.156\, C^*_{Cu} - \\ - 2.031\, C^*_{Cu}C^*_{H_2SO_4},\ mV \quad (9)$$

for the anode.

As suggested by the polynomials, each of the process parameters investigated has a definite and significant direct effect on the absolute value of steady-state cathodic overpotential, especially the effect of the electrolyte temperature, resulting in a reduction of the resultant polarization of the cathode by about 60 mV on the average if increased from 30 ^{o}C to 50 ^{o}C. In case of low-copper electrolytes, the effect of temperature rise is by far above average as suggested also by term $T^{*}\ c^{*}_{Cu}$, the interaction represented by the most significant coefficient, which shows that in case of a negative value (that is, the value next to the lower level) of c^{*}_{Cu}, this interaction results in an additional decrease in the polarization of the cathode beyond that caused by the primary effect. A similarly strong effect of the interaction of temperature and current density, resulting in a stronger reduction of cathode polarization in the range of high current densities than in case of low current densities, is also detectable.

The effect of a reduction of the copper concentration in the electrolyte from 40 g/l to 30 g/l and an increase of the current density from 200 A/m^2 to 300 A/m^2 on cathode polarization is approximately identical in the range investigated.

Even in the relatively wide range (90 ... 180 g/l) investigated, the sulfuric acid content was found to affect the cathode polarization only slightly. This is reasonable since theoretically, the electrode processes are not affected directly by the sulfuric acid concentration, the (diffusion) polarization can certainly be increased to a minor extent by an increasing sulfuric acid concentration indirectly, that is, through impeding the migration of the copper ions.

In case of the anode, the effect of each factor is much less significant since the absolute value of the overvoltage of the anode is much lower than that of the cathode. As suggested by the interpolation polynomial of polarization, the primary effect of the sulfuric acid content on anode polarization has not been significant either. This reduced effect can be attributed to the much more intensive anodic natural convection, having a strong effect on material transport beside which the counteraction of the sulfuric acid content through impeding migration shrinks into insignificance.

The relative intensity of the other primary effects on anode polarization can be explained in a way similar to what has been said in the case of cathode polarization. It is worth mentioning that the slight increase of anode polarization with increasing copper concentration in the

electrolyte against the expectations based on theoretical considerations can again be attributed to the effect of natural convection which is reduced in this case as a result of the decreasing difference in density along the anode.

3.2. Main components of polarization taking place on the copper electrode

A special computer system for electrolysis control and data collection has been developed to co-ordinate the control of electrolyzing current and overvoltage measurements and to separate the activation component building up very fast (within a few milliseconds), and the diffusion component developing at a slow rate (within minutes), of the overvoltage by controlling the rate of data collection as required.

Using a combination of fast (about 6000 data/s) and slow (1 datum/s) phases of measurement started with the fast phase upon switching on of the current, the transient section of the curve for the two main polarization components could be clearly distinguished as illustrated in Fig. 2, showing the transient values of the two basic polarization components upon switching on. In the figure, the sections denoted by even and odd numbers are sections of the same curve under the given conditions but illustrated along a different time axis for each component. E.g. curve section 2 is a result of the fast phase of measurement immediately after switching on, followed by section 4 showing a much slower change.

There is a considerable difference between anode and cathode in the resultant polarization and also the distribution between the main components resulting from activation and diffusion is different. Under the above conditions, the average values of 37 mV and 15 mV are reached by the activation overvoltage of the cathode and anode in $\sim$ 7 ms and $\sim$2 ms, respectively. The superimposing stabilized value of 20 mV and 4 mV is reached by the diffusion polarization component within an approximately identical time, $\sim$45 s, on the cathode and anode, respectively. The difference in activation polarization is in agreement with the ratio theoretically expectable on the basis of the charge transfer kinetics. A stabilization of the diffusion overvoltage may take place as a result of natural convection. Hence, the rather low value on the anode justifies the assumptions with regard to the intensity of natural convection along its surface.

Although the above results comply with the expectations, it seemed to be still reasonable to test the separation of the two overvoltage components

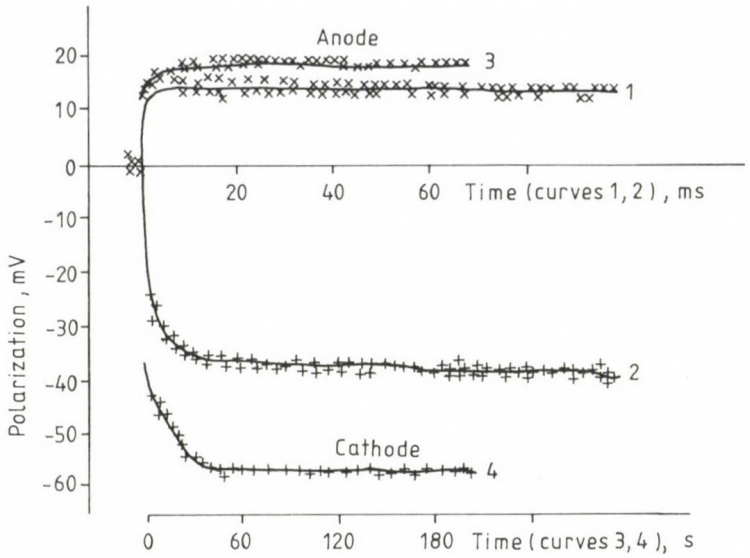

Fig. 2. Most important components of polarization on the copper electrode (300 A/m^2, 50 ^{o}C, 40 g/l Cu, 180 g/l H_2SO_4)

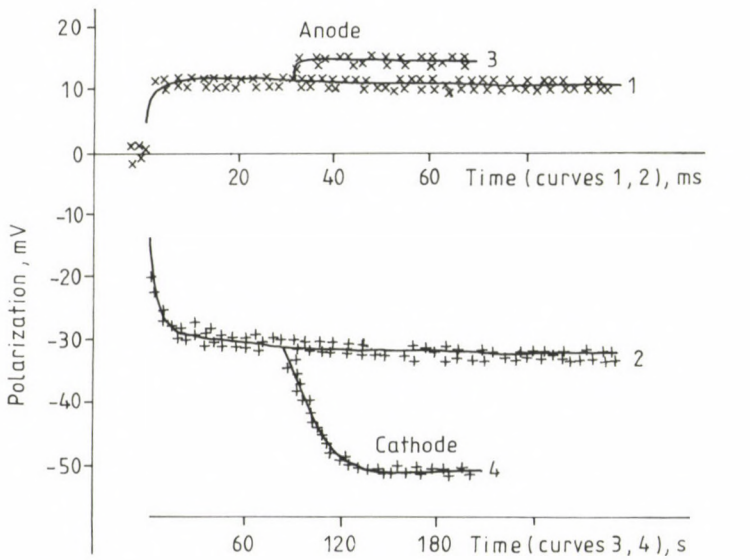

Fig. 3. Verification of the features of most important polarization components by nitrogen blowing
(300 A/m^2, 50 ^{o}C, 40 g/l Cu, 180 g/l H_2SO_4)

by a different method as well. In doing so, nitrogen has been introduced in between the electrodes by means of special submerged pipes to bring about an intensive turbulent electrolyte motion.

Figure 3 illustrating the result clearly shows that the build-up of the fast polarization component has not been retarded by the introduction of N_2. Furthermore, as can be seen on the basis of the position of the curves obtained by fast and slow data collection as compared with each other, this rapidly developing overvoltage reaches its stabilized value during the time of N_2 blowing while the diffusion polarization develops in the regular way according to expectations after the N_2 feed has been stopped. All these results are in agreement with what has been assumed so far with regard to polarization taking place on the copper electrode.

3.3. Dependence of overvoltage, developing on the copper electrode, on current density

In the course of an independent series of experiments, the structure of the overvoltage was found to change as a function of the current density.

As shown by Fig. 4, the activation polarization term, more significant under the given conditions, changes approximately in accordance with Tafel's relationship. On the basis thereof, the effect of the charge transfer step is rightly assumed to be predominant under quasi-operating conditions and on the other hand, the typical values of the most important kinetic parameters of the electrode processes can be determined.

The absolute value of the activation polarization can be expressed on the basis of theoretical relationship (3) as a function of the absolute value of current density in the following general form applicable both to the anode and cathode:

$$e_{ep}^{act} = \frac{RT}{\alpha_e F} \ln \frac{j}{j_0} = \frac{RT}{\alpha_e F} \ln \frac{1}{j_0} + \frac{RT}{\alpha_e F} \ln j = A + B \ln j \qquad (10)$$

where

e_{ep}^{act} — activation type part of polarization for any of the electrodes (anode or cathode), V;

α_e — transfer coefficient of the electrode tested (α_c, α_a);

j — absolute value of current density, A/m^2;

j_0 — exchange current density, A/m^2;

A, B — constants (determined by regression).

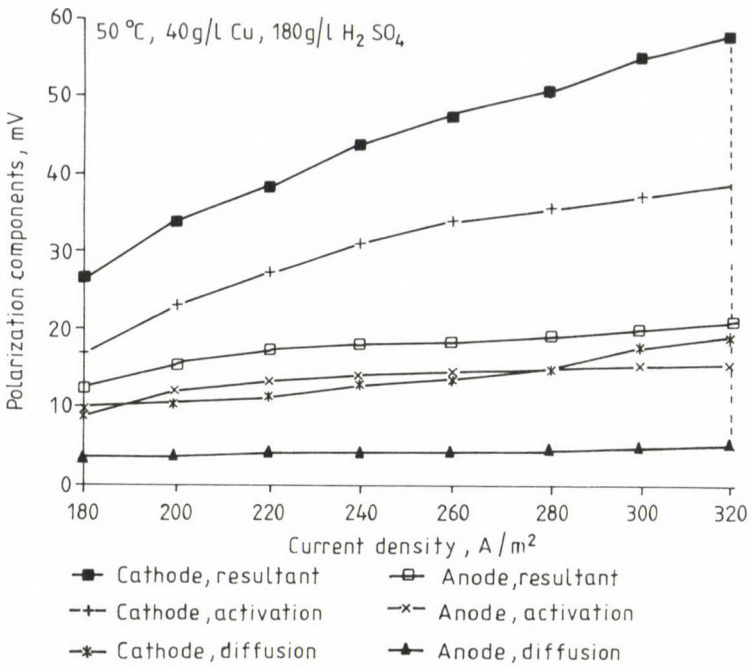

Fig. 4. Components of polarization as a function of current density

With the regression calculation performed in accordance with the logarithmic relationship, the results tabulated in Table 3 are obtained.

In case of the cathode polarization of higher value measurable more accurately, there is an acceptable correlation (r^2) between the regression equation of the form suggested by theory and the experimental results. On the basis of a comparison of the theoretically expectable values of the transfer coefficients (α) and/or exchange current densities (j_o) and those determined by regression (Table 3), we can say that deviations from the ideal conditions of investigation of electrode kinetics (using pulse current and special electrodes) towards the actual conditions of a continuous electrolysis may affect the process in two different ways:

-- As compared with the growth rate expectable on the basis of the pulse technique based electrode kinetic data (Table 1), the actual rate of increase of the activation polarization as a result of an increase of the current density was lower, certainly because of the higher experienced value of the transfer coefficient as compared with the theoretical value. The transfer coefficient depends directly on the structural and energetic con-

Table 3. Theoretically expectable values of kinetic characteristics and the values calculated on the basis of the experimental results

Characteristics	Cathodic value		Anodic value	
	actual	expectable	actual	expectable
r^2 (correlation coefficient)	0.9762	—	0.8954	—
B, V	0.03762	0.05566	0.01038	0.01855
α, J/V	0.74	0.5	2.68	1.5
A, V	-0.1768	-0.2563	-0.0436	-0.0733
j_0 (with theoretical transfer coefficient)	25	100	11	50
j_0 (with actual transfer coefficient)	110	100	66	50

ditions of the double layer and the electrochemical metallic surface. Accordingly, a structure resulting in an energetically more favourable incorporation and dissolution of the metal ions is most likely developed by the electrodes used in a longer-lasting electrolysis. This may be the result of spontaneously active spots and/or of foreign matters (ions) getting in touch with the surface, modifying the energy conditions.

The activation polarization may be increased by certain adsorbed foreign matters (impurities) disturbing or even partially blocking the active sports of the electrode surface. This effect manifests itself essentially in that the polarization curve is shifted in accordance with the direction of lower exchange current densities. However, in case of the synthetic electrolyte used, this effect is certainly less significant.

4. Effect of periodic current reversal (PCR) technology on polarization

The effect of this mode of operation, resulting in a transient state almost continuously, on the electrode polarization is a complex question. Therefore, it is necessary that the problem be investigated experimentally.

To increase the effect of PCR electrolysis resulting in a reduction of the polarization, increase of the time or the current density of reverse cycles seems to be an obvious method. However, this would considerably reduce the current efficiency at the same time. Therefore, a ratio of 20 : 1 of forward and reverse cycles shall most reasonably be used in accordance with the general practice. At the same time, the value of reverse current

intensity is usually adjusted to half of the value of forward current for similar reasons.

However, no definite basis for determination of the proper length of the cycles is available and therefore no uniform practice has developed.

In the course of investigation of the transient values of the cathodic overvoltage, the build-up of both the activation type and diffusion type component was found to take a much longer time under practical conditions than their decay. In case of activation polarization, this can most likely be attributed to the change of the electrode surface in off-load periods when new dislocations reducing the activation energy demand of the metal dissolution are taking place. At the same time, a rapid increase of the diffusion overvoltage may be hindered by the increasing natural convection. However, no significant differences between the rates of build-up and decay are shown by the curves of anodic activation polarization. Also this has a bearing on the above explanation since in case of the dissolution process, the chemical effect in the off-load period can certainly not result in a significant change.

On the basis of all what has been said above, the average value of the cathodic overvoltage is assumed to be lower in case of PCR operation where the cycles are shorter and the current is switched on and off more frequently.

The measurements to compare the polarization characteristics of d.c. operation and the different modes of PCR operation included four consecutive stages:

-- measurement of off-load base point,

-- d.c. measurement,

-- measurement of off-load transient section,

-- PCR measurement.

The assumptions have proved right as shown by the cathode polarization curves of the PCR processes illustrated in Fig. 5. The curves clearly show the favourable effect of the shorter cycles, resulting in a remarkable reduction of polarization in case of the PCR process using forward cycles of 0.1 s and reverse cycles of 0.005 s. This result leads us to believe that the technical feasibility of the practical application of this pulsed current operation as an advanced version of the PCR technology is worth studying.

An undesirable effect of current reversal applied in the PCR technology is the relatively poor utilization of the current. However, this disad-

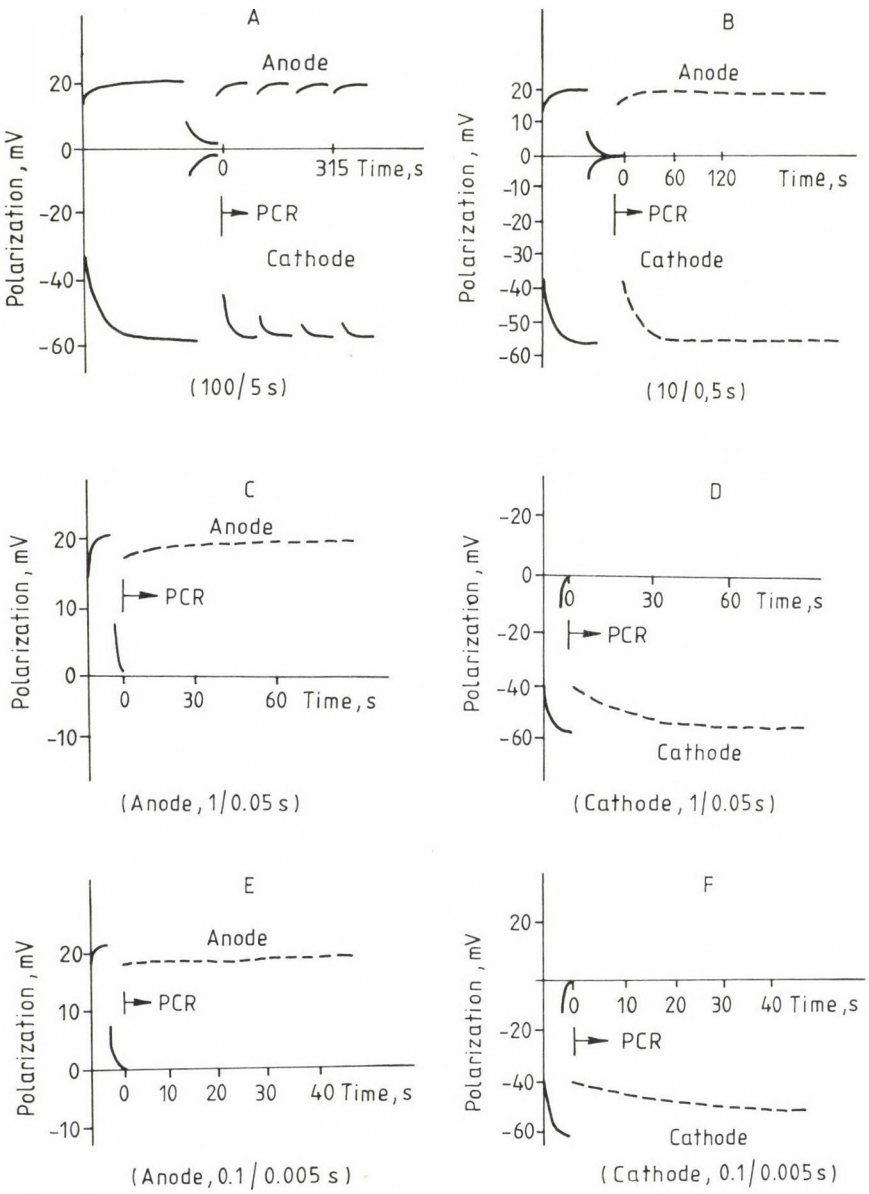

Fig. 5. Polarization in the forward cycles in case of different cycle lengths (forward: 300 A/m^2, reverse: 150 A/m^2, 50 ^{o}C, 40 g/l Cu, 180 g/l H_2SO_4)

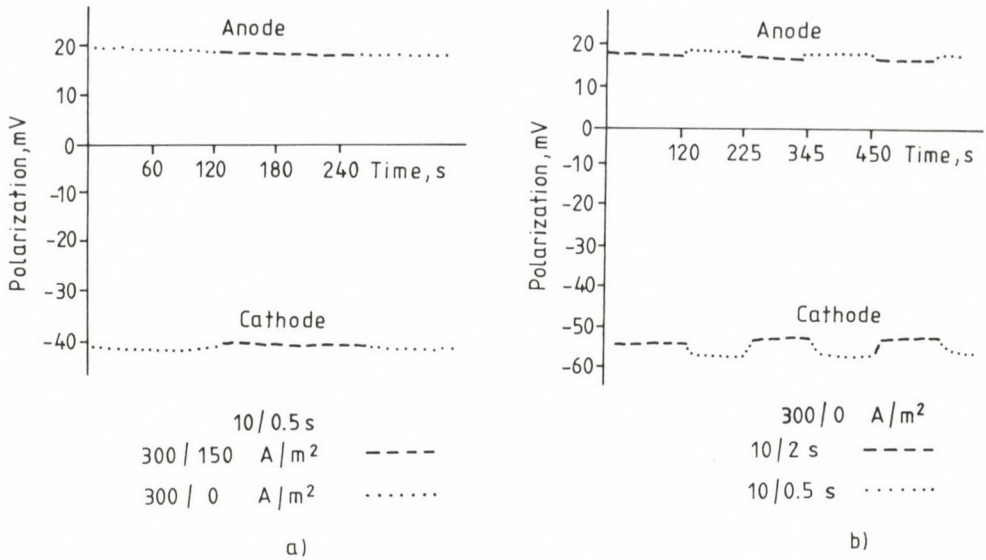

Fig. 6. a) Effect of reverse current density on polarization taking place in the forward cycles. b) Effect of reverse cycle lengths on polarization taking place in the forward cycles

vantage can be offset to some extent by the reduced aptitude to short circuiting resulting from the more favourable conditions of metal deposition. The current efficiency could also be improved by reducing the reverse current intensity and/or the relative duration of reverse cycles which would, however, reduce the advantages offered by the PCR mode of operation. The results experiments where the different values of reverse current and reverse cycle time are used alternately are illustrated in Fig. 6. As clearly shown by the curves, an increase of the reverse (or interruption) cycle times may result in a more significant decrease in cathode polarization than an increase of the return current density.

It seems therefore reasonable to use current interruption instead of current reversal in the PCR technology and to increase the duration of the interruption cycles to make up for the effect of return current missing in this case. Although this method results in a somewhat reduced productivity, it offers all the advantages of the PCR technology while leaving the current efficiency unaffected.

REFERENCES

1. Szepessy, A. Mrs. - Kékesi, T. - Juhász, A. - Pásztor, G.: Investigation of electrolytic copper refining by PCR technology (in Hungarian). Final Report. Metallurgical Department, University of Miskolc, 1986

2. Erdey-Grúz, T.: Kinetics of electrode processes (in Hungarian). Publishing House of the Hungarian Academy of Sciences, Budapest 1969

3. Mattson, E. - Bockris, J.O.M.: Galvanostatic studies of the kinetics of deposition in the copper + copper-sulphate system. Trans. Faraday Soc. (1959), 1586--1601

4. Bockris, J.O.M. - Enyo, M.: Mechanism of electrodeposition and dissolution processes of copper in aqueous solutions. Trans. Faraday Soc. (1962), 1187—1202

5. Stankovic, Z.D.: Kinetic parameters of anodic dissolution and cathodic deposition of copper. Erzmetall, 4 (1981), 215—218

6. Stankovic, Z.D.: Electrochemical dissolution and deposition of copper. Erzmetall, 2 (1983), 91—94

7. Nigretto, J.M. - Jozefowicz, M.: La reduction electrochimique du Cuivre(II) sur electrodes metalliques. I. Electrochim. Acta, 16 (1971), 297—306

8. Bockris, J.O.M. - Kita, H.: The dependence of charge transfer and surface diffusion rates on the structure and stability of an electrode surface: Copper. J. Electrochem. Soc., 109, 10 (1962), 928—939

9. Turner, D.R. - Johnson, G.R.: The effect of some addition agents on the kinetics of copper electrodeposition from a sulphate solution. I. Cathode potential — Current density relation. J. Electrochem. Soc., 109, 9 (1962), 798—804

10. Brown, O.R. - Thirsk, H.R.: The rate-determining step in the electrodeposition of copper form aqueous cupric sulphate solution. Electrochim. Acta, 4 (1983), 383—393

11. Kékesi, T.: Origin, characteristics and controllability of polarization in electrolytic copper refining (in Hungarian). Cand. Sci. Thesis, Hungarian Academy os Sciences, 1991

Acta Technica Acad. Sci. Hung., 105 (3), pp. 173—181 (1993)

PHASE TRANSFORMATION WITH CHANGE IN CONCENTRATION

PROHÁSZKA, J.*

(Received: 17 February 1993)

The phase transformations may be very complex when they are connected with changing chemical compositions. In these cases the deciding factors are not only the critical size of the new seeds, but the effective volumes (V_{cr}) around the new grains, containing the chemical components needed for the changing concentration. The effective volumes are complex functions of the critical size of the new grains, the chemical compositions of the original and new phases and the diffusion rates of the elements in motion. There are examples associated with the Fe-Fe_3C and Fe-C(graphite) alloy systems showing the critical size of the effective volumes both in the metastable and stable systems.

In technological practice, the type, number, magnitude and distribution of the phases determining the properties of the structural materials can be modified in many cases in accordance with the technical requirements by controlling the phase transformations. However, the characteristic features of the phase transformation processes largely depend on the difference between the chemical composition of the new phase and the original phase or phases. In thermodynamic systems where the phase transformation is not accompanied by a change in concentration, e.g. in case of pure metals or, in multicomponent systems, alloys in which there is only one point of contact between liquidus curves and/or surfaces and solidus curves and/or surfaces, the phase transformation can be described simply because the chemical composition of the original phase and the new phase is identical. However, such alloy systems can seldom be found among the structural materials used in practice.

Much larger is the number of alloys where the phase transformation is accompanied by a change in concentration. These phase changes are used, in

*Prohászka, János, H-1118 Budapest, Rozmaring u. 9, Hungary

Akadémiai Kiadó, Budapest

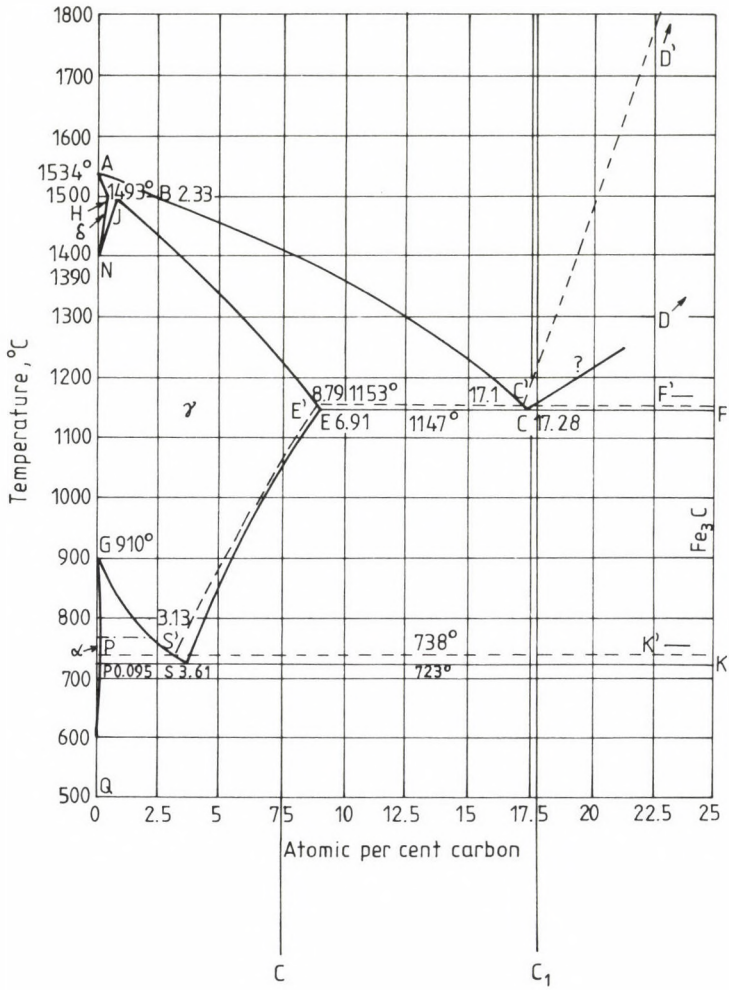

Fig. 1

practice, to improve the properties of the alloys. It is enough to mention here the hardening of steels and the transformation of the cementite structure into a partially graphite structure. At the same time, there is no change in concentration in the course of recrystallization which occurs most frequently in malleable alloys.

Some details of phase transformations accompanied by a change in concentration are discussed below. Excellent examples are the phase transformations of steel and cast iron, the most frequently used structural materials. Let us first consider the conditions under which stable graphite

or metastable iron carbide may be produced in a Fe-C alloy in the course of cooling.

Let the carbon content of an alloy selected according to phase diagram $Fe\text{-}C_{graphite}$ or $Fe\text{-}Fe_3C$ (Fig. 1) be c_1 = 18 atom %. In the course of the cooling of the melt, at 1240 ^{o}C where the temperature of the melt is equal to the liquidus temperature the $Fe\text{-}C_{graphite}$ system, graphite ought to crystallize out of the melt according to the conditions of equilibrium /1/. However, because of the considerable differences in concentration between the melt and the graphite, this would be possible only if sufficient time were available so that in a critical volume V_{cr} where, originally, every 100 atoms consisted of 82 Fe atoms and 18 C atoms, only C atoms would be present after the phase transformation. That means that all Fe atoms must disappear from the critical volume with C atoms of a minimum number required to build up the critical nucleus diffusing at the seed. As shown in every day practice, crystallization of the metastable Fe_3C takes place under the usual conditions of cooling in most cases, instead of development of graphite, the equilibrium phase. Let the causes of this phenomenon be investigated. The critical size of the nucleus, r^{x}, in the new phase is /2/

$$r^{x} = \frac{2\gamma}{\Delta G} = \frac{2\gamma T_{El}}{L\Delta T} \tag{1}$$

where γ is the specific surface energy associated with the phase boundary of the melt and the graphite, ΔG the free-enthalpy difference, T_{El} = 1240 ^{o}C the equilibrium temperature of melt→graphite transformation, L the latent heat associated with the phase transformation while $T_{El} - T = \Delta T$ is the extent of undercooling.

The critical volume of the nucleus is

$$V_{cr} = \frac{32\pi}{3} \cdot \frac{\gamma^3}{\Delta G^3} = \frac{32\pi}{3} \frac{\gamma^3 T_{El}^3}{L^3 \Delta T^3} \tag{2}$$

Similar equations can be written also for melt→iron carbide phase transformation for, as a matter of fact, the physical parameters of the melt and the iron carbide. Here we know only one quantity with acceptable certainty and we know that, because of the metastability of the iron carbide, the value of ΔG for the latter phase transformation is lower. This must manifest itself in the surface energy of the boundary between the melt and

the solid phase as well as in the latent heat since $G_g < G_v$. T_{Ev} = 1160 °C, the subscript v indicates iron carbide.

What conclusions can be drawn from what has been written so far? As has been demonstrated in practice, isothermal conditions cannot be ideally maintained. There are always fluctuations. A deviation from the ideal isotherm is useful only in the direction of lower temperatures, all the more because without undercooling, development of the critical nucleus is impossible. In melt→graphite phase transformation, the difference between both "equilibrium" temperatures is 80 °C. A lower melt temperature is required so that an undercooling resulting in the development of iron carbide will take place. It is not difficult to adjust a temperature difference lower than 80 °C to provide for graphite formation. Still, a graphite structure is seldom produced from the melt in practice (let alone in the case of alloys consisting not purely of Fe and C which are produced for this very reason, i.e. to contribute to graphitization).

Note that the liquidus curves of the phase diagram (Fig. 1) and the values of temperatures estimated on the basis of these curves are rather uncertain. However, a temperature difference of 40 °C instead of the value of 80 °C read from the curves would not alter the case because undercooling is a condition also for iron carbide formations and thus the undercooling of the graphite is always much greater than that of the carbide.

For what reason does iron carbide, the phase of the metastable system, appear, in most cases, instead of the graphite structure? This occurs in spite of the fact that, according to equation (2), the critical volume of the graphite is much smaller than that of the iron carbide at the instant of formation. The same occurrence is experienced in practice, that is, a quasi-equilibrium graphite system takes place usually only after a long and expensive annealing process.

The development of the metastable phase can be mainly attributed to two substantial reasons: 1. to the change in concentration and 2. to the different specific volume of the new phase as compared with the old one. Also, the reduction in free enthalpy suggests that phase transformation is taking place. The G free enthalpy of a given equilibrium phase α is

$$G_\alpha = U_\alpha - TS_\alpha + PV_\alpha \qquad (3)$$

where U_α is the internal energy, S_α the entropy, P the pressure while V_α is the specific volume. Unfortunately, for calculation of the equilibrium con-

ditions, we do not know the accurate value of every thermal characteristic in the equations. The reduction in free enthalpy ΔG in the course of given phase transformation $\alpha \rightarrow \beta$ is

$$\Delta G = U_\alpha - U_\beta - T(S_\alpha - S_\beta) + P(V_\alpha - V_\beta) \tag{4}$$

The reduction in free enthalpy in the course of phase transformation is

$$\Delta G_{l-g} = U_l - U_g - T(S_l - S_g) + P(V_l - V_g) \tag{4a}$$

for graphite and

$$\Delta G_{l-v} = U_l - U_v - T(S_l - S_v) + P(V_l - V_v) \tag{4b}$$

for iron carbide; where subscripts l, g and v indicate the liquid, graphite and iron carbide, respectively. If we take only the configuration entropy into account, which is permissible, then the reduction in free enthalpy can be attributed to the internal energy and to quantity $P(V_1 - V_2)$. No acceptable data have been found for the internal energy. However, the product of the pressure and specific volume is -0.313 P for melt→graphite transformation and +0.01 P for melt→iron carbide transformation. This means that, because of the large specific volume of the graphite (0.444 cm^3/g) as compared with the melt, the volume the graphite atoms taken up is 3.5 times larger than the space taken up by the melt earlier. As a result, the graphite applies pressure to its environment, that is, to the melt of a much smaller specific volume (~0.127 cm^3/g), and thus it decreases the reduction in free enthalphy. At the same time, the melt-iron carbide transformation results in reduction in volume, contributing, thus to the reduction in free enthalpy. However, this does not alter the relationship $\Delta G_{l-g} < \Delta G_{l-v}$.

The effect of the difference in concentration between the old phase and the new phase and, in most cases, the development of the metastable phase instead of the stable phase can be evaluated on the basis of the volume of the old phase required for the number of atoms. The number of C atoms required for the critical volume of graphite is

$$n^* = \frac{m^*}{G_C} N = \frac{V_{cr}\,\rho_C}{G_C} N \tag{5}$$

where m^{*} is the mass of the critical nucleus, G_C the atomic weight of carbon, and N is Avogadro's number. This number of C atoms requires a volume V'_{cr} of the melt, which can be estimated on the basis of the following considerations:

The ratio of Fe and C atoms in the melt is 4.55 and therefore the number of C atoms indispensable for the development of the cementite nucleus is distributed in a volume V'_{cr}. Total number of atoms in volume V'_{cr}

$$n^{*)} = \frac{m^{*)}}{G_l} N = \frac{V'_{kr}\, \rho_l}{G_l} N \tag{6}$$

where $m^{*)}$ is the mass of the melt, G_l the average "atomic weight" of the components while ρ_l is the density of the melt.

Average atomic weight of the melt

$$G_l = C(G_C - G_{Fe}) + G_{Fe} \tag{7}$$

where G_{Fe} and G_C represent atomic mass of iron and carbon, respectively. We can conclude from what we have written, that the ratio of the necessary critical volume V'_{cr} and the critical nucleus of the

$$\frac{V'_{cr}}{V_{cr}} = \frac{\frac{1}{C_l}\left[C_l(G_C - G_{Fe}) + G_{Fe}\right]}{G_C} \cdot \frac{\rho_C}{\rho_l} \tag{8}$$

where ρ_C and ρ_l are the density of the graphite and the melt, respectively. With the quantities given above substituted, for equation (8) the necessary critical volume from which graphite can be built up in the critical nucleus in the melt→graphite phase transformation was found to be about 6.3 times as large as the volume of the critical nucleus.

However, this estimated number would be correct only if no C atoms were present in the immediate vicinity of the critical nucleus within the estimated critical volume. This appears to be impossible. It is difficult to estimate the distribution of the concentration of C atoms. Namely, an average concentration of the C atoms in the vicinity of the graphite nucleus is unlikely to occur as the concentration is continuously reduced by the con-

siderable C demand for the formation and increase of the nucleus. Thus the concentration of C in the vicinity of the nucleus lies certainly below the average value and the C atoms flow towards the nucleus from a distant environment with an average carbon concentration. Hence, in this case, diffusion of the C atoms takes place in the direction of the concentration gradient. This movement of the atoms in a direction other than the usual one is enforced by the reduction in free enthalpy.

The same arguments apply to the movement of Fe atoms flowing in opposite direction. The Fe atoms must disappear from the graphite nucleus, increasing the Fe concentration while reducing the C concentration in the immediate vicinity. Of course, also the diffusion of Fe atoms takes place in the direction of the concentration gradient in the course of formation and increase of the nucleus. Because of this atomic movement and the deviation from average concentration distribution, the effective volume, V'_{cr}, is, by all means, larger than the calculated value. Also this contributes considerably to much slower phase transformations with changes in concentration as compared with transformations where the concentration of the original phase and the new phase is identical.

A similar result can be obtained in case when the cementite phase transformation of the melt is considered. In this case, three Fe atoms in the critical nucleus are bound, to every C atom in the iron carbide nucleus. Let n_v^* be the total number of atoms in the critical nucleus, while

$$V_{crV} = \frac{n_v^* G_v}{\rho_v N} \tag{9}$$

the critical volume (subscript v represents iron carbide).

Using the above formula, equation (8) describing the ratio of the critical volumes can be rewritten as

$$\frac{V'_{cr}}{V_{cr}} = \frac{\frac{1}{C_l}\left[C_l(G_C - G_{Fe}) + G_{Fe}\right]}{\frac{1}{C_v}\left[C_v(G_C - G_{Fe}) + G_{Fe}\right]} \cdot \frac{\rho_v}{\rho_l} \tag{10}$$

With the appropriate values substituted, the effective volume required to build up the critical nucleus of Fe_3C was found to be only one and a half times as large in melt→cementite phase transformation of the same melt as the volume of the critical nucleus. As a matter of fact, all that has been

said earlier with regard to the diffusion of the atoms constituting the nucleus is also true in this case.

Finally, let us consider the process taking place along line E-S of the phase diagram (Fig. 1), where secondary cementite appears in place of graphite in solid phase. Assume that the carbon concentration of austenite, C_c, is 7.5 at. %.

Now equation (10) can be written for austenite-graphite transformation as

$$\frac{V'_{cr}}{V_{cr}} = \frac{\frac{1}{0.075}\left[0.075(12.01 - 55.85) + 55.85\right]}{\frac{1}{0.25}\left[0.25(12.01 - 55.85) + 55.85\right]} \frac{7.694}{7.86} \qquad (11)$$

The result obtained with these values shows that C atoms required to build up the graphite nucleus are found in a volume of austenite 17 times as large as the volume of the critical nucleus of the graphite. Also the fact that the volume of the graphite nuclues is approximately 3.5 times as large as the volume taken up earlier by the austenite shall be taken into consideration. Another factor retarding the development of the graphite nucleus is the resultant high hydrostatic compression.

From the same austenite, C atoms required for graphite formation may accumulate from a volume 3.8 times as large as for the formation of cementite. In this case, the volume of Fe_3C so produced is smaller than the volume of the austenite, but in this case, the development or increase of the nucleus is not retarded by the resultant hydrostatic tensile stress.

Summary

Some metallurgical events and processes to be taken into consideration in investigating the appearance of stable and metastable phases in phase transformations with change in concentration have been discussed. Two Fe-C and Fe-Fe_3C alloys of different concentrations have been considered and examples to illustrate the "effective" volume (V'_{cr}) of the original melt or solid solution required to build up the new phase. In case of both alloys, the development of the stable phase was accompanied with high compression stresses and also atoms from very distant regions were required for the accumulation of the component at a lower concentration of the alloy to build up the critical nucleus.

Appearance of the metastable phase in place of the stable phase can be attributed to the fact that in both cases the development of the stable phase is retarded, while the development of the metastable phase is promoted by the stresses acting around both the effective volume and the nucleus. In our opinion, this is the principal reason for development of metastable phases instead of stable phases in alloys, a phenomenon often experienced in practice.

REFERENCES

1. Hansen, M.: Constitution of binary alloys. McGraw—Hill Co., London, 1958
2. Christian, J.W.: The theory of transformations in metals and alloys. Pergamon Press, London 1965

Acta Technica Acad. Sci. Hung., 105 (3), pp. 183—195 (1993)

DISTRIBUTION OF IRON AND SILICON IN A HETEROGENEOUS ALUMINIUM-CRYOLITE SYSTEM

SILLINGER, N.*

(Received: 8 November 1990)

Iron and silicon are the most important impurities in aluminium produced by means of the Hall-Héroult process. Laboratory studies of the equilibrium conditions of impurities developing between the electrolytic and metallic phases as well as the rate of development of equilibrium are described. Without electrolysis the equilibrium was found to be characterized by the constant ratio of concentrations of impurities measured in both phases while in case of electrolysis by the stabilization of concentrations in the cryolitic phase. In the latter case equilibrium develops at a slower rate, the process is retarded by increasing current intensity.

As a result of the more positive electrode potential of iron and silicon than that of aluminium part of the impurities can be removed from the electrolyte by aluminium by cementation. The change of concentration of impurities measured in electrolyte and in aluminium has been investigated in a high-purity graphite crucible of a diameter of 38 mm and 200 mm and a volume of 140 ccm and 800 ccm, respectively, at a temperature of 990-1000 ^{o}C. The material of the crucible contained less than 10 g/t Fe and 10 g/t Si. Two parts of cryolite have been added to one part of 4N-purity aluminium in each crucible (molar ratio: 2.8-2.9, CaO: 0.16%, Fe_2O_3: 0.05%, SiO_2: 0.08%).

In investigating the change of iron and silicon concentrations with time, reactions were found to take place between aluminium and electrolyte heated together even before melting of the electrolyte. Therefore, aluminium shall be poured into the crucible only after the electrolyte has molten.

In both crucibles of different sizes identical rate of change in concentrations has been measured within the permissible limit of measurement

*Sillinger, Nándor, H-1015 Budapest, Szabó Ilonka u. 35-37, Hungary

Akadémiai Kiadó, Budapest

errors. The Fe and Si concentrations measurable in aluminium after 1 hour have reached more than 95% of the concentrations measured 4 to 5 hours later. Therefore, the values of distribution have been determined on the basis of concentrations measured after 2 hours of holding time at a stabilized temperature in each case.

The effect of the change of electrolysis parameters has been investigated under the following test conditions:

-- Al_2O_3 2-7%
-- AlF_3 2-11%
-- CaF_2 0.5-3%
-- temperature 960-1000 ^{o}C.

The results obtained for different parameters showed that the effects of the different parameters lay within the dispersion of the results of experiments repeated under identical conditions.

The values of distribution of iron between aluminium and electrolyte vary in the range of

$$\frac{[Fe]}{(Fe)} = 5.5 - 11$$

(where $[Fe]$ denotes the Fe concentration in aluminium and (Fe) that in electrolyte), the typical value being 7 (Fig. 1).

The values of distribution of silicon vary in the range of

$$\frac{[Si]}{(Si)} = 5 - 12.5,$$

the most probable value being 7 also in this case (Fig. 2).

The values of distribution obtained for both iron and silicon approximately correspond to the maximum concentration ratio that can seldom be measured in the electrolysis cells, but lie above the typical values.

With a view to study thoroughly the precipitation of iron and silicon, an electrolysis cell has been designed and constructed (Figs 3 and 4). The size of the cell corresponds to a scale of 1 : 1000 as compared with the industrial-scale cell and the current intensity of the test cell can be regulated in the range of 0-100 A. An ID 200 mm high-purity graphite crucible with a volume of 800 ccm is located in the interior of the regulable electric resistance heated furnace. A Ø 60 mm pre-baked anode is protruding into the crucible in coincidence with the centreline, made of high-purity self-baking anode paste.

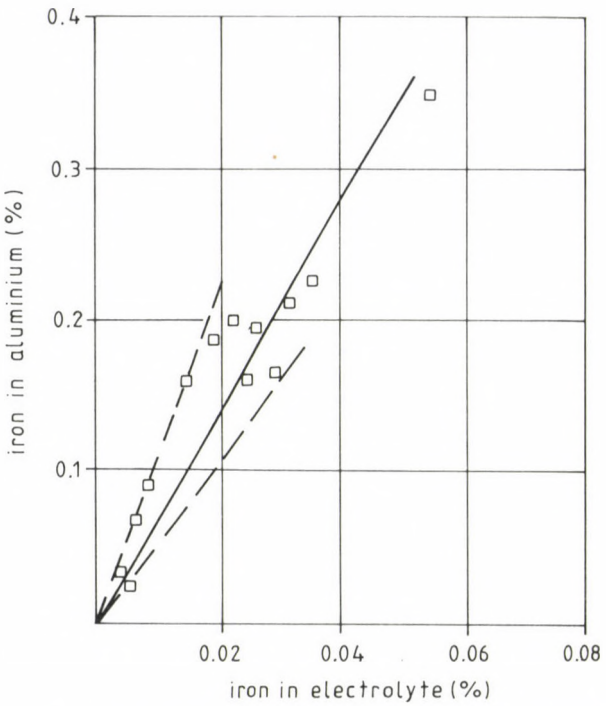

Fig. 1. Distribution of iron between aluminium and electrolyte

The electrolysis cell is closed, the anode gas generated in the course of electrolysis can be exhausted through the lid of the crucible and a cooling system. N_2 gas can be introduced at more points into the cell to displace air and to cool the interior. Aluminium samples can be taken through the lid of the crucible in the course of electrolysis by means of a vacuum sampling pipe. Samples of electrolyte of higher melting temperature have been obtained congealing the electrolyte on a tungsten stick.

The anode gas exhausted gets first into a filter with dust bag. From here it can be introduced into a scrubber. 2.5-3.6 kg of 4N purity aluminium and 6.5-7.5 kg cryolite with an Fe content of 0.04-0.07% and an Si content of 0.04-0.23% have been used for the experiments.

Higher than liquidus temperature has been selected for the electrolysis. Hence, an operating temperature of 980-990 ^{o}C has been used in general.

As many as 48 experimental electrolyses have been carried out with the laboratory cell with cycle times of 2-10 hours and a current intensity of 50 A in general, or less in some cases.

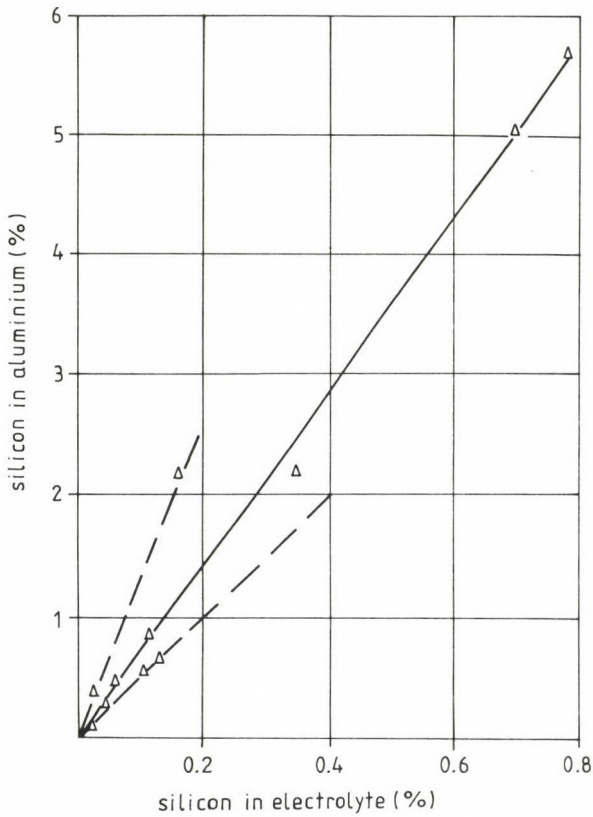

Fig. 2. Distribution of silicon between electrolyte and aluminium

In the course of electrolysis, aluminium and electrolyte samples have been taken at intervals of 10 minutes to 1 hour without interruption of the current supply. The dust filter has been emptied after every 2-4 hours of electrolysis to obtain dust qualitities suitable for analysis.

After scrubbing with either water or NaOH solution no appreciable quantities of Fe and Si compounds have been found in the scrubber connected after the dust filter. As much as 1-4% of silicon and 6-28% of iron reached the scrubber with the anode gas presumably in the form of very small dust particles not retained by the filter cloth.

Alumina in an amount of 3-6% has also been mixed to the electrolyte in every experiment in order to avoid the anode effect.

On the basis of the results of a large number of measurement, it was found that the iron and silicon concentrations of aluminium and electrolyte

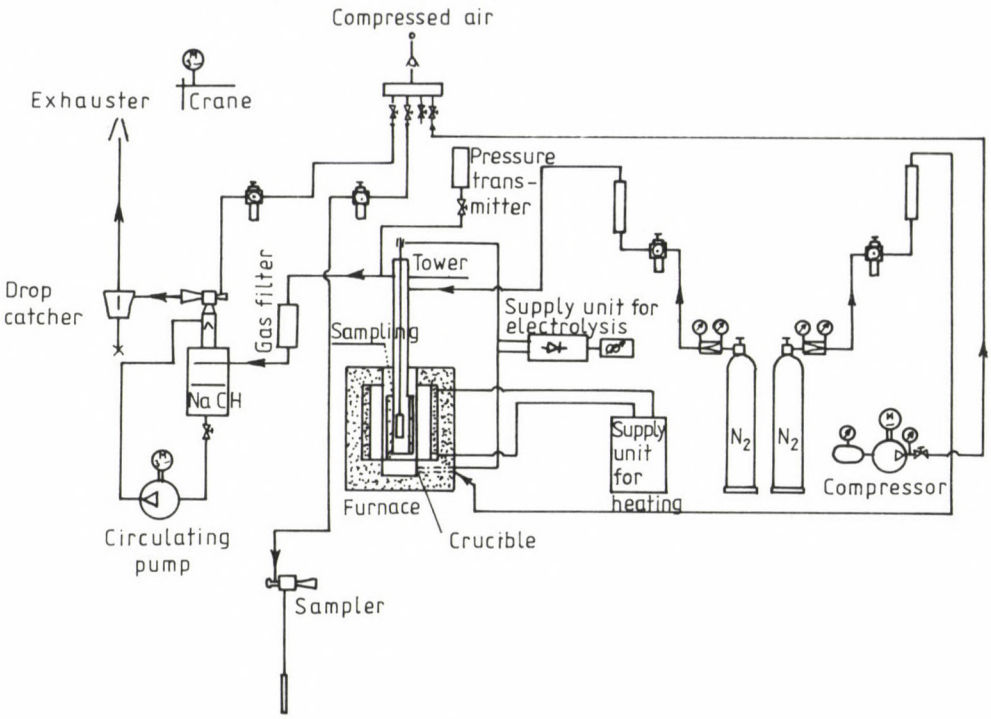

Fig. 3. Block diagram of the laboratory electrolysis cell

stabilize after 2-3 hours. The concentration changes at a slower rate in case of electrolysis than in cementation (Figs 5, 6).

The ratio of $\frac{[Me]}{(Me)}$ concentration developing at different values of current intensity under identical conditions decreases as the current intensity increases (Table 1).

On the basis of the change of Fe and Si concentrations in the aluminium melt with time, the reaction order has been determined by means of the differential equations /4/:

$$\frac{dc}{dt} = k \cdot (c_o - c)^r, \qquad (1)$$

where

c — instantaneous Fe and/or Si concentration in aluminium,

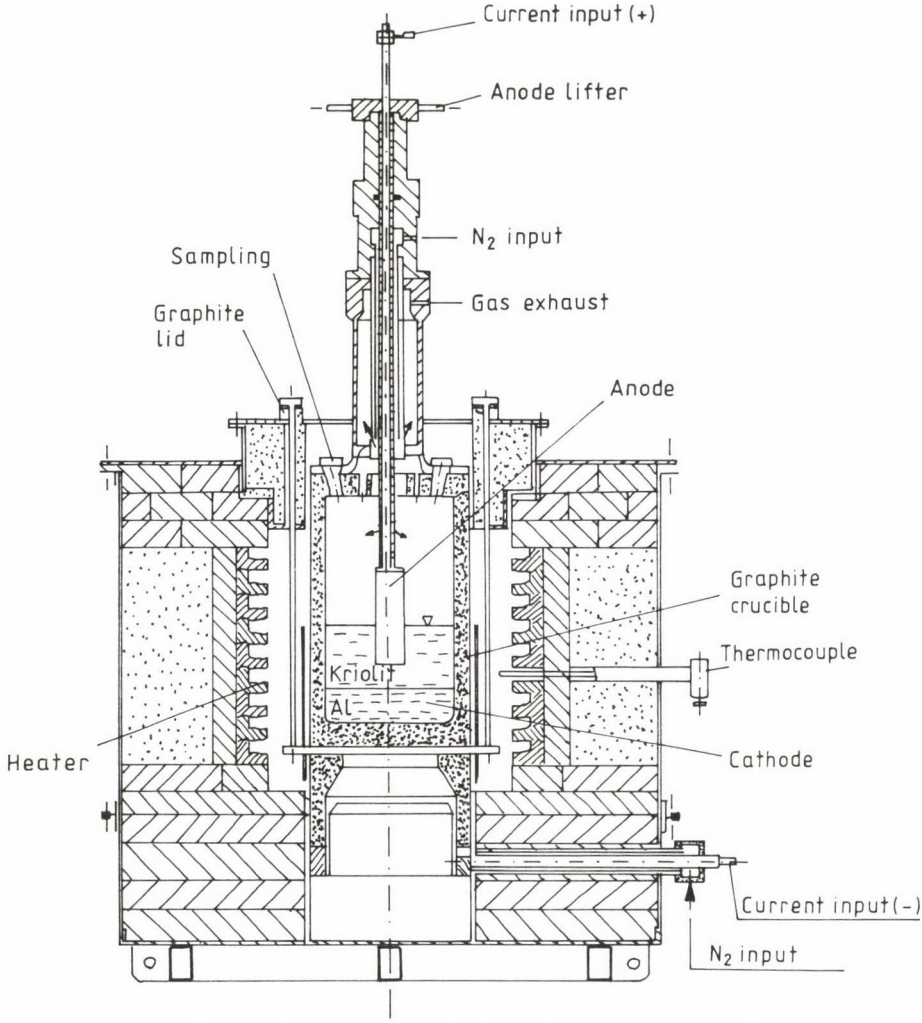

Fig. 4. Construction of the laboratory electrolysis cell

c_o — equilibrium concentration of Fe and/or Si in aluminium in the given test,

t — time,

k — constant,

r — number expressing the reaction order.

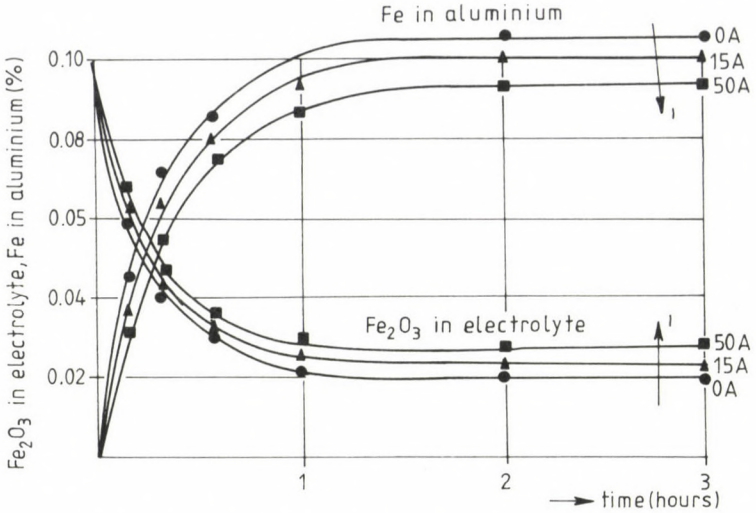

Fig. 5. Change of iron concentration in electrolyte and aluminium

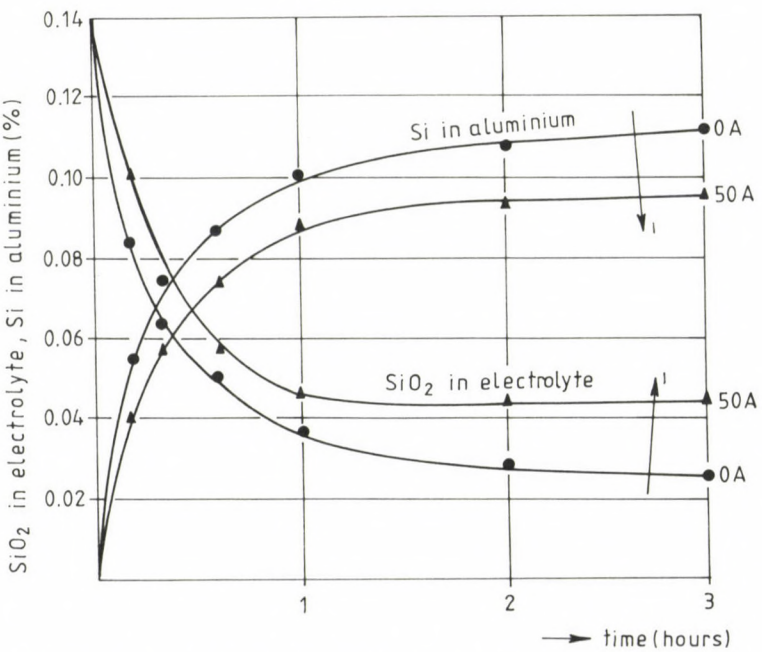

Fig. 6. Change of silicon concentration in electrolyte and aluminium

Table 1. Ratio of Fe and Si equilibrium concentration between aluminium and cryolite

Current intensity (A)	$\frac{[Fe\%]}{(Fe\%)}$	$\frac{[Si\%]}{(Si\%)}$
0	7.9	9.4
5	7.6	7.4
15	6.5	6.2
50	4.9	4.8

With the data illustrated in a $\lg \frac{dc}{dt}$ - $\lg (c_o - c)$ co-ordinate system, straights have been obtained, indicating a reaction order of

1.5 for cementation and electrolysis in case of silicon precipitation while

1.2 for cementation and

0.7 for electrolysis in case of iron precipitation.

Experimental electrolyses using cryolite and aluminium melts of different Fe and Si concentrations at a uniform current intensity of 50 A showed that the ratio of stabilized concentrations is not a given value contrary to the case of cementation while the Fe and Si concentrations of the electrolyte stabilized within relatively narrow limits after 2-3 hours:

— Fe concentration of electrolyte: 0.008-0.02%,

— Si concentration of electrolyte: 0.006-0.016.

E.g. electrolysis by means of aluminium cathode containing 0.5% of Fe and 0.5% of Si at a current intensity of 50 A in a cryolite melt containing 0.11% of Fe and 0.065% of Si resulted after 5 hours in a Fe concentration of 0.017% and a silicon concentration of 0.012%, corresponding to a distribution of 40 for iron and 49 for silicon between aluminium and electrolyte.

In an electrolyte containing 8-10% of AlF_3, the stabilized Fe and Si concentration is lower than in an electrolyte without additive, the typical values approaching the lower limit of the concentration ranges given above.

A reduction of the electrolyte temperature by 40 ^{o}C resulted in no measurable effect upon stabilized concentrations.

In the different experiments, the quantities of fly dust leaving with the anode gas varied between 0.8 and 2.2 g/h. The quantity of fly dust increased slightly with increasing current intensity while it remained unaffected by changes in the electrolyte composition.

Typical dust composition:

Fe	0.2-0.5%
Si	0.8-1.5%
C	2-5%
Al	18-24%
Na	17-22%
F	30-39%.

The results of the experiments have been evaluated by thermodynamic calculations.

Although FeF_2 and SiF_4 compounds are assumed to be present in cryolite melt by most authors, the cementation equilibrium conditions of oxides have been calculated to compare with the conditions developing in electrolysis where not fluorides, but oxides are decomposing.

Cementation reactions:

$$3\,(FeO) + 2\,[Al] = 3\,[Fe] + (Al_2O_3) \qquad (2)$$

and

$$3\,(SiO_2) + 4\,[Al] = 3\,[Si] + 2\,(Al_2O_3), \qquad (3)$$

where the parentheses () indicate the molten electrolyte phase while the brackets [] the molten aluminium phase.

The conditions of equilibrium of the reactions can be calculated on the basis of standard free enthalpy:

$$\Delta G_2^o = \Delta G^o_{Al_2O_3} - 3 \cdot \Delta G^o_{FeO} = - RT \cdot \ln K_2,$$

$$\Delta G_3^o = 2 \cdot \Delta G^o_{Al_2O_3} - 3 \cdot \Delta G^o_{SiO_2} = - RT \cdot \ln K_3.$$

With the equilibrium constants written with the equilibrium activities and taking into consideration that the activity of aluminium can be considered to be equal to 1:

$$K_2 = \frac{a_{(Al_2O_3)} \cdot a^3[Fe]}{a^2[Al] \cdot a^3[FeO]} = a_{(Al_2O_3)} \cdot \left(\frac{a[Fe]}{a_{(FeO)}}\right)^3,$$

$$K_3 = \frac{a^2_{(Al_2O_3)} \cdot a^3[Si]}{a^4[Al] \cdot a^3_{(SiO_2)}} = a^2_{(Al_2O_3)} \cdot \left(\frac{a[Si]}{a_{(SiO_2)}}\right)^3.$$

Numerical values of equilibrium constants at 960 °C and 1000 °C (1233 and 1273 K, respectively):

At 1233 K: $K_2 = 2.72 \cdot 10^{28}$ $K_3 = 8.24 \cdot 10^{16}$

At 1273 K: $K_2 = 2.20 \cdot 10^{27}$ $K_3 = 1.50 \cdot 10^{16}$

Decomposition voltage of the metallic compound in electrolysis:

$$E_{Me} = \frac{\Delta G_{MeO}}{-Z \cdot F} = \frac{\Delta G^{O}_{MeO}}{-Z \cdot F} + \frac{RT}{-Z \cdot F} \ln \frac{A_{(MeO)}}{A_{[Me]}} \tag{4}$$

where

E -- decomposition voltage (V),

G^{O}_{MeO} -- standard free enthalpy of formation of MeO compound (J/gmol),

Z -- valence of Me metal in MeO compound,

F -- Faraday constant (96 500 As),

A -- instantaneous activity.

The reactions of decomposition instead of formation of the compounds will be used for calculations in what follows. Accordingly, the negative sign will not be used in the denominator of formula (4).

Assuming that CO_2 gas is generated on the carbon anode in electrolysis of SiO_2 and FeO like in case of aluminium

$$2\ Al_2O_3 + 3\ C = 4\ Al + 3\ CO_2 \tag{5}$$

$$E_{Al} = \frac{3\Delta G^{O}_{CO_2} - 2\ \Delta G^{O}_{Al_2O_3}}{12\ F} + \frac{RT}{12\ F} \ln \frac{A^{4}_{[Al]} \cdot f^{3}_{CO_2}}{A^{2}_{(Al_2O_3)} \cdot A^{3}_{C}}$$

$$2\ FeO + C = 2\ Fe + CO_2 \tag{6}$$

$$E_{Fe} = \frac{\Delta G^{O}_{CO_2} - 2\ \Delta G^{O}_{FeO}}{4\ F} + \frac{RT}{4\ F} \ln \frac{A^{2}_{[Fe]} \cdot f_{CO_2}}{A^{2}_{(FeO)} \cdot A_{C}}$$

$$SiO_2 + C = Si + CO_2 \tag{7}$$

$$E_{Si} = \frac{\Delta G^{O}_{CO_2} - \Delta G^{O}_{SiO_2}}{4\ F} + \frac{RT}{4\ F} \ln \frac{A_{[Si]} \cdot f_{CO_2}}{A_{(SiO_2)} \cdot A_{C}}\ .$$

With the activity of aluminium and carbon assumed to be one and the formulae for the three decomposition voltages reduced to a common denominator we obtain

$$E_{Al} = \left[\frac{G^{o}_{CO_2}}{4F} - \frac{G^{o}_{Al_2O_3}}{6F} + \frac{RT}{6F} \ln \frac{1}{A_{(Al_2O_3)}} \right] + \frac{RT}{4F} \ln f_{CO_2}$$

$$E_{Fe} = \left[\frac{G^{o}_{CO_2}}{4F} - \frac{G^{o}_{FeO}}{2F} + \frac{RT}{2F} \ln \frac{A_{[Fe]}}{A_{(FeO)}} \right] + \frac{RT}{4F} \ln f_{CO_2}$$

$$E_{Si} = \left[\frac{G^{o}_{CO_2}}{4F} - \frac{G^{o}_{SiO_2}}{4F} + \frac{RT}{4F} \ln \frac{A_{[Si]}}{A_{(SiO_2)}} \right] + \frac{RT}{4F} \ln f_{CO_2}$$

The expression of CO_2 is identical in the formulae of all the three decomposition voltages (framed with dashed line). It means that CO_2 reduces the decomposition voltage to the same extent in each case. This reduction will be 1.02 V at 1233 K, the usual temperature of electrolysis, provided the partial pressure (or fugacity) of CO_2 generated on the anode is identical with air pressure that is its value is one.

At the beginning of the electrolysis, the metal of more positive electrode potential is the first to deposition the anode. Then, as the process advances, also the decomposition voltage increases with an increasing $A_{[Me]}/A_{(MeO)}$ ratio to reach the value of decomposition voltage of the next metal, from that time on, both metals are deposited together on the anode. E.g. in case of a combined deposition of aluminium and silicon:

$$E_{Al} = E_{Si}$$

$$\frac{-\Delta G^{o}_{Al_2O_3}}{6F} + \frac{RT}{6F} \ln \frac{1}{A_{(Al_2O_3)}} = -\frac{\Delta G^{o}_{SiO_2}}{4F} + \frac{RT}{4F} \ln \frac{A_{[Si]}}{A_{(SiO_2)}} .$$

With the above equation rearranged we obtain:

$$2\,\Delta G^{o}_{Al_2O_3} - 3\,\Delta G^{o}_{SiO_2} = -RT \ln \frac{A^{2}_{(Al_2O_3)} \cdot A^{3}_{[Si]}}{A^{3}_{(SiO_2)}} ,$$

which is essentially the formula of the equilibrium constant of cementation reaction /3/. A similar relationship applies also to co-deposition of alu-

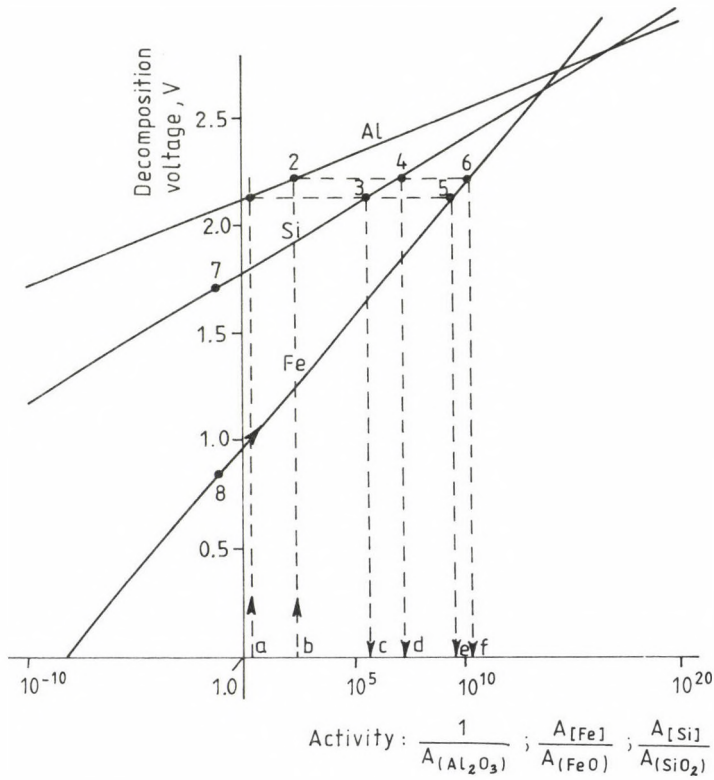

Fig. 7. Decomposition voltage of iron oxide, silicon oxide and aluminium oxide at 1233 K as a function of activity

minium and iron. Hence, according to formal thermodynamic calculations, a co-deposition of metals starts at concentration ratios where cementation without electrolysis has just been completed. Assuming identical alumina concentration, the value of $A_{[Me]}/A_{(MeO)}$ ratio therefore had to be higher than what would characterize the cementation equilibrium.

It has been proved that the conditions of co-deposition are not affected by the carbon anode taking part in the reactions of electrolysis. In Fig. 7 the values of decomposition voltage of aluminium oxide, iron oxide and silicon oxide as a function of activity in case of an indifferent anode at a temperature of 1233 K are illustrated diagrammatically.

The concentration range of 1.5-8% Al_2O_3 typically occurring in electrolysis cells is indicated by points a and b along the abscissa. According-

ly, in case of an inert anode, the decomposition voltage of aluminium oxide varies between points 1-2. Starting e.g. from points 7 and 8, the cementation equilibrium of silicon and iron takes place between points 3-4 and 5-6, respectively. Characteristic of the typical points is an order of magnitude of 10^6-10^7 for silicon while about 10^{10} for iron along the abscissa. At the same time, a value between 1 and 5 has been measured for the distribution of Fe and Si between aluminium and electrolyte in terms of molar fraction in cementation experiments. Hence, there is a difference of 6 to 10 orders of magnitude between calculated and measured values.

Two reasons have been found to explain this enormous difference /5/:

-- iron oxide and silicon oxide enter into reaction with the constituents of the electrolyte, resulting in a more stable compound than the electrolyte;

-- part of the iron and silicon compounds is not in dissolved state in the electrolyte.

REFERENCES

1. Alton, T. - Tabernaux - Curtis, J.: Light Metals (1976), 209—222
2. Grjotheim, K. - Matiasovsky, K.: Aluminium (1983), 687—693
3. Johansen, H. G.: Light Metals (1977), 253—260
4. Berecz, E.: Physicochemistry (in Hungarian). Budapest, Tankönyvkiadó 1980, 41—417
5. Sillinger, N. - Horváth, J.: Light Metals (1990), 369—376

Acta Technica Acad. Sci. Hung., 105 (3), pp. 197—209 (1993)

INVESTIGATION OF THE SPECIFIC ENERGY CONSUMPTION OF PCR COPPER REFINING

SZEPESSY, A.* - KÉKESI, T.**

(Received: 8 November 1990)

On-site measurements were made on every day of a complete anode cycle to investigate the most important parameters of PCR (Periodic Current Reversal) electrolytic copper refining, a technology introduced recently, for all the cells of an electrolysis tank. On the basis of the results, the changes of current efficiency and tank voltage components as a function of time and the reasons for these changes were determined. Bearing in mind the results, possibilities of reducing the specific energy consumption were investigated. It was found that the advantages offered by PCR operation of high current density could be fully utilized only if the electrodes were prepared, and the tank operated, more carefully.

DC electrolysis, the conventional process, is still widely used in electrolytic copper refining. At the same time, the PCR (Periodic Current Reversal) process is finding increasing use with a view to increase the productivity of copper refining. Today more than 16% of the world's cathode copper production results from PCR electrolysis. The production figures of PCR copper refining plants are shown in Table 1.

The PCR technology, essentially a patented Austrian version, was introduced in Csepel Metal Works in 1985. Measurements were made at the copper electrolysis plant of Csepel Metal Works to determine the specific energy consumption of the PCR process and to evaluate the results comparatively.

The specific energy consumption of PCR electrolytic refining can be calculated on the basis of relationship

$$N = a \frac{E}{\eta_{eff}}, \quad \text{kAh/kg of copper,} \tag{1}$$

*Szepessy, Andrásné, H-3524 Miskolc, Adler Károly u. 36, Hungary

**Kékesi, Tamás, H-3532 Miskolc, Tátra u. 13, Hungary

Akadémiai Kiadó, Budapest

Table 1. Production figures of plants using PCR technology /1—7/

		Rio Tinto Patino	James Bridge Copper Works	Tamano Smelter	Ural-elektromeg	Montanwerke Brixlegg	Csepel Metal Works
Cathode production	t/a	109000	56000	96000		32812	17500
Current density	A/m^2	330	350	350	360	358	245
Current utilization	%	95—96	90	95.8	86—89	90	92
Specific electric energy consumption	kWh/t	437	500	377	445	444	415
Specific steam consumption	t/t	0.75	0.25	0.18		0.80	0.31
Anode residue	%		20	14.4		18.4	11.2

where

a — constant calculated on the basis of the electrochemical equivalent, 0.8437 kAh/kg of copper,

E — cell voltage, V,

η_{eff} — effective current efficiency.

The cell voltage and its components have been measured directly as the potential difference between the appropriate points of the distributor bars and electrodes of the tank investigated. The points of measurement and the definition of the voltage components are given in Fig. 1. A test contact has been used to measure the potential of metallic components while the gross polarization voltages have been evaluated by means of a copper reference electrode. Voltage has been measured by means of an MM 2002 digital multimeter of an accuracy of about 1 mV in every case.

The daily average voltage for the entire tank has been calculated on the basis of the daily values of voltage for 56 cells. The values of voltage characteristic of the given cathode cycles, illustrated in Fig. 2, were determined as the average of the mean values for days associated with the different cathode cycles. Finally, the average values of voltage characteristic of the entire anode cycle have been obtained as the mean value of voltages for the three cathode cycles (Fig. 3).

The effective current efficiency, expressing the efficiency of the electrochemical work, can be calculated in the knowledge of the useful (I_h) and effective (I_{eff}) current:

$$\eta_{eff} = \frac{I_h}{I_{eff}} \cdot 100, \ \% . \qquad (2)$$

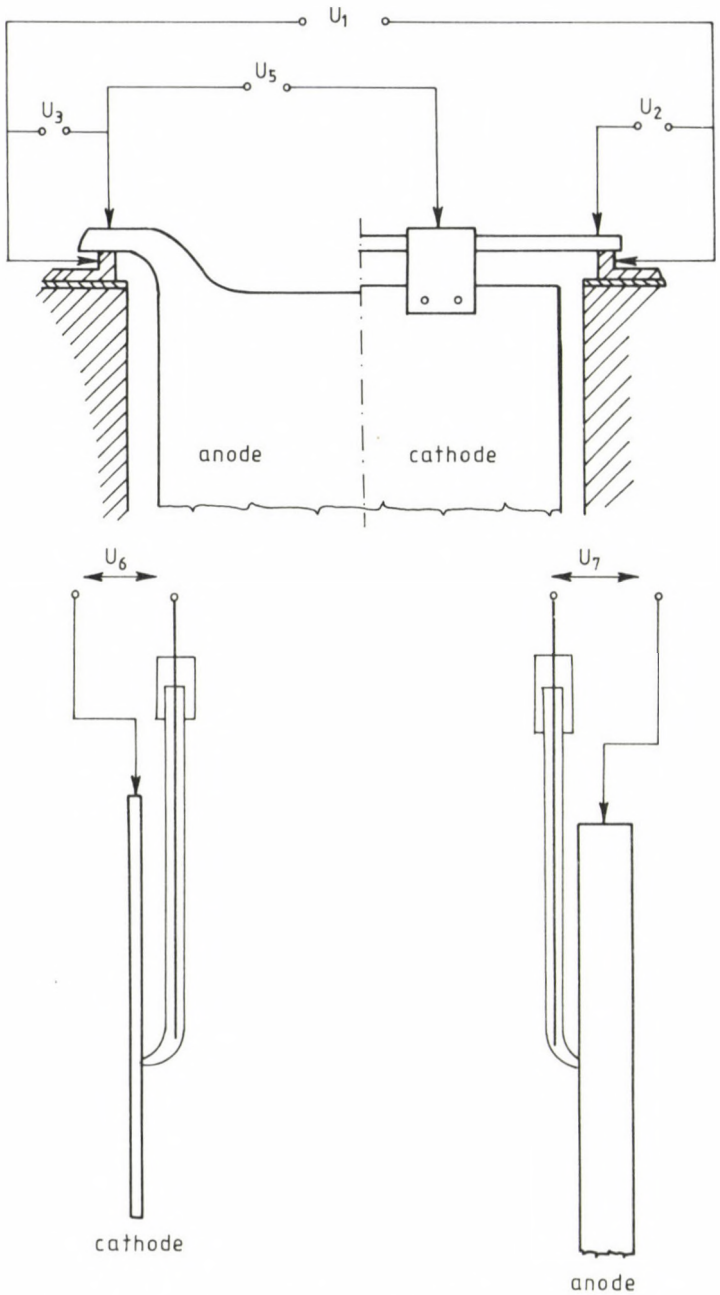

Fig. 1. Voltage measurements
(U_1 — cell voltage, U_2 — cathode contact voltage drop, U_3 — anode contact voltage drop, U_5 — anode-cathode voltage, U_6 — cathodic polarization, U_7 — anodic polarization)

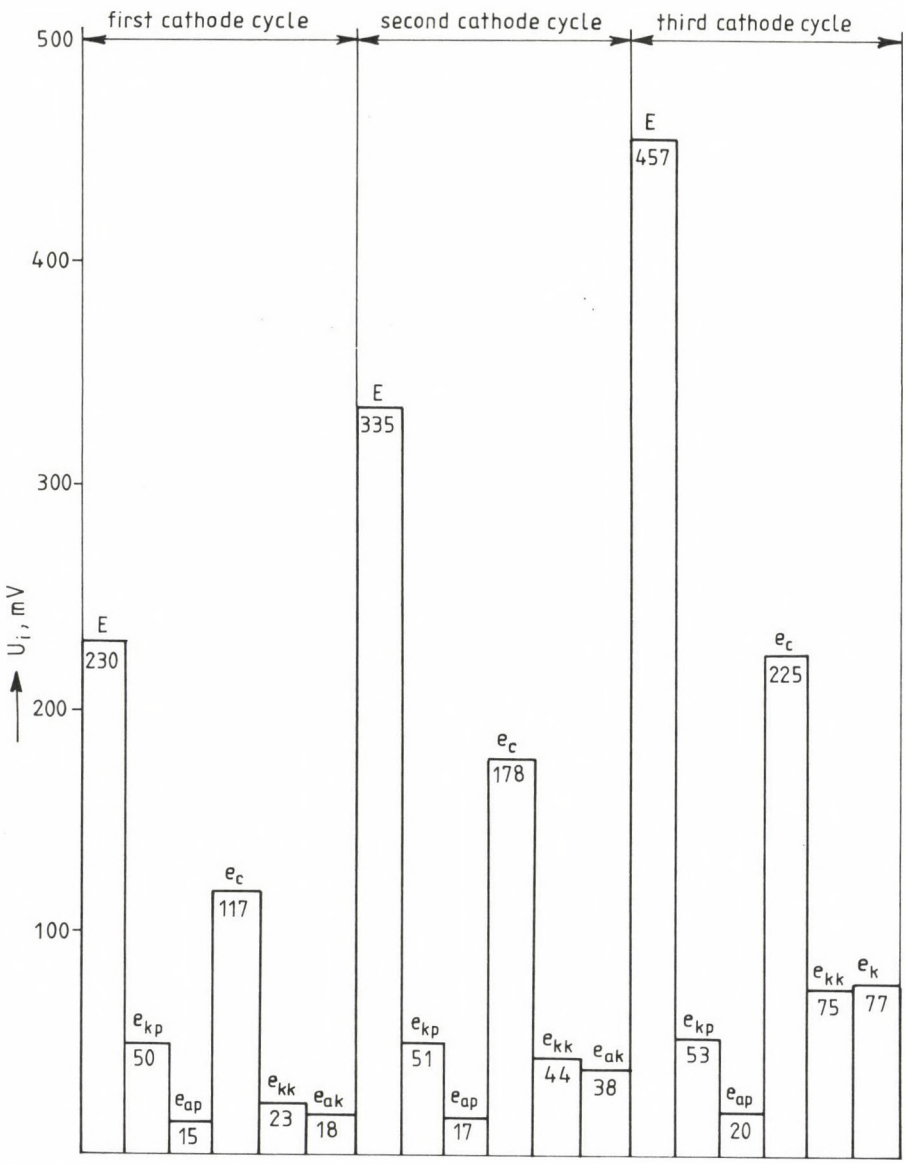

Fig. 2. Average values of voltage for the different cathode cycles in mV
(E — cell voltage, e_{kp} — cathodic polarization, e_{ap} — anodic polarization, e_c — electrolyte voltage drop, e_{kk} — cathode contact voltage drop, e_{ak} — anode contact voltage drop)

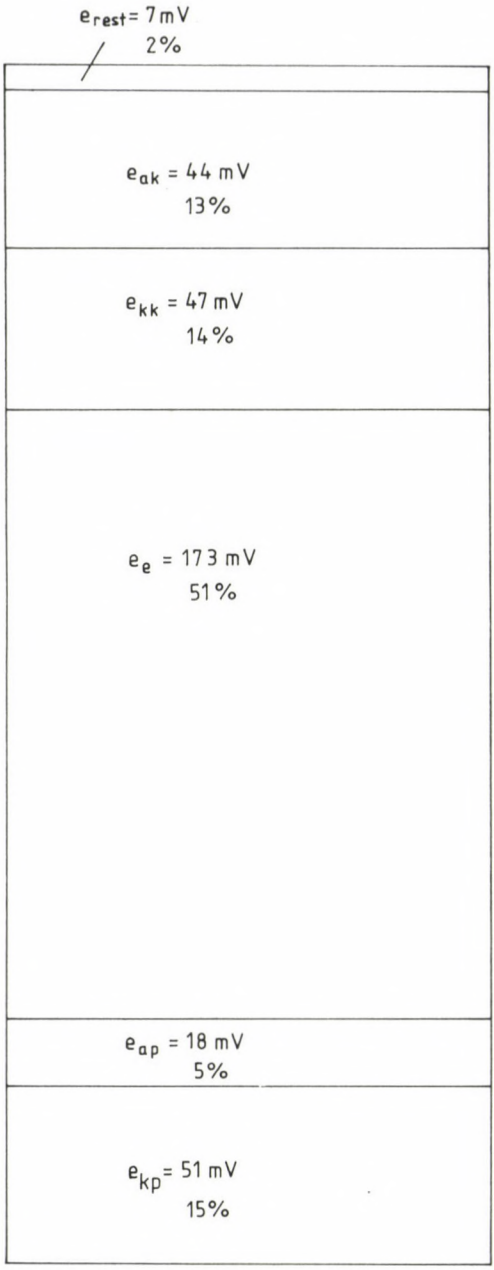

Fig. 3. Average values of voltage for the entire anode cycle

Useful current is the net current resulting in actual metal deposition on the cathodes:

$$I_h = a \cdot 10^3 \cdot 60 \cdot \frac{m}{t}, \quad A, \tag{3}$$

where

a -- 0.8437 kAh/kg,

m -- mass of deposited metal, kg,

t -- time of metal deposition, min.

Effective current is the weighted net current resulting in cathodic cation deposition:

$$I_{eff} = \frac{(I_+ t_+ - I_- t_-)}{t_p}, \quad A, \tag{4}$$

where

I_+ -- forward current intensity, A,

t_+ -- forward current time, s,

I_- -- reverse current intensity, A,

t_- -- reverse current time, s,

t_p -- cycle time, s.

The values of useful and effective current intensity have been determined for each of 29 cathodes of the experimental electrolysis tank of the plant on 19 different days of a complete anode cycle.

Useful current flowing through cathode j within time Δt_j was calculated according to relationship (3). The change in mass of the different cathodes, Δm_j, was determined on the basis of change in the apparent weight F_{ji} of the cathodes with the lift force subtracted from it, using the following formula:

$$\Delta m_j = (F_{j2} - F_{j1}) \frac{\rho_{Cu}}{\rho_{Cu} - \rho_e}, \quad kg. \tag{5}$$

The mass of the cathodes was measured by means of a device developed by the staff of the Department of Nonferrous Metallurgy, illustrated schematically in Fig. 4. The electrolyte and cathode copper density (ρ_e and ρ_{Cu}) has been measured by means of an aerometer and an aeropycnometer, respectively.

To calculate the value of effective current flowing through cathode j by means of relationship (4), the forward and reverse current has been determined using formulae

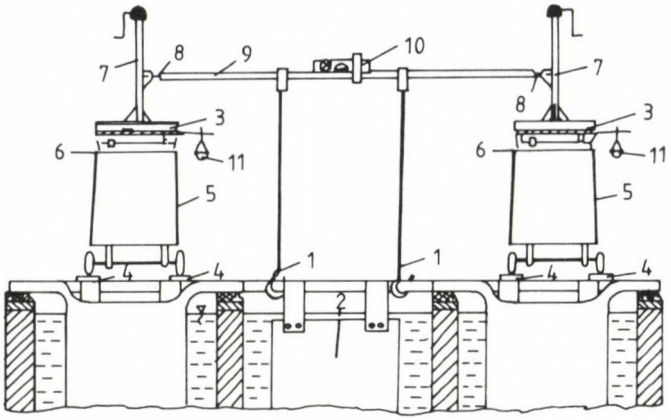

Fig. 4. Measuring device for determination of current efficiency (1 — lifting hook, 2 — cathode, 3 — scale, 4 — plank, 5 — rubber pad, 7 — threaded jack, 8 — plastic connection stub, 9 — rod, 10 — level, 11 — tare)

$$I_{j+} = \frac{U_{j+} - U_{jo}}{R_{kj}}, \quad A \tag{6}$$

and

$$I_{j-} = \frac{U_{j-} - U_{jo}}{R_{kj}}, \quad A, \tag{7}$$

where

U_{j+} — voltage drop along a definite length of the cathode rod, resulting from forward current, V,

U_{j-} — voltage drop along a definite length of the cathode suspension bar, resulting from reverse current, V,

U_{jo} — measured correction of base point shift resulting from temperature rise of the instrument, V,

R_{kj} — resistance of given length of the cathode suspension bar, ohm.

The voltage drops were measured by means of a test contact. The amplified output signal was read from a digital multimeter.

Relationship

$$R_{kj} = \rho_{20}\left[1 + \alpha_{20}(T_j - 20)\right]\frac{l}{A}, \quad \text{ohm} \tag{8}$$

was used to calculate the resistance of a definite length of the cathode suspension bar, where

ρ_{20} — specific electric resistance of copper at 20 °C, $0.0178 \cdot 10^{-6}$ ohm·m,

α_{20} -- temperature coefficient of the electric resistance, $3.92 \cdot 10^{-3}$ $1/^{o}C$,
T_j -- cathode suspension bar temperature, ^{o}C,
l -- length of the cathode suspension bar section, 0.15 m,
A -- cathode suspension bar cross section, $5.76 \cdot 10^{-4}$ m^2.

The cathode temperature was measured by means of a thermistor temperature sensor.

On a given day, the overall effective current efficiency was calculated as the average for the entire tank, using relationship

$$\bar{\eta}_{eff} = \frac{\sum_{j=1}^{n} \eta_{j_{eff}}}{n}, \quad \%, \tag{9}$$

where
n -- number of cathodes of an evaluable current efficiency.

The average current efficiency for the entire cathode cycle ($\bar{\bar{\eta}}_{eff}$) is given by the arithmetic mean of the daily averages. In calculating the average for the entire anode cycle, $\bar{\bar{\bar{\eta}}}_{eff}$, an average weighted by the number of days of the cathode cycles has been calculated on the basis of the mean values of the three cathode cycles. The change of average effective current efficiency with anode cycle time is illustrated in Fig. 5.

The values of average specific energy consumption of the experimental electrolysis tank per cathode cycle and day can be read from Fig. 6, where, for the sake of evaluation, the values of $\bar{\eta}_{eff}$ and $\bar{E}$ are also indicated.

The production figures of the copper electrolysis plant of Csepel Metal Works are comparable with the production figures of Montanwerke Brixlegg, Austria because the process developed there and used also in Csepel differs fundamentally from the PCR technology used by the other plants shown in Table 1. As compared with the PCR technology used in general, the Austrian process uses a considerably shorter cycle time and a higher current pulse rate in order to reduce efficiently overvoltage.

In case of a current density of 242 A/m^2 similar to that used at the copper refining plant of Csepel Metal Works, the specific energy consumption of Montanwerke Brixlegg is 341 kWh/t, the productivity 86 kg of copper per m^2 of tank surface, while in case of a rated current efficiency of 95%, the value of cell voltage is 384 mV /13/.

Although the specific energy consumption for the first cathode cycle (340.73 kWh/t) corresponds to the Austrian value considering that, because of the large number of short-circuited cells resulting in a very low current

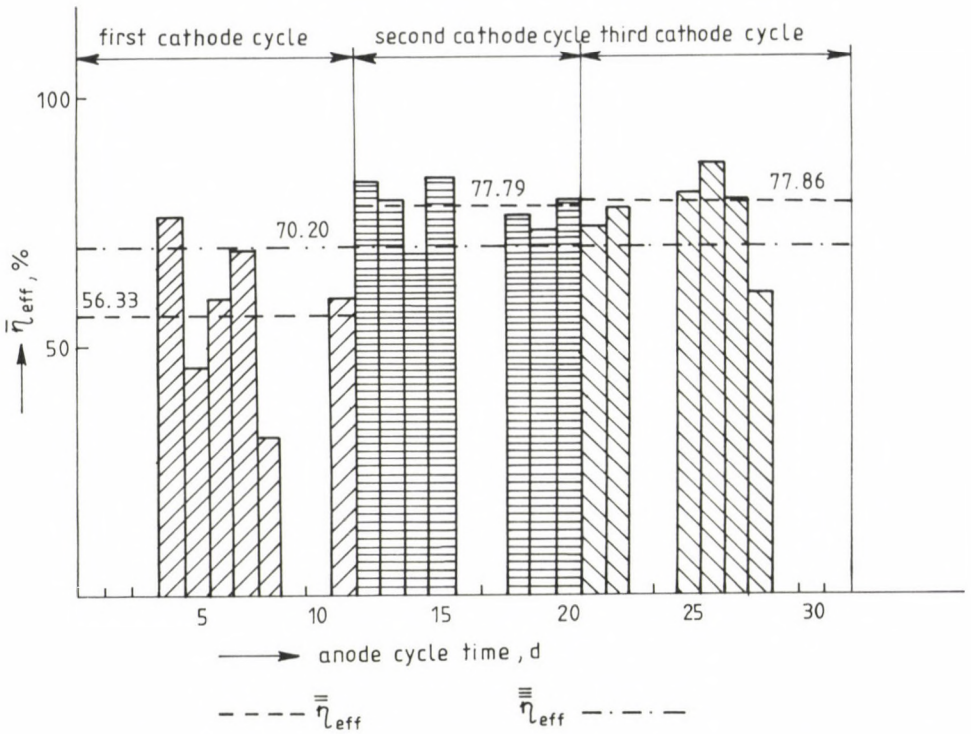

Fig. 5. Change of average effective current intensity as a function of anode cycle time

efficiency (56.33%), the cell voltage is only 218 V (as compared to about 378 mV in case of normal operation), the productivity per unit tank surface is as low as 54.49 kg/m^2·d (the tank surface being 2.67 m^2), which is only 65% of what is normally expectable in case of such an energy consumption.

The conditions of the second cathode cycle are optimal as proved clearly by data in Fig. 6. As a result of the much more uniform current supply ($\bar{\bar{\eta}}_{eff}$ = 77.79%), the cell voltage (333 mV) is comparable with the Brixlegg value and also the specific energy consumption of 377 kWh/t is acceptable. The productivity is fairly good in this cycle (94.88 kg/m^2·d).

In the third cycle, the current efficiency is practically identical with that of the second cycle ($\bar{\bar{\bar{\eta}}}_{eff}$ = 77.86%). However, the value of cell voltage averages at 460 mV due to the poor shape of worn anodes and contaminated contacts, which is by about 80 mV higher than in Brixlegg. As a result, the specific energy consumption is unacceptably high, its value lying at 520 kWh/t. A still acceptable productivity (81.54 kg/m^2·d) can be achieved only at the expense of an additional energy of about 180 kWh/t.

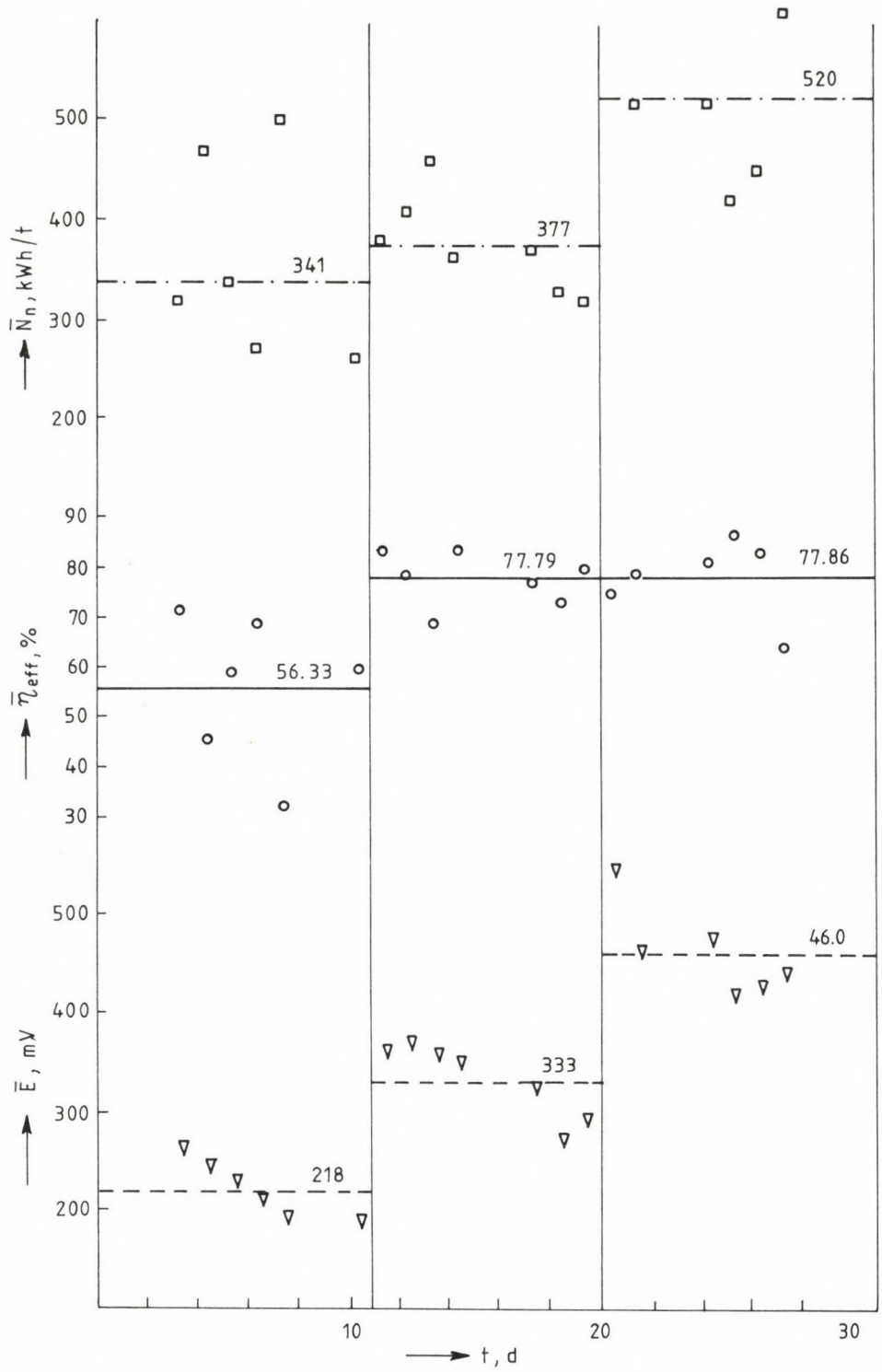

Fig. 6. Change of specific energy consumption as a function of anode cycle time

The results of our investigations suggest that, under the conditions of the Csepel copper refining plant, the economic efficiency of the process is determined by the current efficiency in the initial period of electrolytic refining while by the cell voltage towards the end of the process.

In the first cathode cycle, an improvement of the productivity can be expected from increased current efficiency.

The effective current efficiency of a PCR process depends, in addition to the values of reverse current time and current intensity, largely on the symmetry of currents of the tank. Due to uneven distribution of current among the cathodes, there is a significant difference in the efficiency of the electrochemical work between the different cells of the tank. The productivity of cells of high resistance, which let minimum current flow through even in case of a high tank voltage, is low and thus also the specific energy consumption of these cells is unfavourable. At the same time, in some cells of undesirably low resistance, the current intensity may lie well above the optimum value under given circumstances, moreover, even short circuits between metallic components may occur in the worst case, resulting in a significant increase in specific energy consumption.

The main factors responsible for the uneven current distribution among the cathodes are the variable quality of the cathode contacts and the geometrical asymmetry of the cells in combination. The accurate geometry of the cells is of decisive importance in respect of the processes speeded up due to the increased current density as emphasized also in the relevant literature. In England /2/ and in Japan /3/, plastic distance pieces and a special device developed for this puprose provide for the vertical position of dimensionally accurate anodes and cathodes as well as for a constant electrode spacing. Jacobi /9/ underlines the advantages of continuous anode casting, mass control during anode casting, the ideal crystal structure and smoothness of metal deposited on titanium plate as well as of pressure straightening of the deposited metal.

The symmetry of the cells and thus also the inclination of the electrodes to short circuit depends on the time of electrolytic refining. In the course of electrolysis, even perfectly symmetric cells may become asymmetric after some time due to uneven dissolution and deposition of the metal and displacement of the electrodes.

Under experimental conditions, the effective current efficiency changed as a function of time (days of cathode cycle) in the three cathode cycles according to the following relationships:

$$\bar{\bar{\eta}}_{\text{eff I}} = 64.72 - 1.23\ t, \quad \% \tag{12}$$

$$\bar{\bar{\eta}}_{\text{eff II}} = 79.82 - 0.42\ t, \quad \% \tag{13}$$

$$\bar{\bar{\eta}}_{\text{eff III}} = 79.12 - 0.26\ 6, \quad \%. \tag{14}$$

The current efficiency was lowest in the first cathode cycle because at that time, the thickness of the anode was still considerable and the close electrode spacing -- about 3.5 cm -- favoured the development of short circuits.

The current efficiency reduces in every cathode cycle as a function of cycle time. This is explained by the increasing unevenness of the cathode surface as the cathode cycle advances, resulting in a reduction of the electrode spacing. According to /9/, the unevenness of the cathode surface increases exponentially with the time of the cathode cycle. On the basis of similar experiences at James Bridge plant, England, the time of cathode cycles has been reduced to 7 days /2/.

The effect of the cathode cycle time that is the slope of the lines reduces with the advance of the anode cycle. A reason for this is that in case of an electrode spacing of 4 cm and 4.5 cm in the second and third cycle, respectively, the effect of the unevenness of the cathode surface loses in strength. Another reason is a reduction of the electric charge input in the course of the anode cycle: values of 60.346, 57.646 and 47.059 Ah/m^2 have been measured for the three cathode cycles. 'Aging' of the cathodes occurred at the earliest in the first from among cycles of identical time. The critical value of 50 000 Ah/m^2, permissible in case of an effective current density of 235 A/m^2 and a cycle time of 10 days, has been most exceeded by the input charge in this cycle.

In the third cycle, the specific energy consumption can be reduced first of all by reduction of the cell voltage.

From among the cell voltage components, both the electrolyte and contact voltage drops increase in the course of the anode cycle as seen in Fig. 2. The increasing electrolyte voltage drop results fundamentally from the increasing electrode spacing due to diminution of the anode as well as from the reducing useful anode surface, an inherent feature of given tank construction. At the same time, the current efficiency is affected favourably by an electrode spacing increasing with the cathode cycles. The contact voltage drop depends on the mass of electrodes and quality of contact. A re-

duction in the mass of the anodes contributes to the increasing anode contact voltage drop but the effect of contamination of the distributor bars is decisive in this respect. This is proved by the fact that, in the course of the anode cycle, the cathode contact voltage drop increases continuously in spite of renewal of the cathodes in every cycle. The contacts and conductor rails must therefore be kept clean: in case of the 'CUP BUS BAR' system developed in Japan, the contacts are continuously washed.

REFERENCES

1. Palacios, C. - De Pesquera, M.Ga.: Expansion of the Rio Tinto Patino tankhouse at Huelva. Extractive metallurgy of copper. Vol. 1: Pyrometallurgy and electrolytic refining. New York 1976. Met. Soc. AIME, 569—587

2. Owen, M. - Jacobi, J.S.: High intensity refining of copper at James Bridge. Journal of Metals 27, 4 (1975), 10—15

3. Kitamura, T. et al.: Design, construction and operation of periodic reverse current process at Tamano. Extractive metallurgy of copper. Vol. 1: Pyrometallurgy and electrolytic refining. New York 1976. Met. Soc. AIME, 525—538

4. Orehov, M.A. et al.: Osvoenie elektrolititsheskovo rafinirovania medi s reversom toka pri optimalnoi plotnosti toka. Cvetni Metalli, 8 (1980), 18—22

5. Wöbking, H. - Wörz, H.: Sieben Jahre Erfahrung mit Umkehrstrom (PCR) in der Kupferraffinations-elektrolyse der Vereinigte Metallwerke Ranshofen-Berndorf AG, Montanwerke Brixlegg. Erzmetall 29, 11 (1976), 483—486

6. Wöbking, H. - Wörz, H.: Theoretische Grundlagen und praktische Auswirkungen des PCR-Verfahrens in der Kupferraffinations-elektrolyse. Erzmetall 32, 2 (1979), 53—57

7. Wöbking, H. - Wörz, H.: Grundlagen des PCR-Verfahrens und Ergebnisse bei dessen Anwendung in der Raffinationselektrolyse der Montanwerke Brixlegg. Erzmetall 33, 7—8 (1980), 395—399

8. Bertha, J. et al.: PCR technique in electrolytic copper refinement and a new environment friendly way for the extraction of valuable metals from electrolyte solutions. Erzmetall 32, 7—8 (1979), 335—337

9. Jacobi, J.S.: Present trends in electrolytic refining of copper and lead. Raffinationsverfahren in der Metallurgie (Refining processes in metallurgy). Int. Symp. Hamburg, 20—22 October 1983. A 2., 11—20

10. Schab, D. - Roedel, G.: Anordnung zur Kurzschlussprüfung für die Stromumkehrelektrolyse. DDR Patent Nr. 206690

11. NME Department of Metallurgy: Investigation of electrolytic PCR copper refining technology (in Hungarian). Miskolc, 1986 (Final Report)

12. Kékesi, T. - Mrs. Szepessy, A. - Majoros, M.: Qualification of electrolytic copper refining on the basis of ideal and measured cell resistances (in Hungarian). BKL (Journal of Mining and Metallurgy) — Metallurgy 120, 8—9 (1987), 405—409

13. Krüger, J.: Neue Technologien der Metallherstellung. Zeitschrift für Metallkunde 74, 2 (1983), 61—67

Acta Technica Acad. Sci. Hung., 105 (3), pp. 211—224 (1993)

OPTIMISATION OF COLD STRIP ROLLING

VOITH, M.[1] - DERNEI, L.[2] - ZUPKÓ, I.[3] - VOITH, K.[4]

(Received: 8 November 1990)

The paper gives an analysis of the conditions of achieving the maximum one-hour output of a cold rolling train — in addition to meeting the requirements of flat-lying and form conformity. It is established that there is a close accordance between the adjustable rolling parameters (height reduction, rolling speed, front and back strip tension, roller bending, zone cooling) for the purpose of meeting the above requirements, and the possibilities of ensuring them is pointed out. The steady achievement of this accordance is possible either on a rolling train with process control, or for lack of it, a pass schedule should be developed which ensures meeting the condition of flat-lying with a high hit probability of maximum output.

The simulation mathematical model of computer aided optimum cold rolling technology, and the attainable results under the given limiting conditions, respectively, are illustrated by diagrams.

Quality demands made by modern strip manufacturing industries, especially on form parameters, have increased considerably in recent years. Due to the deformation laws of rolling, each technological operation has its effect on the shaping the final form.

On rolling trains without roll throat controlling automation, it is usually impossible to exploit the maximum nominal speed permissible mechanically because of the random choice of technological parameters. This utilization is limited by the internal stresses (corrugation, strip failure) arising from non-uniform deformation.

As far as productivity is concerned, only such a cold rolling technology can be considered to be optimum which ensures that the largest quantity of rolled products of a given material grade be processed starting from the specified initial dimensions on a given set of rolls per unit of time.

[1]Voith, Márton, H-3529 Miskolc, Dessewffy u. 20, Hungary

[2]Dernei, László, H-3530 Miskolc, Király u. 8, 7/1, Hungary

[3]Zupkó, István, H-3530 Miskolc, Dankó P. u. 5, Hungary

[4]Voith, Katalin, H-1048 Budapest, Sárpatak u. 3, III/8, Hungary

Akadémiai Kiadó, Budapest

According to the optimality criterion of quality requirements, the aim is to roll a cold strip which meets the requirements of flat-lying (form conformity) beyond dimensional accuracy meeting the up-to-date specializations.

Therefore, the development of optimum cold rolling technology requires that several conditions be met simultaneously, and cannot generally dispense with the employment of computers. In the course of developing this technology, it is possible to establish the speed range, the minimum and maximum stretching forces, the maximum rolling force and moment to be applied, the engine outputs, the necessary heat dissipation capacity, of the cooling-lubricating media, the primary crowning of the rolls, the operation range of roll bending equipment, etc.

Only the computed data can serve as a basis for determining with complete objectivity how and what to choose the values of the characteristic basic parameters (e.g. primary crowning) of a rolling train expediently for a particular range of products: For the primary parameters of rolling, it is expedient to choose the roll system (around primary crowning) with characteristics corresponding to the highest theoretical one-hour rating. By using the computed values, it is possible to determine the theoretical one-hour rating of the roll system chosen in this way for the manufacture of smaller batch weights.

1. Operation experiments

The validity of the physical and mathematical relationships for the optimization of cold rolling technology has been checked in actual experiments in several mills. The characteristic data of rolling technology were measured and registered in the manufacture of products of various dimensions and quality. In the course of these measurements -- in addition to the usual data of rolling technology -- the temperature of the roll jacket was registered along a generatrix at three different places by means of a specific measuring technology (Fig. 1).

Figure 2 shows the character of change of jacket temperature and rolling speed, with the time of the parameters registered. It can be clearly seen that while the rolling speed is practically constant ($v \cong 8$ m/s) in the five passes, the steady-state temperature of the roll body measured in the middle of it and at the strip changes in the successive passes (Fig. 3).

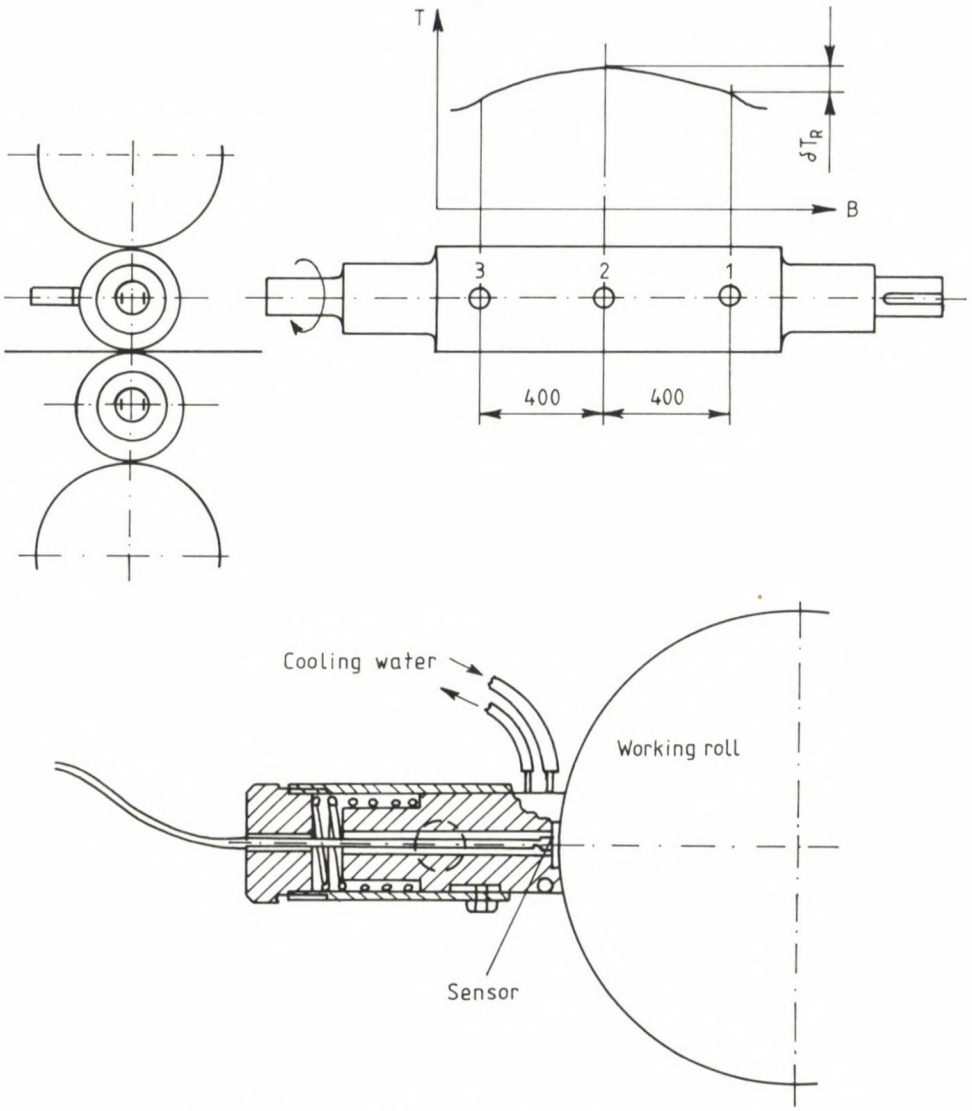

Fig. 1. Location of the temperature measuring pick-up boxes

In cold strip rolling, however, if there is no roll throat controlling automation on the roll stand, stabilization of the calorific condition of the rolls is to be achieved in order that the change in thermal crowning of the rolls of large masses, and therefore of high thermal inertia (of high time constant) should not influence the roll throat or the flat-lying of the strip being rolled. The sine qua non for stabilizing the calorific condition

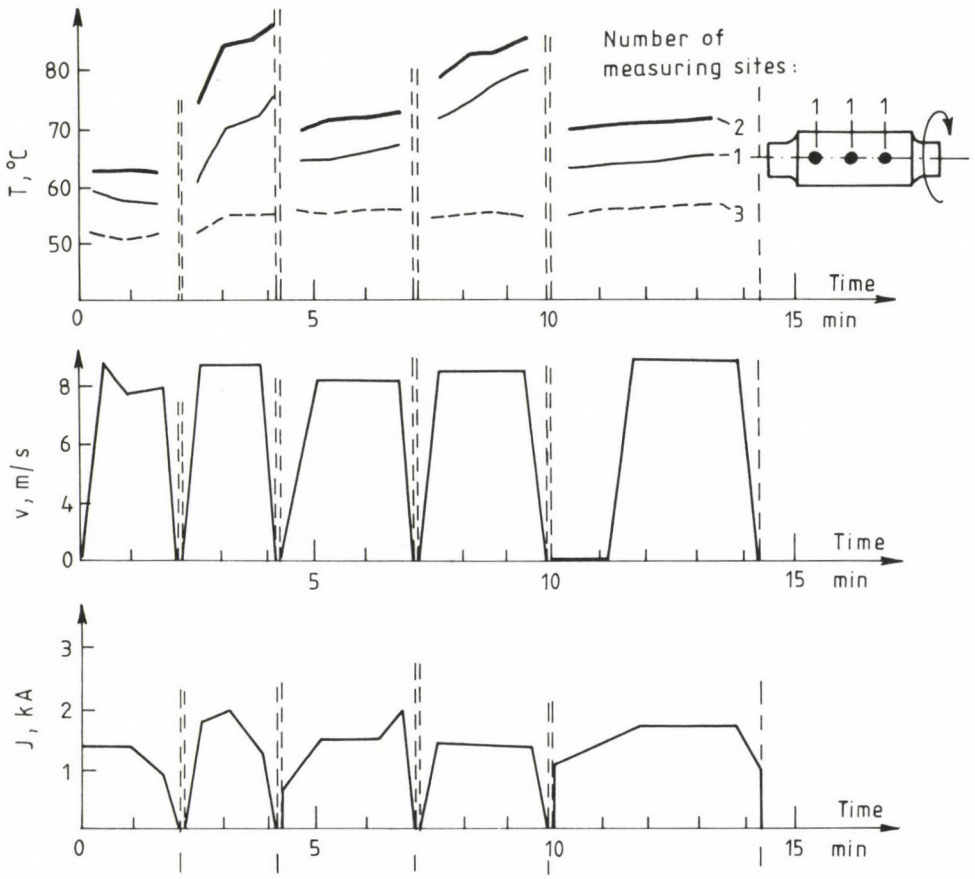

Pass :	1	2	3	4	5
h , mm	2.9	2.4	2.0	1.7	1.5
Δh, mm	0.6	0.5	0.4	0.3	0.2

Fig. 2. Change in the temperature of the roll jacket with the time (mild steel; b_0 = 380 mm; h_0 = 3.5 mm)

is that the amount of heat (heat fluxes) entering and dissipated from the roll body should be equal. The amount of heat extracted is the resultant of the cooling effect of the cooling-lubricating emulsion (first of all of the amount of the emulsion) and of the cooling effect of the roll journals.

As a result of the data obtained from the numerous operation experiments, it was possible to enhance the reliability of the theoretical relationship.

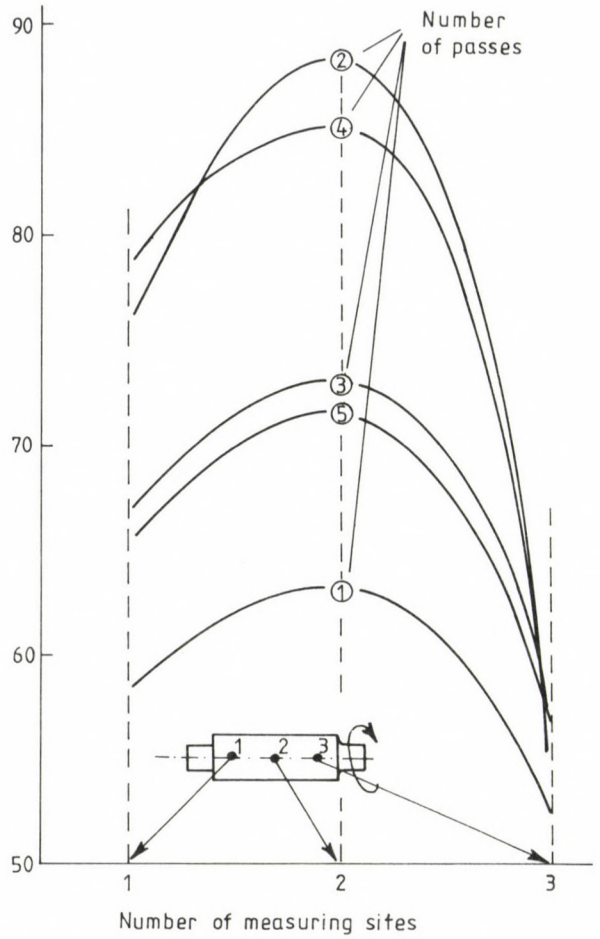

Fig. 3. The temperature of the roll jacket in the individual passes

2. Basic technological principles

Earlier when setting up a pass schedule for cold rolling, the height reduction to be achieved in the pass under examination served as a starting point, and the dimension of the roll throat to be set(s) was determined from the resultant spring constant of the plasticity curve and the roll stand (Fig. 4). The upper limit of the height reduction was determined by the slipping of the strip and by the limit of forces and moment, respectively. The roll crowning necessary for the height reduction chosen in this way can

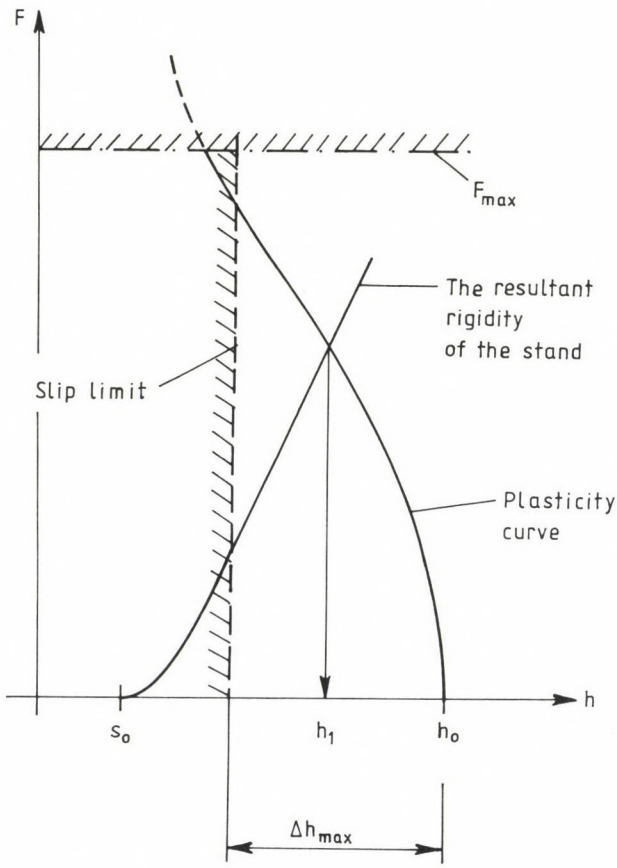

Fig. 4. Setting the roll throat (characteristic diagram)

theoretically be determined as a function of the elastic deformation of the material being rolled and that of the rolls as well as a function of thermal crowning. So far pass scheduling allowed us to relate any rolling speed to the deformation chosen. Rolling speed, however, affects thermal crowning and the resultant deformation of the roll throat, respectively, through heat generation, as well. This, in turn, can and has to be corrected by bending the rolls.

In the individual passes, the related rolling characteristics are to be chosen so that their effect should lead to the achievement of the desired resultant deformation by means of the roll throat developed in the pass. When determining the roll throat, the following should be taken into consideration:

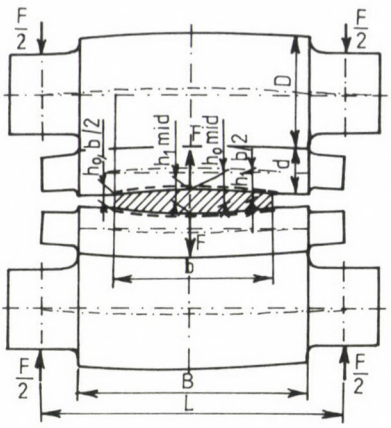

Fig. 5. The form of the roll throat

-- the form of the entering strip (lenticularity; δh_0);

-- the elastic deformation of the rolls (at the centre-line: y_{elas}), which depend on the flattening of the rolls in addition to the bending of the centre-lines of the working rolls and the grip rollers computed with the consideration of compatibility;

-- the primary crowning ground on the rolls (for the diameter: $2y_0$);

-- the force necessary for deforming the material (plasticity curve);

-- the thermal crowning proportional with the rolling speed and the amount of deformation (y_{therm}).

The rolling characteristics must be harmonized so that the strip should remain flat-lying after each pass. This condition can be expressed as follows: the relative height reduction (ε) and the elongation (λ), respectively, should be equal all along the strip width (Fig. 5):

$$\delta h_1 = \frac{h_1}{h_0} \cdot \delta h_0 = (1 - \varepsilon) \cdot \delta h_0.$$

The resultant dimensional deviation of the roll throat along the strip width should therefore be exactly δh_1:

$$\delta h_1 = h_{1,\,mid} - h_{1,\,b/2} = 2. \; y_{throat,\,b/2}.$$

3. Working point of rolling

On the basis of those mentioned above, the optimum crowning can be determined for a single pass. That is: a strip with given lenticularity δh_o can be rolled with rolls of a given primary crowning only at related speed and height reduction. Namely, an increase in height reduction leads, first of all, to an increase in the rolling force, which, in turn, increases the elastic bending of the rolls and the roll throat. An increase in the rolling speed, in turn, causes the heating of the rolls, thus increasing the thermal expansion of the rolls, and narrowing the roll throat, respectively. In Fig. 6, this phenomenon is illustrated for positive, planparallel and negative ground primary crowning. In the figure, $F(y_o)$ represents the force necessary for levelling the ground primary crowning (in case of a negative primary crowning it is a virtual force), the fan curve representing the force required for repressing the thermal crowning.

On the basis of Fig. 6, it is possible to determine the rolling force necessary for forming the roll throat meeting the geometrical requirements of flat-lying strip.

For a given strip tensioning, the rolling force depends on the speed and the deformation (Fig. 7), that is the working point of rolling is the common

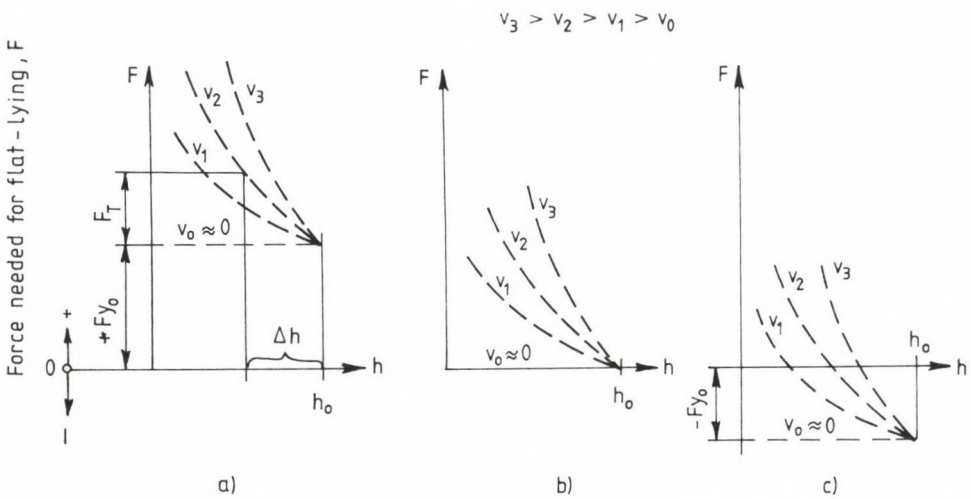

Fig. 6. The force needed for "straightening" the roll generatrix
a) the roll has a positive primary crowning
b) the roll is cylindrical
c) the roll has a negative primary crowning

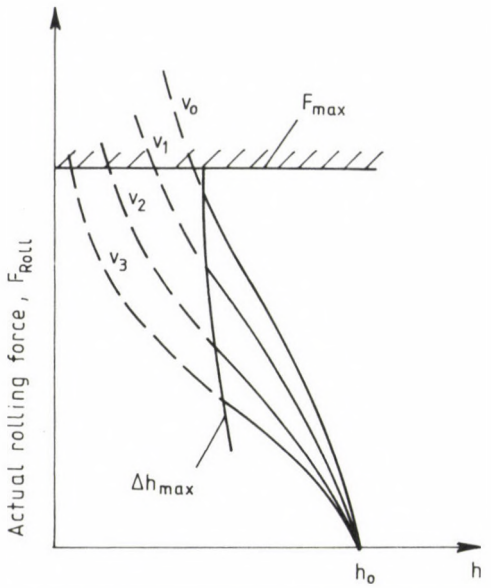

Fig. 7. Plasticity curve (the actual rolling force)

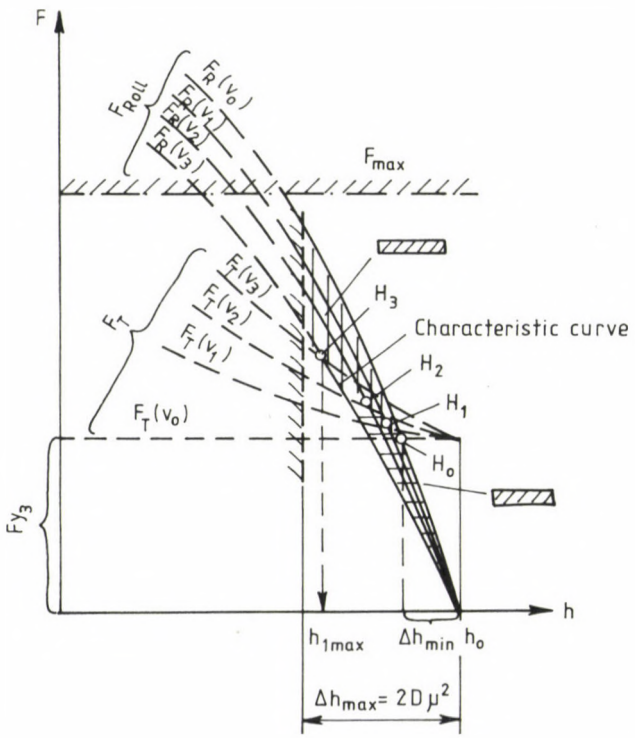

Fig. 8. The new characteristic diagram of cold rolling

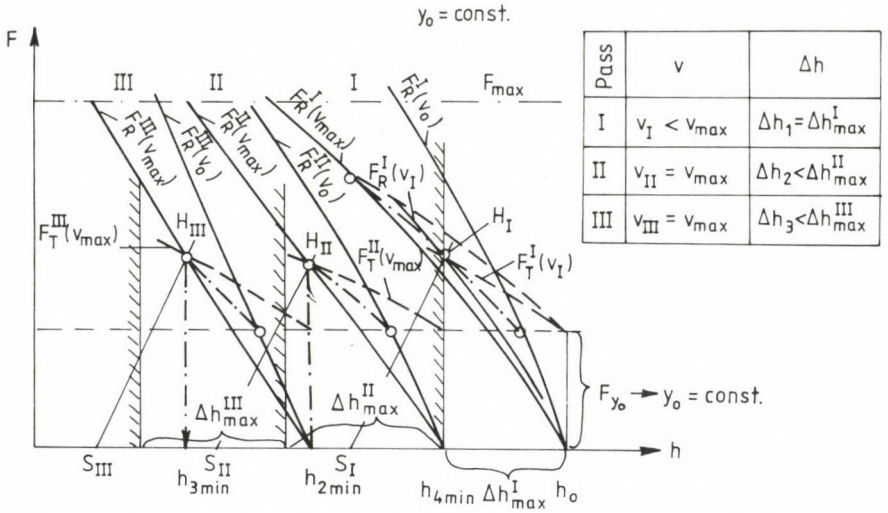

Fig. 9. Determining the working points of rolling for a reversing stock

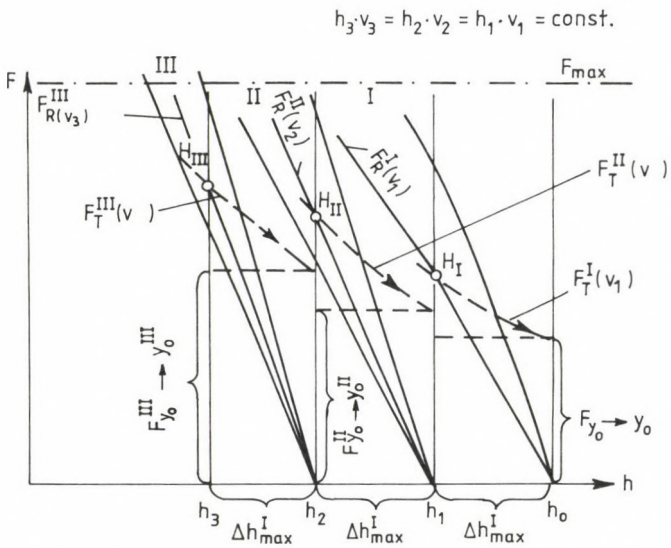

Fig. 10. Determining the working points of rolling for a continuous train

solution of the required force and the plasticity curve (actual force). The principle of determining graphically the working point of rolling is illustrated in Fig. 8. In the figure, the thick line linking the intersection points of the curves with equal rolling speeds, the so-called working

points, represents the characteristic curve of the rolling train as related to the pass under examination.

The figures show the application of the principles set forth to three passes of reversing four-high rolling mill (Fig. 9) and to those of continuous roll train (Fig. 10).

4. The influence of roll roughness

In rolling trains both with and without roll throat controlling automation, the size of the achievable deformation and/or that of the rolling speed is limited both by the quantity of the heat of deformation and that of friction. Our suggestion is: if the surface of the working rolls shows a roughness determined by the rolling condition, the energy equalling the quantity of the heat of friction "saved" in this way need not be consumed (energy-saving cold rolling). In another approach, the energy saved can be utilized for increasing the speed of rolling and/or that of deformation per pass.

With all the principles outlined above taken into account, it is possible to develop a cold rolling technology for which the maximum strip temperature is pre-determined and the maximum lenticularity of the final product is specified.

The optimization possibilities of cogging technology for aluminium foil with three passes are presented as a concrete example of application.

The final result of the calculation run with the unchanged basic data of the processing technology (Fig. 11, variation W) is: the working rolls ground with a primary crowning of $2y_o$ = +100 µm and with a stone of roughness K = 220 at present make possible on the application of extremely low speed level specified operationally, as the temperature of the final product reaches the flash-point of the lubricating oil, nevertheless: T_{strip} = 109 °C. (This consistency also proves the reliability of the program.) In addition, the calorific condition of the rolls is different for each pass (the spreading range has been blackened), but the time constant of the development of the thermal crowning is high, so the danger of non-uniform deformation and rupture is present. The situation is rendered even worse by the fact that roll throat controlling (e.g. exertion of a bending force) would be needed in all passes, because of the not absolutely accurate choice of the primary crowning. All the above said proves that on rolling trains with-

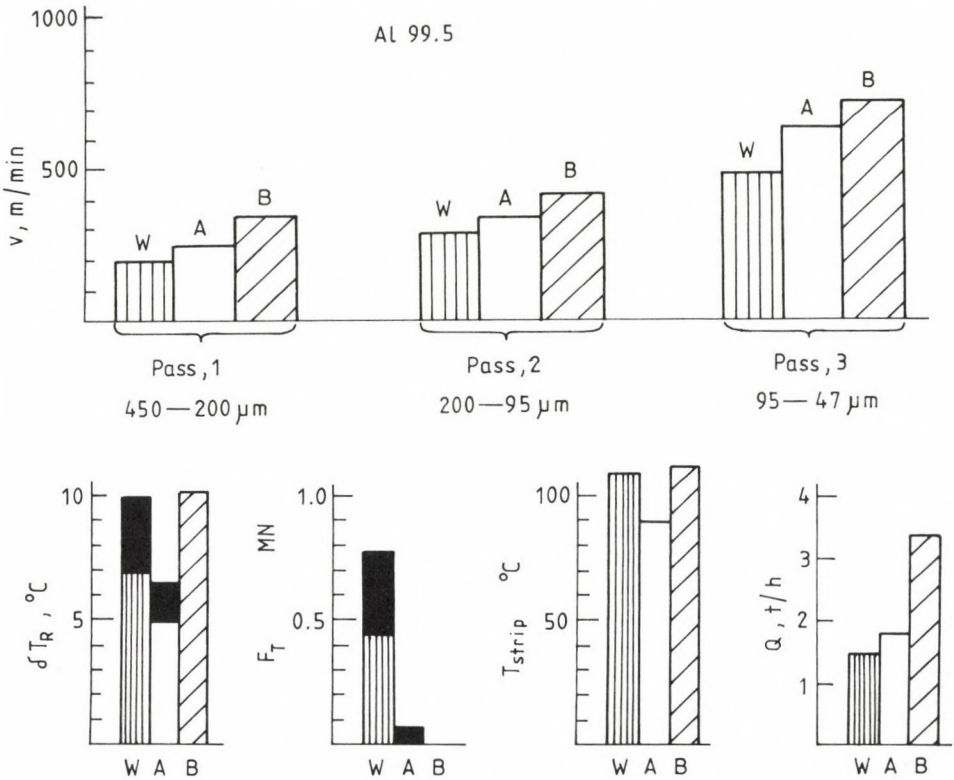

	Fineness of the grinding wheel K	The ground primary crowning of the rolls $2y_o$, μm
W	220	+100
A	320	+100
B	320	+80

Blackened area : spreading range

Fig. 11. Comparison of the characteristic parameters

out roll throat controlling automation, it is generally not feasible to utilize the maximum speed permissible mechanically because of the random choice of the technological parameters. It is limited by the internal stresses arising from the non-uniform deformation (corrugation, strip rupture).

The rolling parameters in variant A in Fig. 11 were determined for the following conditions: the ground primary crowning is the same ($2y_0$ = +100 μm), but the grain refinement of the grinding wheel is better: K = 320 (instead of K = 220). It can be established that under these conditions the rolling speed improves in all passes, and by varying the strip tensions it is possible to achieve a condition when there is practically no need for external roll bending. Through this modification, the theoretical one-hour output of the rolling train for three passes increases from Q = 1.48 t/h to Q = 1.9 t/h (an increase of ∼ 28%), but the flash-point of the lubricating oil (110 ^{o}C) is not closely approached as the finishing rolling temperature is only T_{strip} = 92.2 ^{o}C.

For the purpose of increasing the heat flows (increasing the thermal crowing of the roll), it was examined to what extent the primary crowning, which is originally $2y_0$ = +100 μm, could be changed, and after several calculations it was found that its extreme value, supposing with an unchanged series of height-reduction assumed, is yielded in the form: $2y_0$ = +80 μm. (Variant B in Fig. 11.) The level of speed achievable with rolls of such primary crowning and ground with a fineness of K = 320 comes near the mechanical maximum (it is 839 m/min for the stand under examination). On the basis of the calculated values, it has been rendered possible to establish the fact that the theoretical one-hour output can be increased to Q = 3.2 t/h at the output finishing temperature T_{strip} = 112.4 ^{o}C.

5. Conclusion

It can be established that by understanding the physical relationships, by setting them up and applying them correctly, that is, by mere engineering activity, it will be possible to meet the requirement of flatlying with a high hit probability even with roll trains without form controlling equipment. On trains already equipped with form control, the process described contributes to choosing the working point in a way which facilitates achieving the maximum capacity with a minimum of control activity (e.g. roller bending, zone cooling, etc.).

REFERENCES

1. Guillot, C.: Berechnung von Walzenbiegung und Bombierung für ein Quarto-Nachwalzgerüst. Archiv für das Eisenhüttenwesen 41 (1970), 7, 653—660

2. Hinkfoth, R. - König, B. - Vogt, E. - Becker, H.: Berechnung der Walzspaltform über die Bandbreite beim Kaltwalzen von Bändern auf Quartogerüsten. Neue Hütte 17 (1972), 7, 412—418

3. Schippert, L.: Increase of speed in aluminium cold-rolling. Bányászati és Kohászati Lapok, Metallurgy (1978), 5, 223—229

4. Horiguchi, F.: 1750 mm Al Cold Mill for CHEMOLIMPEX (Hungary). Ishikawajima-Harima Heavy Industries Co. Ltd. Tokyo, Japan. Tokyo, 1980

5. Voith, M.: Optimization of the technology of cold strip-rolling. Bányászati és Kohászati Lapok, Metallurgy 115 (1982), 3, 93—99

6. Voith, M. - Dernei, L.: Computer-optimized cold-rolling. Techniques Publications of the University of Miskolc, II. Metallurgy 26 (1982), 3—4, 223—247

7. Voith, M.: Consideration for the effects of temperature in optimization of plastic metal-working techniques. Doctor-thesis, Hungarian Academy of Sciences. Budapest, 1983

8. Voith, M. - Dernei, L.: New ways in cold strip-rolling. Technical-Economic Publications, Duna Iron and Steel Works XXV/4—5 (1985), 45—55

9. Kiss, E. et al.: Plastic Metalworking. Cold Rolling (196—250) and Plastic Metalworking of Aluminium Alloys (547—647). Tankönyvkiadó, Budapest, 1987

10. Voith, M. - Dernei, L. - Zupkó, I. - Kokas, T. - Horváth, Á.: Computer aided design of cold rolling techniques. Bányászati és Kohászati Lapok, Metallurgy 120 (1987), 8—9, 347—350

11. Dernei, L. - Voith, M. - Zupkó, I.: Technical evaluation of the reconstruction of the four-high rolling stand of Salgótarján Metallurgical Works. Bányászati és Kohászati Lapok, Metallurgy 123 (1990), 5, 204—208

12. Voith, M. - Dernei, L. - Voith, K.: Complex optimization of cold strip rolling. 5th International Rolling Conference, Imperial College, London, 11—13 September 1990. 458—465

NOTICE TO CONTRIBUTORS

Papers in English* are accepted on condition that they have not been previously published or accepted for publication.

Manuscripts in two copies (the original type-written copy plus a clear duplicate one) complete with figures, tables, and references should be sent to

Acta Technica
Nádor u. 7. I. 118
Budapest, Hungary
H-1051

Although every effort will be made to guard against loss, it is advised that authors retain copies of all material which they submit. The editorial board reserves the right to make editorial changes.

Manuscripts should be typed double-spaced on one side of good quality paper with proper margins and bear the title of the paper and the name(s) of the author(s). The full postal address(es) of the author(s) should be given in a footnote on the first page. An abstract of 50 to 100 words should precede the text of the paper. The approximate locations of the tables and figures should be indicated in the margin. An additional copy of the abstract is needed. Russian words and names should be transliterated into English.

References. Only papers closely related to the author's work should be referred to. The citations should include the name of the author and/or the reference number in brackets. A list of numbered references should follow the end of the manuscript.

References to periodicals should mention: (1) name(s) and initial(s) of the author(s); (2) title of the paper; (3) name of the periodical; (4) volume; (5) year of publication in parentheses; (6) numbers of the first and last pages. Thus: 5. Winokur, A.—Gluck, J.: Ultimate strength analysis of coupled shear walls. American Concrete Institute Journal 65 (1968) 1029-1035

References to books should include: (1) author(s)' name; (2) title; (3) publisher; (4) place and year of publication. Thus: Timoshenko, S.—Gere, J.: Theory of Elastic Stability. McGraw-Hill Company. New York, London 1961

Illustrations should be selected carefully and only up to the necessary quantity. Black-and-white photographs should be in the form of glossy prints. The author's name and the title of the paper together with the serial number of the figure should be written on the back of each print. Legends should be brief and attached on a separate sheet. Tables, each bearing a title, should be self-explanatory and numbered consecutively.

Authors will receive proofs which must be sent back by return mail.

Authors will receive 50 reprints free of charge.

* Hungarian authors can also submit their papers in Hungarian.

HU ISSN 0865-7440

ACTA TECHNICA

ACADEMIAE SCIENTIARUM HUNGARICAE

EDITOR-IN-CHIEF: P. MICHELBERGER

VOLUME 105
NUMBER 4

MECHANICAL ENGINEERING — M/2

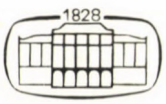

AKADÉMIAI KIADÓ, BUDAPEST 1993

ACTA TECHNICA

A JOURNAL OF THE HUNGARIAN ACADEMY OF SCIENCES

Acta Technica publishes original papers, preliminary reports and reviews in English, which contribute to the advancement of engineering sciences.

Acta Technica is published by

AKADÉMIAI KIADÓ
Publishing House of the Hungarian Academy of Sciences
H-1117 Budapest, Prielle K. u. 19—35

Subscription information

Orders should be addressed to

AKADÉMIAI KIADÓ
H-1519 Budapest, P.O. Box 245

Subscription price for Volume 105 (1993) in 4 issues US$ 80.00, including normal postage, airmail delivery US$ 20.00.

Acta Technica is abstracted/indexed in Applied Mechanics Reviews, Current Contents–Engineering, Technology and Applied Sciences, GeoRef Information System, Science Abstracts.

Acta Technica Acad. Sci. Hung., 105(4), pp. 225—253 (1993)

EXAMINATION OF THE POSSIBILITY OF APPLYING LATENT HEAT STORES AND THE PROCESS OF HEAT RECOVERY FOR PREHEATING AUTOMOTIVE ENGINES PRIOR TO STARTING

KISSNÉ HUNYADI, I.*

(Received: 29 July 1989)

With the aid of heat stores waste heat risen from the running of internal combustion engines of vehicles can be used for preheating engines of low temperatures prior to starting. Owing to this fact cold starting problems can be reduced in case of diesel engines.

In order to decrease the mass and the volume of heat stores in vehicles it is expedient to use latent heat-storing materials. These storing materials store heat in the form of solid-fluid phase changing energy at constant temperatures and their specific storing capacity is usually more favourable than that of sensible heat stores.

The heat stored in order to preheat engines should be regained in a relatively small time, which process is hindered by the increasing amount of heat resistance of the solidifying phase changing material.

The applied hybrid-heat-store system contains both phase changing and sensible heat-storing materials.

The sensible part also transfers heat between the engine and the latent heat-storing material. The optimal placement of the latent heat-storing material makes it possible to insure great heat-storing capacity and quick heat regaining. This optimalization has been carried out by examining the instationary solidification process of the latent heat-storing material both in theory and in practice.

1. Introduction, emergence of the problem

It is obvious that greater storage capacity can be achieved within a relatively smaller volume with the application of latent heat-storage materials capable of storing heat in the form of solid-liquid phase-change energy at a constant temperature than with the application of heat-sensible heat stores, in which the temperature is always changing.

During the operation of the internal combustion engines of motor-vehicles, a significant amount of waste heat will be accumulated, which is emitted into the environment through cooling water and the exhaust gases,

*Kissné Hunyadi, Ildikó, H-1126 Budapest, Vöröskő u. 21, Hungary

Akadémiai Kiadó, Budapest

respectively. By means of a heat store mounted on the vehicle, a fraction of the waste heat can be recovered and used independently from the operation of the engine. In this way, the amount of heat accumulated in the heat store can be utilized for heating up the engine, as well as certain parts of the fuel supply system prior to starting up the engine cooled down under the extremely cold weather conditions. By doing this, the problems of cold starting occurring especially with the diesel engines can be considerably minimized.

In order to reduce the volume and mass of the heat store, the application of solid-liquid latent heat storage substances is very advantageous. But due to the poor thermal conductivity of the phase-change storage substances, the latent heat stores require a special heat-exchange geometry with a view to maintain an effective heat input in the course of the melting process, or to maintain a sufficiently high rate of heat recovery during solidification, respectively.

With a heat store to be applied for the preheating of the engine prior to starting, it is especially important that the recovery of the stored heat, and consequently, the rate of heating the engine should not be limited by the thermal resistance within the heat-storage substances. Since only 8-10 minutes can be taken up by heating up the engine prior to starting. In case of a longer preheating time, the amount of heat emitted into the environment will considerably increase, and in addition, it is more advantageous also with respect to the operation of a preheat-time if only a few minutes precedes the action of starting.

With a view of achieving those said above, the establishment of the most appropriate engine-preheat system, the most appropriate latent heat geometry, and within the framework of this, the optimal location of the storage material are set as a target in this paper.

2. Comparison between the different heat-storage systems applicable to the preheating of engines

With the heat-storage systems utilizing the heat of the exhaust gases, the heat-storage medium is heated up by the hot exhaust gases leaving the engine in operation.

The engine cooled down badly in a vehicle out-of-operation for more hours can be heated up through the cooling-water system of the engine by

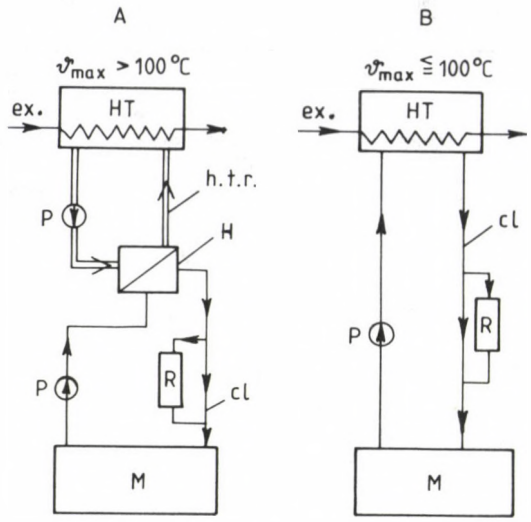

Fig. 1. Heat-storage engine preheating system
(HT — Heat store, H — heat exchanger, M — motor, P — pump, R — radiator, cl — coolant of the engine, h.t.r. — heat transmission liquid, ex. — exhaust gas)

means of the thermal energy recovered from the isolated heat store prior to restarting /1/.

Depending on the temperature level of the heat storage, the heat store can be coupled to the cooling-water system of the engine either directly or indirectly, above a storage temperature of 100 ^{o}C. In Fig. 1, the schematic diagram of two heat-storage engine-preheat systems of different layout are represented.

With system "A", the storage of heat takes place at a temperature above 100 ^{o}C.

A heat-exchanger should be inserted between the heat store and the water-circuit of the engine, and the energy stored can be extracted from the heat store by means of heat-transfer medium.

With system "B", where the maximum temperature of the heat store does not exceed 100 ^{o}C, the heat store can be connected directly to the water-circuit of the engine. During the preheating of the engine, the coolant is circulated by a water-pump operated by a storage-battery, and so the stored heat is delivered directly from the heat store into the engine.

Both those variants enable the simultaneous charging and discharging of the heat store. In this way, it becomes feasible to utilize the energy recovered continuously from the exhaust gases during the operation of the vehicle for heating it through the heat store inserted.

Table 1. Characteristics of heat-storage materials

Latent heat-storage materials				
Denomination	Temperature of phase-change	Phase-change heat kJ/kg	Density kg/m^3 Solid	Liquid
KOH-NaOH	180	230	2100	2000
LiCI-$LiNO_3$	184	259	1850	1700
KNO_3-$NaNO_3$	142	176	2000	1890
α-Naftol	95	163	1160	1150
$Ba(OH)_2 \cdot 8H_2O$	78	275	2100	1800
Sensible heat-storage material				
Frost-resisting coolant	C ~ 3.8 kJ/kg			
Heat-resisting oil	C ~ 2.1 kJ/kg			

The temperature level of the heat store is basically determined by the heat-storage substance applied. With variant "A", only the latent heat-storage substances found in the medium temperature range and having a melting temperature of 100-200 ^{o}C can be generally applied. With variant "B", only the latent heat-storage substances found in the lower temperature range and having a melting temperature of 70-100 ^{o}C, or the cooling-water itself as a sensible heat-storage substance can also be applied in the capacity of a heat-storage medium.

Table 1 contains the melting temperature, the phase-change heat, etc. of the phase-change heat-storage materials (PCM) examined. The heat-exchange geometry of the heat store, and the mode of location of the storage material are substantially influenced by the physical properties of the heat-storage material to be applied.

Various heat-storage constructions were developed with the use of the heat-storage substances included in Table 1, and their thermal behaviour was examined partly with the help of mathematical models, and partly experimentally. With the purpose of selecting the optimal engine-preheat system and the heat-storage material to be applied, the following were investigated:

- thermal, physical and chemical properties of the heat-storage material (e.g. melting temperature, heat of fusion, thermal conductance, reversibility of the crystallization processes, stability of the storage medium, etc.),
- particular limits imposed to the applicability of the heat-storage substances (e.g. chemical instability due to local overheating, considerable

overpressure due to the overheating of the medium positioned in the closed system),

- thermal capacity related to the unit-weight and unit-volume of the entire heat-storage system,
- efficiency of heat recovery, the available rate of engine preheat,
- sophisticated character of the system's layout,
- the cost per unit of the heat-storage material, the expected total cost of the system.

As it can be seen from the comparison of the two variants, variant "B" seems to be the more favourable one. From among the latent heat-storage substances of low temperature, barium hydroxide octahydrate shows the highest phase change energy. By applying it, the highest specific storage capacity can be achieved with respect to the weight and volume of the entire heat-storage system. While the most dynamic engine-preheat process can be achieved with the use of the sensible-heat hot water heat store containing anti-freeze compound. The cost of the two systems is nearly identical.

With the application of a hot water heat store built into buses, there were already favourable operational experiences obtained to solve the problems connected with cold starting of diesel engines /2, 3/.

With the favourable dynamic property of the hot water heat-storage system used for preheating the engine retained, the specific weight and volume of the heat store can be reduced with the help of developing the so-called hybrid heat store, which equally contains both latent and sensible heat-storage substances.

3. Development of hybrid heat stores

The latent heat-storage material: barium hydroxide octahydrate to be applied will be melted at a temperature of 78 ^{o}C under the influence of heat input, and the molt can be heated further on up to 95-100 ^{o}C. At a temperature above it, the chemical transformation of the heat-storage material, and as a consequence, a considerable reduction in the storage capacity should be reckoned with.

Therefore, barium hydroxide must not get into a direct thermal contact with the exhaust gases having an average temperature of 300-370 ^{o}C. With the construction of the hybrid heat store represented in Fig. 2, this problem can be avoided in a way that the exhaust gases are heating the water con-

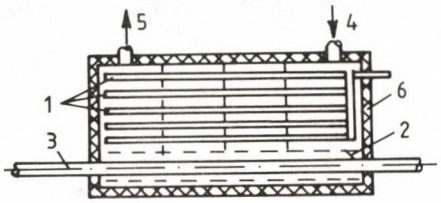

Fig. 2. Layout of a hybrid heat store
(1 — latent material PCM in closed tube systems, 2 — anti-freeze liquid (coolant), 3 — exhaust gases from the engine, 4 — coolant leaving the engine, 5 — coolant flowing towards the engine, 6 — insulation)

tained in the store (anti-freeze compound). Barium hydroxide closed in the tubes is positioned within the water-space, and consequently, it can get into thermal contact only with the water surrounding it.

If the temperature of water, under the influence of heat input, exceeds the melting temperature 78 ^{o}C of the latent substance, then the melting process of the latent substance will get going, and the heat will be stored at a temperature of 78 ^{o}C in the form of phase-change energy. The phase-change heat of the latent substance can be recovered only if the temperature of the surrounding water is reduced under 78 ^{o}C. In this case, water absorbs the heat released during the crystallization process of the latent substance. The latent substance is within a closed system in a static state, and under thermal influence it changes its temperature and phase, respectively. With the development of the so-called "passive" latent heat store of this kind, the poor thermal conductivity of the storage material should be taken into consideration. The latent substances should be positioned and distributed into smaller units, and the required storage capacity can be formed through the connection of those units. With this in view, several examinations were carried out to make use of the latent heat-storage substances in the utilization of solar energy /4, 5/. In addition, the development of special heat-exchange geometries was devised, too, with the aim of reducing the considerable thermal resistance encountered especially during the process of solidification, e.g. with the use of inner fins /6, 7/. The utilization of the stored heat for preheating the engines raises an additional special requirement exerting influence upon the layout of the heat store. A relatively longer period of time is available for charging the heat store. On the contrary, the process of discharging the heat store, i.e. the recovery of heat should take place at a very rapid rate taking only 8-10 minutes. Furthermore, it should be taken into consideration that the heat-

store application involves the increase in the weight of the vehicle at the expense of useful load, therefore the minimization of the weight should be an important aspect when latent substances are used. In order to meet those requirements, we should have a thorough knowledge of the heat-transfer process occurring during the phase-change in latent substances.

4. Examination of the unsteady-state heat-transfer process of latent heat-storage substances

4.1. Theoretical examination of the solidification process with cylindrical geometry

Melting and solidification processes of latent heat-storage substances are included within the scope of unsteady-state heat transfer, and even within this, it plays a special role since the process of phase-change involves either the process of energy absorption or the release of energy. Melting and solidification processes differ from each other only in the sign of the energy in question, since for the melting process heat input is required, while during solidification, energy is released. Consequently, when examining the phase-change process at the first approach, it is sufficient to be confined to the process of solidification only, so much the more because with the given problem, the process of heat recovery seems more critical. The process of the unsteady-state heat transfer is characterized by the spatial variation of the solid-liquid phase boundary. When examining the process, the main task is to determine the position of the phase-boundary as a function of time, and all the other characteristics, e.g. the temperature distribution, the transmitted heat, etc. depend on the former. The solution of the problem is aggravated by the non-linear boundary condition describing the heat-flux of the phase-boundary.

Most of the examinations performed so far and dealing with the analytical treatment of the solidification problem are based on the so-called Neumannian solution. This applies only in case the temperature of the external surface of the solidified layer remains unchanged, but this holds only in the case of infinitely large heat-transmission coefficient k. The Neumannian solution cannot be applied to the majority of solidification problems occurring in practice since the wall-temperature generally changes with the time, and there are only a few special cases to which an exact analytical solution can be given /8/.

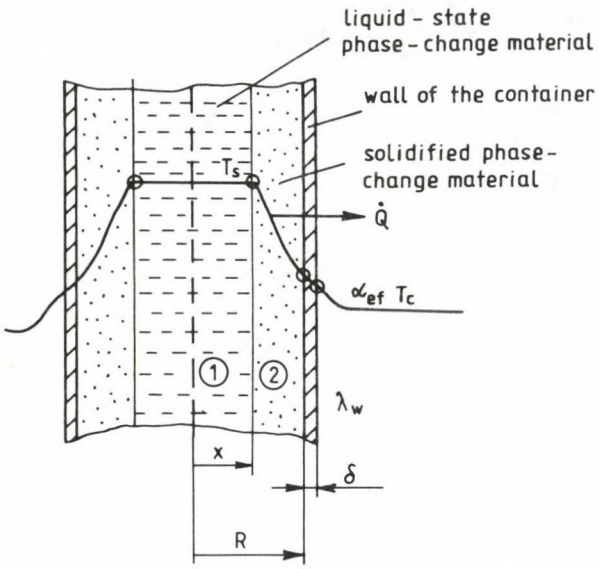

Fig. 3. Solidification of phase-change material (PCM)

In practice, however, in most cases it is not the detailed temperature range which is of interest, but only the partial or full solidification time of the material. The approximate solidification time can be predicted in a very simple manner if the enthalpy change of the layer already solidified is neglected in comparison to the enthalpy change encountered with the process of phase change /9/.

In Fig. 3 the schematic representation of the solidification process of the phase-change material contained in a cylindrical vessel is shown. It is assumed that the total quantity of the liquid indicated by index 1 was at a phase-change temperature T_s already at the initial solidification process. This assumption excludes the gravitational flow within the liquid storage material, or the heat convection between the phases along the solidification front, respectively. Index 2 symbolizes the solid phase. The cylinder is surrounded by coolant of temperature T_c. The condition for the start of the solidification process is that $T_c < T_s$. There is a temperature difference between the coolant and the vessel, the magnitude of which depends on heat-exchange coefficient α_{ex} of the coolant. Even within the vessel-wall, there occurs a temperature gradient, which depends on the thickness δ of the wall, and heat-conduction coefficient λ_w. The position of the solidification front is indicated by local-coordinate x. In the fol-

lowing, with t symbolizing the time, the approximate value of the heat-flux occurring during solidification will be on the basis of energy balance:

$$- \dot{Q} \approx \rho_1 \cdot \Delta i_s \frac{dV_1(x)}{dx} \cdot \frac{dx}{dt} \tag{1}$$

where Δi_s is the specific enthalpy change occurring during phase-change, $dV_1(x)$ indicates the volumetric change of the liquid, dx symbolizes the displacement of the solidification front, and $\frac{dx}{dt}$ is the rate of progression of the solidification front. As it was mentioned before, the enthalpy-change of layer 2 can be neglected, since $c_{p_2}(T_s - T_c) \ll \Delta i_s$. It can be assumed that in the solid layer, the steady-state temperature profile sets in in each point of time. Then, heat-flux Q can be given as follows:

$$\dot{Q} = k \cdot A (T_s - T_c) \tag{2}$$

Heat transmission coefficient k will be:

$$\frac{1}{k} = \frac{1}{\alpha_{in}} + \frac{\delta}{\lambda_w} + \frac{1}{\alpha_{ex}} \tag{3}$$

or

$$\frac{1}{k} = \frac{1}{\alpha_{in}(x)} + \frac{1}{k_{ex}} \tag{4}$$

where k_{ex} is the external heat-transmission coefficient.

Thermal resistance $\frac{1}{\alpha_{in}(x)}$ within the internal cylindrical shell, with the assumption of a steady-state temperature profile and with the thermal resistance of the solid layer taken exclusively into consideration, will be:

$$\frac{1}{\alpha_{in}(x)} = \frac{R}{\lambda_2} \cdot \ln \left(\frac{R}{x}\right) \tag{5}$$

For the further treatment of the solidification problem and the determination of progression rate dx/dt of the solidification front, it is expedient to reduce the mathematical equations to a dimensionless form. For this purpose, the following dimensionless characteristics will be introduced:

ξ -- dimensionless local co-ordinate

$$\xi \equiv \frac{x}{R}, \tag{6}$$

Biot-number:

$$Bi \equiv \frac{k_{ex} \cdot R}{\lambda_2} \tag{7}$$

phase change coefficient Ph

$$Ph \equiv \frac{\rho_1 \Delta i_s}{\rho_2 \cdot c_{p2} (T_s - T_c)} \tag{8}$$

dimensionless time (Fourier-number):

$$\tau_e \equiv \frac{a_2 \cdot t}{R_2} \equiv \frac{\lambda_2 \, t}{\rho_2 \, c_{p2} \, R^2} \tag{9}$$

$\frac{1}{Nu(\xi)}$ dimensionless internal thermal resistance for cylindrical geometry with the use of relationship (5) will be:

$$\frac{1}{Nu(\xi)} = - \ln \xi \tag{10}$$

From equations /1--5/, the following relationship is yielded for the motion of the solidification front with the use of dimensionless characteristics:

$$1 + Ph \left(\frac{1}{Bi} + \frac{1}{Nu(\xi)} \right)_{\xi} \cdot \frac{d\xi}{d\tau} = 0 \tag{11}$$

With the solution of differential equation /11/ between limits: $\xi = 1$ representing the wall of the cylinder, and $\xi = \frac{x}{R}$ representing the instantaneous position of the solidification front, the following are yielded for the dimensionless theoretical solidification time:

$$\tau_{emin} = \frac{Ph}{Bi} \left[\frac{1}{2} + \frac{\xi^2}{2} \right] + Ph \left[\frac{1}{4} + \frac{\xi^2}{4} (2 \ln \xi - 1) \right] \tag{12}$$

At the cylinder wall ($\xi = 1$), the solidification time: $\tau_e = 0$. In the centre of the cylinder ($\xi = 0$), the dimensionless theoretical solidification time will be:

$$\tau_{emin} = \frac{Ph}{2} \left(\frac{1}{2} + \frac{1}{Bi} \right) \tag{13}$$

Owing to the neglection of the enthalpy-change within the solidified layer, equations /12, 13/ will provide the required minimal solidification time. Actual solidification time τ_e exceeds this minimal value τ_{emin} determined theoretically all the more, the smaller the phase-change coefficient is, and the larger the Biot-number is. Ratio $\varepsilon = \tau_e / \tau_{emin}$ can be given with the help of the curves determined numerically by Tao /10/. The diagram shows the required value for cylindrical geometry as a function of Biot-number, and shows this value as the parameter of the reciprocal of the phase-change coefficient.

4.2. Comparison between the function describing the solidification time and the results measured experimentally

The full process of the crystallization of latent heat-storage substances at a constant temperature takes place only in an ideal case with some special substances. In the majority of cases, the liquid is subcooled below the temperature of melting prior to the initial crystallization process, or else crystallization, i.e. the solidification of the liquid is initiated only subsequent to subcooling. This phenomenon can be reduced with the use of the so-called core-forming additives, or else by local subcooling /11/. The determination of the appropriate additives is the task of chemical technology.

The phase-change process is also influenced by the convective effects occurring in the liquid heat-storage substances. In the molt, buoyant force and gravitational flow arise under the influence of the temperature difference, which results in convective heat transfer at the solid-liquid interface. Depending on the extent of heat convection, the heat-transfer process of the latent material deviates from the non-steady-state heat-transfer process requiring pure heat convection, as it was determined in the foregoing, and this, in turn, exerts an influence on the phase-change time. The effect of convection presents itself in different ways during the melting or the solidification, respectively, and it also depends on the mode of locating the heat-storage material. During melting, a considerable convection should be reckoned with in each case. Although, at the initial phase of melting, heat conduction has a decisive role, but with the progression of melting, the convective effects are more and more increasing, and this, in turn, involves the acceleration of the melting process /12/.

Table 2. Thermal and physical characteristics of barium hydroxide

Composition:	$Ba(OH)_2 \cdot 8\ H_2O$ 95 vol%
	H_2O 4 ~ 5 vol%
Different additives	~ 1 vol%
Phase-change heat /16/	$\Delta i_s = 275$ kJ/kg
Temperature of phase-change /16/	$T_s = 78$ °C
Density of liquid phase at temperature 80 °C	$\rho_1 = 1800$ kg/m^3
Density of the solid phase /17/	$\rho_2 = 2100$ kg/m^3
Thermal conductance of the solid phase	$\lambda_2 \sim 1.18$ W/mK
Specific heat of the solid phase	$c_{p2} \approx 1.047$ kJ/kg, K

During the solidification of the phase-change material, the magnitude of convection depends also upon the extent of overheating the liquid. The experiments performed for the sake of examining the solidification of the liquid surrounding a cooled flat plate or cylindrical surface show that the natural flow developing in the overheated liquid shows down the rate of freezing /13/. When the solidification of a heat-storage material located in a horizontal tube is examined, it can be seen that the effect of natural convection is smaller, and it takes its effect only at the initial phase of solidification. The experiments carried out with the help of various latent materials resulted in the statement that the effect of convection can be neglected even in the case of an overheated liquid, inasmuch the Stephan-number is: $Ste = c_{p2}(T_s - T_c)/\Delta i_s < 1$ /14/.

In the course of heat-flux measurement, experiments performed with the help of naphtalene of a very poor thermal conductivity as located in a horizontal cylindrical tube, Japanese researchers pointed out that during the process of solidification, the heat transfer within the tube resulted almost entirely from heat conduction /15/.

Phase-change involves volumetric change, and as a consequence, hollow cavities are formed in the solid material due to shrinkage, and this can slow down the process of solidification to a considerable extent.

For checking those effects, the experimental examination of the phase-change process of barium hydroxide octahydrate is required to apply, and the comparison between the experimental data and the theoretical predictions is necessitated. Table 2 contains the physical and thermal characteristics of the phase-change material.

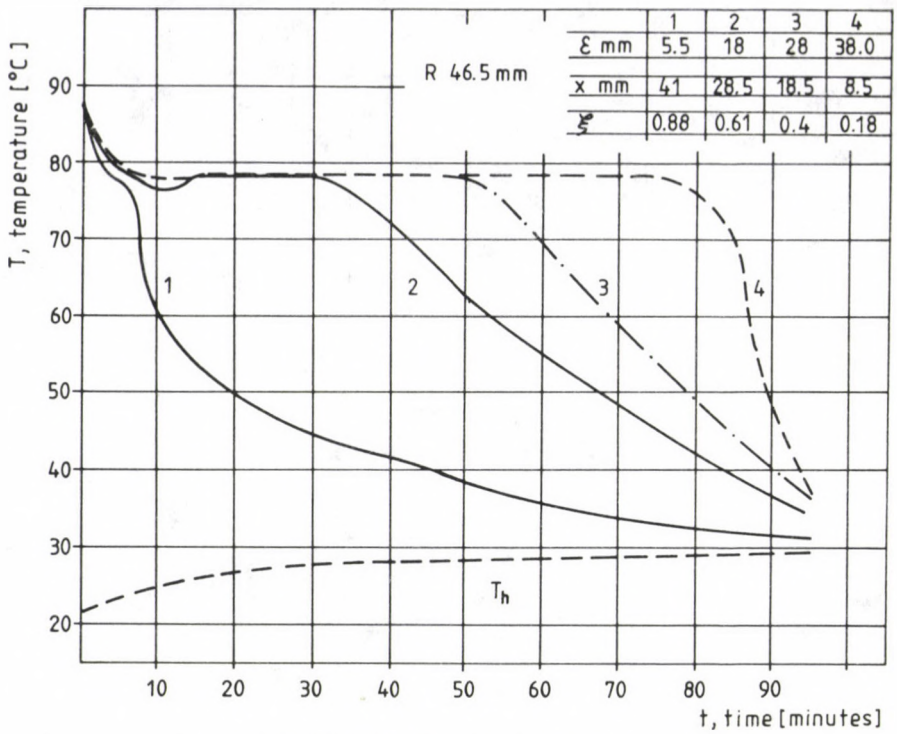

Fig. 4. Solidification diagrams of barium hydroxide, PCM
(— Layer thickness)

For experiments, barium, hydroxide located into a closed cylindrical vessel of dimensions Ø 46.5 x 100 mm was overheated in a water-bath of 95 °C. Afterwards, it was cooled down in a water-bath of 25 °C, and under such circumstances, the solidification times were examined. The temperature of the heat-storage material was sensed in four points along the radius.

In Fig. 4, the typical temperature variation curves, which are characteristic of barium hydroxide octahydrate as a latent material, are represented, where the subcooling of the liquid can be observed well. Since barium hydroxide also contains a core-forming additive, the subcooling was only of some °C. In temperature-measuring point 1 closest to the wall, no solidification section of constant temperature could be observed due to rapid cooling. However, a little way off the wall, the constant temperature of the phase-change could be measured distinctly.

Solidification time was determined with the consideration of $\pm$ 2 °C range of the phase-change temperature, that is the time during which the liquid phase of 80 °C turns into a solid phase of 76 °C. With the use of the

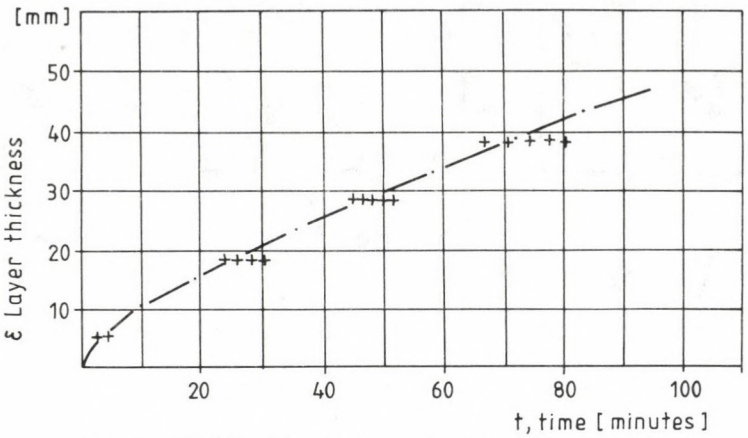

Fig. 5. Solidification time as a function of layer thickness

results obtained in the course of more series of measurements, in Fig. 5 the solidification times defined in the way described above are represented as a function of the thickness of the solidified layer.

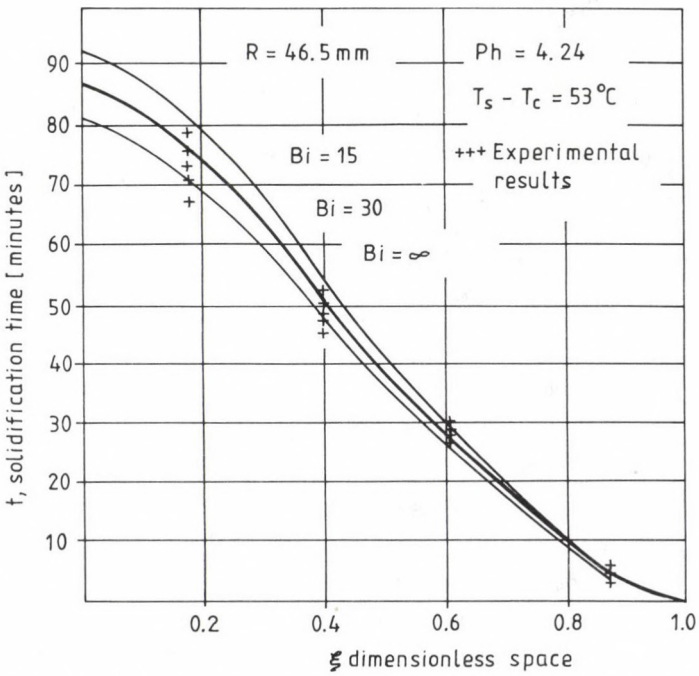

Fig. 6. Solidification time of barium hydroxide as a function of dimensionless space

In Fig. 6, the theoretical solidification time curves of $Ba(OH)_2$ 8 H_2O are shown as a function of dimensionless space at different Biot-numbers with the use of relationships (9) and (12). In the course of experiments, Bi was about Bi $\sim$ 30.

When the times measured experimentally are compared to curves Bi = 30, it can be stated that at the initial phase of solidification, they are somewhat above the theoretical value. This fact can be explained by the initial overheating of the material and the convection due to the vertical position of experimental tube. With the progression of the solidification front, the measured solidification times fall somewhat below the theoretical curve where Bi = 30. The reason for it is that about 5% water was added subsequently to pure $Ba(OH)_2$ 8 H_2O. Without any additional water, barium hydroxide is melting incongruently, the substance is disintegrated, and the phase-change heat is considerably reduced /18/. The larger the additional water-volume is, the fewer problems arise concerning the constancy of charging and discharging cycles, and in this way, the disintegration of the substance can be avoided, however, the storage capacity will become smaller due to water content. The congruent melting requires at least 4% additional water. In the course of experiments, the disintegration of the substance was prevented by providing additional water content, nevertheless the storage capacity was reduced by 5%, and as a consequence, the solidification time also became shorter.

However, the deviation of the theoretical curve from the measured values is not considerable. It can be stated that function (12) based upon pure heat conduction describes the solidification process of barium hydroxide adequately from qualitative point of view, and therefore, in the following, it can be applied to the determination of the optimal dimensions of the tubes used for locating latent substances in them.

4.3. Determination of the optimal tube radius

For the determination of tube sizes used for locating latent substances, such a condition should be taken into consideration that the stored heat should be recovered relatively quickly, i.e. within 8 minutes, and besides, the minimal specific weight should be possibly achieved. For this purpose, the heat-flux encountered during the solidification process of the latent heat-storage material should be examined, which is varying as a function of the solidification front.

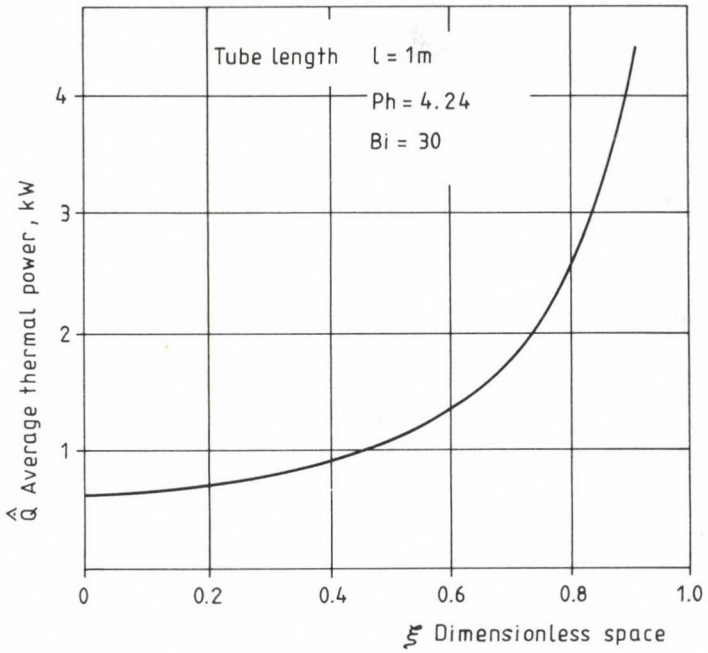

Fig. 7. Average thermal power occurring during solidification

The heat transferred by the solidified substance in a tube of length ℓ will be:

$$dQ = \rho_1 \cdot \Delta i_s \cdot 2 \cdot \pi \cdot x \cdot dx \cdot \ell \tag{14}$$

With relationship (14) integrated between limits x and R, and with introduced dimensionless coefficient ξ applied, the following is yielded:

$$Q(R, \xi) = \rho_1 \Delta i_s \pi R^2 (1 - \xi)^2 \cdot \ell \tag{15}$$

From relationships (8), (9) and (12), the solidification time will be:

$$t(R, \xi) = \frac{\rho_1 \Delta i_s \varepsilon R^2}{2 \lambda_2 (T_s - T_c)} \cdot \left[\frac{1}{Bi} - \frac{\xi^2}{2Bi} + \frac{1}{2} + \frac{\xi^2}{2} (2 \cdot \ln \xi - 1) \right] \tag{16}$$

The average heat-flux will be yielded as the quotient of relationships (15) and (16) as far as dimensionless spot ξ is reached.

The variation of function $\dot{Q}(\xi) = Q(R, \xi)/t(R, \xi)$ for the barium hydroxide contained in a tube of unit length is represented in Fig. 7. Proceeding from the jacket of the cylinder ($\xi = 1$) towards the centre of it ($\xi = 0$), the average heat emission rate is decreasing in a very intensive way, i.e. the average thermal power is decreasing with the progression of the solidification front.

When the process of solidification has been completed, the average thermal power with respect to the total solidification time can be determined by the limit value ($\xi = 0$) of the function (in Fig. 7 ξ = the value pertaining to 0):

$$\hat{\dot{Q}}(\xi = 0) = \frac{2\pi\lambda_2(T_s - T_c)}{\varepsilon\left(\frac{1}{2} + \frac{1}{Bi}\right)} \tag{17}$$

The variation of function $\hat{\dot{Q}}$, or its limit value determined by relationship (17) is independent from tube radius R, and as a consequence, the examination of the heat-flux will not result in an optimal tube radius.

In the following, it will be examined to what extent the specific storage capacity will be influenced by the size of the tubes used for locating the latent heat storage substances in them.

The amount of the heat transferred during the final solidification of the latent heat-storage material of mass m_{lat} will be:

$$Q_t \approx m_{lat} \cdot \Delta i_s = R^2 \pi \rho_1 \cdot \Delta i_s \cdot n \cdot \ell \tag{18}$$

where n is the number of tube-stores. (The enthalpy-change resulting from the already solidified and cooled layers, as well as from the cooling of tubes was neglected.) The joint mass of the latent storage materials and the tubes enveloping them will be:

$$m_t = n \cdot \ell \cdot \pi \left\{R^2 \rho_1 + \left[(R + s)^2 - R^2\right] \rho_{met}\right\} \tag{19}$$

where s is the thickness of the tube wall.

From relationships (18) and (19), the specific storage capacity related to the total mass will be:

$$\frac{Q_t}{m_t} \approx \frac{\Delta i_s}{1 + \left[\left(\frac{R + s}{R}\right)^2 - 1\right]\frac{\rho_{met}}{\rho_1}} = f_1(R) \tag{20}$$

The value of function $f_1(R)$ is increasing proportionally with the increase of R, its limit value is: Δi_s. It is more advantageous to use a tube of greater diameter and smaller wall thickness.

The total solidification time of the latent heat-storage material is a function of the tube radius, the material characteristics and the Biot-number.

From relationships (8), (9) and (13), the following will be yielded:

$$t(R) = \frac{\rho_1 \Delta i_s \varepsilon R^2 \left(\frac{1}{2} + \frac{1}{Bi}\right)}{2 \cdot \lambda_2 (T_s - T_c)} \tag{21}$$

Function t(R) is a monotonic increasing one, the solidification time is increasing proportionally with the square of the radius. Let it be examined how the average thermal power gained from the latent heat-storage material of mass m_{lat} will be changing. On the basis of relationships (18) and (21):

$$\frac{Qt}{t(R)} = \frac{2 \cdot \lambda_2 (T_s - T_c) \cdot m_{lat}}{\rho_1 \varepsilon \left(\frac{1}{2} + \frac{1}{Bi}\right) \cdot R^2} = f_2(R) \tag{22}$$

Providing the environmental effects and the material characteristics are constant,

$$f_2(R) = \frac{c \cdot m_{lat}}{R^2}$$

i.e. the value of function $f_2(R)$ in case of increasing radius will decrease proportionally with R^2. A greater average thermal power will be yielded if mass m_{lat} is located in tubes of smaller diameter. The product of the required tube-number and tube-length will be:

$$n \cdot \ell \cdot (R) = \frac{m_{lat}}{\rho_1 R^2 \pi} \tag{23}$$

In Fig. 8, the variation of functions t(R), $f_1(R)$, $f_2(R)$ and $n.\ell(R)$ can be seen with barium hydroxide of a unit mass (m_{lat} = 1 kg), and tube length ℓ = 1 m.

According to the functions represented, barium hydroxide should be located in fewer tubes of greater radius with respect to the reduction of the

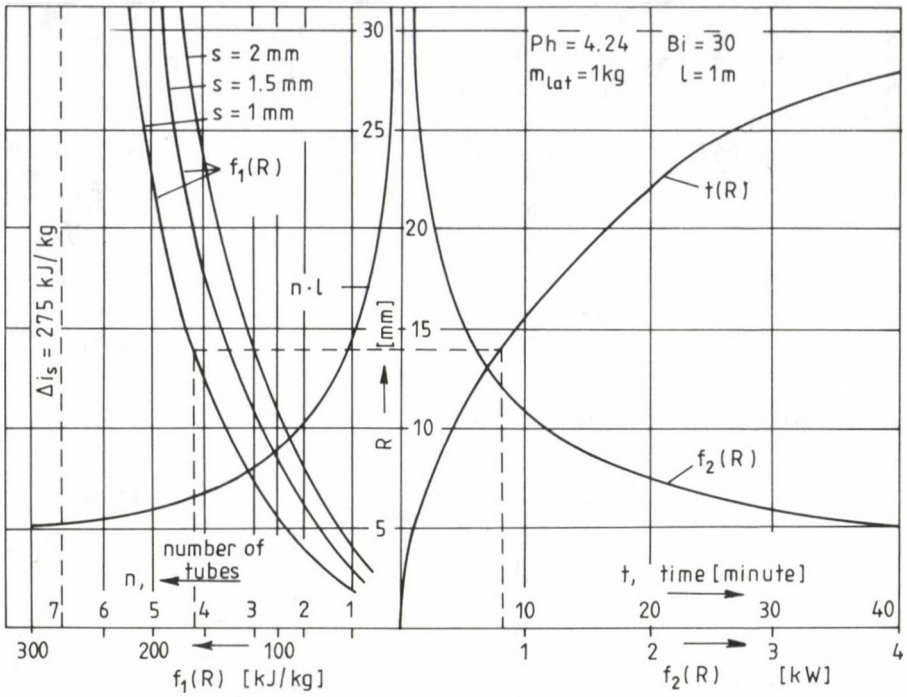

Fig. 8. Variation of function t(R), $f_1(R)$, $f_2(R)$, $n \cdot \ell(R)$ of barium hydroxide

total mass of the heat store, while it should be located in more tubes of smaller radius with respect to the quick heat recovery. When determining the optimal tube radius, the practical condition should be taken into account as a basis, that the recovery of the stored heat should take place within about 8 minutes for the preheating of a diesel-engine. This time will practically determine the tube radius to be applied, with R ~ 14 mm, and with wall thickness of 1 mm, the specific latent heat storage capacity related to the total mass will be ~165 kJ/kg.

5. Improvement of the heat-transfer process of latent substances with the use of metal-matrix structure

5.1. Experimental results

The poor thermal conductivity of the solid phase exerts a bad limiting influence upon the heat-flux developing during the solidification of latent

TUBE STORE			INSERT MATERIAL			
inward diameter	wall thickn.	tube length	size [mm] $l_1 \times l_2$		No. of fins n	Layout
D [mm]	s [mm]	l [mm]	I	II		
19.5	1	110	80 × 100	72 × 100	4	
26	1	110	158 × 100	143 × 100	6	
32	1	110	240 × 100	226 × 100	8	
38	1	110	296 × 100	294 × 100	8	
			0.25	0.4	Wire thickness d [mm]	
			1.2	2.5	Mesh spacing k [mm]	

Fig. 9. Geometric data of test-tubes and metal matrix structures applied

substances. With the reduction of the thermal resistance of solid layers, the heat-flux can be increased with the storage material characteristics unchanged, and as a consequence, the solidification time will decrease. Researchers have already dealt with success with the improvement of the heat transport taking place in paraffins /6/.

Thermal conductivity of paraffins is about five-eight times smaller than that of salt hydrate applied here. In order to improve the heat transport, different finned geometries, aluminium-cell structures and thin tape matrix (of explofoil type) were used, respectively. As a function of 2-10% volumetric ratio of metal structures, solidification rates higher by 4-7-times were obtained. It can be expected that with the examined heat-storage problem, too, the metal structures located into barium hydroxide will result in the reduction of solidification time, and as a consequence, the radius of the tube-store can be increased. During experiments, metal matrix structures forming special inward longitudinal fins made of wire-mesh screen texture were located into the heat-storage tubes of different diameter. The so-

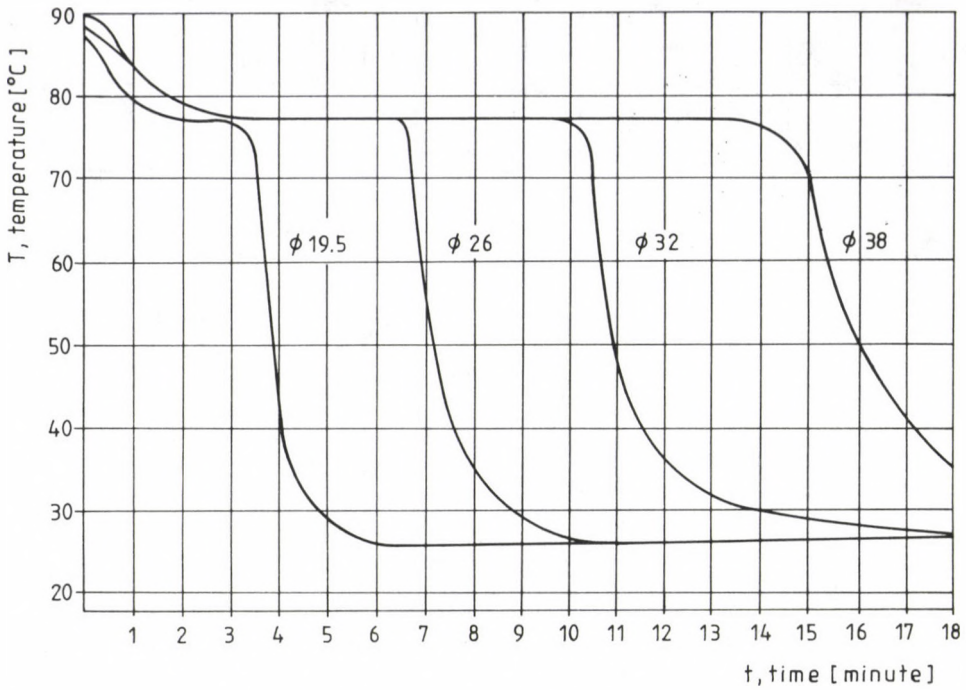

Fig. 10. Cooling curves without insert material

lidification time of the storage material was measured with the help of thermocouples positioned in the centre of the tube-store. The length of the tubes was selected for multiple value of the diameter, and as a consequence, it could be assumed that the solidification time in the point examined was not influenced by the heat-flux developed at both ends of the tubes. Two inserts of wire mesh screen of different spacing were used for the examinations, and besides, measurements even without inserts were performed with the aim of drawing comparison between the single solidification times. The dimension of the tube-stores and inserts used for the examinations, and the layout of the inward fins, respectively, formed from the latters are shown in Fig. 9. The layout of the structure was developed in a way that a fraction of the metal fins possibly approach the centre of the tube. With this in view, every other fin with the 8-fin layout projected as far as the centre, and the fins between those were taken shorter.

The tube-stores were charged with liquid barium hydroxide up to about 95% of their volume, then they were closed for the experiments.

For the solidification and melting processes to be examined, the closed tube-stores were put into a thermostat of the specified temperature.

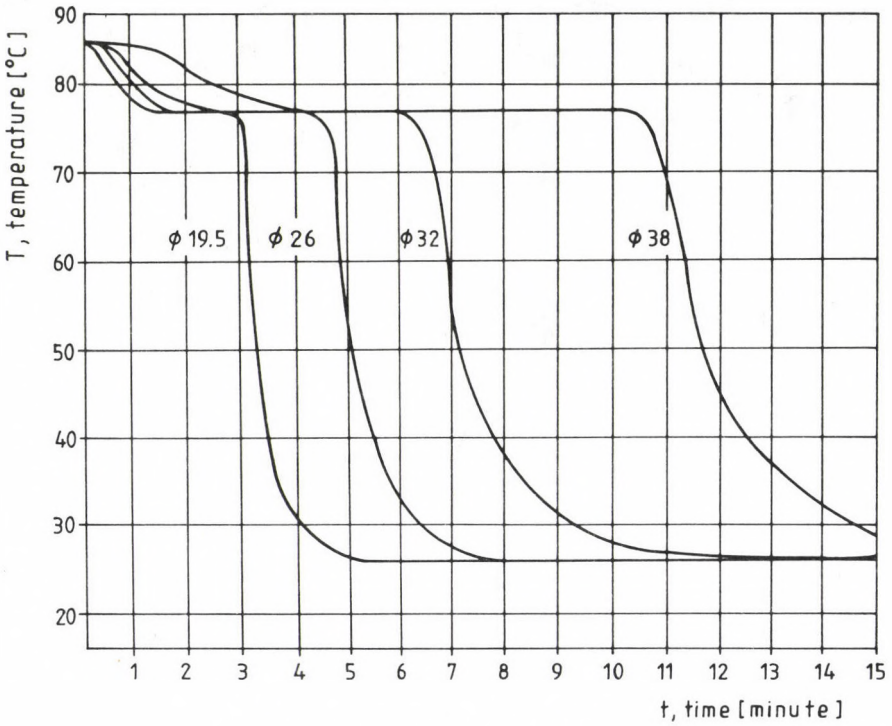

Fig. 11. Cooling curves of PCM with insert material I

In the course of the solidification process, the cooling water circumfluent the tubes was circulated at a very intensive rate for achieving a possibly better external heat transfer, or a possibly greater Biot-number. The arrangement of the tube was a horizontal one. In Fig. 10, the cooling curves measured with tubes of different diameter are represented without metal structures inserted. In Figs 11 and 12, the temperature variation is shown as a function of time in case of two different metal matrix structures applied.

In each case, the metal matrix structure reduced the crystallization time of the material.

The "denser" mesh screen made of thinner wire I resulted in a slower cooling process with the overheated liquid by retarding the motion of the liquid, consequently, the convective effects were reduced (Fig. 11), and a decisive heat conduction had developed even in the case of cooling the overheated liquid. This effect could not be observed with the thicker insert material II of "looser" mesh spacing (Fig. 12). The metal insert structure increased the cooling rate of the solidified phase. A tendency of opposite

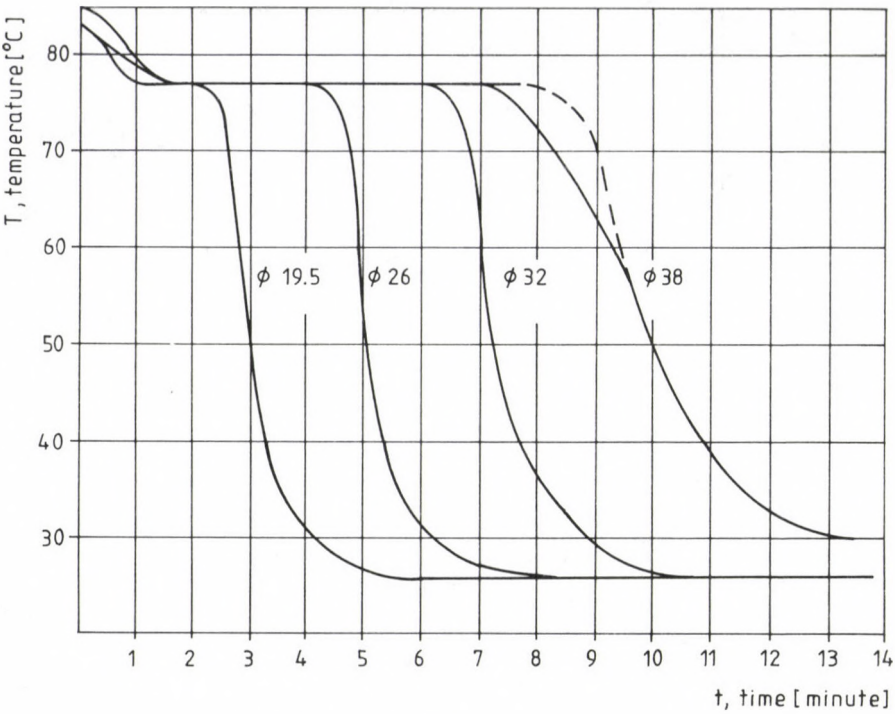

Fig. 12. Cooling curves of PCM with insert material II

character was observed with the tube of Ø 38 filled with insert material II. The reason for this assumedly was the fact that the material solidified earlier in the point of measurement in the tube centre than within the "interfin" spaces around it, and this, in turn, resulted in slower cooling of the solid central core. This phenomenon was visualized by the corrected cooling curve traced in a dashed line and was used for the determination of the solidification time. The time belonging to the $\pm$ 2% range of the 78 ^{O}C phase-change temperature was considered as the phase-change time (see point 4.2). Each series of measurement was repeated several times, and their average value was used for the determination of the solidification time for the total mass of material without any inserts, or with different metal matrix structures applied, respectively. In Fig. 13, the reduction of the average solidification time can be seen as a function of the volumetric ratio of the metal insert material, which reduction will be greater by 1.35-1.8-times with a volumetric ratio of 2-3% taken into consideration.

The result obtained in this way, and compared to the measurements of other researchers /6/ can be considered a favourable one because the thermal

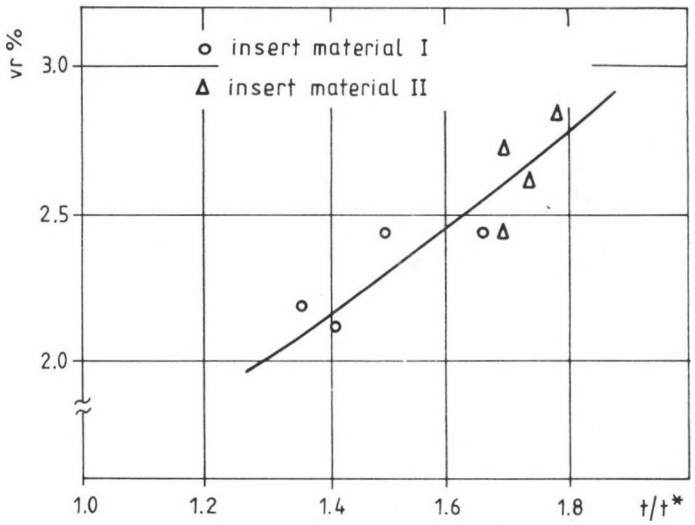

Fig. 13. Decrease in solidification time as a function of volumetric ratio of the metal material

conductivity of salt hydrate under examination is much better than that of the paraffins examined by the researchers, and consequently, the application of the metal structure results in an essentially smaller reduction in the solidification time. Insert material I, which is a mesh screen made of thinner wire, occupied a smaller volume but it decreased the solidification time to a lesser extent, while the application of the mesh screen made of thicker wire II involved a decrease of greater proportion in the solidification time.

5.2. Expression of measurement results by mathematical functions

The method described in point 4 is used for the mathematical simulation of the heat transfer taking place during the solidification of the phase-change material supplied with metal matrix insert. Essentially, the metal matrix structure changes the thermal resistance in the solid layer by its metal structure of lower thermal resistance through which a fraction of heat is transmitted into the external layers or the tube wall, respectively.

This phenomenon is decisively determined by the volumetric ratio of the metal structure and the thermal conductivity of the metal substance to be applied, but with an identical volumetric ratio, it is the mode of lo-

cating the metal structure, the thickness of wire, the spacing of the mesh wiring, etc. which play a role in this respect, too.

The precise consideration and prediction of the effects encounter unsolvable difficulties, therefore an approximate solution is applied. With an identical geometric arrangement, the possibility of drawing a good comparison is offerred in a way that instead of thermal conductivity λ_2 of the solid phase, the following equivalent heat conduction coefficient λ_2^* will be defined like this:

$$\lambda_2^* = \lambda_2 \frac{V_{lat}}{V_t} + \lambda_{met} \frac{V_{met}}{V_t} \cdot \delta \tag{24}$$

where using the notations of Fig. 9

$$\frac{V_{met}}{V_t} = \frac{2\, d^2\, \ell_1}{D^2\, k}$$

λ_{met} is the thermal conductivity of metal structures, and δ is the geometric factor depending on the mode of locating the metal structure (with thickness, spacing of mesh wiring, contact with the wall, number of fins, etc.). The metal mesh screen structure prevents still more the convective effect poor enough for other reasons, too, occurring at the interface of the liquid and solid phases, and in this way, pure heat conduction can be assumed. Under the influence of the metal insert structure, the shape of the solidification front will be changed, since the crystallization process is starting at the fin surfaces. Due to this fact, the mathematical description of the motion of the solidification front runs into difficulties, and differential equation (11) will not be suitable for that purpose. However, the total solidification time of the material can be determined with a good approximation under boundary condition $\xi = 0$ with the help of equivalent heat conduction coefficient (heat conductance) λ_2^* defined by relationship (24). The changed dimensionless time τ^*_{emin} will be on the basis of relationship (5):

$$\tau^*_{emin} = \frac{\lambda_2^* \cdot t^*}{\rho_2\, c_{p2}\, R^2} \tag{25}$$

or the changed Biot-number will be:

$$Bi^{*} = \frac{k_{ex} \cdot R}{\lambda_2^{*}} \tag{26}$$

From relationships (25), (26) and (13), as well as with the consideration of ratio $\varepsilon = {}^{\tau e^{*}}/_{\tau^{x}_{emin}}$, the solidification time of latent substance $t^{*}(R)$ of a metal matrix structure applied can be calculated similarly to relationship (21) as follows:

$$t^{*}(R) = \frac{\rho_1 \Delta i_s R^2 \left[\frac{1}{2} + \frac{1}{Bi^{x}}\right]}{2 \lambda_2^{*} (T_s - T_c)} \tag{27}$$

In the course of experiments, the coolant was circulated very intensively around the tubes containing latent substances, and as a result, a very high Biot-number was obtained, and so the value of 1/Bi did not exert any influence on the comparison between the individual measurements.

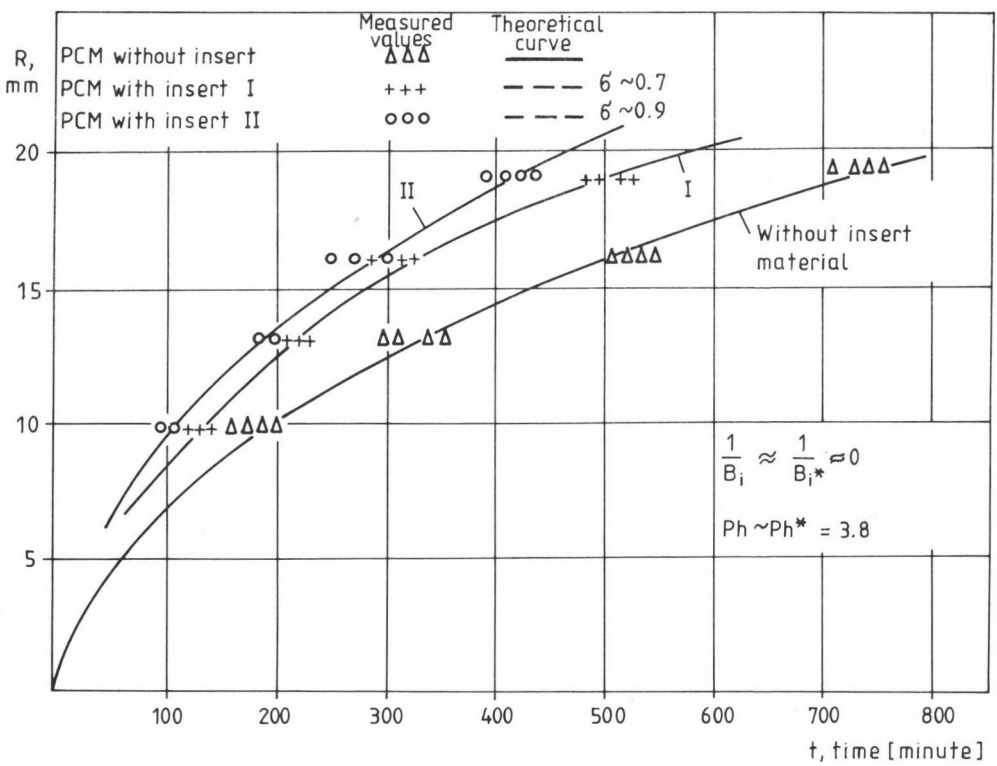

Fig. 14. Experimental and theoretical solidification times of PCM (barium-hydroxide) located in tube with insert material

In Fig. 14, the total solidification time of the latent substance measured experimentally is represented with tubes of different diameter in the three cases examined, i.e. without any material inserted, and with the use of two insert materials of different quality, respectively.

With the help of relationship (21), the theoretical solidification time of the latent substance without any insert material was determined taking into consideration the fact that, due to the excess water content of the latent substance, the phase-change heat is less by 5% according to the measurements than the value contained in Table 2. The values determined mathematically by function (21), and those measured experimentally coincide very well.

In case of applying different insert materials, the solidification time of the latent substance can be given by relationship (24), or (27), respectively, in a mathematical form. However, geometric factor δ occurring in relationship (24) is not known directly. On the basis of measurements performed with the help of metal matrix structure inserted into latent substances, researchers established that $t/t^{*} \approx \lambda_2/\lambda_2^{*}$ /6/. With the help of the measured solidification time, the value of δ can be calculated from relationships (24) and (27) with the assumption of this proportionality. In Fig. 15, the values of geometric factor δ determined in this way are represented. Independently of the volume occupied, insert material II made of thicker

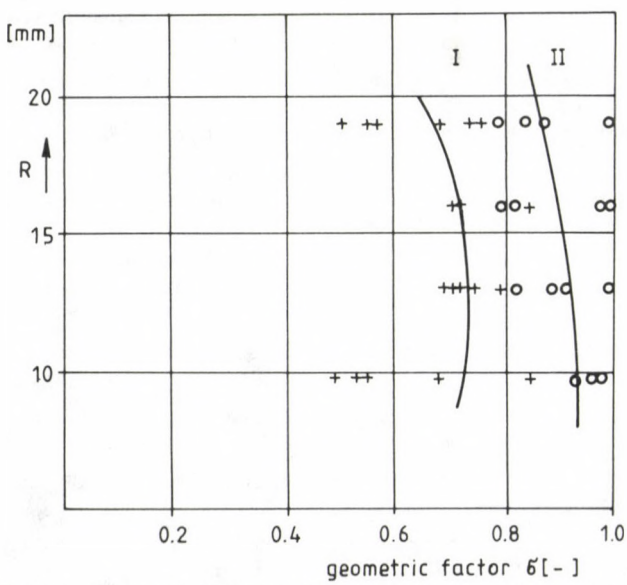

Fig. 15. Value of geometric factor δ with different metal insert structures

wire proved to be more effective. This fact harmonizes with the result experienced by researchers when examining fined geometries, where the increase of fin thickness resulted in the increase of the heat-flux during the solidification of latent substances /19/. With the metal matrix structures, in addition to the wore thickness, other geometric factors play an important role, too, e.g. the layout of the inward fin structure made of mesh wiring, the number of fins, the spacing of mesh wiring, etc. consequently, the values obtained for δ are valid only for the layout and the mesh screen type represented in Fig. 9 examined, here $\delta_I \sim 0.7$ and $\delta_{II} \sim 0.9$ can be assumed.

The function of solidification time determined by the values of geometric factor δ can be seen in Fig. 14, and it is in good agreement with the values measured.

The applied metal matrix structure improves the heat transfer process, as it was expected. In this way, the radius of the tube-store can be increased from 14 mm to 19 mm, and with the application of the insert material of type II, an unchanged solidification time and an identical average heat-flux is obtained, respectively.

REFERENCES

1. Utilization of waste heat of the engines of pay-load vehicles for the preheating and heating of the heat storage engines in buses. Research Report of the Institute of Vehicles Engineering at the Technical University, Budapest, 1986 (in Hungarian)

2. Kissné Hunyadi, I.: Heizung bzw. Vorheizung von Autobussen und Erleichterung des Kalstartes von Dieselmotoren unter Verwendung der in einem Wärmereservoir gespeicherte Energie der Auspuffgase. Technik des Fahrkonforts CSSR. Tatranska Lomnica, 1988, 59—67

3. Experimental results achieved in the vehicle heating and engine preheating system of hot water heat storage. Institute of Vehicles Engineering at the Technical University of Budapest. Research Report, 1988 (in Hungarian)

4. Van Gallen, E.: Experimental result of a latent heat storage system based on sodium acetate trihidrate in a stabilizing colloidal polymer matrix, tested as a component of a solar heating system (C. den Queden, ed.). Thermal Storage of Solar Energy, 147—156

5. Abhat, A. - Aboul-Enein, S. - Malatidis, N.A.: Heat-of-fusion Storage System for Solar Heating Application (C. den Queden, ed.). Thermal Storage of Solar Energy, 157—171

6. De Joung, A.G. - Hoogendoorn, C.J.: Improvement of heat transport in paraffins for latent heat storage systems (C. den Queden, ed.). Thermal Storage of Solar Energy, 123—133

7. Kissné Hunyadi, I.: A survey of latent heat stores. Energiagazdálkodás, XXIX, No. 10. (1988), 448—453 (in Hungarian)

8. Carslow, H.S. - Jaeger, I.C.: Conduction of heat in solids. Clarendon Press, Oxford, 1946 (1. edition, reprinted in 1960, 1962, 1965, 1967), p. 285

9. VDI-Wärmeatlas. 3. Auflage 1977. Ed. 11—13

10. Tao, L.C.: Generalized numerical solution of freezing a saluted liquid in cylinders and spheres. A.I.Ch.E-I.13. 1967, 1, pp. 165—169

11. Wolff, D.: Zur Auslegung eines Latentwärmespeichers mit Rippenrohren. Dortmund, 1980. Dissertation

12. Ho, C.-J. - Viskanta, R.: Heat transfer during inward melting in a horizontal tube. Int. J. Heat Mass Transfer, Vol. 27, No. 5. (1984), 705—716

13. Viskanta, R. - Bathelt, A.G. - Hale Jr., N.W.: Latent heat-of-fusion energy storage: Experiments on heat transfer during solid-liquid change. In Alternative Energy Sources III. Volume I. Solar Energy. Hamisphere Publ. Corp. Washington DC, 1983

14. Viskanta, R. - Gan, West Lafayette, G.: Inward solidification of a superheated liquid in a cooled horizontal tube: Wärme und Stoffübertragung 17. (1982), 39—46

15. Katayama, Kozo - Saito, Akio, etc.: Heat transfer characteristics of the latent heat thermal energy storage capsule. Solar Energie. Vol. 27, No. 2. (1984), 91—97

16. Wright, J.D.: The design and economics of direct-contact salt hydrate storage systems. 2nd World Congress of Chemical Engineering. Montreal, Canada, October 1981, 4—9

17. Krause, S. - Tamme, R.: Operation of a 25 kWh barium hydroxide latent heat storage unit in the power range 2-6 kW. DFVLR. Stuttgart, M.k.

18. Furbo, S.: Heat storage with incongruently melting salt hydrate as storage medium based on the extra water principle. Thermal Insulation Lab., Technical University of Denmark, Meddelelse Nr. 108. 1980

19. Aboul-Enein, S.: Wärmeübertragung in einem latentwärmespeicher mit berippten Ringspaltrohr-Wärmeaustauscher. Institut für Kernenergetik der Universität Stuttgart. Dissertation, 1982

Acta Technica Acad. Sci. Hung., 105(4), pp. 255—277 (1993)

A COMPUTER ORIENTED FORMULATION OF DYNAMICS FOR ROBOT MANIPULATORS

KÖVECSES, J.*

(Received: 29 January 1993)

In this paper, a method for the dynamic analysis of robot manipulators has been developed. The equations of motion are derived by using Appell's equations, stated in a very simple form. The resulting equations are an explicit set of closed form second-order highly non-linear and coupling differential equations, which can be used for dynamic computer simulation and the computation of the joint generalized forces. Differential relationships are presented in order to reduce the number of necessary computations. This paper contains a comparison of the computational complexity of some existing methods for deriving the equations of motion.

1. Introduction

In order to perform the dynamic simulation of a robot manipulator, it is necessary to derive the equations of motion describing the dynamic behaviour of a manipulator. At the present time, there are several methods for that purpose, such as the Lagrange—Euler method /6—11/, the Newton—Euler method /12—15/, the Kane's method /21—22/, the Appell's method /17—20/ and so on. Each method has its advantages and disadvantages. For example, the Newton—Euler method is very useful when inverse dynamics (computing joint torques/forces) is presented, but it is not suitable for the dynamic simulation (direct dynamics) of a robot manipulator. The Lagrange—Euler method is better for that purpose, but the structure of the Lagrange's equations demands many complex computations.

When deriving the equations of motion for a robot manipulator, the Appell's method /1/ may be very useful. (Remark: Gibbs published his results

*Kövecses, József, H-8200 Veszprém, Bartók B. u. 25, Hungary

Akadémiai Kiadó, Budapest

in 1879 considering holonomic systems, while Appell's investigations in 1899 includes nonholonomic constraints leading to the same expression, see /1/.)

Using Appell's equations to express a complete set of equations of motion requires little effort. In the case of rigid links, it is necessary to investigate only the second derivative of the 4x4 homogeneous transformation matrices with respect to time. The proposed formulation is suitable for the computation of dynamics of the general robot manipulators with either rotational or translational joints.

2. Formulation of kinematics

In order to describe the translational and rotational relationships between adjacent links of the robot manipulator, it is necessary to set up the local co-ordinate systems on the links according to the Hartenberg–Denavit representation /5/. The base reference frame is fixed on the base (i.e. link 0). The joints of the robot manipulator are the points of articulation between the links and are numbered so that joint i connects links (i-1) and i. An orthogonal co-ordinate system is fixed in link i as follows:

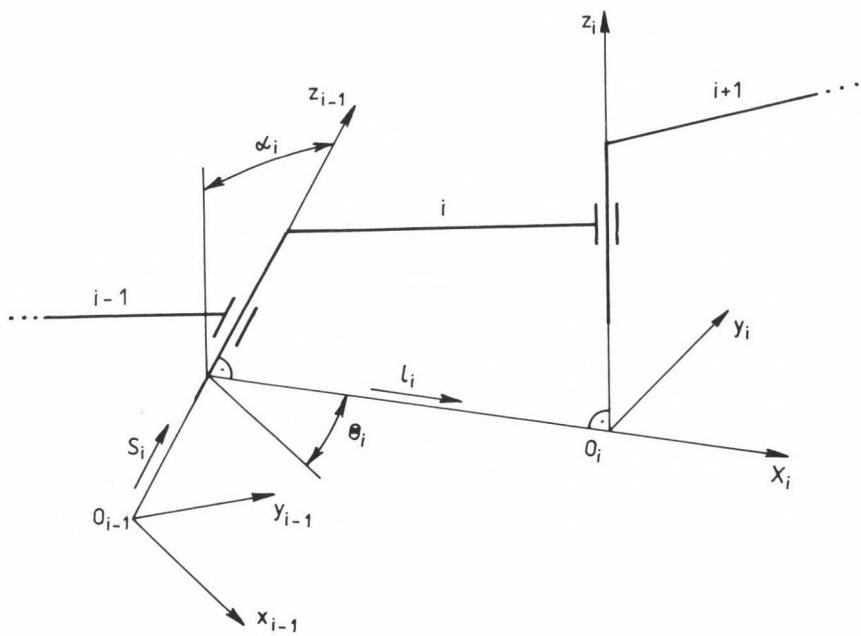

Fig. 1. Foundation of co-ordinate systems

z_i is directed along the axis of joint (i+1);

x_i lies along the common normal from z_{i-1} to z_i; and

y_i completes the right co-ordinate.

The relative position of two adjacent links is completely described by the following four parameters (shown in Fig. 1):

s_i -- distance between axes x_{i-1} and x_i measured along axis z_{i-1};

θ_i -- angle between axes x_{i-1} and x_i measured in the right-hand sense around axes z_{i-1};

α_i -- angle between axes z_{i-1} and z_i measured in the right-hand sense around axis x_i; and

l_i -- distance between the origins of the co-ordinate systems (i-1) and i measured along axis x_i ($l_i \geq 0$).

If the joint i is a rotational one, then θ_i is the joint variable; if the joint i is a translational one, then s_i is the joint variable. Symbol q_i will designate the variable for joint i (it would be s_i or θ_i).

Vector $\underline{q} = [q_1, q_2, \ldots, q_n]^T$ represents the generalized co-ordinates of the robot manipulator, and completely specifies the position (in the case of rigid links) where $[\,]^T$ denotes the transpose of $[\,]$.

Let ${}^{i-1}\underline{\underline{H}}_i$ be the 4x4 homogeneous transformation matrix from co-ordinate system i to (i-1), then

$$ {}^{i-1}\underline{\underline{H}}_i = \left[\begin{array}{c|c} {}^{i-1}\underline{\underline{h}}_i & {}^{i-1}\underline{p}_i \\ \hline \underline{0}^T & 1 \end{array}\right], \tag{1} $$

where ${}^{i-1}\underline{\underline{h}}_i$ represents the 3x3 rotation matrix relating to the orientation of co-ordinate systems (i-1) and i, and ${}^{i-1}\underline{p}_i$ represents a 3x1 position vector relating to the origin of co-ordinate systems (i-1) and i with respect to co-ordinate system (i-1) (denoting the upper index), and

$$ {}^{i-1}\underline{\underline{h}}_i = \begin{bmatrix} \cos\theta_i & -\cos\alpha_i \sin\theta_i & \sin\alpha_i \sin\theta_i \\ \sin\theta_i & \cos\alpha_i \cos\theta_i & -\sin\alpha_i \cos\theta_i \\ 0 & \sin\alpha_i & \cos\alpha_i \end{bmatrix} \tag{2} $$

and

$$ {}^{i-1}\underline{p}_i = [l_i \cos\theta_i \quad l_i \sin\theta_i \quad s_i]^T. \tag{3} $$

Let ${}^{i-1}\underline{\underline{H}}_k$ be the 4x4 homogeneous transformation matrix form co-ordinate system k to co-ordinate system (i-1), then

$$ {}^{i-1}\underline{\underline{H}}_k = \left[\begin{array}{c|c} {}^{i-1}\underline{\underline{h}}_k & {}^{i-1}\underline{p}_k \\ \hline \underline{0}^T & 1 \end{array}\right] = {}^{i-1}\underline{\underline{H}}_i \; {}^{i}\underline{\underline{H}}_{i+1} \cdots {}^{k-1}\underline{\underline{H}}_k , \tag{4} $$

where ${}^{i-1}\underline{\underline{h}}_k$ is the 3x3 rotation matrix from co-ordinate system k to co-ordinate system (i-1), and ${}^{i-1}\underline{p}_k$ is the 3x1 vector from the origin of co-ordinate system (i-1) to the origin of co-ordinate system k with respect to co-ordinate system (i-1). The transformation matrix ${}^{0}\underline{\underline{H}}_k$, which will be denoted by $\underline{\underline{H}}_k$, is the 4x4 homogeneous transformation matrix from co-ordinate system k to the base reference co-ordinate system, then

$$ \underline{\underline{H}}_k = \left[\begin{array}{c|c} & \\ \underline{\underline{h}}_k & \underline{p}_k \\ & \\ \hline \underline{0}^T & 1 \end{array}\right] = {}^{0}\underline{\underline{H}}_1 \; {}^{1}\underline{\underline{H}}_2 \cdots {}^{k-1}\underline{\underline{H}}_k . \tag{5} $$

If we define ${}^{i-1}\underline{\underline{h}}_{i-1} = \underline{\underline{E}}_3$ (the 3x3 identity matrix and ${}^{i-1}\underline{p}_{i-1} = \underline{0}$ (a 3x1 zero vector), then ${}^{i-1}\underline{\underline{h}}_k$ and ${}^{i-1}\underline{p}_k$ satisfy the backward recursive formulations

$$ {}^{i-1}\underline{\underline{h}}_k = {}^{i-1}\underline{\underline{h}}_{k-1} \; {}^{k-1}\underline{\underline{h}}_k \tag{6} $$

and

$$ {}^{i-1}\underline{p}_k = {}^{i-1}\underline{p}_{k-1} + {}^{i-1}\underline{\underline{h}}_{k-1} \; {}^{k-1}\underline{p}_k . \tag{7} $$

Since matrix ${}^{i-1}\underline{\underline{h}}_k$ is an orthonormal one, the inverse of ${}^{i-1}\underline{\underline{H}}_k$ can be written as

$$ ({}^{i-1}\underline{\underline{H}}_k)^{-1} = \left[\begin{array}{c|c} {}^{i-1}\underline{\underline{h}}_k^T & -{}^{i-1}\underline{\underline{h}}_k^T \; {}^{i-1}\underline{p}_k \\ \hline \underline{0}^T & 1 \end{array}\right] \tag{8} $$

where

$$ {}^{i-1}\underline{\underline{h}}_k^T = {}^{k-1}\underline{\underline{h}}_k^T \; {}^{k-2}\underline{\underline{h}}_{k-1}^T \cdots {}^{i-1}\underline{\underline{h}}_i^T . \tag{9} $$

Equations (1)–(9) will be used for deriving the following differential relationships. From (1)–(3), have

$$\frac{\partial {}^{i-1}\underline{\underline{H}}_i}{\partial q_i} \cong {}^{i-1}\underline{\underline{\Delta}}_i \; {}^{i-1}\underline{\underline{H}}_i , \tag{10}$$

where

$${}^{i-1}\underline{\underline{\Delta}}_i = \left[\begin{array}{cc} {}^{i-1}\underline{\underline{\delta}}_i & {}^{i-1}\underline{d}_i \\ \hline \underline{0}^T & 0 \end{array}\right] ; \tag{11}$$

$${}^{i-1}\underline{\delta}_i = \begin{cases} [0 \;\; 0 \;\; 1]^T, & \text{if joint } i \text{ is a rotational one,} \\ [0 \;\; 0 \;\; 0]^T, & \text{if joint } i \text{ is a translational one,} \end{cases} \tag{12}$$

and

$${}^{i-1}\underline{d}_i = \begin{cases} [0 \;\; 0 \;\; 0]^T, & \text{if joint } i \text{ is a rotational one,} \\ [0 \;\; 0 \;\; 1]^T, & \text{if joint } i \text{ is a translational one.} \end{cases} \tag{13}$$

Symbol "$\sim$" can be considered as an operator, hence for any 3x1 vector $\underline{a} = [a_x \; a_y \; a_z]^T$, we define a 3x3 skewsymmetric matrix $\underline{\underline{\tilde{a}}}$ as

$$\underline{\underline{\tilde{a}}} = \begin{bmatrix} 0 & -a_z & a_y \\ a_z & 0 & -a_x \\ -a_y & a_x & 0 \end{bmatrix} . \tag{13}_1$$

The differential relationships related to the local co-ordinates (first investigated by Paul /3/) will be derived from the mathematical viewpoint. From (5)

$$\frac{\partial \underline{\underline{H}}_k}{\partial q_i} = \underline{\underline{0}}, \quad \text{if} \quad i > k, \tag{14}$$

and

$$\frac{\partial \underline{\underline{H}}_k}{\partial q_i} = {}^0\underline{\underline{H}}_1 \; {}^1\underline{\underline{H}}_2 \cdots {}^{i-2}\underline{\underline{H}}_{i-1} \frac{\partial {}^{i-1}\underline{\underline{H}}_i}{\partial q_i} {}^i\underline{\underline{H}}_{i+1} \cdots {}^{k-1}\underline{\underline{H}}_k, \quad \text{if} \quad i \leq k. \tag{15}$$

Substituting (10) into (15)

$$\frac{\partial {}^{k}\underline{\underline{H}}}{\partial q_i} = {}^{0}\underline{\underline{H}}_{1}\,{}^{1}\underline{\underline{H}}_{2}\cdots{}^{i-2}\underline{\underline{H}}_{i-1}\,{}^{i-1}\underline{\underline{\Delta}}_{i}\,{}^{i-1}\underline{\underline{H}}_{i}\,{}^{i}\underline{\underline{H}}_{i+1}\cdots{}^{k-1}\underline{\underline{H}}_{k} =$$

$$= {}^{k}\underline{\underline{H}}\left[({}^{i-1}\underline{\underline{H}}_{k})^{-1}\,{}^{i-1}\underline{\underline{\Delta}}_{i}\,{}^{i-1}\underline{\underline{H}}_{k}\right] = {}^{k}\underline{\underline{H}}\,{}^{k}\underline{\underline{\Delta}}_{i}\,, \tag{16}$$

where ${}^{k}\underline{\underline{\Delta}}_{i}$ is the 4x4 differential transformation matrix from co-ordinate system i to co-ordinate system k /3/.

Evaluating equation (16)

$${}^{k}\underline{\underline{\Delta}}_{i} = \left[\begin{array}{c|c} {}^{k}\tilde{\underline{\delta}}_{i} & {}^{k}\underline{d}_{i} \\ \hline \underline{0}^{T} & 0 \end{array}\right], \tag{17}$$

where

$${}^{k}\underline{\delta}_{i} = {}^{i-1}\underline{h}_{k}^{T}\,{}^{i-1}\underline{\delta}_{i}\,, \tag{18}$$

and

$${}^{k}\underline{d}_{i} = {}^{i-1}\underline{h}_{k}^{T}\left[({}^{i-1}\tilde{\underline{\delta}}_{i}\,{}^{i-1}\underline{p}_{k}) + {}^{i-1}\underline{d}_{i}\right]. \tag{19}$$

Symbol ${}^{k}\underline{\delta}_{i}$ is the unit vector of rotation axes of joint i with respect to co-ordinate system k, vector ${}^{k}\underline{d}_{i}$ represents the moment of ${}^{k}\underline{\delta}_{i}$ to the origin of co-ordinate system k with respect to co-ordinate system k, if joint i is a rotational one. Symbols ${}^{k}\underline{\delta}_{i} = \underline{0}$ (the 3x1 zero vector), and ${}^{k}\underline{d}_{i}$ are the unit vector of translation axes of joint i with respect to co-ordinate system k, if joint i is a translational one.

For the sake of the next sections, let the first and second derivatives of ${}^{k}\underline{\underline{H}}$ (k = 1,2,...,n) be investigated with respect to time. $\dot{{}^{k}\underline{\underline{H}}}$ is then written (symbol "·" denotes the total time derivative) as follows:

$$\frac{d\,{}^{k}\underline{\underline{H}}}{dt} = \sum_{i=1}^{k}\frac{\partial {}^{k}\underline{\underline{H}}}{\partial q_i}\dot{q}_i = {}^{k}\underline{\underline{H}}\left(\sum_{i=1}^{k}{}^{k}\underline{\underline{\Delta}}_{i}\,\dot{q}_i\right) = {}^{k}\underline{\underline{H}}\left[\begin{array}{c|c} {}^{k}\tilde{\underline{\omega}}_{k} & {}^{k}\underline{v}_{k} \\ \hline \underline{0}^{T} & 0 \end{array}\right], \tag{20}$$

where using (12), (13) and (17), (18), (19)

$$ {}^{k}\underline{\omega}_{k} = \sum_{i=1}^{k} {}^{k}\underline{\delta}_{i}\,\dot{q}_{i} = {}^{k-1}\underline{\underline{h}}_{k}^{T}\,({}^{k-1}\underline{\omega}_{k-1} + {}^{k-1}\underline{\delta}_{k}\,\dot{q}_{k}), \quad {}^{0}\underline{\omega}_{0} = \underline{0} \tag{21} $$

and

$$ {}^{k}\underline{v}_{k} = \sum_{i=1}^{k} {}^{k}\underline{d}_{i}\,\dot{q}_{i} = {}^{k-1}\underline{\underline{h}}_{k}^{T}\,({}^{k-1}\underline{v}_{k-1} + {}^{k-1}\tilde{\underline{\underline{\delta}}}_{k}\,{}^{k-1}\underline{p}_{k}\,\dot{q}_{k} + {}^{k-1}\underline{d}_{k}\,\dot{q}_{k} + $$

$$ + {}^{k-1}\tilde{\underline{\omega}}_{k-1}\,{}^{k-1}\underline{p}_{k}), \quad {}^{0}\underline{v}_{0} = \underline{0} \tag{22} $$

if joint k is a translational one then ${}^{k-1}\underline{\delta}_{k} = \underline{0}$, if joint k is a rotational one then ${}^{k-1}\underline{d}_{k} = \underline{0}$. From equation (20), the second derivative of $\underline{\underline{H}}_{k}$ with respect to time is:

$$ \frac{d^2\underline{\underline{H}}_{k}}{dt^2} = \underline{\underline{H}}_{k} \left[\begin{array}{c|c} {}^{k}\dot{\tilde{\underline{\omega}}}_{k} & {}^{k}\dot{\underline{v}}_{k} \\ \hline \underline{0}^{T} & 0 \end{array}\right] + \dot{\underline{\underline{H}}}_{k} \left[\begin{array}{c|c} {}^{k}\tilde{\underline{\omega}}_{k} & {}^{k}\underline{v}_{k} \\ \hline \underline{0}^{T} & 0 \end{array}\right] = $$

$$ = \underline{\underline{H}}_{k} \left[\begin{array}{c|c} {}^{k}\dot{\tilde{\underline{\omega}}}_{k} + {}^{k}\tilde{\underline{\omega}}_{k}^{2} & {}^{k}\dot{\underline{v}}_{k} + {}^{k}\tilde{\underline{\omega}}_{k}\,{}^{k}\underline{v}_{k} \\ \hline \underline{0}^{T} & 0 \end{array}\right] = \underline{\underline{H}}_{k} \left[\begin{array}{c|c} {}^{k}\underline{\underline{B}}_{k} & {}^{k}\underline{b}_{k} \\ \hline \underline{0}^{T} & 0 \end{array}\right] = \underline{\underline{H}}_{k}\,{}^{k}\underline{\underline{W}}_{k}, \tag{23} $$

where, from equations (21) and (22) and by using equations (11), (18) and (19), the following backward recursive equations can be developed:

$$ {}^{k}\dot{\underline{\omega}}_{k} = {}^{k-1}\underline{\underline{h}}_{k}^{T}\,({}^{k-1}\dot{\underline{\omega}}_{k-1} + {}^{k-1}\tilde{\underline{\omega}}_{k-1}\,{}^{k-1}\underline{\delta}_{k}\,\dot{q}_{k} + {}^{k-1}\underline{\delta}_{k}\,\ddot{q}_{k}), \quad {}^{0}\dot{\underline{\omega}}_{0} = \underline{0} \tag{24} $$

$$ {}^{k}\dot{\underline{v}}_{k} = {}^{k-1}\underline{\underline{h}}_{k}^{T}\,[{}^{k-1}\dot{\underline{v}}_{k-1} + {}^{k-1}\dot{\tilde{\underline{\omega}}}_{k-1}\,{}^{k-1}\underline{p}_{k} + {}^{k-1}\tilde{\underline{\omega}}_{k-1}\,({}^{k-1}\tilde{\underline{\omega}}_{k-1}\,{}^{k-1}\underline{p}_{k}) + $$

$$ + 2\,{}^{k-1}\tilde{\underline{\omega}}_{k-1}\,({}^{k-1}\tilde{\underline{\delta}}_{k}\,{}^{k-1}\underline{p}_{k})\dot{q}_{k} + {}^{k-1}\tilde{\underline{\delta}}_{k}\,{}^{k-1}\underline{p}_{k}\,\ddot{q}_{k} + {}^{k-1}\tilde{\underline{\delta}}_{k}\,({}^{k-1}\tilde{\underline{\delta}}_{k}\,{}^{k-1}\underline{p}_{k})\dot{q}_{k}^{2} + $$

$$ + {}^{k-1}\tilde{\underline{\omega}}_{k-1}\,{}^{k-1}\underline{d}_{k}\dot{q}_{k} + {}^{k-1}\underline{d}_{k}\ddot{q}_{k}\,], \quad {}^{0}\dot{\underline{v}}_{0} = \underline{0}. \tag{25} $$

The above equations seem to be very complex ones but when evaluating them, one obtains much simpler forms than the above ones because of using quan-

tities with respect to the local co-ordinate systems. Equations (24) and (25) can be rewritten into the following forms:

$$ {}^{k}\dot{\underline{\omega}}_k = {}^{k}\underline{\varepsilon}_k + {}^{k}\underline{w}_k , \tag{26} $$

where

$$ {}^{k}\underline{\varepsilon}_k = {}^{k-1}\underline{\underline{h}}_k^T \left({}^{k-1}\dot{\underline{\omega}}_{k-1} + {}^{k-1}\underline{\delta}_k \ddot{q}_k \right), \tag{27} $$

and

$$ {}^{k}\underline{w}_k = {}^{k-1}\underline{\underline{h}}_k^T \left({}^{k-1}\underline{\omega}_{k-1} \times {}^{k-1}\underline{\delta}_k \right) \dot{q}_k , \tag{28} $$

and

$$ {}^{k}\dot{\underline{v}}_k = {}^{k}\underline{a}_k + {}^{k}\underline{u}_k , \tag{29} $$

where

$$ {}^{k}\underline{a}_k = {}^{k-1}\underline{\underline{h}}_k^T \left[{}^{k-1}\dot{\underline{v}}_{k-1} + {}^{k-1}\dot{\tilde{\underline{\omega}}}_{k-1} \, {}^{k-1}\underline{p}_k + {}^{k-1}\tilde{\underline{\delta}}_k \, {}^{k-1}\underline{p}_k \ddot{q}_k + {}^{k-1}\underline{d}_k \ddot{q}_k \right] \tag{30} $$

and

$$ {}^{k}\underline{u}_k = {}^{k-1}\underline{\underline{h}}_k^T \left[{}^{k-1}\tilde{\underline{\delta}}_k \left({}^{k-1}\tilde{\underline{\delta}}_k \, {}^{k-1}\underline{p}_k \right) \dot{q}_k^2 + {}^{k-1}\tilde{\underline{\omega}}_{k-1} \left({}^{k-1}\tilde{\underline{\omega}}_{k-1} \, {}^{k-1}\underline{p}_k \right) + \right. $$

$$ \left. + 2 \, {}^{k-1}\tilde{\underline{\omega}}_{k-1} \left({}^{k-1}\tilde{\underline{\delta}}_k \, {}^{k-1}\underline{p}_k \right) \dot{q}_k + {}^{k-1}\tilde{\underline{\omega}}_{k-1} \, {}^{k-1}\underline{d}_k \dot{q}_k \right]. \tag{31} $$

In equations (26) and (29), terms ${}^{k}\underline{\varepsilon}_k$ and ${}^{k}\underline{a}_k$ contain the generalized accelerations. They are very important for the direct dynamics of a robot manipulator.

For the sake of the next sections, let the partial derivative of vectors ${}^{k}\dot{\underline{\omega}}_k$ and ${}^{k}\dot{\underline{v}}_k$ ($k = 1,2,\ldots,n$) be investigated with respect to the generalized accelerations $\ddot{q}_j$ ($j = 1,2,\ldots,k$). (n is the number of links of the robot.) If $j > k$, then

$$ \frac{\partial {}^{k}\dot{\underline{\omega}}_k}{\partial \ddot{q}_j} = \frac{\partial {}^{k}\dot{\underline{v}}_k}{\partial \ddot{q}_j} = 0. \tag{32} $$

From equations (24) and (25), the following backward recursive equations can be developed

$$\underline{\beta}_{kj} = \frac{\partial^{k}\dot{\underline{\omega}}_{k}}{\partial \ddot{q}_{j}} = \frac{\partial^{k}\dot{\underline{\varepsilon}}_{k}}{\partial \ddot{q}_{j}} = {}^{k-1}\underline{\underline{h}}_{k}^{T} \cdots {}^{j-1}\underline{\underline{h}}_{j}^{T}\, {}^{j-1}\underline{\delta}_{j} = {}^{k-1}\underline{\underline{h}}_{k}^{T} \frac{\partial^{k-1}\dot{\underline{\omega}}_{k-1}}{\partial \ddot{q}_{j}}, \qquad (33)_{a}$$

$$k = j+1,\ldots,n$$

and

$$\frac{\partial^{j}\dot{\underline{\omega}}_{j}}{\partial \ddot{q}_{j}} = {}^{j-1}\underline{\underline{h}}_{j}^{T}\, {}^{j-1}\underline{\delta}_{j}, \qquad (33)_{b}$$

and

$$\underline{\eta}_{kj} = \frac{\partial^{k}\dot{\underline{v}}_{k}}{\partial \ddot{q}_{j}} = \frac{\partial^{k}\underline{a}_{k}}{\partial \ddot{q}_{j}} = {}^{k-1}\underline{\underline{h}}_{k}^{T}\left[\frac{\partial^{k-1}\dot{\underline{v}}_{k-1}}{\partial \ddot{q}_{j}} + \frac{\partial^{k-1}\dot{\tilde{\underline{\omega}}}_{k-1}}{\partial \ddot{q}_{j}}\, {}^{k-1}\underline{p}_{k}\right], \quad k = j+1,\ldots,n \qquad (34)_{a}$$

$$\frac{\partial^{j}\dot{\underline{v}}_{j}}{\partial \ddot{q}_{j}} = {}^{j-1}\underline{\underline{h}}_{j}^{T}\,({}^{j-1}\tilde{\underline{\delta}}_{j}\, {}^{j-1}\underline{p}_{j} + {}^{j-1}\underline{d}_{j}). \qquad (34)_{b}$$

3. The acceleration energy function

According to /1/, the acceleration energy function (called Gibbs function) of body i can be written in the form:

$$G_{i} = \frac{1}{2}\int_{m_{i}} \underline{z}_{i}^{T}\,\underline{z}_{i}\, dm, \qquad (35)$$

where $\underline{z}_{i}$ is the 3x1 acceleration vector of any arbitrary point of body i, and m_{i} is the mass of body i.

The acceleration energy function of a robot manipulator is defined by:

$$G = \sum_{i=1}^{n} G_{i} = \sum_{i=1}^{n} \frac{1}{2}\int_{m_{i}} \ddot{\underline{R}}_{i}^{T}\ddot{\underline{R}}_{i}\, dm = \frac{1}{2}\sum_{i=1}^{n}\int_{m_{i}} \mathrm{Tr}(\ddot{\underline{R}}_{i}\ddot{\underline{R}}_{i}^{T})\, dm, \qquad (36)$$

where n is the number of links of the robot, Tr() represents the trace of (), $\underline{R}_{i} = [\underline{r}_{i}^{T} \mid 1]^{T}$ and $\underline{r}_{i}$ is a 3x1 vector from the base reference co-ordinate system to any arbitrary point of link i. By using (5) in equation (36)

$$\underline{R}_i = H_i \, {}^{i}\underline{R}_i, \qquad i = 1,\ldots,n \tag{37}$$

where $\underline{\underline{H}}_i$ is the 4x4 homogeneous transformation matrix, ${}^{i}\underline{R}_i$ is a 4x1 vector (see the above row) and ${}^{i}\underline{r}_i$ is a 3x1 vector from the origin of co-ordinate system i to any arbitrary point of link i with respect to co-ordinate system i. Symbol ${}^{i}\underline{r}_i$ is a constant vector at the time when the links of the robot manipulator are assumed to be rigid. By using equations (36) and (37), the Gibbs function can be written in the form

$$G = \frac{1}{2} \sum_{i=1}^{n} \mathrm{Tr}(\ddot{\underline{\underline{H}}}_i \, {}^{i}\underline{\underline{K}}_i \, \ddot{\underline{\underline{H}}}_i^{T}), \tag{38}$$

where ${}^{i}\underline{\underline{K}}_i$ is a 4x4 matrix called pseudoinertia matrix /3/. By using equations (35)—(37), ${}^{i}\underline{\underline{K}}_i$ can be written in the form:

$${}^{i}\underline{\underline{K}}_i = \int_{m_i} ({}^{i}\underline{R}_i \, {}^{i}\underline{R}_i^{T}) \, dm = \left[\begin{array}{c|c} {}^{i}\underline{\underline{K}}_i & m_i \, {}^{i}\underline{\bar{r}}_i \\ \hline m_i \, {}^{i}\underline{\bar{r}}_i^{T} & m_i \end{array}\right], \tag{39}$$

where ${}^{i}\underline{\bar{r}}_i$ is the 3x1 position vector of the mass center of link i with respect to its own co-ordinate system, and

$${}^{i}\underline{\underline{K}}_i = \begin{bmatrix} {}^{i}J_{ixx} & {}^{i}J_{ixy} & {}^{i}J_{ixz} \\ {}^{i}J_{iyx} & {}^{i}J_{iyy} & {}^{i}J_{iyz} \\ {}^{i}J_{izx} & {}^{i}J_{izy} & {}^{i}J_{izz} \end{bmatrix}, \tag{39}_1$$

where

$${}^{i}J_{ixx} = \frac{1}{2}(-{}^{i}J_{ix} + {}^{i}J_{iy} + {}^{i}J_{iz}), \tag{39}_2$$

$${}^{i}J_{iyy} = \frac{1}{2}({}^{i}J_{ix} - {}^{i}J_{iy} + {}^{i}J_{iz}), \tag{39}_3$$

$${}^{i}J_{izz} = \frac{1}{2}({}^{i}J_{ix} + {}^{i}J_{iy} - {}^{i}J_{iz}). \tag{39}_4$$

Matrix ${}^{i}\underline{\underline{k}}_i$ is built of the matrix elements of the inertia tensor of link i with respect to co-ordinate system i. ${}^{i}\underline{\underline{K}}_i$ is a time-invariant matrix because vector ${}^{i}\underline{r}_i$ related to the local co-ordinate system i is constant.

By using (23), G can be further written in the form:

$$G = \frac{1}{2} \sum_{i=1}^{n} \mathrm{Tr}(\underline{\underline{H}}_i \, {}^{i}\underline{\underline{W}}_i \, {}^{i}\underline{\underline{K}}_i \, {}^{i}\underline{\underline{W}}_i^T \, \underline{\underline{H}}_i^T), \tag{40}$$

and by expanding the middle three terms

$$G = \frac{1}{2} \sum_{i=1}^{n} \mathrm{Tr} \left(\underline{\underline{H}}_i \begin{bmatrix} {}^{i}\underline{\underline{B}}_i & {}^{i}\underline{b}_i \\ \underline{0}^T & 0 \end{bmatrix} \begin{bmatrix} {}^{i}\underline{\underline{K}}_i & m_i \, {}^{i}\underline{r}_i \\ m_i \, {}^{i}\underline{r}_i^T & m_i \end{bmatrix} \begin{bmatrix} {}^{i}\underline{\underline{B}}_i^T & \underline{0} \\ {}^{i}\underline{b}_i^T & 0 \end{bmatrix} \underline{\underline{H}}_i^T \right). \tag{41}$$

It is not difficult to show that the product of the middle three matrices results a matrix whose bottom row and right-hand column are all zeros. Premultiplying by $\underline{\underline{H}}_i$ and postmultiplying by its transpose makes use of only the rotation part of the transformation. The trace of a matrix is invariant under such an operation. Therefore, it is necessary to investigate the trace of the inner three terms of the above expression. After evaluation, the product of the middle three matrices will be:

$$G = \frac{1}{2} \sum_{i=1}^{n} \mathrm{Tr}({}^{i}\underline{\underline{B}}_i \, {}^{i}\underline{\underline{K}}_i \, {}^{i}\underline{\underline{B}}_i + m_i \, {}^{i}\underline{b}_i \, {}^{i}\underline{r}_i^T \, {}^{i}\underline{\underline{B}}_i^T + m_i \, {}^{i}\underline{\underline{B}}_i \, {}^{i}\underline{r}_i \, {}^{i}\underline{b}_i^T + m_i \, {}^{i}\underline{b}_i \, {}^{i}\underline{b}_i^T). \tag{42}$$

With the use of the rules of matrix operations, G can be rewritten into the form

$$G = \frac{1}{2} \sum_{i=1}^{n} \Big\{ {}^{i}\dot{\underline{\omega}}_i^T \, {}^{i}\underline{\underline{J}}_i \, {}^{i}\dot{\underline{\omega}}_i + 2m_i \, {}^{i}\dot{\underline{v}}_i^T ({}^{i}\tilde{\dot{\underline{\omega}}}_i \, {}^{i}\underline{r}_i) + m_i \, {}^{i}\dot{\underline{v}}_i^T \, {}^{i}\dot{\underline{v}}_i +$$

$$+ 2 \Big[{}^{i}\underline{\omega}_i^T \, {}^{i}\underline{\underline{K}}_i ({}^{i}\tilde{\underline{\omega}}_i \, {}^{i}\dot{\underline{\omega}}_i) + m_i \, {}^{i}\dot{\underline{v}}_i^T ({}^{i}\tilde{\underline{\omega}}_i ({}^{i}\tilde{\underline{\omega}}_i \, {}^{i}\underline{r}_i)) - m_i \, {}^{i}\underline{v}_i^T ({}^{i}\tilde{\underline{\omega}}_i ({}^{i}\tilde{\underline{\omega}}_i \, {}^{i}\underline{r}_i)) +$$

$$+ m_i \, {}^{i}\dot{\underline{v}}_i^T ({}^{i}\tilde{\underline{\omega}}_i \, {}^{i}\underline{v}_i) \Big] + f({}^{i}\underline{\omega}_i, \, {}^{i}\underline{v}_i) \Big\}, \tag{43}$$

where ${}^{i}\underline{\underline{J}}_i$ is the matrix of the inertia tensor of link i around the origin of its own co-ordinate system with respect to the same co-ordinate system.

This new form of the acceleration energy function is written by dynamical and kinematical quantities with respect to the local co-ordinate systems. In these co-ordinate systems the dynamical quantities are time-invariant during the motion, and the kinematical quantities can be developed by recursive equations according to (21), (22), (24) and (25). All these characteristics will reduce the required computations.

4. Equations of motion

Appell's equations (according to /1/) can be written in the form:

$$\frac{\partial G}{\partial \ddot{q}_j} = Q_j, \qquad j = 1,2,\ldots,n \tag{44}$$

where Q_j is the generalized force associated with co-ordinate q_j. First of all, the left-hand side of equations (44) must be investigated. From (26) through (34) and (43)

$$\frac{\partial G}{\partial \ddot{q}_j} = D_j + C_j, \tag{45}$$

where

$$D_j = \sum_{i=j}^{n} \left[{}^i\underline{\omega}_i^T \, {}^i\underline{\underline{J}}_i \frac{\partial {}^i\dot{\underline{\omega}}_i}{\partial \ddot{q}_j} + m_i \frac{\partial {}^i\dot{\underline{v}}_i^T}{\partial \ddot{q}_j} ({}^i\underline{\underline{\tilde{\omega}}}_i \, {}^i\underline{\Gamma}_i) + m_i \, {}^i\dot{\underline{v}}_i^T \left(\frac{\partial {}^i\dot{\underline{\underline{\tilde{\omega}}}}_i}{\partial \ddot{q}_j} {}^i\underline{\Gamma}_i \right) + \right.$$

$$\left. + m_i \, {}^i\dot{\underline{v}}_i^T \frac{\partial {}^i\dot{\underline{v}}_i}{\partial \ddot{q}_j} \right], \tag{46}$$

and

$$C_j = \sum_{i=j}^{n} \left[{}^i\underline{\omega}_i^T \, {}^i\underline{\underline{K}}_i ({}^i\underline{\underline{\tilde{\omega}}}_i \frac{\partial {}^i\dot{\underline{\omega}}_i}{\partial \ddot{q}_j}) + m_i \frac{\partial {}^i\dot{\underline{v}}_i^T}{\partial \ddot{q}_j} ({}^i\underline{\underline{\tilde{\omega}}}_i ({}^i\underline{\underline{\tilde{\omega}}}_i \, {}^i\underline{\Gamma}_i)) + \right.$$

$$\left. + m_i \, {}^i\underline{v}_i^T ({}^i\underline{\underline{\tilde{\omega}}}_i ({}^i\underline{\underline{\tilde{\Gamma}}}_i \frac{\partial {}^i\dot{\underline{\omega}}_i}{\partial \ddot{q}_j})) + m_i \frac{\partial {}^i\dot{\underline{v}}_i^T}{\partial \ddot{q}_j} ({}^i\underline{\underline{\tilde{\omega}}}_i \, {}^i\underline{v}_i) \right], \tag{47}$$

vectors $\underline{\beta}_{ij}$ and $\underline{\eta}_{ij}$ are defined by equations (33) and (34). The generalized force Q_j ($j = 1,2,\ldots,n$) on the right-hand side of equations (44) contains effects of external and internal forces acting on the robot manipulator at joint j. In many practical cases, it is sufficient to assume that each joint can be considered as an ideal constraint and only the joint forces or torques, and the gravity forces act on the robot manipulator. Hence, by using the principle of virtual work /2/, Q_j can be written in the form:

$$Q_j = \sum_{k=1}^{n} m_k \underline{Y}^T \frac{\partial \underline{H}_k}{\partial q_j} {}^k\underline{\bar{R}}_k + \tau_j, \qquad j = 1,2,\ldots,n \tag{48}$$

where τ_j is the joint force or torque acting at joint j,

$$\underline{Y}^T = \left[\underline{g}^T \mid 0\right]^T, \tag{49}$$

g is the 3x1 gravitational acceleration vector in the base co-ordinate system, and

$${}^k\underline{\bar{R}}_k = \left[{}^k\underline{\bar{r}}_k^T \mid 1\right]^T. \tag{50}$$

It is worth mentioning that the gravitational acceleration vector can be included in the acceleration energy function, so the effects of the gravitational loading can be calculated by evaluating the left-hand side of Appell's equations. This method results in the same expression as the one using the principle of virtual work (48).

It is not difficult to show, that

$$\frac{\partial \underline{H}_k}{\partial q_j} = \frac{\partial \dot{\underline{H}}_k}{\partial \dot{q}_j} = \frac{\partial \ddot{\underline{H}}_k}{\partial \ddot{q}_j}, \qquad k,j = 1,2,\ldots,n \tag{51}$$

and by using the above relationships, equation (48) can be rewritten into the form

$$Q_j = N_j + \tau_j, \qquad j = 1,2,\ldots,n \tag{52}$$

where

$$N_j = \sum_{k=j}^{n} m_k \underline{r}^T \frac{\partial \ddot{H}_k}{\partial \ddot{q}_j} k\bar{R}_k. \tag{53}$$

Using the results of section 2 and expanding equation (53)

$$N_j = \underline{g}^T \sum_{k=j}^{n} m_k \underline{\underline{h}}_k \left(\frac{\partial^k \dot{\underline{\underline{\omega}}}_k}{\partial \ddot{q}_j} k\underline{\Gamma}_k + \frac{\partial^k \dot{\underline{v}}_k}{\partial \ddot{q}_j} \right), \qquad j = 1,2,\ldots,n \tag{54}$$

In the above equations all the kinematical quantities were derived by using recursive equations. According to (45) and (52) the equations of motion of the robot manipulator can be rewritten into the form:

$$D_j(\ddot{\underline{q}},\dot{\underline{q}},\underline{q}) + C_j(\dot{\underline{q}},\underline{q}) = N_j(\underline{q}) + \tau_j, \qquad j = 1,2,\ldots,n \tag{55}$$

where

$$\ddot{\underline{q}} = \left[\ddot{q}_1 \quad \ddot{q}_2 \quad \ldots \quad \ddot{q}_n\right]^T, \tag{55}_1$$

$$\dot{\underline{q}} = \left[\dot{q}_1 \quad \dot{q}_2 \quad \ldots \quad \dot{q}_n\right]^T, \tag{55}_2$$

$$q = \left[q_1 \quad q_2 \quad \ldots \quad q_n\right]^T. \tag{55}_3$$

Equations (55) are an explicit set of ordinary, second order, highly non-linear and coupling differential equations. The meaning of each side of these equations will be investigated later. It is worth mentioning that in general there are no closed-form solutions to this set of equations.

4.1. Solving the inverse problem

Equations (55) can be rewritten into the form

$$D_j + C_j - N_j = \tau_j, \qquad j = 1,2,\ldots,n \tag{56}$$

Equation (56) is in the so-called inverse dynamic form. If all the generalized co-ordinates, velocities and accelerations are known, then the actual driving forces or torques can be calculated.

A computational algorithm can be stated as follows:

Algorithm 1.:

1. Input the link paramters: l_i, α_i, θ_i, s_i, m_i, $^{i}\underline{r}_i$ and $^{i}\underline{\underline{J}}_i$ for i = = 1,2,...,n;
2. Input the joint variables q_i, velocities $\dot{q}_i$, accelerations $\ddot{q}_i$ for i = = 1,2,...,n;
3. Compute the 3x3 relative transformation matrices $^{i-1}\underline{\underline{h}}_i$ and the position vectors $^{i-1}\underline{p}_i$ by relationships (2) and (3) for i = 1,2,...,n;
4. Compute $^{i}\underline{\omega}_i$ and $^{i}\underline{v}_i$ with backward recursion by equations (21) and (22) for i = 1,2,...,n;
5. Compute $^{i}\dot{\underline{\omega}}_i$ and $^{i}\dot{\underline{v}}_i$ with backward recursion by equations (24) and (25) for i = 1,2,..,n;
6. Compute $\underline{\beta}_{ik}$ and $\underline{\eta}_{ik}$ with backward recursion by equations (33) and (34) for k = 1,2,...,n and i = k,k+1,...,n;
7. Compute the terms D_k, C_k and N_k by equations (46), (47) and (54) for k = 1,2,...,n;
8. Compute the joint generalized forces τ_k by equation (56) for k = = 1,2,...,n;
9. End.

4.2. Solving the direct problem

It is not difficult to see that the closed-form solution of equations (55) generally does not exist except for some simple special cases. Hence, a numerical integration scheme must be used in order to compute the generalized co-ordinates, velocities and accelerations forward in time in the case of given initial conditions and driving forces or torques.

Equations (55) and (56) are now in the inverse dynamic form. To convert them into the simulation (direct dynamic) form, one must extract the coefficients of the second derivatives of the generalized co-ordinates to compose a nxn mass matrix M for the system. Elements of matrix $\underline{\underline{M}}$ are M_{jk} k,j = 1,...,n. Afterwards, the second and first derivatives together make up the derivative of the state vector, which can be used in one of the available integration schemes to solve for the state as a function of time for given initial conditions and generalized forces.

According to (26)—(31) and (46), term D_j in equation (55) can be divided into two following parts:

$$D_j = A_j + C'_j, \qquad j = 1,2,\ldots,n \tag{57}$$

where

$$A_j = \sum_{i=j}^{n} \left[{}^i\underline{\varepsilon}_i^T \, {}^i\underline{\underline{J}}_i \frac{\partial^i \dot{\underline{\omega}}_i}{\partial \ddot{q}_j} + m_i \frac{\partial^i \dot{\underline{v}}_i^T}{\partial} ({}^i\underline{\tilde{\varepsilon}}_i \, {}^i\underline{r}_i) + m_i \, {}^i\underline{a}_i^T \left(\frac{\partial^i \dot{\underline{\tilde{\omega}}}_i}{\partial \ddot{q}_j} {}^i\underline{r}_i \right) + \right.$$

$$\left. + m_i \, {}^i\underline{a}_i^T \frac{\partial^i \dot{\underline{v}}_i}{\partial \ddot{q}_j} \right], \tag{58}$$

and

$$C'_j = \sum_{i=j}^{n} \left[{}^i\underline{w}_i^T \, {}^i\underline{\underline{J}}_i \frac{\partial^i \dot{\underline{\omega}}_i}{\partial \ddot{q}_j} + m_i \frac{\partial^i \dot{\underline{v}}_i^T}{\partial \ddot{q}_j} ({}^i\underline{\tilde{w}}_i \, {}^i\underline{r}_i) + m_i \, {}^i\underline{u}_i^T \left(\frac{\partial^i \dot{\underline{\tilde{\omega}}}_i}{\partial \ddot{q}_j} {}^i\underline{r}_i \right) + \right.$$

$$\left. + m_i \, {}^i\underline{u}_i^T \frac{\partial^i \dot{\underline{v}}_i}{\partial \ddot{q}_j} \right]. \tag{59}$$

Term A_j in equation (57) contains only the second derivative of the generalized co-ordinates, and C'_j contains the first derivative of the generalized co-ordinates. Term A_j must be investigated in order to set up matrix $\underline{\underline{M}}$. A_j can be considered as the product of the jth row vector $\underline{M}_j$ of matrix $\underline{\underline{M}}$ and the vector of the generalized accelerations $\ddot{\underline{q}}$. Hence by extracting coefficients M_{jk}

$$\frac{\partial A_j}{\partial \ddot{q}_k} = M_{jk}, \qquad j,k = 1,2,\ldots,n \tag{60}$$

and expanding the above equations

$$M_{jk} = \sum_{i=\max(j,k)}^{n} \left[\frac{\partial^i \underline{\varepsilon}_i^T}{\partial \ddot{q}_k} {}^i\underline{\underline{J}}_i \frac{\partial^i \dot{\underline{\omega}}_i}{\partial \ddot{q}_j} + m_i \left(\frac{\partial^i \dot{\underline{v}}_i^T}{\partial \ddot{q}_j} \frac{\partial^i \tilde{\underline{\varepsilon}}_i}{\partial \ddot{q}_k} {}^i\underline{r}_i \right) + \right.$$

$$\left. + m_i \frac{\partial^i \underline{a}_i^T}{\partial \ddot{q}_k} \left(\frac{\partial^i \dot{\underline{\tilde{\omega}}}_i}{\partial \ddot{q}_j} {}^i\underline{r}_i \right) + m_i \frac{\partial^i \underline{a}_i^T}{\partial \ddot{q}_k} \frac{\partial^i \dot{\underline{v}}_i}{\partial \ddot{q}_j} \right]. \tag{61}$$

By using equations (33) and (34), it is not difficult to show that $\underline{\underline{M}}$ is a symmetric matrix,

$$M_{jk} = M_{kj}. \tag{62}$$

Therefore, it is only needed to compute coefficients M_{jk} for $j \geq k$. The other ones can be obtained from (62).

Now the equations of motion of the robot manipulator can be rewritten into the form:

$$\sum_{k=1}^{n} M_{jk} \ddot{q}_k + F_j = N_j + \tau_j, \qquad j = 1,2,\ldots,n \tag{63}$$

where

$$F_j = C_j + C'_j. \tag{64}$$

Equations (63) are in the so-called dynamic simulation form. The first term represents the inertial effects at joint j, term F_j represents the Coriolis and centripetal effects at joint j, N_j represents the gravity loading at joint j, and τ_j is the actual joint torque or force at joint j. It is stated without proof that matrix $\underline{\underline{M}}$ is always a non-singular one (resulting from the structure of Appell's equations see /1/), hence its inverse $\underline{\underline{M}}^{-1}$ exists.

Converting equations (63) into matrix form:

$$\underline{\underline{M}}\,\underline{\ddot{q}} + \underline{F} = \underline{N} + \underline{\tau}, \tag{65}$$

where

$$\underline{F} = \underline{F}(\underline{\dot{q}},\underline{q}) = \left[F_1\ F_2\ \ldots\ F_n\right]^T, \tag{66}$$

$$\underline{N} = \underline{N}(\underline{q}) = \left[N_1\ N_2\ \ldots\ N_n\right]^T \tag{67}$$

and

$$\underline{\tau} = \underline{\tau}(t) = \left[\tau_1\ \tau_2\ \ldots\ \tau_n\right]^T. \tag{68}$$

In order to obtain solution to equation (65), a single-step, direct, numerical integration method is used. This method is designed to solve the first-order differential equations of the form /23/

$$\dot{\underline{y}} = \underline{f}(\underline{y},t), \qquad \underline{y}(t_0) = \underline{y}_0, \tag{69}$$

where $\underline{y} = [y_1\ y_2\ \ldots\ y_{2n}]^T$ is a time-dependent state vector, $\underline{f}(\underline{y},t)$ is a 2nx1 vector function, and $\underline{y}_0$ is the value of $\underline{y}$ at a given point t_0. Hence, equation (65) must be converted to a set of first-order differential equations by using appropriate vector and matrix notation. Since $\underline{\underline{M}}$ is a positive definite non-singular matrix, equation (65) can be solved for the generalized acceleration vector as follows:

$$\ddot{\underline{q}} = \underline{\underline{M}}^{-1} (\underline{N} + \underline{\tau} - \underline{F}) = \ddot{\underline{q}}(\dot{\underline{q}},\underline{q}). \tag{70}$$

Let the state vector $\underline{y}$ be the following 2nx1 vector

$$\underline{y} = \begin{bmatrix} \underline{q} \\ \dot{\underline{q}} \end{bmatrix}, \tag{71}$$

and its time derivative

$$\dot{\underline{y}} = \begin{bmatrix} \dot{\underline{q}} \\ \ddot{\underline{q}} \end{bmatrix} = \begin{bmatrix} \dot{\underline{q}} \\ \underline{\underline{M}}^{-1} (\underline{N} + \underline{\tau} - \underline{F}) \end{bmatrix} = \underline{f}(\underline{y},t). \tag{72}$$

The initial conditions $\underline{y}_0 = [\underline{q}(t_0)\ \dot{\underline{q}}(t_0)]^T$ are known. The investigated time domain must be divided into subintervals. It is assumed that the length of each subinterval h is equal. h is called the time step size. Integrating equation (72)

$$\int_{\underline{y}_0}^{\underline{y}_1} d\underline{y} = \int_{t_0}^{t_1} \underline{f}(\underline{y},t)\, dt, \tag{73}_1$$

and

$$\underline{y}_1 = \underline{y}(t_1) = \underline{y}_0 + \int_{t_0}^{t_1} \underline{f}(\underline{y},t)\, dt, \tag{73}_2$$

where $t_1 = t_0 + h$. If h is taken appropriately small the above equations can be rewritten as:

$$\underline{y}_1 = \underline{y}_0 + h\underline{f}(\underline{y}_0,t\ ). \tag{74}$$

By using the initial conditions the 2nx1 vector $\underline{f}(\underline{y}_0,t_0)$ can be calculated by equations (72). Hence, the generalized co-ordinates and velocities at time t_1

$$\underline{y}_1 = \begin{bmatrix} \underline{q}(t_1) \\ \dot{\underline{q}}(t_1) \end{bmatrix} = \begin{bmatrix} \underline{q}(t_0) \\ \dot{\underline{q}}(t_0) \end{bmatrix} + h \begin{bmatrix} \dot{\underline{q}}(t_0) \\ \ddot{\underline{q}}(t_0) \end{bmatrix} . \tag{75}$$

Solution vector $\underline{y}_1$ at time $t_0 + h$ can then be used to evaluate the accelerations at the new point at time t_1. Vector $\underline{y}_1$, as well as the acceleration vector can be used to define function $\underline{y}_1 = \underline{f}(\underline{y}_1,t_1)$, which can be used to advance the numerical integration another step to reach a new point at time t_2. This process is continued until the end of the desired simulation time.

In general, the method is defined by the equation

$$\begin{bmatrix} \underline{q}(t_{n+1}) \\ \dot{\underline{q}}(t_{n+1}) \end{bmatrix} = \begin{bmatrix} \underline{q}(t_n) \\ \dot{\underline{q}}(t_n) \end{bmatrix} + h \begin{bmatrix} \dot{\underline{q}}(t_n) \\ \ddot{\underline{q}}(t_n) \end{bmatrix} . \tag{76}$$

This formula can also be obtained by using Taylor's series and dropping the higher order (nonlinear) terms in these series.

A computational algorithm for the direct problem can be stated as follows:

Algorithm 2.

1. Input the link parameters: l_i, α_i, Θ_i, s_i, m_i, $^i\underline{r}_i$ and $^i\underline{\underline{J}}_i$ for i = = 1,2,...,n;
2. Input the joint torque or force function τ_i (t) for i = 1,2,...,n;
3. Input the joint variables q_i, velocities $\dot{q}_i$ at time t_0 for i = 1,2,...,n (initial conditions);
4. Compute the relative transformation matrices $^{i-1}\underline{\underline{h}}_i$ and the position vectors $^{i-1}\underline{p}_i$ at time t_0 by relationships (2) and (3) for i = 1,2,...,n;
5. Compute $^i\underline{\omega}_i$ and $^i\underline{v}_i$ with backward recursion by equations (21) and (22) at time t_0 for i = 1,2,...,n;
6. Compute $^i\underline{w}_i$ and $^i\underline{u}_i$ with backward recursion by equations (24) and (25) at time t_0 for i = 1,2,...,n;
7. Compute $\underline{\beta}_{ik}$ and $\underline{\eta}_{ik}$ with backward recursion by equations (33) and (34) at time t_0 for k = 1,2,...,n and i = k,k+1,...,n;
8. Compute terms F_k and N_k by equations (47), (54), (59) and (63) at time t_0 for k = 1,2,...,n;

9. Construct the mass matrix $\underline{\underline{M}}$ by equations (61) and (62) at time t_0;
10. Compute the generalized acceleration vector $\ddot{\underline{\underline{q}}}$ by equation (70) at time t_0;
11. Compute the vectors of generalized co-ordinates and velocities at time t_1 by equation (75) choosing an appropriate time step size h;
12. Let be $t_0 = t_1$ and $t_1 = t_2$ and repeat the algorithm from step 4, until $t_1 = t_e$ (t_e is the end of the desired simulation time interval);
13. End.

It is easy to see that the dynamic simulation is a more difficult problem than the inverse dynamics. The integration method for solving the set of equations of motion used in this algorithm (called Euler's method) is simple but not very accurate. However, this meghod require fewer computations than the other ones (for example Runge–Kutta methods, predictor–corrector methods) and by using iterative steps it can be rendered more accurate.

5. Conclusions

A new and efficient method for derivation and solution to the dynamical model of general robot manipulators consisting of rigid links has been developed in this work. Both the inverse dynamics and the direct dynamics of robot manipulators can be solved by using this method in a simple way. Efficient computational schemes can be developed. The whole computational process for deriving the complete set of dynamic equations of motion of a robot manipulator with n degrees of freedom requires at most $(14n^2 + 80n)$ multiplications and $(12n^2 + 54n)$ additions; for $n = 6$, at most 984 multiplications and 756 additions are required.

In order to prove the efficiency of the proposed computational schemes, a Pascal program was written. By using an AT 386 computer, the required execution time is less than 0.007 s when the solution to inverse dynamics of a PUMA 560 robot manipulator is calculated. The possible simplifications of the algorithm deriving from the selected configuration of the robot manipulator have not been taken into account.

It is possible to compare the method proposed in this paper with some other existing methods in use and computational complexity. This comparison is shown in Table 1.

In conclusion, the methods proposed by Uicker, Huston–Passerello and Harlow /21/, Bejczy and Lee /9/, Vukobratovic and Pontkonjak /7/ can be used

Table 1

Method	Multiplic.	Additions	Dir.	Inv.
Uicker—Kahn (Lagrange—Euler)	$f(n^4)$ /if n = 6/ /66271/	$f(n^4)$ /if n = 6/ /51548/	yes	yes
Huston—Passerello (Kane)	$f(n^4)$ /≈ 10000/	$f(n^4)$ /≈ 10000/	yes	yes
Bejczy—Lee (Lagrange)	$f(n^4)$ /≈ 10000/	$f(n^4)$ /≈ 10000/	yes	yes
Hollerbach (Lagrange)	$f(n)$ /2195/	$f(n)$ /1719/	no	yes
Vukobratovic—Pontkonjak (Lagrange)	$f(n^3)$ /2899/	$f(n^3)$ /2068/	yes	yes
Vukobratovic—Pontkonjak (Appell)	$f(n^3)$ /2929/	$f(n^3)$ /2431/	yes	yes
Chang-Jin Li 1. (Lagrange)	$f(n^3)$ /1436/	$f(n^3)$ /1017/	yes	yes
Chang-Jin Li 2. (Lagrange)	$f(n^2)$ /783/	$f(n^2)$ /670/	yes	yes
Luh—Walker—Paul (Newton—Euler)	$f(n)$ /852/	$f(n)$ /738/	no	yes
Kane—Levinson (Kane)	$f(n)$ /646/	(fn) /394/	no	yes
Vukobratovic—Li—Kircanski (Newton—Euler)	$f(n^3)$ /992/	$f(n^3)$ /775/	yes	yes
Richard—Levesque (Appell)	$f(n)$ /834/	$f(n)$ /678/	no	yes
This paper (Appell)	$f(n^2)$ /984/	$f(n^2)$ /756/	yes	yes

to compute both the inverse and direct dynamics for robot manipulators. But the number of operations involved by these methods is of order $f(n^4)$ and $f(n^3)$ and much larger than the method proposed in this paper. The Newton—Euler method /13/ proposed by Luh—Walker and Paul, the Kane's method /22/ proposed by Kane and Levinson and the Appell's method /20/ proposed by

Richard and Levesque are comparable to the method of computational efficiency proposed in this paper but they can be used only to solve the inverse dynamics for robot manipulators, not the direct one. So, they cannot be applied to design the control system and the dynamic simulation for robot manipulators. The Kane's method /22/ seems to be very efficient in solving the inverse dynamics, but this method was used only to solve the inverse dynamics of a Stanford manipulator (a special type of manipulators). The method proposed in this paper requires 378 multiplications and 219 additions in solving the inverse dynamics of this Stanford manipulator.

The method developed by Vukobratovic, Li and Kircanski /14/ is able to compete with the method proposed in this paper, but the number of operations of this method depends on n^3. Hence, the method proposed in this paper is superior when investigating robot manipulators consisting of many links. The methods developed by Chang-Jin Li 610/, /11/ are really able to compete with the method proposed in this paper either in use or in computational efficiency. The number of operations involved by these methods approximates that of the method proposed in this paper. However, these methods are mainly developed for solving the inverse problem. Hence, the method proposed in this paper can be more advantageous than the methods proposed by Chang-Jin Li in solving the direct problem.

Finally, it should be noted that the method proposed in this paper is an efficient method to establish and to solve the equations of motion for robot manipulators.

ACKNOWLEDGEMENT

The author would like to thank Dr. Béla Király — University of Miskolc, Department of Mechanics — and Dr. Imre J. Rudas — Bánki Donát Polytechnic, Department of Computer Science — for their valuable comments and suggestions.

REFERENCES

1. Gantmacher, F.: Lectures in analytical mechanics. Mir Publishers. Moscow 1970
2. Meirovitch, L.: Methods of analytical dynamics. McGraw—Hill, New York 1970
3. Paul, R.P.: Robot manipulators: Mathematics, Programming and Control. MIT Press, Cambridge 1981
4. Shabana, A.A.: Dynamics of multibody systems. John Wiley and Sons. New York 1989

5. Denavit, J. - Hartenberg, R.S.: A kinematic notation for lower-pair mechanisms based on matrices. ASME Journal of Appl. Mech. 1955, 215—221

6. Hollerbach, J.M.: A recursive lagrangian formulation of manipulator dynamics and a comparative study of dynamics formulation complexity. IEEE Trans. on Syst. Man and Cybern. 1980 Nov., 730—736

7. Vukobratovic, M. - Pontkonjak, V.: Two new methods for computer forming of dynamic equations of active mechanisms. Journal of Mechanisms and Machine Theory, 1979, No. 3

8. Chang-Jin Li: A new method for dynamic analysis of robot manipulators. IEEE Int. Conf. on Robotics and Automation 1986. San Francisco, 1986 April 14—17

9. Bejczy, A.K. - Lee, S.: Robot arm dynamic reduction for control. Proc. of 22nd IEEE Conf. on Decision and Control. San Antonio. TX, 1983

10. Chang-Jin Li: A new method for dynamic analysis of robot manipulators. IEEE Trans. on Syst. Man and Cybern. 1988 Jan./Feb. 105—114

11. Chang-Jin Li: A new lagrangian formulation of dynamics for robot manipulators. ASME Journal of Dyn. Syst. Meas. and Control, 1989 Dec. 559—567

12. Stepanenko, Y. - Vukobratovic, M.: Dynamics of articulated open-chain active mechanisms. Math. Biosc. 1976, 137—170

13. Luh, J.S. - Walker, M.W. - Paul, R.P.: On-line computational scheme for mechanical manipulators. ASME Journal of Dyn. Syst. Meas. and Control. 1980, 103—110

14. Vukobratovic, M. - Li Shi-Gang - Kircanski, N.: An efficient procedure for generating dynamic manipulator models. Robotica, 1985, 147—152

15. Shir-Kuan Lin: A new composite body method for manipulator dynamics. Journal of Robotic Systems, 1991 Apr. 197—219

16. Ju, M.S. - Mansour, J.M.: Comparison of methods for developing the dynamics of rigid-body systems. Int. Journal of Robotics Research, 1989 Dec. 19—27

17. Desoyer, K. - Lugner, P.: Recursive formulation for the analytical or numerical application of the Gibbs—Appell method to the dynamics of robots. Robotica, 1989, 343—347

18. Stammers, C.W.: Dynamics of a robotic arm: Gibbs—Appell and Lagrange formulations compared. Proc. of the 1985 Conf. on Mechanisms and Machinery, Cranfield 1985 Sept. 17—18

19. Rudas, I.: Dynamic modelling of industrial robots based on Gibbs function (in Hungarian). Gép, 1983 nov. 424—429.

20. Richard, M.J. - Levesque, B.: An efficient dynamic formulation for a manipulator based on Appell's equations. Flexible Mechanism, Dynamics and Robot Trajectories. Presented at the 21st Biennial Mechanism Conference, Chicago. 1990 Sep. 16—19

21. Huston, R.L. - Passerallo, C.E. - Harlow, M.W.: Dynamics of multirigid-body systems. ASME Journal of Applied Mechanics 1983 Dec. 1071—1078

22. Kane, T.R. - Levinson, D.A.: The use of Kane's dynamical equations in robotics. Int. Journal of Robotics Research. 1983, 1—21

23. Shampine, L.F. - Gordon, M.K.: Computer solution of ordinary differential equations, the initial value problem. Freeman and Company, San Francisco 1975

Acta Technica Acad. Sci. Hung., 105(4), pp. 279—300 (1993)

CALCULATION OF SHRINK FITS WITH THE CONTACT PRESSURE DEPENDENT FRICTION COEFFICIENT TAKEN INTO CONSIDERATION

NÉMETH, V.*

(Received: 28 February 1990)

Shrink fits range among economically most favourable joint types. However, an accurate and reliable design of shrink fits requires that the contact problem of elastic bodies be solved and the microgeometrical characteristics be taken into consideration.

In the paper, a method has been developed for shrink fit calculations, permitting the effect of microgeometrical characteristics to be taken into consideration in up-to-date computational methods (finite element method, boundary element method). On the basis of the necessary parameters, the standard ISO fit to be specified is determined by the algorithm.

1. Introduction

In calculating for shrink fits, the fit to be determined is the one assuming transmission of given torque. For this purpose, a contact problem of two bodies that is the axle and the wheel must be solved, assuming unilateral relation between the two bodies. This means that they are either in contact or separated from each other. Accordingly, the normal component of the surface traction can be non-positive only. It makes the problem more difficult that the zone of the contact is unknown and thus the problem is non-linear.

Earlier, different "ad hoc" methods has been used to solve the contact problems of elastic bodies. Later, in the seventies, methods based on variational methods have been preferred. Two important trends can be observed: a mathematical approach based on functional analysis and an approach reflecting the engineering aspect.

*Németh, Viktor, H-4400 Nyíregyháza, Inczédy sor 11/B, III/15, Hungary

Akadémiai Kiadó, Budapest

The first trend is based on the theory of unilateral relations. Panagiotopoulos /1, 2/, Fremond /4/, Villaggio /5/, Kravchuk /6/ and Tereschchenko /7/ deal with the mathematical theory of unilateral relations.

Among authors representing the other threnḍ, Kalker /8, 9, 10/, Fredriksson /11, 12/, Andersson /13/, Páczelt /14, 15, 16/ and Rozin /17/ shall be mentioned first of all. By means of functional analysis, these authors treat the problems of unilateral relations in general. As a matter of fact, this leads to variational unequalities, a modern branch of functional analysis.

Naturally it leads to one of the modern branch of the functional analysis, to the variational inequalities.

Except for /11/ each of the mentioned works, typically neglects the influence of surface roughness, nonlinearity resulting from surface roughness and the coefficient of friction depending on contact pressure.

Among publications, /11/ was the first to investigate the change of the coefficient of friction while load is being applied on the analogy of plasticity followed by a work of Michalowski and Mroz /18/.

Scheffler /19/ investigates the effect of coefficient of friction, considered to be constant, on contact pressure in case of shrink fits.

In determination of the limiting torque of shrink fits, the dependence of the coefficient of friction on contact pressure cannot be neglected, nor can be the fact that the microgeometry and the hardness of the contact surfaces unequivocally determine the interpenetration of the two surfaces after fitting and that, on the other hand, has an effect on the contact pressure.

The intention of this paper is to give a method for calculating shrink fits that takes the unilateral relation into account and permits the mentioned problems, resulting from the influence of microgeometry, to be trated numerically. The contact force calculations are based on in situ shrink fit tests.

The method presented here is based on the finite element method and, from among the possible variational principles, it uses the minimum principle of potentional energy supplemented with the discontinuity potential taking into consideration the specified discontinuity (or fit allowance in case of shrink fits) /20/.

Concerning the laws describing the friction characteristics and the interaction of microgeometry and contact pressure this work relies upon the work of Kragelski and Mihin /21/ in first line.

2. Application of the selected variational principle to shrink fit calculations

Let the axle and the wheel be denoted by 1 and 2, respectively. The axle and the wheel are divided into N_1 and N_2 elements, so the total number of the elements is $N = N_1 + N_2$. The elements compose element pairs on the contact surface, the number of node pairs being n. The volume of the body is denoted by V. The body surfaces are separated into three domains: A_u for displacements, A_p for surface load, A_c^{ej} being the common contact surface of elements e and j.

Vectors and tensors with covariant and contravariant components are denoted by subscripts and superscripts, as required.

The strain tensor field derived from the displacement vector field is determined by continuity equation

$$a_{ij} = \frac{1}{2}\,(u_{i;j} + u_{j;i}) \tag{1}$$

where a denotes the covariant derivative, C^{ijkl} is the matrix of fourth order of the material constants; q_i is the volumetric force intensity vector; $(p_o)^i$ is the surface traction specified for A_p; p^i is the contact stress (used as a Lagrange multiplier); and $(h^{ej})_i$ is the specified discontinuity between elements e and j (Fig. 1).

All the free field equations, boundary and fit conditions of the boundary problem are given by the stationary value of functional

$$\pi(u_i, p^i) = \sum_{e=1}^{N} \Big[\int_{V^e} \frac{1}{2}\, C^{ijkl} a_{ij} a_{kl} - q^i u_i)\,dV - \int_{A_p^e} (p_o)^i u_i\, dA \Big] + \sum_{e=1}^{N-1} \sum_{j=e+1}^{N} \int_{A_c^{ej}} \Big[p^i\, (u^2)_i - (u^1)_i + (h^{ej})_i \Big]\, dA. \tag{2}$$

In case of the functional used, the continuity eauation, Hooke's law and the kinematical boundary conditions must be satisfied "a priori". This must be taken into consideration in approximation of the different fields. Let the discretization be carried out accordingly. Co-ordinates x^1, x^2, x^3 are denoted by x.

UNLOADED STATE

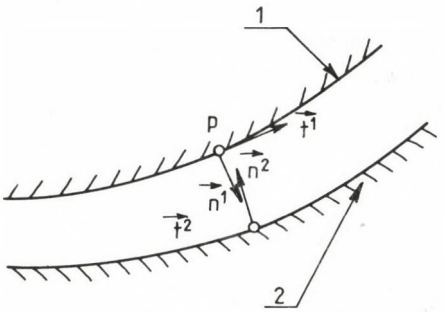

DEFORMED STATE

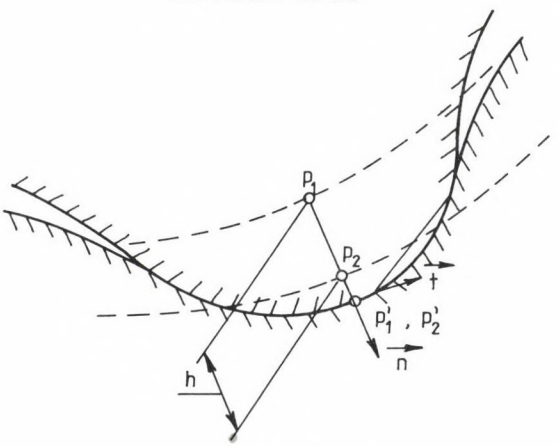

Fig. 1. Fit conditions
(kinematical $\mathbf{u}_C^2 - \mathbf{u}_C^1 + \mathbf{h} \geq \mathbf{0}$: dynamical $\mathbf{P}_C^2 + \mathbf{P}_C^1 = \mathbf{0}$)

Fields u_i, a_{ij}, p^i are approximated in the following way:

$$u_i \longrightarrow \phi^e(x)\mathbf{u}^e + \mathbf{u}_o^e, \tag{3}$$

$$a_{ij} \longrightarrow \partial\left[\phi^e(x)\mathbf{u}^e + \mathbf{u}_o^e\right] = \mathbf{B}^e(x)\mathbf{u}^e, \tag{4}$$

$$p^i \longrightarrow \mathbf{P}^e(x)\mathbf{p}^e, \tag{5}$$

where $\phi^e(x)$, $\mathbf{B}^e(x)$ and $\mathbf{p}^e(x)$ — approximation matrices; ∂ — differential operator matrix; $\mathbf{u}_o^e$ — displacement vector satisfying the kinematical boundary conditions specified for A_u; $\mathbf{u}^e$ and $\mathbf{p}^e$ are vectors composed of nodal values of given fields.

Let the following notation be introduced:

$$C^{ijkl} \longrightarrow \mathbf{D}(x), \tag{6}$$

$$q^i \longrightarrow \mathbf{q}(x), \tag{7}$$

$$(p_o)^i \longrightarrow \mathbf{p}_o(x), \tag{8}$$

$$(h^{ej})_i \longrightarrow \mathbf{h}(x), \tag{9}$$

$$\mathbf{K}^e = \int_{V^e} \left[\mathbf{B}^e(x)\right]^T \mathbf{D}^e(x)\mathbf{B}^e(x)dV, \tag{10}$$

$$\mathbf{f}^e = \int_{V^e} \left[\phi^e(x)\right]^T \mathbf{q}(x)dV + \int_{A_p^e} \left[\phi^e(x)\right]^T \mathbf{p}_o(x)dA, \tag{11}$$

$$\mathbf{A}^e = \int_{A_c^{ej}} \left[\mathbf{P}^e(x)\right]^T \phi^{\ominus}(x)dA, \tag{12}$$

$$\mathbf{b}^e = \int_{A_c^{ej}} \left[\mathbf{P}^e(x)\right]^T \mathbf{h}(x)dA, \tag{13}$$

where transposition is marked which superscript T. With the elements connected, we obtain equation

$$\pi(\mathbf{u},\mathbf{p}) = \frac{1}{2}\,\mathbf{u}^T\mathbf{K}\mathbf{u} - \mathbf{u}^T\mathbf{f} - \left[\mathbf{u}^T\mathbf{A}^* - (\mathbf{b}^*)^T\right]\mathbf{p} + C, \tag{14}$$

where $\mathbf{u}$ is the generalized displacement vector, $\mathbf{p}$ is the generalized surface traction vector and C is a constant. Making use of the Khun--Thucker theory of quadratic programming /23/, the potential energy (14) will be minimum if

$$\left.\begin{aligned} \mathbf{K}\mathbf{u} - \mathbf{f} - \mathbf{A}^*\mathbf{p} &= 0 \qquad (15a)\\ \mathbf{y} = \mathbf{A}^*\mathbf{u} - \mathbf{b}^* &\leqq 0 \qquad (15b)\\ \mathbf{p}^T\mathbf{y} &= 0 \qquad (15c) \end{aligned}\right\}$$

In case of both the wheel and the axle, the generalized displacement vector $\mathbf{u}$ is divided in two parts. The co-ordinates belonging to the contact surface are denoted by c while those co-ordinates belonging to the other nodes by e. Thus vector $\mathbf{u}$ can be written as

$$\mathbf{u} = \begin{bmatrix} \mathbf{u}_c^1 \\ \mathbf{u}_e^1 \\ \mathbf{u}_c^2 \\ \mathbf{u}_e^2 \end{bmatrix}. \tag{16}$$

If $\mathbf{K}, \mathbf{A}^*$ and $\mathbf{f}$ are partitioned accordingly, then the equation (15a) will be:

$$\begin{bmatrix} \mathbf{K}_{cc}^1 & \mathbf{K}_{ce}^1 & \mathbf{0} & \mathbf{0} \\ \mathbf{K}_{ec}^1 & \mathbf{K}_{ee}^1 & \mathbf{0} & \mathbf{0} \\ \mathbf{0} & \mathbf{0} & \mathbf{K}_{cc}^2 & \mathbf{K}_{ce}^2 \\ \mathbf{0} & \mathbf{0} & \mathbf{K}_{ec}^2 & \mathbf{K}_{ee}^2 \end{bmatrix} \begin{bmatrix} \mathbf{u}_c^1 \\ \mathbf{u}_e^1 \\ \mathbf{u}_c^2 \\ \mathbf{u}_e^2 \end{bmatrix} - \begin{bmatrix} \mathbf{f}_c^1 \\ \mathbf{f}_e^1 \\ \mathbf{f}_c^2 \\ \mathbf{f}_e^2 \end{bmatrix} - \begin{bmatrix} \mathbf{A}^T \\ \mathbf{0} \\ -\mathbf{A}^T \\ \mathbf{0} \end{bmatrix} \mathbf{p} = \mathbf{0}. \tag{17}$$

Introducing matrix

$$\mathbf{S}^i = \mathbf{K}_c^i - \mathbf{K}_{ce}^i (\mathbf{K}_{ee}^i)^{-1} \mathbf{K}_{ec}^i \tag{18}$$

and vector

$$\mathbf{w}^i = \mathbf{f}_c^i - \mathbf{K}_{ce}^i (\mathbf{K}_{ee}^i)^{-1} \mathbf{f}_e^i \qquad \Big\} \; i = 1,2 \tag{19}$$

we obtain from (17)

$$\mathbf{u}^1 = (\mathbf{S}^1)^{-1} (\mathbf{w}^1 + \mathbf{A}^T \mathbf{p}) \tag{20}$$

and

$$\mathbf{u}^2 = (\mathbf{S}^2)^{-1} (\mathbf{w}^2 - \mathbf{A}^T \mathbf{p}). \tag{21}$$

After partitioning equation (15b)

$$\mathbf{A}(\mathbf{u}_c^1 - \mathbf{u}_c^2) - \mathbf{b} \leqq \mathbf{0}. \tag{22}$$

Substituting expressions (20) and (21) into (22) and introducing notation

$$\mathbf{H} = \mathbf{A} \left[(\mathbf{S}^1)^{-1} + (\mathbf{S}^2)^{-1} \right] \mathbf{A}^T \tag{23}$$

and

$$\mathbf{z} = \mathbf{A}\left[(\mathbf{S}^1)^{-1}\mathbf{w}^1 - (\mathbf{S}^2)^{-1}\mathbf{w}^2\right] \tag{24}$$

we obtain

$$\mathbf{Hp} - \mathbf{b} + \mathbf{z} \leqq \mathbf{0}. \tag{25}$$

Since the loadability of shrink fits depends fundamentally on contact pressure and friction coefficient (besides geometrical parameters) and because the normal component of discontinuity $\mathbf{h}^{ej}$ has been stipulated (i.e. half of the fit allowance), equation (25) can be reduced. If we have to determine loadability, the problem can be treated as a normal contact problem considering that from among stress characteristics, the friction coefficient depends on pressure alone. However, this will be possible only if the bending load of the axle and the displacement of the two bodies as compared with each other need not be taken into consideration.

If the matrix composed of the 3k+1st elements of the 3k+1st rows of $\mathbf{H}$ is denoted by $\mathbf{H}_N$ and $-\mathbf{p}_N$, $\mathbf{b}_N$ and $\mathbf{z}_N$ are vectors composed of the 3k+1st elements of given vectors, then

$$\mathbf{H}_N\mathbf{p}_N + \mathbf{b}_N - \mathbf{z}_N = \mathbf{0} \tag{26}$$

can be written instead of (25).

Of course this transformation assumes that vectors $\mathbf{p}$ and $\mathbf{b}$ have been constructed in such a way contact pressure $\mathbf{p}$ and half of fit allowance h are the 3k+1st elements of these vectors and vector $\mathbf{z}$ corresponds them as well.

Note that the reduced equation (26) will also be obtained if the discontinuity potential is formulated so as to contain contact pressure p_N, displacement in normal direction u_N and the specified initial gap in normal direction h. In this case matrix $\mathbf{A}$ determined by (12) should contain n x 3n instead of 3n x 3n elements and vector $\mathbf{b}$ should have n elements only. Thus, using the expressions (23) and (24) inequality (26) would be obtained directly.

Since vector $\mathbf{p}_N$ contains the values of nodal contact pressure neither of its' elements can be negative, if a unilateral relation is assumed. Therefore, (26) must be completed with this condition.

In shrink fits, the specified fit assumes a constant fit allowance h. Introducing notation $\mathbf{y}_N$,

$$\mathbf{b}_N = \mathbf{y}_N\, h, \tag{27}$$

the programming problem to be solved can be written as

$$\mathbf{w} = \mathbf{H}_N\mathbf{p}_N + \mathbf{y}_N h - \mathbf{z}_N \geq \mathbf{0} \tag{28a}$$

$$\mathbf{p}_N \geq \mathbf{0}\,, \tag{28b}$$

$$\mathbf{p}_N^T\mathbf{w} = \mathbf{0} \tag{28c}$$

which is essentially dual problem No. III of quadratic programming. For solution of (28), different methods can be found in literature /22—24/. Should also the microgeometrical characteristics of surfaces, be taken into consideration, then the contacting bodies will approach to each other, i.e. fit allowance h decreases and therefore the pressure decreases as well.

3. Taking into consideration relation $h = h(p_N)$

When the axle and the wheel are manufactured a fit allowance h_o is used between the two structural elements. The fit diameter of the axle will then by 2h larger than the bore diameter of the weel. Upon assembly the distance between the contact surfaces reduces by a value depending on the microgeometric and hardness characteristics and contact pressure. In the literature, this is called fit loss /25/. Fit loss Δh belonging to the diameter used by Schmaltz /26/ is determined, as follows:

$$\Delta h = 5{,}4(R_{a1} + R_{a2}). \tag{29}$$

Relationship (29) takes only the mean roughness of the axle and wheel into consideration. According to research by Kragelski /27—29/ and Mihin /30, 31/ the surface layer in contact can be elastic unsaturated or saturated and plastic unsaturated (elastic-plastic) or saturated. The relationships for determination of the value of friction coefficient and Δh vary depending on the above four states. It shall therefore be investigated first which of the above states may be occur in case of shrink fits. According to /27/, elasto-plastic state will develop on the contact surface if the contact pressure is

$$p \geq \frac{14.5 \cdot HB_2^5(1 - \nu_2^2)}{\Delta_1^2 E_2^4}\,, \tag{30}$$

where HB_2 -- Brinell-hardness of the contact surface of the wheel, E_2 -- Young's modulus of the wheel, ν_2 -- Poisson's number and Δ_1 complex roughness characteristic of the contact surface of the axle. The Brinell-hardness shall be treated as a stress characteristic. Thus, if Nmm^{-2} is used as a unit of measurement, shall be multiplied by 9.81.

With relationship (30) investigated in case of characteristic of shrink fits, we find that practically only the elastic-plastic and the plastic saturated state can take place. According to /28/, Δh can be determined by means of the same relationship for both states. For the limit of slip,

$$\Delta h = - R_{max} \sqrt{\frac{p}{HB_2}}, \tag{31}$$

since the fit allowance corresponds to a negative initial gap. In terms of mean roughness, relationship (31) is

$$\Delta h = - 4.5 R_{a2} \sqrt{\frac{p}{HB_2}}, \tag{32}$$

where the fact that the surface of the bore is rougher than the surface specified for the axle has been utilized. Thus equation (28a) can be written as

$$\mathbf{H}\mathbf{p}_N + \mathbf{y}_N(h_o - \Delta h) - \mathbf{z}_N = \mathbf{0}. \tag{33}$$

The Hildreth--d'Esopo method based on the Gauss--Seidel algorithm /23/ will be modified in compliance with equations (28b), (28c) and (33). In doing so, equation (33) is written for node i and iteration step k. According to the Gauss--Seidel algorithm, the k-th approximation of pressure $(p_N)_j$ (j = = 1,2,...,i-1) is used in the k-th step. Thus (33) can be written as

$$\sum_{j=1}^{i-1} (H_N)_{ij}(p_N^k)_j + (H_N)_{ii}(p_N^k)_i + \sum_{j=i+1}^{n} (H_N)_{ij}(p_N^{k-1})_j + (y_N)_i h_o + \tag{34}$$

$$+ (y_N)_i 4.5 R_{a2} \sqrt{\frac{(p_N^k)_i}{HB_2}} - (z_N)_i = 0,$$

where the sign of inequality is omitted according to the Hildreth---d'Esopo method. Introducing notation

$$A_i = \sum_{j=1}^{i-1} (H_N)_{ij}(p_N^k)_j + \sum_{j=i+1}^{n} (H_N)_{ij}(p_N^{k-1})j + (y_N)_i h_o - (z_N)_i \tag{35}$$

and

$$B_i = - (y_N)_i \frac{4.5R_{a2}}{\sqrt{HB_2}}, \tag{36}$$

the equation for $(p_N^k)_i$ will be

$$(H_N)_{ii}(p_N^k)_i - B_i \sqrt{(p_N^k)_i} + A_i = 0. \tag{37}$$

First we take condition (28b) into consideration to show the case of unilateral connection. If the bodies separate from each other, then $(p_N^k)_i = 0$ that is $\Delta h = 0$, thus, in this case, the equation to be analysed is

$$(H_N)_{ii}(p_N^k)_i + A_i = 0, \tag{38}$$

from this

$$(p_N^k)_i = - A_i/(H_N)_{ii}. \tag{39}$$

Thus, if

$$- A_i/(H_N)_{ii} \leqq 0, \tag{40}$$

then the bodies will spearate from each other and, according to (28b), $(p_N^k)_i = 0$. On the other hand, if

$$- A_i/(H_N)_{ii} > 0, \tag{41}$$

then $(p_N^k)_i > 0$ and, according to (28c), $w = 0$. In this case, equation (37) is valid. From (37),

$$\sqrt{(p_N^k)_i} = \frac{B_i \pm \sqrt{B_i^2 - 4(H_N)_{ii}A_i}}{2(H_N)_{ii}}. \tag{42}$$

Since the decrease of the fit allowance is Δh, pressure $(p_N^k)_i$ from equation (42) is lower than the pressure calculatable in accordance with (39) that is with the reducing distance between the surfaces left out of consideration, i.e.

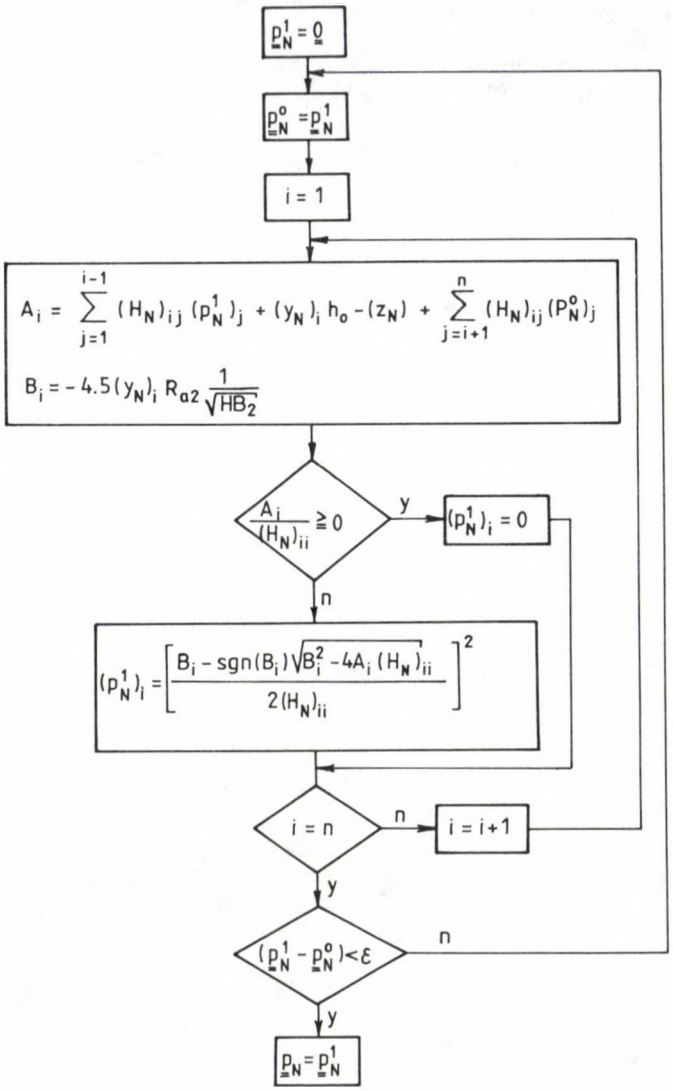

Fig. 2. Calculating the generalized contact pressure vector

$$\left[\frac{B_i \pm \sqrt{B_i^2 - 4(H_N)_{ii} A_i}}{2(H_N)_{ii}} \right]^2 < - \frac{A_i}{(H_N)_{ii}} . \tag{43}$$

Reducing inequality (43)

$$B_i^2 \pm B_i \sqrt{B_i^2 - 4(H_N)_{ii} A_i} < 0, \tag{44}$$

and taking (41) into account we obtain

$$\sqrt{B_i^2 - 4(H_N)_{ii}A_i} > |B_i| , \tag{45}$$

thus (44) will be satisfied, if the negative sign applies to $B_i > 0$ while the positive sign to $B_i < 0$. Therefore, the solution of (37) is

$$(p_N^k)_i = \left[\frac{B_i - \mathrm{sgn}(B_i)\sqrt{B_i^2 - 4(H_N)_{ii}A_i}}{2(H_N)_{ii}}\right]^2 . \tag{46}$$

Now we have all the relationships required for iteration. The Flow Diagram of the method is given in Fig. 2. Determination of initial value h_0 will be discussed later.

4. Calculation of limiting torque

In the knowledge of generalized contact pressure vector p_N, the pressure at given point of element e is

$$p(x,h) = \mathbf{P}^e(x)\mathbf{p}^e(h), \tag{47}$$

where the dependence of the contact pressure on the actual value of fit allowance $h = h_0 - \Delta h$ is indicated. The limiting torque of the joint upon slip will then be

$$M = \frac{d_1}{2}\sum_{e=1}^{N-1}\sum_{j=e+1}^{N}\int_{A_c^{ej}} \mu(p(x,h))p(x,h)dA, \tag{48}$$

where d_1 -- fit diameter and μ is the coefficient of friction depending on pressure.

In the previous section, we said that in shrink fits, elastic-plastic or plastic saturated state could occur on surface A_c. On the basis of /21/, elastic-plastic state will occur if

$$p < 0.0625HB_2, \tag{49}$$

otherwise the state is plastic saturated.

The pressure dependence of the friction coefficient is different in either of both states but the two relationships can be written in a lumped form according to /21/ as follows:

$$\mu = \frac{\tau_o}{HB_2} + \beta + k\,\Delta_1^{0.5}\left(\frac{p}{HB_2}\right)^{\lambda}, \tag{50a}$$

$$k = 0.5 \quad \text{and} \quad \lambda = 0.25 \quad \text{if} \quad p < 0.0625HB_2, \tag{50b}$$

$$k = 0.9 \quad \text{and} \quad \lambda = 0.5 \quad \text{if} \quad p \geq 0.0625HB_2. \tag{50c}$$

The frictional force results from molecular interaction as well as from the deformation of the highest points of roughness /31, 32/. In relationship (50a), the sum of the first two terms gives the so-called molecular friction coefficient. The value of the shear stress is

$$\tau_n = \tau_o + \beta p, \tag{51}$$

where τ_o and β are frictional characteristics, their values being determined experimentally /27, 33/. Should residual deformation occur in the contact zone, then, in molecular dimensions, the contact pressure and the normal stress will be equal to the Brinell-hardness of the material on the basis of /21/. Therefore, the molecular friction coefficient is

$$\mu_M = \frac{\tau_n}{p} = \frac{\tau_o}{HB} + \beta\,. \tag{52}$$

Thus the limiting torque of the joint can be calculated from (48) where function $u(p(x,h))$ shall be defined according to (50). If the integration according to (48) is made by means of the Gauss--Legendre quadrature formula, the values of the contact pressure and friction coefficient shall be calculated for the so-called Gauss-points.

5. Selection of the initial value of the iteration

The initial value of iteration h_o, is determined on the basis of the approximate assumption that the contact pressure is constant. Let b be the width of the wheel on the contact surface. Then the loadability of the joint will be

$$M = \frac{1}{2}\mu(\bar{p})d_1^2\pi b\bar{p}, \tag{53}$$

where $\bar{p}$ is the pressure considered to be constant. On the basis of taking into account (50) and (52),

$$\bar{p} = \frac{2M}{\left[\mu_M + k\Delta_1^{0.5}\left(\frac{\bar{p}}{HB_2}\right)^{\lambda}\right] d_1^2\pi b}. \tag{54}$$

Relationship (54) can be treated as a recursive formula of the method of successive approximations /34/. This method can be used if the absolute value of the first derivative of function (54) with respect to $\bar{p}$ is less then one. From (54) we get

$$\bar{p} = \frac{k\Delta_1^{0.5}}{2\mu(\bar{p})}\left(\frac{\bar{p}}{HB_2}\right)^{\lambda}, \tag{55}$$

which considering the values possible in practice, is certainly less than one. In this way, an initial value of $\bar{p} = 0$ can be used in recursive formula (54) for determination of $\bar{p}$.

On the basis of (32), the fit allowance loss according to $\bar{p}$ is

$$\Delta h = -4.5Ra_2\sqrt{\frac{\bar{p}}{HB_2}}. \tag{56}$$

If the contact pressure is assumed to be constant, the nodal values of h from (28a) will not be constant. The initial gap according to equation (28a) is

$$h_i = \frac{(z_N)_i - \bar{p}\sum_{j=1}^{n}(H_N)_{ij}}{(y_N)_i} + \Delta h \tag{57}$$

in the i-th node.

The initial value, h_o, may be the arithmetical mean of the values of h_i calculated from (57).

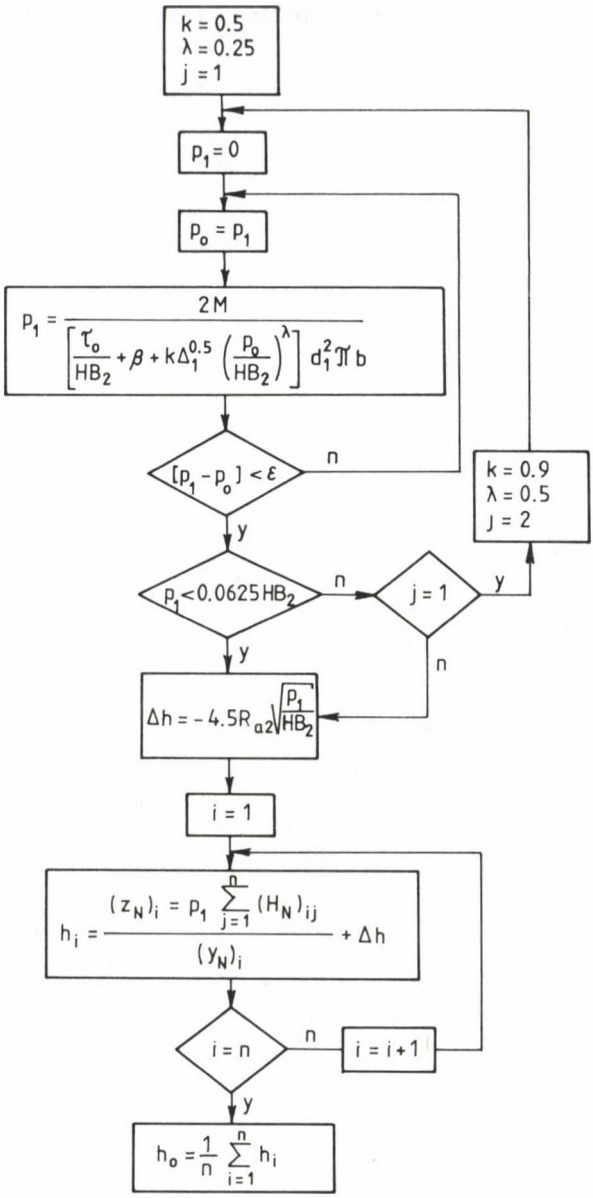

Fig. 3. Determination of initial value of fit allowance

$$h_o = \frac{1}{n} \sum_{i=1}^{n} h_i . \tag{58}$$

The Flow Diagram for calculation of h_o is given in Fig. 3.

6. Determination of the fit

The result of calculating for the frictional torque of shrink fits includes determination of the standard ISO fit where M is the limiting torque the value of which is usually double or triple as compared with the working torque.

Once the fit allowance h associated torque M is determined, then, using the standard hole tolerance system to determine the fit (with tolerance H provided for wheel bore), the upper limit deviation of the fit diameter of the axle must satisfy the following condition on the basis of /23/:

$$FE_1 \geq m(T_1 + T_2) + 2h, \tag{59}$$

where T_1 and T_2 are fit diameter tolerance range widths for the axle and wheel, $m = 0.35$ and $m = 0.5$ in case of manually adjusted or automatic manufacturing process, respectively.

The algorithm presented in the previous sections is suitable for calculation of torque M associated with given fit allowance h. Hence, in the calculation, the least upper limit deviation (FE_1) still satisfying inequality (59) shall be found for initial value h. After this, by means of the presented algorithm, torque M_o associated with fit allowance

$$h'_o = \frac{(FE_1)_o - m(T_1 + T_2)}{2} \tag{60}$$

shall be determined.

If $M_o < M$, the next ISO upper limit deviation for which $(FE_1)_1 > (FE_1)_o$ shall be formed. Otherwise the next value satisfying condition $(FE_1)_1 < (FE_1)_o$ shall be selected. According to (60), the value of fit allowance h_1 and then the value of torque M_1 associated with it shall be calculated and compared with M again. The procedure shall be continued until the least ISO upper limit deviation $(FE_1)_i$ is found for which $M_i \geq M$.

The problem can be programmed by defining the matrices of tolerance range T_{dm} lower limit deviation AE_{dq} for the computer. The matrix of the tolerance range gives the width of the tolerance range as a function of the ISO class and fit diameter. The matrix of the lower limit deviation gives the value of lower limit as a function of fit diameter, letter or serial number indicating the position of the tolerance range (in case of shrink

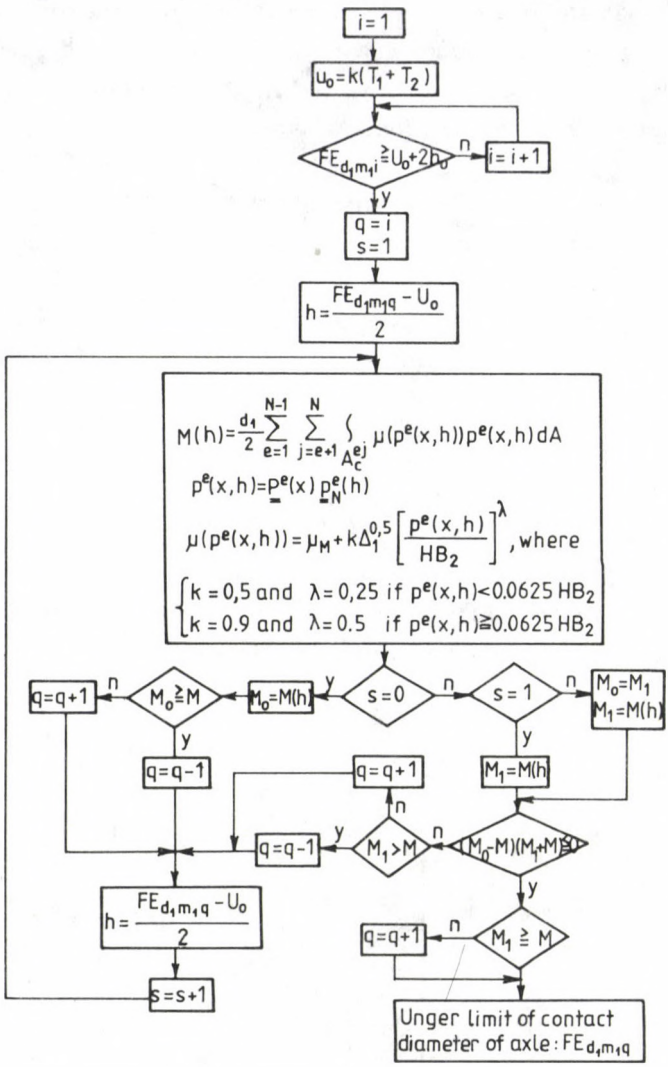

Fig. 4. Determination of fit

fitted joints: p, r, s, t, u, v, x, y, z, za, zb, zc). By means of these matrices, the upper limit depending on the fit diameter, class of fit and position of the tolerance range can be expressed as

$$FE_{dmq} = AE_{dq} + T_{dm}. \tag{61}$$

The algorithm for calculation of standard tolerance is given in Fig. 4.

Note, that the presented algorithm is advantageous in that the stiffness matrices requiring a significant computational effort, the load vectors and matrix $\mathbf{H}_N$, as well as vectors $\mathbf{y}_N$ and $\mathbf{z}_N$ that can be calculated from them need be determined only once, because they are constant during the iteration.

For maximum fit allowance, also strength calculations are required in addition to functional calculation of the elements. In the wheel, a limited plastic deformation shall reasonably be allowed as in this way, both the utilization and the safety of operation of the shrink fit can be improved. This work assumes plastic deformation in the domain of surface roughness only.

7. Numerical results

Compared below are results that can be obtained by means of different methods, including the well-known Lamé method assuming plane strain /25/. Therefore, a shrink fit between axle and wheel, illustrated in Fig. 5, is investigated.

Parameters:

d_o = 15 mm
d_1 = 40 mm
d_2 = 100 mm
b = 30 mm

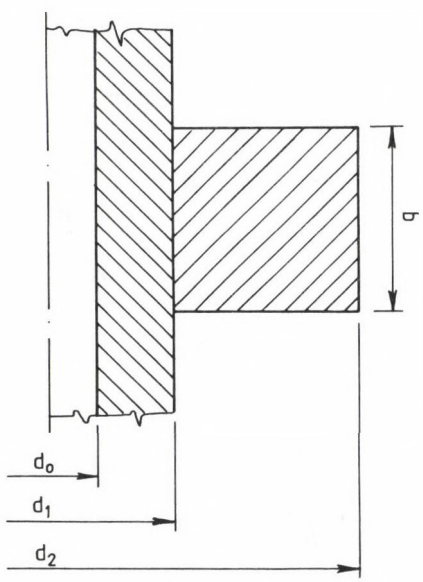

Fig. 5. The shrink fit investigated

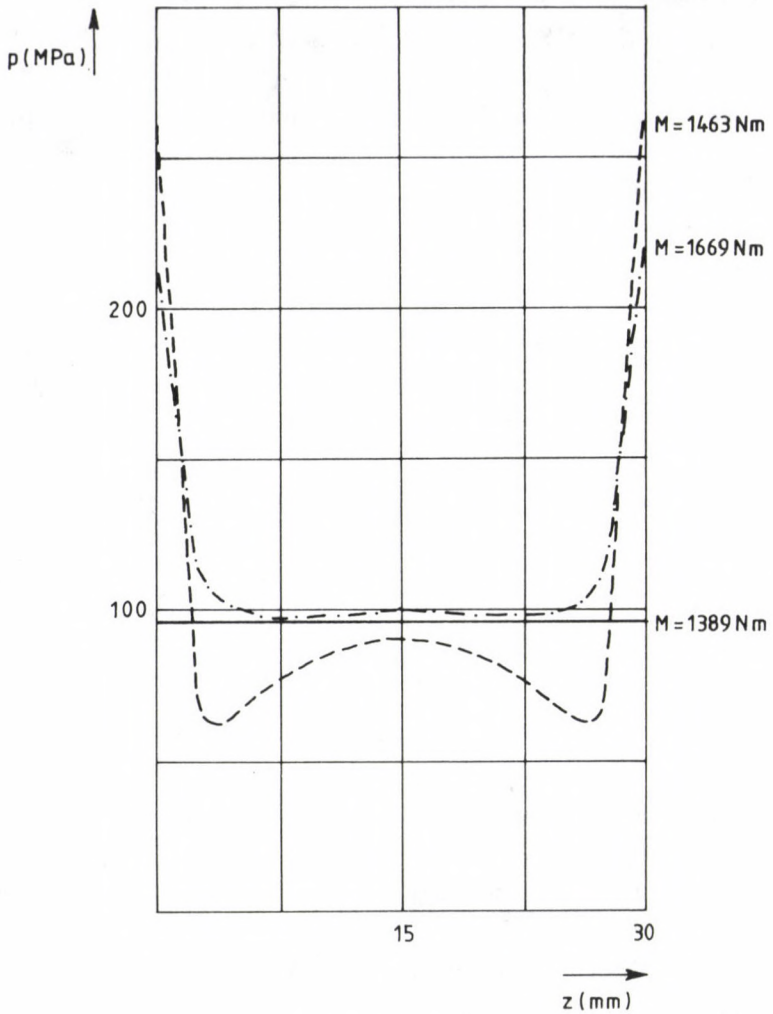

Fig. 6. Numerical results
(—— 1st method (Lamé), ----- 2nd method, -·-·- 3rd method)

h_o = 0.055 mm
$E_1 = E_2 = 2.1 \cdot 10^5$ Nmm^{-2}
$\nu_1 = \nu_2 = 0.3$
HB_2 = 2500 Nmm^{-2}
μ_M = 0.12
Δ_1 = 0.1
R_{a1} = 0.63 μm
R_{a2} = 1.25 μm

The Lamé formulas calculate the fit allowance loss and the friction coefficient on the basis of /29/ and /50/, respectively.

Another method investigated is a finite element method based on functional /2/ with, however, the contact pressure dependence of the fit allowance loss and friction coefficient left out of consideration (that is the procedure is similar to that used in the Lamé method).

The third method is that presented in this work. The results obtained are illustrated diagrammatically in Fig. 6 indicating the pressure distribution and limiting torque calculated by means of the different methods.

Lamé's constant contact pressure gives a good approximation for the internal domain of the wheel only. The pressure distribution obtained by the second method is similar to that according to other works /11, 19/ while the third method is a better approach to the actual measured distribution /25/. The value of limiting torque calculated by means of the third method lies above the value obtained by the second method becase in the third method, also the increase of the value of the friction coefficient in these domains as a result of increasing pressure at the edges of the wheel is taken into consideration.

8. Summary

Shrink fits range among economically most favourable joint types. However, an accurate and reliable design of shrink fits requires that the contact problem of elastic bodies be solved and the microgeometrical characteristics be taken into consideration.

The method presented here can be used first of all for shrink fit calculations but the algorithm developed to take into consideration the contact pressure dependent friction coefficient as well as the reducing distance between the surfaces is suited for use in other contact problems as well. Note that other variational principles lead to the programming problem according to /28/ as well, moreover, as shown in /35/, also the basic equation of the boundary element method can be written in a similar form in case of a discontinuity stipulated in the displacement field.

Hence, a method has been developed for shrink fit calculations, permitting the effect of microgeometrical characteristics to be taken into consideration in up-to-date computational methods (finite element method, boundary element method). On the basis of the necessary parameters, the standard ISO fit to be specified is determined by the algorithm.

REFERENCES

1. Panagiotopoulos, P.D.: Convex analysis and unilateral static problems. Ing. Archiv. 45 (1976), 55—68
2. Panagiotopoulos, P.D.: A variational inequality approach to the inelastic stress-unilateral analysis of cable-structures. Computer and Structures 6 (1976), 133—139
3. Panagiotopoulos, P.D.: Ungleichungsprobleme in der Mechanik. Habilitationsschrift. Aachen 1977
4. Fremond, M.: Dual formulations for potential and complementary energies. Unilateral boundary conditions. Applications to the finite element method. In: The Mathematics of Finite Elements and Applications. Academic Press 1973, 175—188
5. Villaggio, P.: A unilateral contact problem in linear elasticity. J. Elast. 10 (1980), 113—119
6. Kravchuk, A.C.: Postanovky zadachy o kontakte neskolkich deformiruemich tel kak zadachy nelineinovo programmirovania. Prikladnaia matematika i mechanika 42 (1978), 466—477 (in Russian)
7. Tereshenko, V.A.: O nekotorich formulirovkach metoda granitchsnich elementov. Prikladnaia matematika i mechanika 51 (1987), 616—627 (in Russian)
8. Kalker, J.J.: Variational principles of contact elastostatics. J. Inst. Maths. Applics. 20 (1977), 199—219
9. Kalker, J.J.: A survey of the mechanics of contact between solid bodies. ZAMM 57, T3—T17
10. Kalker, J.J.: Numerical contact elastostatics. Variational methods in the mechanics of solids. Ed.: S. Nemat-Nasser. Pergamon Press, Oxford 1980
11. Fredriksson, B.: On elastostatic contact problems with frictions. A finite element analysis. Linköping Studies in Science and Technology. Dissertations No. 6. Linköping 1976
12. Fredriksson, B. - Rydholm, G. - Sjöblom, P.: Variational inequalities in structural mechanics with emphasis on contact problems. Finite Elem. Nonlin. Mech. 2 (1978), 863—884
13. Andersson, T.: The second generation boundary element contact prgoram. In: Boundary Element Method in Engineering. Ed.: Brebbia, C.A. Springer Verlag 1982
14. Paczelt, I.: Primenenie kvadratichnovo programmirovania v kontaktnich zadachach teoriy uprugosty. Publ. Techn. Univ. for Heavy Industry (Miskolc). Series D. Natural Sci. 33 (1979), 171—221 (in Russian)
15. Páczelt, I.: Solution of elastic contact problems by the finite element displacement method. Acta Technica Acad. Sci. Hung. 82, 3—4 (1976), 353—375
16. Páczeli, I.: Contact problem studies in case of elastic systems. DSc. thesis. Miskolc 1981 (in Hungarian)
17. Rozin, L.A.: Variacionnie postanovki zadach dla uprugich system. Izd. Leningradskovo Universiteta 1978 (in Russian)
18. Michalowski, R. - Mroz, Z.: Associated and non-associated sliding rules in contact friction problems. Arch. mech. stosow. 30, No. 3 (1978), 259—276
19. Scheffler, S.: Berechnung elastisch-plastisch beanspruchter Pressverbände im Stillstand und bei Rotation mittels Finiter Elemente. VDI Zeitschriften 1. Nr. 117. Düsseldorf 1984
20. Páczeli, I. - Scharle, P.: The finite element method in continuum mechanics. Műszaki Könyvkiadó, Budapest 1987 (in Hungarian)
21. Kragelskij, I.V. - Mihin, N.M.: Friction and abrasion calculations for machine components. Műszaki Könyvkiadó, Budapest 1987 (in Hungarian)

22. Hildreth, C.G.: A quadratic programming procedure. Nav. Res. Log. Qu. 4. 1957

23. Künzi, H.P. - Krelle, W.: Nichlineare Programmierung. Springer Verlag, Berlin 1962

24. Fridman, V.M. - Chernina, V.S.: Reshenie zadachy a kontakte uprugich tel iteracionnim metodom. Izvestia AN Soviet-Union MTT. 1967. No. 1, 116—120 (in Russian)

25. Lendvay, P.: Strength calculation for connections brought about by pressing and contraction. Műszaki Könyvkiadó, Budapest 1977 (in Hungarian

26. Schmaltz: Technische Oberflächenkunde. Julius Springer-Verlag, Berlin 1936

27. Kragelski, I.V.: Ob ocenke svoistv materialov trutshichcia par. zavodskaia laboratoria, Tom. XXI (1968) (in Russian)

28. Kragelski, I.V.: Trenie i iznos. Mashinostroenie. Moscow 1968 (in Russian)

29. Kragelski, I.V. - Demkin, N.B.: Raschet plotshadei kasania nepodviznovo is skolziaatshevo kontaktov. V kn.: Elektricheskie kontakty. Energia. Moscow 1964 (in Russian)

30. Mihin, N.M.. Trenie v usloviiach plasticheskovo kontakta. Nauka. Moscow 1968 (in Russian)

31. Michin, N.M.: Vneshnee trenie tverdich tel. Nauka. Moscow 1977 (in Russian)

32. Gane, N. - Cox, J. M.: The microhardness of metals at very low loads. Phil. Mag., 22 (1970), 179, 881—884

33. Kawai, N. - Kondo, K. - Nakamura, T.: The frictional mechanism of surface of metals plastically deformed. Bulletin of the J. SME. 17 (1974), 108, 44—46

34. Kis, O. - Kovács, M.: Numerical methods. Műszaki Könyvkiadó, Budapest 1973 (in Hungarian)

35. Németh, V.: Application of the boundary element method to the case of discontinuity specified in the displacement field. 7th National Seminar of Machine Constructors. University of Heavy Industry, Miskolc, 29—31 May, 1989 (in Hungarian)

Acta Technica Acad. Sci. Hung., 105(4), pp. 301—326 (1993)

RECONSTRUCTION OF ROTOR BLADE LOADING FROM IN-FLIGHT MEASURED STRUCTURAL BLADE REACTIONS

Prof. Dr.-Ing. Dr. h.c.(H) H. ÖRY - Dipl.-Ing. H.W. LINDERT*

Institut für Leichtbau, RWTH Aachen, Federal Republic of Germany

(Received: 9 February 1994)

In this paper, a new method for reconstructing rotor blade air loads from measured structural blade reactions of the rotating rotor blade is presented. The measured structural blade reactions may consist of local bending moments, blade deformations, local accelerations or a combination of these. Using known structural and dynamic properties of the blade, the acting air loads on the blade can be reconstructed in the time and geometric domain. Reconstruction results from flight test measurements with Kamov-26 and Hughes 500 helicopters conducted in Hungary are presented in this paper. The efficiency of the employed reconstruction method is also confirmed by reconstructing high frequent blade vortex interactions.

Notation

{ }	vector
[ ]	matrix
C; [C]	damping; damping matrix
[E]	elasticity matrix
H; {H}	participation factor; vector of participation factors; generalized coordinate
K; [K]	stiffness; stiffness matrix
m; [m]	mass; mass matrix
P; {P}	force; force vector
y; {y};{Y}	deflection, blade deformation vector; vector of total blade deflection
$\{\eta\}$	eigenform vector
$[\Phi]$	modal matrix
ω	eigenfrequency
ζ	Lehr-damping factor
SDOF	Single degree of freedom system

indices

dyn	dynamic
gen	generalized
qs	quasi static

*Öry, Huba - Lindert, H.W., D-52062 Aachen, Wüllnerstr. 7, Germany

Akadémiai Kiadó, Budapest

Introduction

Due to their configuration and typical helicopter flight attitudes, the rotor blades of the main and tail rotor systems experience numerous instationary air loadings. Strong structural blade reactions occur particularly from blade vortex interactions (bvi) resulting in heavy dynamic loading of blades, rotor system and fuselage. A satisfying evaluation of such dynamic loadings is only possible if the acting air forces on the blades are known in their time histories and their geometric distribution on the blades. The acting air forces, respectively air loads, can be acquired from theoretical assumptions and calculations, measurements on model rotor blades in wind tunnel tests or from flight test measurements with actual rotor blades.

A method for reconstructing air loads on rotating rotor blades from measured structural blade reactions has been developed at the Institute for Lightweight Aerospace Structures of the Technical University in Aachen (Institut für Leichtbau; RWTH Aachen). The structural blade reactions may consist of local bending moments, blade deformations, local accelerations or a combination of these. The acting blade air loads are reconstructed from the measured blade reactions with the Reconstruction Method (RM), employing simple structural mechanical and dynamical relations and known structural blade properties, as are mass distribution, eigenfrequencies and eigenforms, damping etc. /5,6,13/.

The usual method for determining the air loads on a wing like structure consists of performing pressure measurements on the profile followed by the computation of the normal forces from the pressure data. The latter requires theoretical assumptions and empirical profile coefficient data. On a fixed wing system this method is feasible and relative unproblematic, whereas for rotating rotor blades pressure measurements are difficult to perform and may also result in high costs. The here proposed RM, on the other hand, is easy to use on rotor blades and comparatively inexpensive. Measurement of the required structural blade reactions is performed via commercial strain gauges and miniaturized accelerometers. Our experience has shown, that strain gauge measurement achieves very good results, whereas the use of accelerometers, for instance in blade tip proximity, yields less satisfying results. Both measurement devices can be applied very easily on the blade structure in contrary to pressure measurement devices usually requiring extensive preparation or even structural alteration of the test blade.

Extensive testing with instrumented model rotor blades has been performed in the wind tunnel of the Department of Aerospace Enginering of the Technical University in Aachen. Evaluation of the measured structural blade reactions with the RM showed very good results for the blade air loading at different simulated helicopter flight conditions. In several cases strong bvi were

reconstructed at the appropiate geometric blade locations with the expected interaction development in the time domain /5/. The consequent next step in validating the RM was to perform flight tests with full scale rotor blades on helicopters.

Flight testing with helicopters was possible due to a co-operations agreement between the Technical University in Budapest and the Technical University in Aachen. In a cooperation with the Institute for Vehicle Engineering in Budapest and our Institute, flight tests with Kamov-26 and Hughes 500 helicopters were performed in the autumns of 1989, 1990, and 1991. The helicopters were provided by the Hungarian Air Service at Budaörs. Evaluation of flight test data showed very good results for the blade air loadings. Strong bvi were reconstructed for some flight cases with the Hughes 500 helicopter. Viewing the reconstruction results derived from the measured blade reactions, the RM qualifies itself as an easy to use and efficient method for determining air loads on rotating rotor blades or also fixed wing structures.

Basic equations for the reconstruction method

The RM combines measured structural reactions with basic structural mechanical and dynamical relations in a numerical computations method for determining the acting forces on the considered structure. In our case, the structure is represented by the rotor blade with its specific structural and dynamical properties. An arbitrary spanwise air load on the rotating blade results in a singular elastic blade deformation. From the known blade deformation, respectively blade deflection, and including structural blade properties, the acting forces and their distribution can be determined. A solution to this inverse problem is realized in the RM, allowing the exact determination of the air loads on the rotating blade.

A detailed description of the theoretical background for the RM has allready been given in other papers /1 to 6,13,14,17, 18/. In this paper thus, only a short review of the basic relations will be presented. The special aspects concerning a reconstruction of air loads on a hinged rotating blade have been presented extensively in references /5/ and /6/. In the following description of the RM some basic assumptions concerning the mathematical rotor blade model must be taken into account. The rotor blade is modelled primarily as an one dimesional, linear elastic beam with lumped masses at appropiate locations representing the actual blade mass distribution. It is attached to the main rotor system by an exentric ideal flap hinge. Only the fixed body motion and the elastic blade deformation for the flap degree of freedom are regarded. In a first approximation the coupling between the flap, lag and pitch degrees of freedom are neglected. Coupling effects, nonetheless, can be considered in the RM by an adequate mathematical modelling of the blade structure. The structural mechanical and dynamic properties of the blade are governed by the elasticity matrix [E], abbreviated E-Matrix. The

static E-Matrix is known from theoretical computations or, as in our case, from measurement. The required eigenfrequencies and eigenforms of the rotating rotor blade are computed from the numerically centrifugally stiffened E-Matrix /5,6/.

Basically, the RM is a solution of the rotating rotor blade differential equation of motion

$$[m]\{\ddot{y}\} + [C]\{\dot{y}\} + [K]\{y\} = \{P\} \tag{1}$$

If y, $\dot{y}$ and $\ddot{y}$ are known, eq.(1) yields the sought force vector {P}. Usually, this is not the case. If, for example, only y(t) is known, then a double differentiation with the known problems in numeric differentiation is required. If on the other hand only $\ddot{y}$ is known, a double integration with unknown boundary conditions would be necessary to acquire the missing quantities. A solution to this dilemma can be achieved by generalizing eq.(1) allowing then the direct use of the measured reactions as input quantities. The first step to the generalization is to describe the total rotor blade deflection {Y} as a linear superposition of the rotating blade eigenmodes as follows

$$\begin{aligned} \{y\} &= \sum_{i=1}^{n} \{\eta\}_i H_i = [\Phi]\{H\} \\ \{\dot{y}\} &= \sum_{i=1}^{n} \{\eta\}_i \dot{H}_i = [\Phi]\{\dot{H}\} \\ \{\ddot{y}\} &= \sum_{i=1}^{n} \{\eta\}_i \ddot{H}_i = [\Phi]\{\ddot{H}\} \end{aligned} \tag{2}$$

The quantity $H_{(j)}$ denominates the generalized coordinate of the j_{th} eigenform. The Matrix [Φ] is the modal matrix containing the rotating blade eigenmodes including the fixed body mode due to the eccentric flap hinge. By incorporating eq.(2) in eq.(1) and then multiplying from the left with the transposed modal matrix, the generalized equation of motion for the rotating blade results

$$[\Phi]^T[m][\Phi]\{\ddot{H}\} + [\Phi]^T[C][\Phi]\{\dot{H}\} + [\Phi]^T[K][\Phi]\{H\} = [\Phi]^T\{P\} \tag{3}$$

With

$$\begin{aligned} [\Phi]^T[m][\Phi] &= [m_{gen}] && \textit{generalized mass} \\ [\Phi]^T[C][\Phi] &= [C_{gen}] && \textit{generalized damping} \\ [\Phi]^T[K][\Phi] &= [K_{gen}] && \textit{generalized stiffness} \\ [\Phi]^T\{P\} &= \{P_{gen}\} && \textit{generalized force} \end{aligned} \tag{4}$$

eq.(3) becomes

$$[\omega^2]^{-1}\{\ddot{H}\} + [K_{gen}]^{-1}[C_{gen}]\{\dot{H}\} + \{H\} = [K_{gen}]^{-1}\{P_{gen}\} \qquad (5)$$

Equation (5) is a system of j uncoupled differential equations each representing a single degree of freedom system (SDOF) corresponding to the j_{th} eigenfrequency of the modelled blade. For each eigenfrequency thus results an equation as

$$\frac{1}{\omega_j^2}\ddot{H}_j + \left(\frac{2\zeta_{gen_j}}{\omega_j}\right)\dot{H}_j = \left(\frac{P_{gen}}{K_{gen}}\right)_j - H_j \qquad (6)$$

$$\text{with} \quad \frac{C_{gen_j}}{K_{gen_j}} = \frac{2\zeta_{gen_j}}{\omega_j}$$

Equation (6) can be solved on the complex phase plane if certain boundary conditions are considered. The key to the solution of eq.(6) on the complex phase plane is an inversion of the known method for solving a SDOF differential equation of motion "graphically" on the complex phase plane /5,6/.

For a SDOF system the differential equation of motion can be solved numerically on the complex phase plane. If the time history of P(t) and the initial boundary conditions for x(t) and $\dot{x}(t)$ are known for the SDOF system, then a "graphical" plotting on the complex phase plane for constant time intervalls Δt yields the SDOF system motion coordinate x(t). If instead, the time history of x(t) is known, an inversion of this method allows the determination of the time history for P(t) if certain boundary conditions and assumptions hold. In Fig.1 the loci vectors of the arbitrarily oscillating mass m for three consecutive time instances t_j spaced at konstant time intervalls Δt are shown. Equation (7) describes the geometrical relations required for the inverse solution.

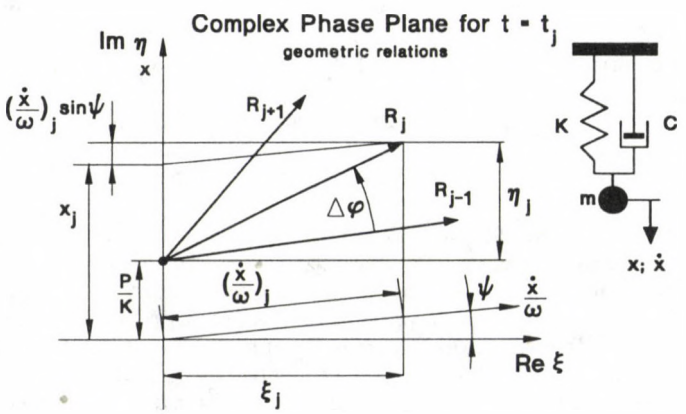

Fig.1 Complex phase plane with loci vectors for a SDOF system

$$\sin\psi = \xi \; ; \qquad \cos\psi = \sqrt{1-\xi^2} \; ; \qquad \Delta t = t_j - t_{j-1}$$
$$\chi = e^{-\zeta\omega\Delta t} \; ; \qquad \Delta\varphi = \omega\sqrt{1-\zeta^2}\,\Delta t \tag{7}$$

The sought force P(t) can be determined with eq.(8). This equation is derived from geometrical relations in Fig.1 with the assumption that the force P(t) be konstant during two consecutive time intervals Δt /5/.

$$\frac{\chi\, x_{j-1} - 2\cos(\Delta\varphi)\, x_j + \frac{1}{\chi}\, x_{j+1}}{\chi - 2\cos(\Delta\varphi) + \frac{1}{\chi}} = \frac{P}{K} \tag{8}$$

The above made assumption for the force time history is valid if the regarded time interval Δt is small enough in the physical sense. To solve eq.(6) respectivly eq.(5) requires the solution of eq.(8) for each rotor blade eigenfrequency $\omega_{(j)}$ substituting x with the generalized coordinate $H_{(j)}$. The result is the generalized force $(P/K)_{(j)gen}$ for each eigenfrequency $\omega_{(j)}$. The determined generalized forces can be easily transformed modaly to the sought force {P}. This modal retransformation is the Modal Reconstruction Method (MRM) affording the exact knowledge of all blade eigenmodes. If some modes are not known exactly, or are not available, the MRM then will yield faulty results. This is even more the case, if the air load has strong changes in its spanwise distribution.

Usually only the first few or some eigenfrequencies and modes are known exactly enough from measurement or theoretical calculation. In this case, implementation of an idea first suggested by Williams /7,8/ into the RM, results in a better convergence of the RM. Williams states that the reaction of a structure to an applied arbitrary force or forces will be the quasistatic response if the loading occurs very slowly, meaning quasistatically. Thus for quasistatic applied loadings the response can be determined directly from the elastic properties of the regarded structure. But if the applied loadings are not quasistatic, then inertial mass forces must be taken into account. A similar train of thought is realized in the "mode-acceleration-method" described by Craig /15/.

Implementation of William's idea into the RM, yields eq.(9), also denominated as the "reconstruction equation".

$$\sum_{i=1}^{k}\left(\left(\frac{P_{gen}}{K_{gen}}\right)_i - H_i\right)[m]\{\eta\}_i\omega_i^2 + [K]\{y\} = \{P\}$$
$$P_{dyn} \quad + \quad P_{qs} \quad = \quad P_{reconstructed} \tag{9}$$

From eq.(9), the air load on the blade can be determined exactly, even if only a few but significantly excited eigenmodes of the rotating blade are known. The first term on the left side

of the equation contains the purely dynamical forces resulting from mass inertia. The second term on the left equation side is the quasistatic part (force) obtained from the elastic blade properties, if the load were applied statically. Superposition of both terms leads to the acting air load on the rotating blade. Equation (9) is derived from eq.(1) by substituting the first two terms in eq.(1) with the terms on the right side of eq.(6).

As stated before, the RM requires knowledge of the rotating blade modal parameters. Centrifugal forces result in a de facto stiffening of the blade structure. As a consequence the eigenfrequencies of the rotating blade will be higher compared to those of the stationary blade. A measurement of the eigenfrequencies or eigenmodes on the rotating blade is very difficult if not impossible. These modal parameters are therefor computed numerically requiring herefor the knowledge of the stiffened blade E-Matrix. Since measurement of the E-Matrix on the rotating blade is equally impossible, the stiffened E-Matrix is computed numerically from the measured static E-Matrix /5,13/.

The modal participation factors $H_{(j)}$ are determined from eq.(2) with the measured structural blade reactions. In accordance to the type of measured reactions, the appropiate quantities are introduced into the rows and columns of the modal matrix $[\Phi]$. These are normalized modal bending moments if the measured reactions are bending moments; and normalized eigenmode amplitudes if the measured reactions are deformations or accelerations. The vector {Y} in eq.(2) contains respectivly the measured structural reactions. It is thus evident that a combination of different structural reaction types is possible.

Flight tests with helicopters

In the autumns of 1989, 1990, and 1991, flight tests with Kamov-26 and Hughes 500 helicopters were performed in Hungary. The helicopters were provided by the Hungarian Air Service at Budaörs airfield near Budapest. Figures 2a and 2b show the test helicopters. Before flight tests could commence, a test blade had to be prepared and instrumented. This was done in a hangar at the Budaörs airport and in a laboratory of the Institute for Vehicle Engineering at the Budapest Technical University. In Fig.3, a flow chart of the preparation, execution and data evaluation tasks belonging to a flight test is shown. A testing campaign can be subdivided in three phases.

I. Measurement of the structural blade properties, preparation and instrumentation of the test blade.
II. Preparation of the test helicopter and flight testing.
III. Preprocessing of the flight test data and evaluation with the reconstruction method.

Fig.2a *Kamov-26 helicopter before flight testing*

Fig.2b *MD Hughes 500 helicopter during flight testing*

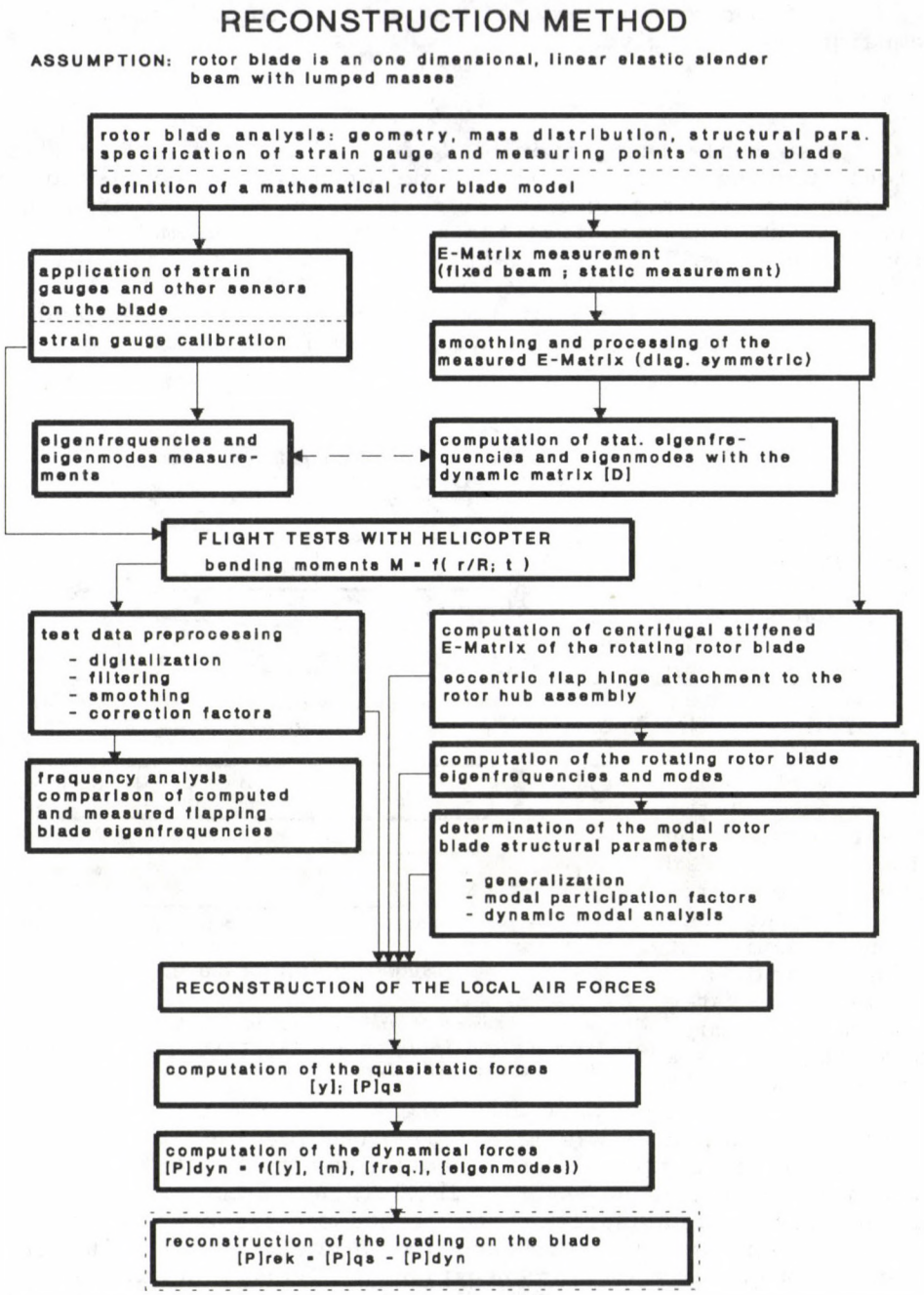

Fig.3 Flow chart of the reconstruction method employed in the helicopter flight testing

Next a short summary of the tasks performed in each test campaign phase is given.

Phase I

A suitable test rotor blade was chosen and prepared for flight testing. Part of the blade preparation consisted of applying the strain gauges to the rotor blade surface, wiring and calibration. Measurement of the structural and geometric blade properties as well as the static eigenfrequencies and E-Matrix were performed. The Kamov-26 and Hughes 500 rotor blades are shown in fig.4 with the positions of the applied strain gauges, lumped mass locations and E-Matrix measuring points.

The applied strain gauges are commercial 350 Ohm 6x12mm gauges. Since it was not allowed to damage or alterate the blade structure or surface, the strain gauges were applied directly to the prepared blade surface, centered on the 1/4-chord line. A measurement point consisted of two strain gauges on the upper and lower blade surfaces. Wiring between measurement points and the telemetric system used for transmitting the signals consisted of 0.25 mm diameter enameled copper wire. The wiring from the upper blade surface strain gauges was laid around the leading blade edge to the lower blade surface. The connection wiring to the telemetric system on the rotor hub was laid in vicinity of the trailing edge of the lower blade surface and bonded in place with special adhesive. Wiring and strain gauges were covered with thin self-adhesive tape showing no negative influence during flight testing.

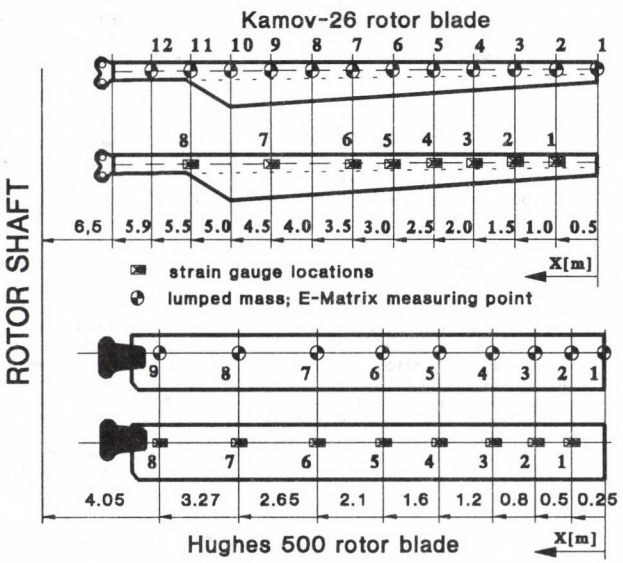

Fig.4 Kamov-26 and MD Hughes 500 helicopter rotor blades with strain gauge and E-Matrix measuring points and the lumped mass locations

The static E-Matrix for the flap degree of freedom is the most important structural parameter required for the RM. The E-Matrix measurements were performed on the horizontally fixed

blade by applying different singular forces at specific blade locations and measuring the elastic blade deformations at the E-Matrix measuring points. From the measured deformations the E-Matrix was derived by evaluating the deformation measurements with a least squares method. The E-Matrix measurements for the Kamov-26 rotor blade were conducted in Budaörs and the Hughes 500 blade E-Matrix measurements at the Budapest University. Figure 5 shows the horizontally fixed Hughes 500 rotor blade and the linear potentiometers used for deformation measurement. Calibration of the strain gauges for flap wise bending moments took place simultaneously during the E-Matrix measurements. The gauges showed linear elastic blade properties in the required measurement range.

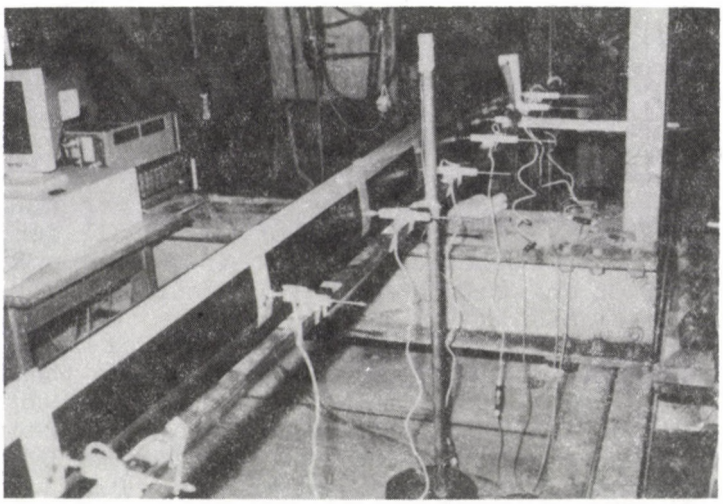

Fig.5 Horizontally fixed MD Hughes 500 rotor blade during E-Matrix measurement at the Institute for Vehicle Engineering, Budapest Technical University.

Phase II

Preparation of the test helicopter consisted mainly in the attachment of the test blade, mounting of the telemetric system, the flap angle and the rotor blade position sensors. Testing of all measurement apparatus parts, calibration of the flap angle sensor and testing of the data aquisition and storing systems are important tasks in this campaign phase.

The test blade on the Kamov-26 helicopter belonged to the lower rotor system. After its attachment to the rotor hub assembly, the strain gauges were connected to the telemetric system. The telemetric system itself was mounted in a special holder attached to a vacant lag damper fitting of the test blade. The telemetric system was mounted on top of the rotor hub during

flight testing with the Hughes 500 helicopter. Figures 6a and 6b show photographs of the telemetric system mounted on the test helicopters. The telemetric system transmits up to 12 different signals simultaneously at 5 milliwatts transmission power to a receiving unit located on the ground. The maximum transmission range is 300 meters in good transmitting conditions. Electric power is supplied by two 6 volt batteries.

Flap angle and rotor blade position are important parameters required for test data evaluation with the RM. A thin steel strip with applied strain gauges was attached at the flap hinge of the test blade as a flap angle sensor. The flapping motion of the test blade deformed the steel strip resulting in a signal proportional to the flapping angle of the blade. The flap angle sensor was calibrated beforehand in the hangar and measured the flapping angle in flight with an maximum error of ±0.25°. The flap angle sensor yielded very good results during all flight tests. The exact rotor blade position during rotor revolution is required so as to be able to assign the measured signals to a specific rotor azimuth angle. A mechanical micro-switch was herefor attached to the rotating part of the lower swash plate on the Kamov-26 helicopter as a position sensor. A steel pin on the non-rotating part of the lower swash plate activated the micro switch for a short intervall during each rotor revolution. The generated rectangular block signal allowed a positioning of the test blade with a maximum error of ±1°. There were no significant mechanical problems with the micro-switch during flight tests with the Kamov-26 helicopter. Because of the higher rotor speed (500 RPM) compared to the Kamov-26 rotor speed (275 RPM), the micro-switch method could not be used on the Hughes 500 helicopter. Instead an infrared emitting diode and phototransistor assembly was used as a switch. During each rotor revolution the phototransistor was activated for a short intervall thus generating a rectangular block signal. This sensor also worked very well with a maximum error of ±1° azimuth angle. The position signal generated by the micro-switch and diode-phototransistor assembly was also used to determine the exact rotor speed during testing.

Flight testing was performed during good weather conditions at Budaörs airfield. A test of the telemetric and data aquisition system was performed before each flight. The flight plan was discussed with the test pilot to ensure correct flight test parameters. A flight test run consisted of several hovering flights at different altitudes after take-off, followed by forward flights at different speeds and low altitude past the telemetric receiving unit. The flight test run was concluded with several hovering flights at different altitudes before landing. The transmitted signals were recorded on a special data recording system during the whole flight. Signals for at least 15 rotor revolutions were recorded in excellent signal quality during each flight past the telemetric receiving unit. This yielded sufficient data to guarantee an evaluation for each flight speed.

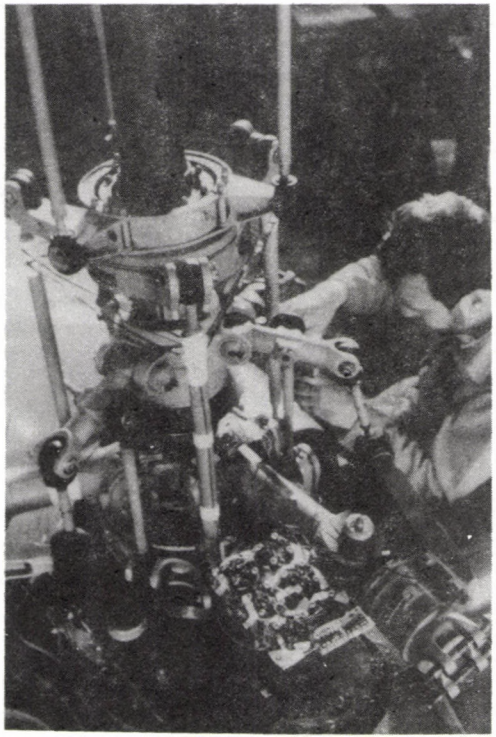

Fig.6a Lower rotor hub assembly of the Kamov-26 helicopter with the telemetric system attached to the vacant lag damper fitting on the blade flap arm (lower right photo corner).

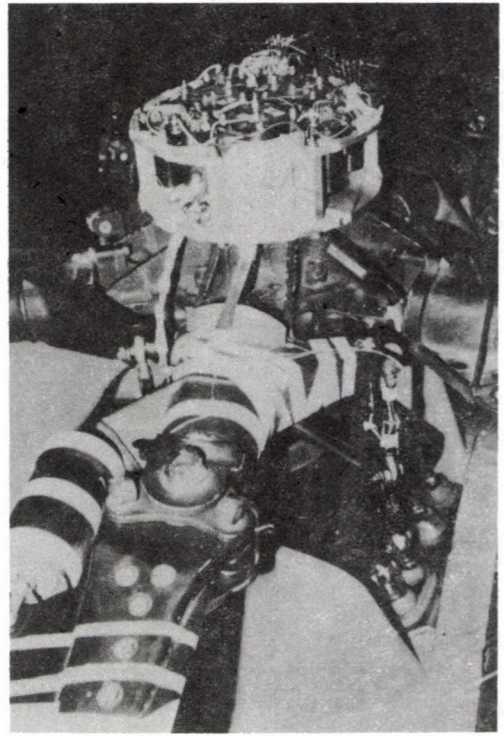

Fig.6b Telemetric system in its aluminium holder mounted on top of the MD Hughes 500 hub assembly. The flap signal sensor is visible in the center of the photo.

Collective pitch and actual flight speed during each helicopter pass of the receiving unit was recorded by the co-pilot. Six complete flight test runs were performed with the Kamov-26 helicopter and four with the Hughes 500.

Phase III

During flight testing, 7 strain gauge, the flap angle, the rotor position and 3 accelerometer signals were transmitted to the telemetric receiving unit. The recorded signals are analog signals which cannot be processed directly by PC software. Digitalization of the signals was performed with a 12-channel transient recorder ensuring simultaneous and time congruent transformation of the signal amplitudes. The sampling rate of the transient recorder was such, that at least 5 complete rotor revolutions were recorded per evaluation data file on diskettes. Noise and transmitting errors were extracted from the data bei appropiate numerical smoothing algorithms and a Fast-Fourier Transformation analysis and synthesis. This preprocessing of the data is also required to extricate the stepping in the data amplitudes introduced by the transient recorder digitalization, or otherwise the evaluation with the RM would show very poor results. Preprocessing of the data was performed without significant alteration of the data time histories quantitatively or qualitatively.

Data evaluation und reconstruction results

Evaluation of the test data with the RM was performed on a small Personal Computer. The time histories of the local flapwise bending moments were obtained from the recorded strain gauge signals by multiplying these with calibration factors measured before flight testing. The elastic blade deformation was determined from the time histories of the bending moments and with the structural and elastical blade properties. The flapping motion of the blade during rotor revolution was accounted for by superimposing the measured flap angle and a rigid body mode to the elastic blade deformation. The rigid body mode is not a linear mode, meaning a straight line, but the first rotating blade eigenmode, which is slightly curved on behalve of the eccentric flap hinge location. The resulting overall blade deflection is the input for the RM.

The reconstruction method described in this paper is a numerical method with the rotor blade modelled as a lumped mass system. The reconstructed air forces act on the lumped masses at their corresponding blade locations (see fig.4). Therefor on the tip mass (mass #1) a non-zero force is reconstructed, which is physically not correct. As each mass location has a definite distance to the next strain gauge location the measured local bending moment at this strain gauge location and the leverage distance to the mass location define a singular force at the mass

location. A shorter distance between strain gauge and mass location would mean a bigger force for the same local bending moment. Nonetheless the reconstructed forces at the mass locations describe the actual continuous air loading on the blade correctly. The reconstructed singular forces can be transformed into a continuous air load distribution with an appropiate transformation algorithm /18,19/. The above said must be kept in mind, viewing the following presented results of the air load reconstructions.

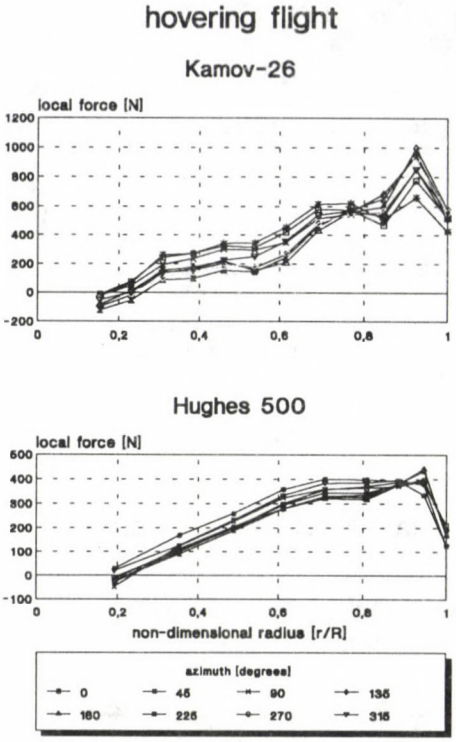

Fig.7 Reconstructed local blade air forces during hover for both helicopters

Some typical reconstruction results of the evaluated flight tests with the Kamov-26 and the Hughes 500 helicopter will be presented next. The reconstructed air forces for the hovering flight of both helicopters show an expected spanwise distribution. The reconstructed rotor lift corresponds very well with the actual helicopter weight measured before flight testing. The reconstructed air loads are depicted in fig.7 whereby the singular local forces are connected by lines to visualize the spanwise air load distribution. The Hughes distribution possibly shows an influence of the air load caused by a weak blade vortex interaction. From the reconstructed air forces computed helicopter rolling and pitching moments are of negligible size, which should be expected in trimmed out flight.

The following forward flight reconstruction results belong to the Kamov-26 helicopter flying at 80 km/h and 140 km/h. The rotor speed is 280 RPM and collective pitch ranges between 7° and 9°. Flight altitude was about 50 meters. In fig.8 the measured flap angle during one rotor revolution for the hovering, 80 km/h and 140 km/h flight case is shown. It is noticeable that the maximum flap angle recedes towards smaller azimuth angles the higher the flight speed is.

The measured local bending moments for both flight speeds depicted in fig.9 show the effect of flight speed on the spanwise moment distribution. At the lower flight speed the major part of

the measured moment distribution is negative, meaning also a negative deformation of the rotor blade. The blade is curved downward (see also fig.10). At the higher flight speed of 140 km/h the moment distribution has more positive parts and is more heavily loaded. This means that the elastic blade deformation oscillates strongly from negative to positive curvature and vice versa as also seen in fig.10.

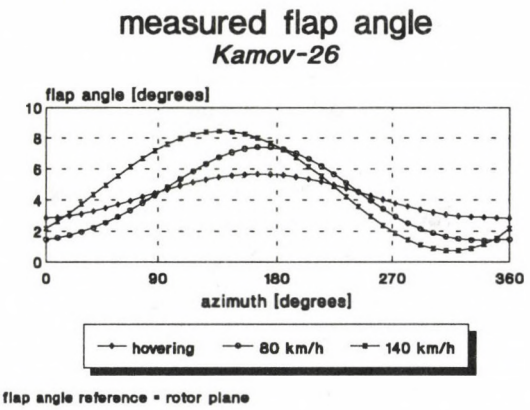

Fig.8 Measured Kamov-26 flap angle during one rotor revolution

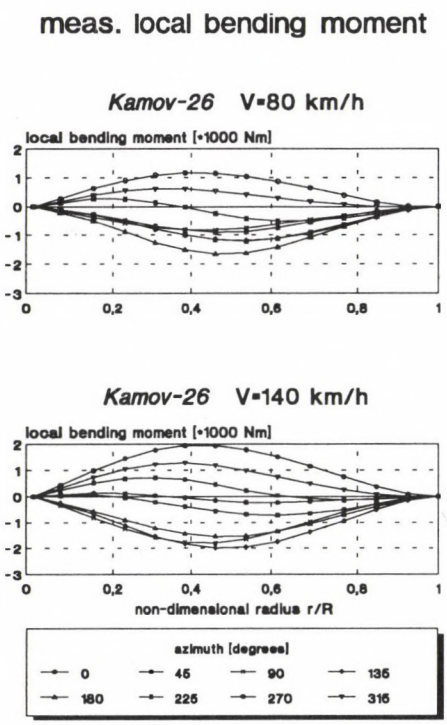

Fig.9 Kamov-26 rotor blade measured local bending moments during one rotor revolution (forward flight).

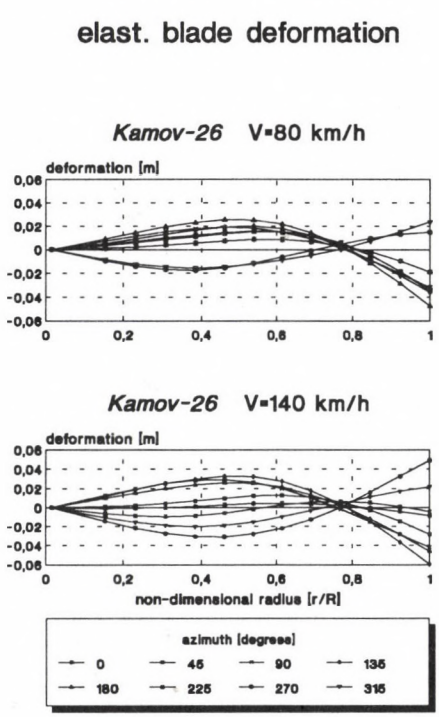

Fig.10 Kamov-26 rotor blade elastic blade deformation during one rotor revolution (forward flight)

It is also noticeable from fig.10, that the blade oscillates mainly in the second rotating eigenmode with some third

eigenmode portions beeing present. The first rotating eigenmode is the "rigid body mode", which defines the flap angle and is not seen in fig.10 as only the elastic blade deformation has been plotted. Superposition of the measured flap angle and the elastic blade deformation from fig.10 yields the overall blade deflection depicted in fig.11. The overall blade deflection is based on the rotor plane as reference plane.

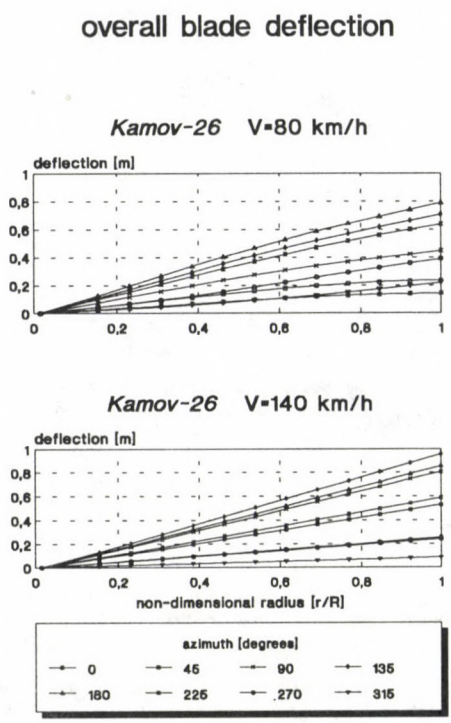

Fig.11 Kamov-26 rotor blade total blade deflection during one rotor revolution (forward flight)

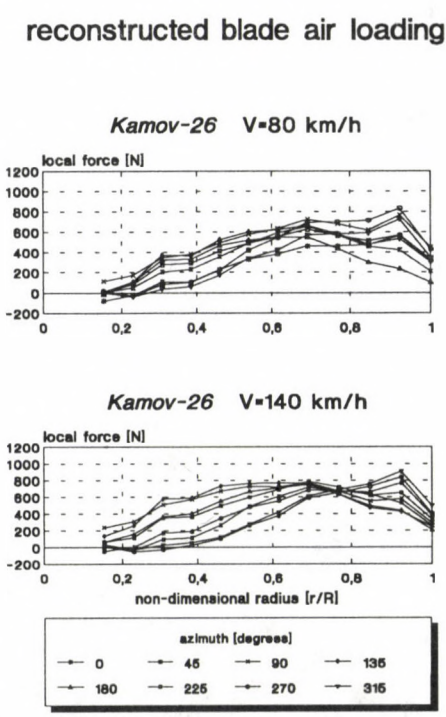

Fig.12 Kamov-26 rotor blade reconstructed local air forces during one rotor revolution (forward flight)

Reconstructed local air forces for both flight speeds are shown in fig.12. In the 80 km/h flight speed case, a relative constant spanwise air force distribution during one rotor revolution is present. This is not so at 140 km/h flight speed. For the advancing blade, between 0° and 180° azimuth angle, the central part of the blade is higher loaded than at the tip and vice versa for the retreating blade (between 180° and 360°). This effect is typical due to the higher air flow at the blade profile for the advancing blade in combination with the cyclic change in blade pitch during one rotor revolution. Cyclic pitch reduces the effective angle of attack for the advancing blade and it is increased for the retreating blade. If this were not so the resulting air forces on the blade would induce a strong helicopter rolling moment to the left. For the advancing blade, the effective blade angle of attack is reduced substantially at the

tip, resulting in a smaller air loading. At the middle part of the blade, the effective angle of attack is still high enough to generate a high blade loading in combination with the augmented air flow due to rotor revolution and forward flight speed. For the retreating blade the contrary is true. A high blade loading is induced at the tip, due to the increase of the effective angle of attack. The middle part of the blade experiences a much lower air flow speed than during the advancing phase. Thus the blade loading is much less and can even achieve negative loads in the innermost blade region, as seen in fig.12. Qualitative representation of the reconstructed local forces are shown in fig.13. Rotor rotation is counter clockwise and the shown distribution are the reconstructed local forces of the test blade during one rotor revolution. At 0° azimuth angle the test blade is positioned exact aft.

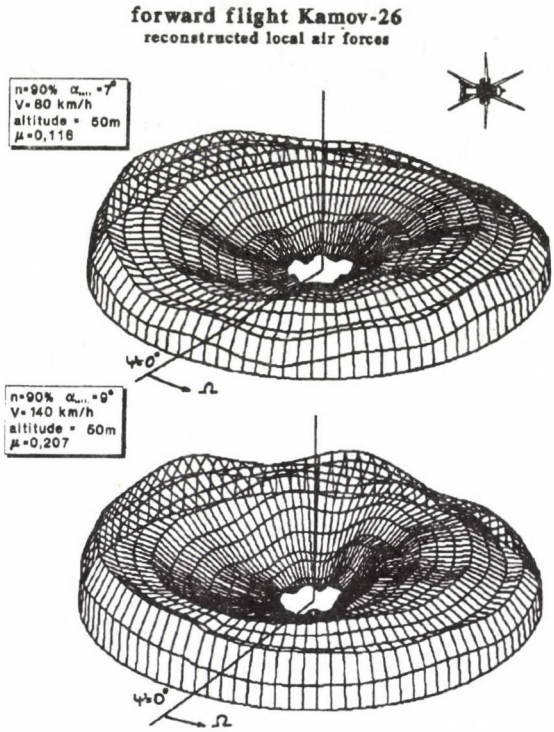

Fig.13 Kamov-26 rotor blade reconstructed local air forces during one rotor revolution (qualitative representation)

Forward flight reconstruction results of the Hughes 500 helicopter show similar results. Its main rotor system is a conventional 5-bladed rotor with aluminium blades. Nominal rotorspeed is about 500 RPM. During forward flight, mean collective pitch ranges between 5° and 9°. The following results belong to forward flight speeds of 180 km/h and 36 km/h.

The measured flap angles during one revolution are shown in fig.14. In contrary to the Kamov-26 helicopter, the maximum flap angle location wanders to higher azimuth angles for higher flight speeds. Again the reference plane is the helicopter rotor plane. It is also noticeable that while the Kamov-26 flapping angle during hovering oscillates strongly this is not the case for the Hughes 500. This is probably due to the different rotor systems of both helicopters.

The elastic blade deformation and the reconstructed local forces for the high speed flight case are shown in fig.15. Here again, the advancing blade has a more heavily loaded blade middle part reaching a loading peak at about 180° azimuth angle. The retreating blade experiences a rise in the tip loading and a decrease in the inner part of the blade. A negative force development is also noted for the innermost blade portion (270°). At about 0° azimuth angle a disturbance in the blade tip region is present which could result from a bvi and interference with the helicopter tail boom. A qualitative representation of the reconstructed forces is shown in fig. 16.

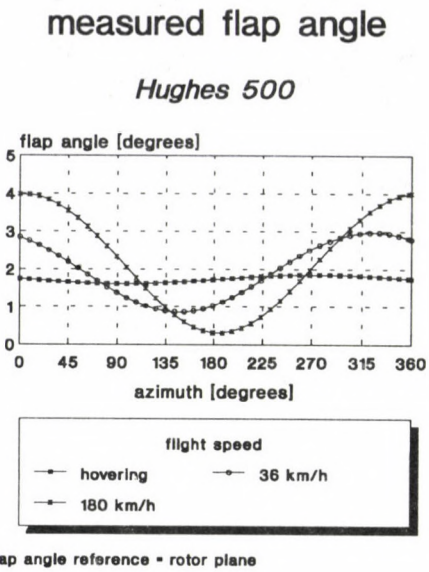

Fig.14 MD Hughes 500 measured flap angle during one rotor revolution

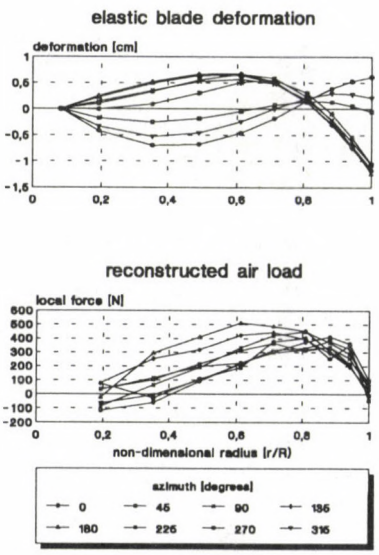

Fig.15 Elastic blade deformation and reconstructed local air forces for the MD Hughes 500 during one rotor revolution

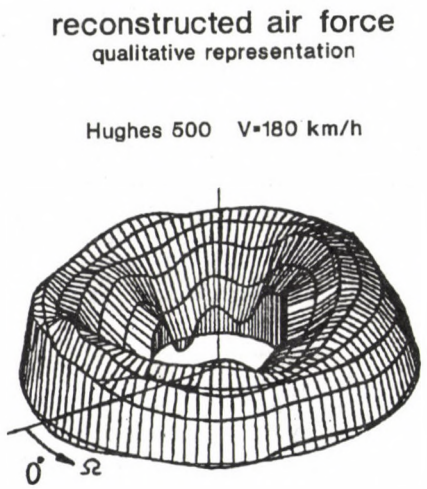

Fig.16 MD Hughes 500 reconstructed local air forces (qualitative representation)

An interesting case is the Hughes 500 at 36 km/h flight speed. Under certain flight circumstances, bvi may occur. Tip vortices of preceding rotor blades encounter the following blade and influence its generation of lift. By passing at close distance underneath the following blade, the tip vortices induce strong air flows perpendicular to the blade profile resulting in a disturbed spanwise load distribution. Such bvi are also responsible for strong vibrational inputs to the blade, rotor hub assembly and fuselage and may also create strong noise. The magnitude of bvi and their locations is mainly governed by the helicopter flight parameters. Depending on flight attitude and flight speed, bvi occur at typical blade locations and azimuth angles during each rotor revolution. The following reconstruction result shows very clearly such bvi on the Hughes 500 blade.

In fig.17 the qualitative representation of the reconstructed forces on the blade show two distinct bvi. Disturbances of the spanwise air load are located at about 80° and 280° azimuth angle. The bvi at 80° is shown in fig.18 for azimuth angles from 68° till 117°. On behalve of the disturbing tip vortice the air load at the blade tip is increased and decreased further inboard. As the interaction continues, the bvi wanders blade inwards. The influence of such a bvi on the blade lift generation ist not negligible any more. In fig.19, the reconstructed force at mass #2 of the test blade is plotted against the azimuth angle. Beginning at about 45°, a decrease in the local force is noted followed by an increase at about 90°. According to the flow orientation in the disturbing tip vortice this should be expected. At about 280° the second interaction at this blade location can be seen starting with an increase followed by a sharp decrease in the reconstructed local force. This too is expected due to the flow orientation in the vortice. The time histories of both bvi follow a sinusoidal pattern also typical of a perpendicular bvi. The second bvi is weaker than the first due to deterioration of the disturbing tip vortices. Regarding the time histories for both force disturbances, which actually result from the same vortices, no doubt is left that the shown effect on blade air loading is originating from bvi.

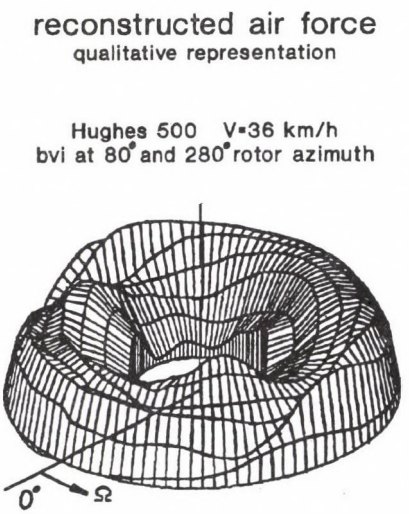

Fig.17 MD Hughes 500 reconstructed blade local air forces at a flight speed of 36km/h with blade vortex interactions

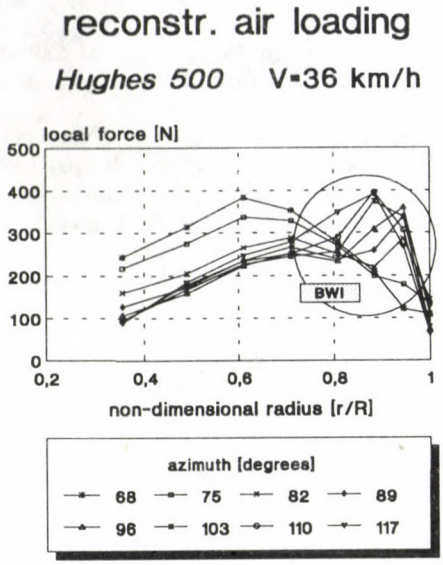

Fig.18 Reconstructed primary blade vortex interaction on the MD Hughes 500 rotor blade at a flight speed of 36km/h

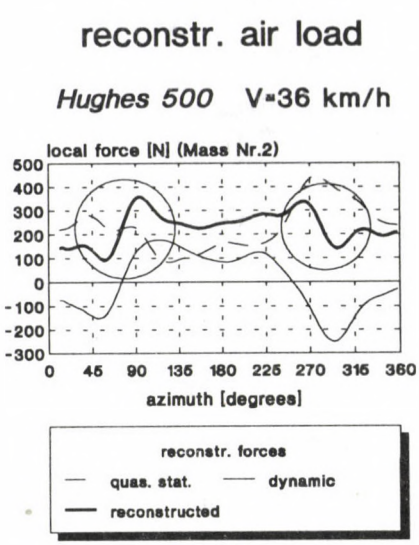

Fig.19 MD Hughes 500 reconstructed local air force at mass #2 with blade vortex interaction at about 80° and 280° azimuth angle

Conclusion

With this paper a new method for determining the air loading on a rotating rotor blade from measured structural blade responses has been presented. Exact knowledge of the blade structural parameters and a modal analysis are required for the described reconstruction method. Evaluation of model rotor blade test data from wind tunnel testing showed very good results. The next consequent step was to validate the method with response data measured during flight testing with helicopters. These were performed in Hungary with Kamov-26 and Hughes 500 helicopters. Execution and evaluation of the flight tests was described in this paper.

Even though only 7 strain gauge signals per test blade were measured, the reconstruction results are very good. The data aquisition system with the telemetric system as main part worked very well and recommends itself as a non-problematic method for data transmission during helicopter flight testing. The reconstruction results show, that in a first approximation coupling of the blade degrees of freedom may be neglected. This is even more so, regarding the first torsional eigenfrequency lying much higher than the first two blade flap eigenfrequencies. Nonetheless, furthergoing investigations must clarify the influence of coupling in the reconstruction method. Further development of

the reconstruction method regarding coupling is necessary and under way.

From the reconstruction results presented in this paper, it can be concluded, that the reconstruction method is suitable for an efficient determination of aerodynamic effects and air loads on rotating rotor blades in the time and geometric domain. High data sampling rates are feasible, which ensure high quality evaluation of high frequent effects as are the bvi on the Hughes 500 rotor blade. Another important aspect of the method is, that relativ few sensors, e.g. strain gauges, are required to obtain good reconstruction results of the air loading. From the known overall blade deflection and with appropiate aerodynamic relations an estimation of self induced air loads on the blade is possible as well /13/. If the acceleration time history of the blade-hub attachment is known, then the helicopter motion induced inertia forces on the blade can also be determined /13/. The above presented reconstruction method proved to be a relative easy to use and inexpensive alternative to complex pressure measurement techniques on rotating rotor blades or any fixed wing configuration. The method itself can also be employed to determine the acting forces on any technical structure as long as the required structural parameters are known.

Acknowledgement

We would like to thank our hungarian partners of the Institute for Vehicle Engineering at the Budapest Technical University, Dr. Istvan Steiger and Dr. Tamas Gausz, for their invaluable help and assistance during flight testing and the preparations for the test campaigns. Thanks also to the Hungarian Air Service for the use of the test helicopters, and especially to Dr. Istvan Gyurkovics, without whose considerable help and engagement the flight tests would not have been possible.

References

1. Öry, H. / Glaser, H. / Holzdeppe, D.:Transient external loads or interface forces reconstructed from structural response measurements. International Conference Spacecraft Structures Proceedings, 12/1985 Toulouse France.

2. Holzdeppe, D. / Öry, H.: Reconstruction of instationary wind load distribution on structures from measured structural response time histories. Journal of Wind Engineering and Industrial Aerodynamics, Vol. 28 (1988) pp. 231-240.

3. Öry, H. / Holzdeppe, D.: Reconstruction of forcing functions based on measured structural responses. 2nd International Symposium on aeroelasticity and structural dynamics, April 1985 RWTH-Aachen.

4. Öry, H. / Glaser, H. / Holzdeppe, D.: Quality of modal analysis and reconstruction of forcing functions based on measured output data. 4th International Modal Analysis Conference (IMAC), Februar 1986 Los Angeles U.S.A.

5. Öry, H. / Lindert, H.W.: Ermittlung der Luftkraftverteilung am rotierenden Rotorblatt aus gemessenen Strukturreaktionen. Proceedings der DGLR-Jahrestagung. September 1992, Bremen, Deutschland.

6. Öry, H. / Lindert, H.W.: Reconstruction of spanwise air load distribution on rotorblades from structural flight test data. Proceedings of the 18th European Rotorcraft Forum, September 1992 in Avignon, Frankreich.

7. Williams, D. / Jones, R.P.N.: Dynamic loads in aeroplanes under given impulsive loads with particular reference to landing and gust loads on a large flying boat. Aeronautical Research Council, Technical Report No.2221, 1948.

8. Williams, D.: The principals underlying the dynamic stressing of aeroplanes. Journal of the Royal Aeronautical Society, 1951 pp. 362-381.

9. Gaukroger, D.R. / Hassal, C.J.W.: Measurement of vibratory displacements of a rotating blade. Vertica Vol.2 1978, pp. 111-120,

10. Gaukroger, D.R. / Payen, D.B. / Walker, A.R.: Application of strain gauge analysis. Sixth European Rotorcraft and Powered Lift aircraft Forum, September 1980 Bristol, England

11. Walker, A.R. / Payen, D.B.: Experimental application of strain pattern analysis (SPA) - Wind tunnel and flight test results. Vertica Vol.14,No.3, 1990 pp.345-359.

12. Scheiman, J. / Ludi, L.H.: Qualitative evaluation of effect of helicopter tip vortex on blade airloads. NASA-TN-D-1637, 1963.

13. Holzdeppe, D.: Beitrag zur Versuchstechnischen Ermittlung der instationären aerodynamischen Belastungen eines Rotorblattes aus Messungen mechanischer Reaktionen des Systems. Dissertation an der RWTH-Aachen, 1987.

14. Glaser, H.: Beitrag zur Ermittlung dynamischer Interfacekräfte zwischen elastischen Teilstrukturen mittels gemessener Strukturantworten. Dissertation an der RWTH-Aachen, 1987

15. Craig, R.: Structural Dynamics - An Introduction to Computer Methods. John Wiley & Sons, New York-Chichester-Brisbane-Toronto 1981

16. William G. Bousman: Estimation of blade airloads from rotor blade bending moments. Proceedings of the Thirteenth European Rotorcraft Forum, September 8-11, 1987 in Arles, France

17. Lindert, H.W.: Arbeits und Ergebnisberichte des Teilprojektes C3 des Sonderforschungsbereiches 25 der DFG

18. Öry, H. / Lindert, H.W.: Calculation of rotor blade air loads from measured structural response data. Zeitschrift für Flugwissenschaften und Weltraumforschung, Vol.17. No.4, August 1993

Acta Technica Acad. Sci. Hung., 105(4), pp. 325—340 (1993)

ACCELERATED EXAMINATION OF THE FATIGUE OF PISTON ENGINES AND RECIPROCATING COMPRESSORS

PÁSZTOR, E.*

(Received: 17 October 1989)

The accelerated examination of the fatigue of piston machines has developed from the procedure elaborated for the determination of friction losses in reciprocating internal combustion engines. In this article, such a procedure is introduced for the determination of friction losses where the engine is operated with the help of external drive within a closed work process. In this case, the mechanical loading of the engine can be, in fact, increased arbitrarily. Together with the increase in the mechanical loading of the engine, the friction and wear, as well as the possibility of fatigue failure will also increase. As a result of the above effects, an accelerated fatigue process is starting in the engine, which significantly reduces the period of the endurance test.

1. Introduction. Importance of the procedure

The life examination of reciprocating internal combustion engines and compressors has proved to be a long-lasting and very expensive procedure. For the determination of service-life or the reliability of the engine, 2-3 thousands of service-hours are required under actual operating conditions if thorough examinations are in question; and they call for an examination period of nearly one year. All those involve the fact that an engine test-bench together with all the complementary instruments and equipment will be in continuous use for nearly a year, the overall expenditure of which represent already a non-negligible share among the expenses spent for development. If in addition to the above expenses, those required for the fuel supply and the wages of the personnel operating the engine are also taken into consideration, then it can be easily seen that the development of an

*Pásztor, Endre, H-1221 Budapest, Honfoglalás út 48/b, Hungary

Akadémiai Kiadó, Budapest

engine-type requiring generally the execution of several endurance tests is a very expensive procedure lasting over more years.

The aim of treating this procedure in this article is to overcome those problems mentioned above by elaborating an examination method the adoption of which contributes to a significant reduction in the period required for the carrying-out of the endurance test of reciprocating machines by the acceleration of the rate of fatigue.

The theory and practice of this method is described here, first of all, with respect to the reciprocating internal combustion engines, however it can be applied to the examination of reciprocating compressors, too.

2. Description of the theoretical basis needed for the examination and the experimental equipment

2.1. Preliminaries of procedure

For determining the friction losses of reciprocating internal combustion engines, author has developed the method based upon the rotation of engines by external drive, the use of which allows a more accurate determination of friction losses than has been possible so far /1—4/. This procedure is suitable for — in addition to determination of friction losses — solving other problems, too, connected with the determination of such parameters which otherwise could not be determined in case of engines operating under actual service conditions, due to the inaccuracy of measurement methods /5/.

As an example, the following can be mentioned: the determination of the reduction in friction losses of engines, in case of using additives in lubricating oil which can reduce the friction and wear /6/, as well as the effect of the filtration grade of lubricating oil exerted upon the friction losses and wear.

The method used for the accelerated examination of the fatigue of reciprocating machines has been developed from the procedure elaborated for the determination of friction wear. Considering that there is sufficient amount of the scientific literature available for studying this procedure, the procedure itself is not described here, however, the individual measurement results connected with the determination of friction losses are used in the elaboration of the accelerated examination method for the fatigue of engines, or else, in proving the applicability of the procedure.

The governing idea of the accelerated examination of engine's fatigue is the fact that by increasing the mechanical and thermal load of engines, as well as by the proper selection of the characteristics of the work processes, an accelerated fatigue process can be brought about. It his case, the engine operates in a closed work process without heat transfer (combustion process) with the help of external drive. Due to this, the possibility of changes in the mechanical and thermal load of the engine is, in fact, ensured between limits taken arbitrarily, which is the basis of the accelerated examination method of the fatigue. Under actual service conditions, and with an engine operated by combution process, the arbitrary change and, first of all, the increase of the mechanical load cannot be performed, and as a consequence, neither an accelerated fatigue process, nor an accelerated service-life examination could be carried out under actual service conditions.

2.2. Description of the theory of procedure, and the testing apparatus

The scheme of the apparatus suitable for the realization of the accelerated examination of fatigue is shown in Fig. 1. Reciprocating internal combustion engine 1 operates in a closed work process. Suction taken place from air-reservoir 4, and the exhaust of the engine gets also into the same reservoir 4. The two air-reservoirs are connected with a pipe-line equipped with a metering orifice 5 of the air volume for the purpose of determining the air-intake of the engine.

The engine operates without combustion process, and this solution serves as a basis for the possibility of determining the friction losses of the engine. Accordingly, the engine should be rotated externally by a drive motor. In our examinations, there was a torque-measuring balance-type electric engine 2 applied in a way shown in Fig. 1. With the help of the direct current torque-measuring engine of balance-type, the engine speed can be regulated accurately, and the total torque-absorption of the engine can be measured with accuracy. When the losses of non-friction character are subtracted from the total torque-absorption of the engine, the friction losses of it can be calculated.

In the cooling system of the engine, oil is circulated instead of water. By adjusting arbitrarily the temperature of oil circulated in oil-boiler 11, the thermal state of the engine, or more exactly, the temperature of the engine components performing rotation or reciprocating movement can be, in fact, adjusted to an arbitrary extent.

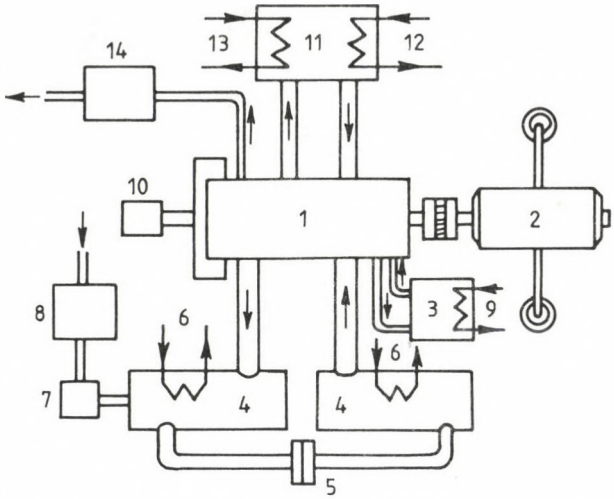

Fig. 1. Scheme of the apparatus suitable for the accelerated examination of fatigue (1 — Engine to be examined, 2 — Torque-measuring balance-type electric motor, 3 — Governor of lubricating-oil temperature, 4 — Air-reservoirs, 5 — Metering orifice, 6 — Heating, 7 — Pressure governor, 8 — Air compressor, 9 — Cooling, 10 — Piston-travel transducer, 11 — Oil boiler, 12 — Cooling, 13 — Heating, 14 — Device metering the volume of crank-case gases)

The so-called crank-case gas losses resulting from the imperfect sealing between the piston and the cylinder walls are measured continuously with the help of measuring device 14, since the quantity of crank-case gases, or the extent of their increase, respectively, provide utterly important information on the fatigue of the engine.

The pressure values measured within the two air-reservoirs are essentially identical, and only a minimal pressure deifference prevailing in them is brought about by the pressure-loss of the metering orifice.

The pressure within the air-reservoirs can be adjusted to an arbitrary extent with the help of air compressor 8 and pressure governor 7. The air compressor serves only for the compensation of crank-case gas losses, so a compressor of only minimal performance, i.e. max. 2-3 KW is required for this purpose.

With the help of the pressure change within the air-reservoirs, the average pressure of the work process in the engine examined, and accordingly, its mechanical load due to the gas pressure can be varied to an arbitrary extent. This possibility serves as one of the bases for the accelerated testing method of the engine's fatigue.

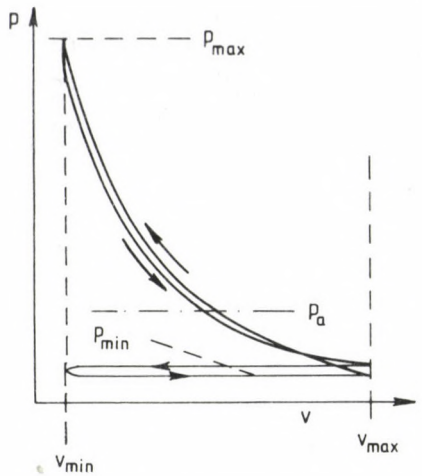

Fig. 2. Idealized p-v diagram of the work process of an externally driven engine without heat transfer

The work process of the engine operating without combustion process is shown in the p - v diagram plotted in Fig. 2. In the figure, average pressure p_a responsible for the greater part of the mechanical load of the engine is also indicated. In accordance with the work process taking place without combustion, indicated mean pressure p_i is zero, moreover it is negative to a small extent, due to the losses arisen. Consequently, average pressure p_a and indicated mean pressure p_i should be separated sharply from each other, because the former one is characteristic of the mechanical load of the engine, while the latter one characterizes the available power of it.

For the purpose of determination of average pressure p_a as a basic characteristic of the engine, average process p_a can be determined -- while the processes of suction and exhaustion, and those of compression and expansion are taken identical, as it is shown in Fig. 2 -- with a good approximation as follows.

As a matter of fact, average pressure p_a can be determined also without the simplifying conditions above, with the help of accurate determination of the characteristics of the work process taking place without heat transfer /4/. According to the investigations of author performed so far, the difference between the final results of the two procedures does not exceed 1%:

$$p_a = \frac{1}{2}\left(p_{min} + \frac{1}{v_{max} - v_{min}} \int_{v_{min}}^{v_{max}} p\,dv\right) \qquad (1)$$

where p_{min} and p_{max} are the lowest and highest pressure values, respectively, of the work process. With a good approximation, the value of p_{min} agrees with that of the pressure built up in air-reservoirs 4. v_{max} and v_{min} are the specific volumes of the working medium in the bottom- and top-dead-centres, respectively.

With respect to the determination of average pressure p_a, compression and expansion are considered such polytropic changes of state which are very near the isentropic ones. With the help of Poisson-ratio valid for the polytropic change of state, equation (1) will have the following form:

$$p_a = \frac{1}{2}\left(p_{min} + \frac{p_{min} \cdot v_{max}^{\underline{n}}}{v_{max} - v_{min}} \int_{v_{min}}^{v_{max}} \frac{dv}{v^{\underline{n}}}\right) \tag{2}$$

where $\underline{n}$ is the average polytropic exponent of the compression and expansion processes.

In the work process examined, both the compression and the expansion are of cooled character owing to the omission of heat transfer. In case of cooled compression and constant isentropic exponent κ, the value of polytropic exponent $\underline{n}$ is reduced, while it increases in case of expansion. The two contradictory changes compensate each other with a good approximation. According to these considerations, first of all, the change in the value of κ should be taken into consideration. Due to theoretical considerations which here cannot be detailed, the value of κ depends, first of all, upon compression ratio $\varepsilon = v_{max}/v_{min}$. With the increase of ε, on the one hand, maximum temperature T_{max} of the work process — which presently coincides with the final temperature of compression — also increases, and on the other hand, due to the increase of ε, the working medium is transformed in an ever growing rate into combustion products as a consequence of the closed work process, because during the operation of the engine only the leakage losses are to be compensated, which — at most — amount only to 0.2-0.3% of the engine's fuel consumption.

According to our repeated iteration calculations, polytropic exponent $\underline{n}$ varies as a function of compression ratio ε in a way shown in Fig. 3. This relationship was used for the determination of average pressure p_a.

With the value of compression ratio $\varepsilon = v_{max}/v_{min}$ introduced in relationship (2), and performing the operations assigned, the following relationship is obtained for the value of p_a:

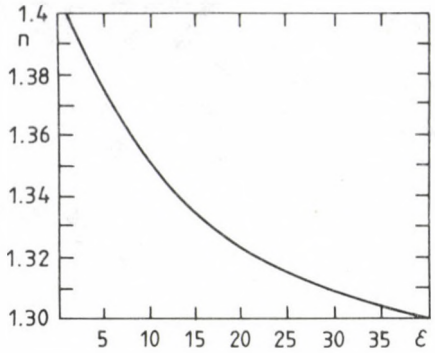

Fig. 3. Variation in the polytropic exponent n of compression and expansion as a function of compression ratio ε

$$p_a = \frac{p_{min}}{2}\left[1 + \frac{\varepsilon^n - \varepsilon}{(n-1)\,(\varepsilon-1)}\right] \tag{3}$$

The calculation results obtained by using relationship (3) are shown in Fig. 4, where functional relationship $\varepsilon = f(n)$ represented in Fig. 3. is taken into consideration. Functions p_{max} = const. are also plotted in the figure. This figure plays a decisive role in our further considerations, and it will be referred to still several times in this paper.

With the proper modification of the work process developed in the engine -- which modification can be easily implemented in the case without combustion process -- basically two kinds of the accelerated service-life examination can be carried out.

In case, average pressure p_a of the work process -- and together with it, the average mechanical load of the engine -- increases in a way that the peak pressure increases only moderately in the meantime, then an accelerated wear process will develop in the engine. The increase of the mechanical load of the engine brings about, first of all, the friction losses of it, and in turn, the increase of it necessarily involves the increase of the wear-rate. In Fig. 5, the increase of the wear losses and that of friction mean pressure p_f, respectively, depending on the thermal state of the engine are shown as a function of average pressure p_a and the mechanical load propor-

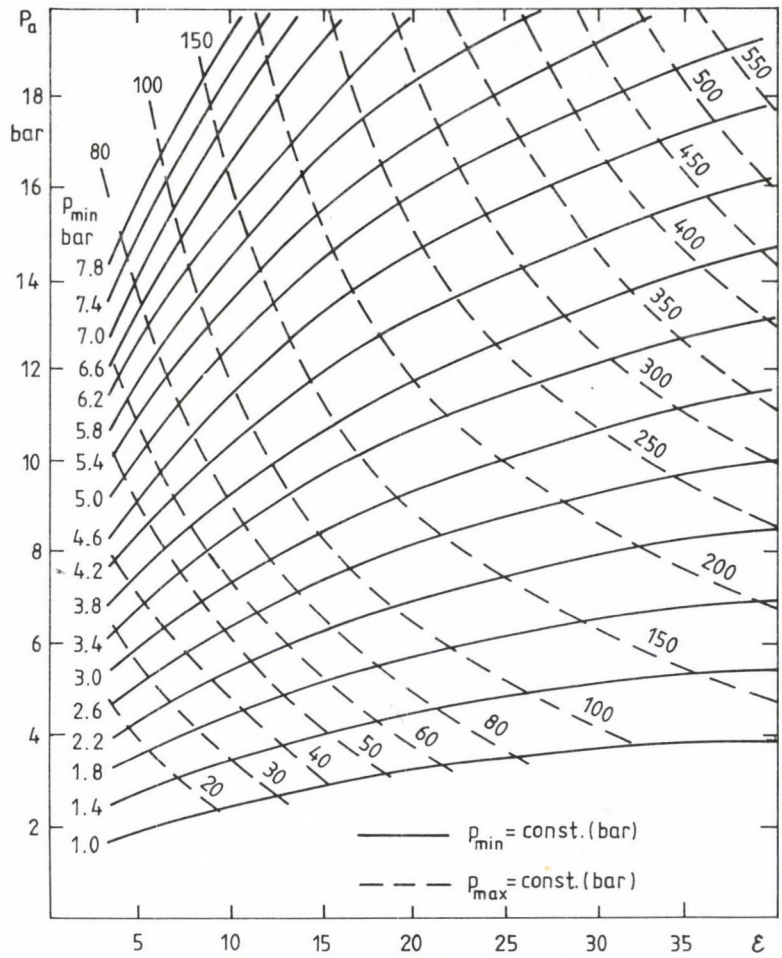

Fig. 4. Variation of average pressure p_a as a function of compression ratio ε in case of different initial pressures p_{min} of the work process. (In the figure, the diagrams p_{max} = const. /maximum pressure of the work process/ are also shown)

tional to it at a constant engine speed. Thermal state t_m of the engine was defined with the average temperature of the cylinder wall and lubricating oil. According to our measurement results, friction mean pressure p_f and as a consequence, the rate of wear increase obviously with the increase of p_a with an arbitrary thermal state of the engine /3/. Consequently, the implementation of the accelerated wear process requires the increase of average pressure p_a. According to the results shown in Fig. 4, to achieve a high average pressure p_a and a moderately increased peak pressure p_{max}, a high

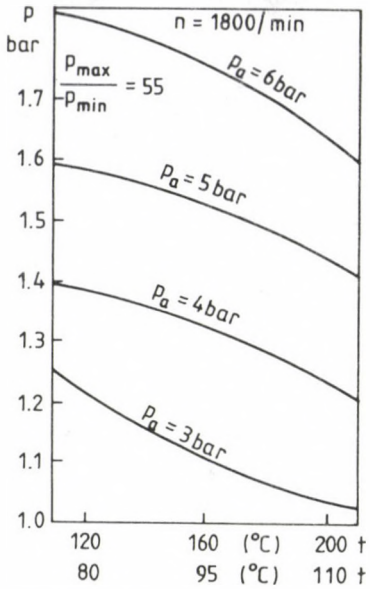

Fig. 5. Variation of friction mean pressure p_f as a function of thermal state of the engine for different average pressures p_a. (The thermal state of the engine is defined by the conjugate values of t_w /temperature of cylinder wall/ and t_o /temperature of lubricating oil/ belonging to each other. Engine-type to be examined: 4-cylinder Csepel diesel engine)

initial pressure p_{min} and a reduced compression ratio ε are required. And though the increase of compression ratio ε also contributes to the increase of average pressure p_a, however in this case, peak pressure p_{max} increases disproportionally, and in turn, it is not the acceleration of wear but instead a premature failure which is brought about in the engine.

With the increase of compression ratio ε of the engine, and with the minimal reduction of initial pressure p_{min}, average pressure p_a of the work process remains nearly constant but, at the same time, compression ratio p_{max}/p_{min} of the work process increases significantly. Together with the increase of compression ratio p_{max}/p_{min}, the magnitude of the forces applied periodically to the crank mechanism also increases, and this, in turn, brings about the fatigue failure of the individual component of the crank mechanism. This forms the basis of the accelerated fatigue of the engine.

The thermal load of the engine and the thermal state of its components can be increased by two sorts of procedures.

One possibility of the above increase is that hot oil (hot air in case of air-cooled engine) is circulated in the cooling system of the engine according to the scheme shown in Fig. 1. It is proved in our experiments /4/

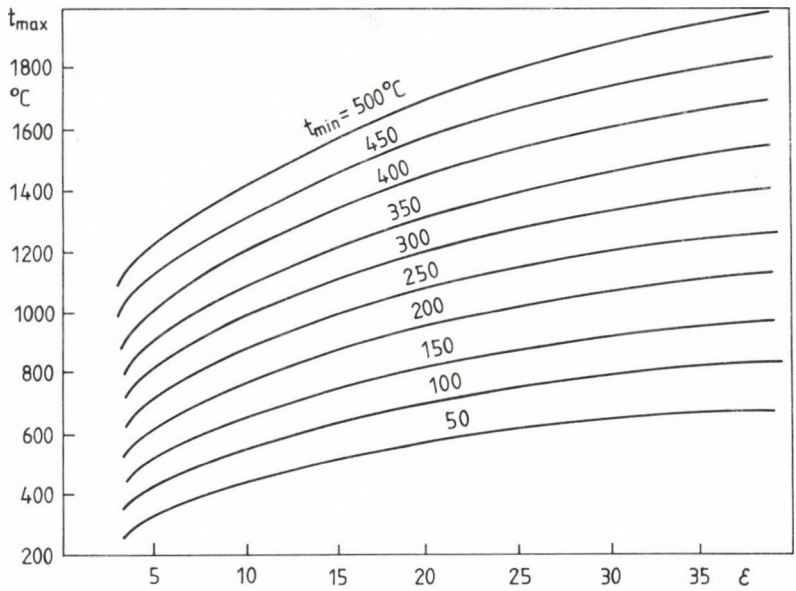

Fig. 6. Variation in maximum temperature t_{max} of the work process without heat transfer as a function of compression ratio, in case of different temperatures t_{min} (minimum temperature of the work process)

that the thermal state of an artificially heated engine driven externally is similar — with a very good approximation — to that of an engine operated with combustion process.

The other method for the possible perfect approximation of the actual thermal state and the increase of thermal load is considered to be the preheating of the inlet working medium in air-reservoir 4 with the help of heating 6. This time, compression temperature t_{max} increases uniequivocally. According to the results of our experiments carried out so far, when t_{max} = = 1400-1500 °C has been achieved, then the thermal state of the engine, and first of all, that of the pistons working under the conditions of a properly intensive external (artificial) heating is identical with a good approximation to the thermal state of the engine working under actual service conditions. In Fig. 6, information is provided on how the final temperature t_{max} of compression representing, at the same time, the maximum temperature of the work process is developing as a function of initial temperature t_{min} with different compression ratios ε. Our calculations were performed with the results shown in Fig. 3 taken into consideration. It can be seen that the achievement of t_{max} = 1400-1500 °C requires acceptably feasible values of t_{min} and ε.

3. The possibilities of the accelerated examination of fatigue

3.1. Realization of the accelerated wear process

Accelerated wear process takes places within an engine if average pressure p_a increases with a limited peak pressure p_{max}. So that, first of all, an accelerated wear process, and by no means an accelerated fatigue process should take place within an engine, the peak pressure is required to be limited between p_{max} = 70-130 bar depending on the make of the engine. The lower limit belongs rather to the light-duty petrol engines, while the upper limit to the heavy-duty diesel engines.

According to our results achieved so far, the value of the average pressure is to be held properly between p_a = 9-15 bar. Here, too, the smaller values belong to petrol engines, while the greater ones to the more bulky diesel engines.

From our results it can be seen clearly, as plotted in Fig. 4, that the limited peak pressure and the high average pressure are conflicting requirements. For the purpose of building up a proper average pressure and a moderate peak pressure, the compression ratio of the engine is required to be adjusted between the values of ε = 8-11, and to build up a pressure of p_{min} = 5-5.5 bar within the air-reservoirs. The sufficient thermal state of the engine is advised to achieve, first of all, by means of external (artificial) heating of the engine since, due to the relatively low compression ratio, the development of, at least, t_{max} = 1300-1400 ^{o}C requires t_{min} = = 400-450 ^{o}C according to the results shown in Fig. 6. According to the results achieved so far, in case of thermically isolated air-reservoirs and pipe-lines, t_{min} = 100-120 ^{o}C temperature will develop within the air-reservoirs at the time of the establishment of thermal balance in the engine. For the development of a temperature of 400-450 ^{o}C within the air-reservoirs, heating-power of 10-20 KW is required. Owing to the increased pressure of air-reservoirs and the increased temperature of those, the stress-dimensioning problems of the reservoirs should be taken into consideration.

The increase in the mechanical load of the engine by means of increasing mass forces is also promoted by the increase in the rpm of the engine. When the accelerated wear process is realized, the maximum rpm of the engine is required to increase by 15-25% of the original maximum rpm. The rpm of the engine should be changed only to a minimal extent during examination, however, this should be done in a way that the average rpm of the engine is reduced only by 10-15% of the maximum rpm.

3.2. Realization of the accelerated fatigue process

The fatigue failure of the engines are effected by intermittent loads resulting from the gas pressure and mass forces. The mass forces are uni-equivocally determined by the construction and the rpm of the engine, while the periodic forces coming from the gas pressure and resulting in fatigue are determined by the character of the work process and its parameters.

For the acceleration of the fatigue failure process, both the peak pressure p_{max} of the work process, and compression ratio p_{max}/p_{min} are to be increased. The value of p_{max} is determined by the joint consideration of p_{min} and ε, while the value of p_{max}/p_{min} depends only on ε. When examining the fatigue failure process, the following values were obtained depending on the make of the engine: the value of p_{max} is between 120-180 bar, while that of p_{max}/p_{min} is, at least, about 100. So that these values can be used in practice, initial pressure p_{min} of the engine should be reduced to the value of about $p_{min} = 1.2\text{-}1.8$ bar. According to Fig. 4, average pressure p_a will be reduced to 5-6 bar, while compression ratio ε should be increased up to the value of 35-40. Due to the high compression ratio, maximum temperature t_{max} of the work process will also increase significantly, and with initial temperature $t_{min} = 350\text{-}450\ ^{C}C$, it will already actually approximate the average value of the maximum temperature measured during the real work process (brought about by combustion process).

It can be seen that, when realizing the accelerated fatigue process, the characteristics of the work process carried out without combustion approximate very well the characteristics of the real work process except the maximum and minimum pressure values of it since it was just our aim to change those during our work.

4. Realization of examination

4.1. Pre-experiments for determining the most unfavourable load of engine during accelerated examination

By means of experiments, the maximum loadability of the engine should be determined from the aspect of the accelerated wear of fatigue at which the failure of the engine does not occur yet, and the sticking-in of the piston or the failure (breakage) of the components do not suffer failure in a short service-time, etc. In order to this measure of loadability can be

determined, the engine should be dismounted after each 30-40 service-hours, the state of the components and, first of all, that of the interfaces of the counterparts sliding over each other should be controlled so as to detect whether there is any crack of fatigue character propagating along any of the components. After the examination, the engine load should be increased by 20-30%, and the pre-experiments should be continued.

The state of the load at which there can be noticed some signs of engine failure, should be reduced by about 10-20%, and this state of load is called the most unfavourable load from the aspect of the accelerated fatigue of the engine. It is obvious that this most unfavourable load is not always identical with those obtained in the examinations of the accelerated wear and fatigue.

4.2. Execution of the actual accelerated examination

In the following, the examination concerning the accelerated wear is described here, but, of course, the method elaborated here can be applied -- with some alterations -- to the accelerated examinations of fatigue, too.

After determining the most unfavourable load, the engine should be operated at this load, and after a service of 50-80 hours, the wear of the components is determined.

It is advised to provide some non-steady state character to the examinations, nevertheless — in order to achieve acceleration of a great extent, the overall average load of the engine should be kept constant in the neighbourhood of the maximum load.

With the dimensions characteristic of the engine wear determined accurately in certain periods, the rate of wear F (Fig. 7) of the individual components can be determined as a function of service-hours. The examination should be carried on until the rate of wear caused under the actual load conditions for a given service-time has been detected. In Fig. 7, this value of wear is symbolized by capital letter A. The arrow in the figure shows the direction of load-increase.

The rate of acceleration (a) is the following:

$$a = \frac{\tau_n}{\tau_a}$$

where τ_n = the service-time required for the achievement of the wear of a given rate under actual (normal) operating conditions

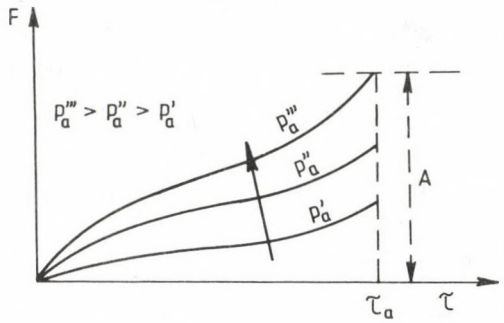

Fig. 7. Variation of engine wear as a function of examination period, in case of different engine loads. (Arrow shows the direction of increase in load)

τ_a = the service-time belonging to the same wear under the conditions of accelerated procedure

The rate of acceleration, according to our experimental results achieved so far, is changing between 5-8 depending of the engine type.

Once the rate of accelerated fatigue has been determined for a given engine type, or even for the given components, the effect of any constructional, materialistic or technological modification exerted upon the service-life can be examined uniequivocally and accurately since the service hours of the accelerated examination are known which provide fatigue of an extent identical with that of the examination carried out during actual service conditions.

In possession of experimental data of sufficient quantity and quality, we have the possibility of elaborating a theory with the help of which wear can be calculated with a good approximation as a function of the engine load, or the rate of acceleration can be predicted.

So that the results of examinations should be reproduced and re-utilized, the array of themes should be recorded as accurately as possible, and when new examinations are to be carried out, every time the same array of themes (examination procedure) should be applied. Such important characteristics of the procedure are for instance: mechanical and thermal load, as well as the engine revolution, the period of change and the type of oil filters, the period of oil change, the grade of oil, the temperature and pressure of lubricating oil, etc. These characteristics can be assumed freely between certain limits but once assumed, the should be kept constant, or else the examinations performed at different points of time cannot be compared with each other.

5. Technical possibilities of the external drive of engines

In Fig. 1, as an example, a torque-measuring balance-type electric engine was used for the external drive of the engine. This is the most accurate and expedient kind of drive. It is obvious that instead of a torque-measuring balance-type electric motor, other reciprocating engines of internal combustion can be used, as well.

In case of engines of high piston displacement and heavy-duty type, the power-demand for rotating an engine of increased mechanical load and external drive amounts to more hundred KW. In case of such an examination, the power-demand for the external rotation of the engine reaches 40-60% of its maximum effective power. In such cases, the drive by an electric engine or another reciprocating one requires already significant investment.

In case of multy-cylinder engines (in practice, really multi-cylinder engines are in question), there is a favourable chance of a simple solution to the external drive of the engine to be examined. In such cases, the engine should be divided into two parts from the aspect of examination, and according to our experiments, about half of the cylinders should be operated as real ones having combustion process in service, while the other half of them should be subject to examination under the conditions of the accelerated fatigue. In this case, the engine is caused to rotate with the help of actually working cylinders, and the useful power of the engine is absorbed by the increased friction of the group of crank-case mechanisms subject to examination under the conditions of accelerated fatigue.

Both the whole examination process and the testing apparatus remain identical with those used with the method introduced in the foregoing, only the cooling circuit and the suction-exhaust system should be split into two parts each, according to the cylinders operating under the condition of combustion process, or without it, respectively. In such a layout, the engine can be started by the original starting apparatus, and a minimal mechanical load should be applied at starting in the section of the engine operating without combustion process (in Fig. 1 atmospheric pressure was built up within air-reservoirs 4), then after the start of the engine-section working normally, the mechanical load of the engine section operating without combustion process can be increased to the extent required.

The only inaccuracy of this procedure is that the friction losses of the externally driven engine section can be determined only from the performance data of the cylinders working normally, and as a consequence, it

can be done only with certain inaccuracy, which is, however, sufficient for the follow-up and checking of the process. As our examinations carried out so far show, in case of engines having effective power about 250-300 KW and above it, this procedure seems to be the most expedient one.

6. Results achieved so far, and the possibilities of co-operation

In the laboratory of the Institute of Vechicle Engineering at the Technical University Budapest for decades, there has been an engine driven externally and operating without combustion process which was developed for the determination of mechanical-frictional losses, as well as for the elaboration of the examination procedure suitable for the accelerated fatigue of engines. In this field, there have been carried out several examinations, and as a result, we have obtained every kind of theoretical know-how and practical experiences required for carrying out any other examinations under this scope.

Author expresses his readiness for the co-operation in case there is any demand for it from the part of designers, developing engineers, manufacturers and users of the internal combustion reciprocating engines and compressors, and for providing any further information and a more detailed description of the theoretical and practical problems arisen during the work with this procedure.

It should be noted that this procedure and the whole examination method comes under the legal protection of the licence.

REFERENCES

1. Pásztor, E.: Determination of the dependence between working process and mechanic efficiency of i.c. engines. Periodica Polytechnica. Bp. Vol. 14. No. 4 (1970)

2. Pásztor, E.: Über die Bestimmung der Reibungsart und des mechanischen Wirkungsgrades bei Verbrennungsmotoren. MTZ. 29 (1968), No. 2, 57—64

3. Pásztor, E.: Methode zur Bestimmung des Reibungsmitteldruckes von Kolben-Verbrennungsmotoren. Acta Tech. Tom. 62 (3—4), 381—408

4. Pásztor, E.: Examination of interconnections between the work process and the mechanical efficiency of i.c. engines (in Hungarian). Thesis for the Academic Doctor's Degree. Manuscript. 1970. Budapest

5. Pásztor, E.: Weiterentwicklungsmöglichkeiten der zur Bestimmung des mechanischen Wirkungsgrades von Hubkolbenverbrennungsmotoren dienenden Näherungsmessverfahren. Acta Techn. Tom. 70 (3—4), 343—369

6. Examination of the efficiency of uniform friction- and wear-reducing ingredient (ESKA). Study. Leader of research activity: Pásztor, E. Institute of Vehicle Engineering at the Technical University Budapest, 1983

Acta Technica Acad. Sci. Hung., 105(4), pp. 341—356 (1993)

ROTATIONAL INERTIA EFFECTS FOR THE FLOW OF A FERROFLUID BETWEEN ROTATING SURFACES OF REVOLUTION

WALICKI, E.* - WALICKA, A.**

(Received: 2 April 1993)

The steady laminar flow of a ferrofluid is considered through a narrow space (slot) between two rotating surfaces of revolution, having a common axis of symmetry.

The linearized equations of motion of a ferrofluid are used in the axially symmetric case, assuming an appropriate system of orthogonal curvilinear coordinates x, ϑ, y.

The obtained solutions of equations of motion have been illustrated by examples of flow through the slot of constant thickness between rotating and fixed conical surfaces, and between rotating and fixed spherical surfaces.

1. Introduction

The steady laminar flows of a viscous fluid through the narrow space between surfaces of revolution have been the object of theoretical and experimental studies /5—7/.

In recent years, a considerable interest has been shown to use ferrofluids in machine designing.

The ferrofluids are colloidal suspensions of fine particles of solid ferromagnetic materials such as magnetite in non-conducting base liquid. The carrier liquid may be a diester base, a hydrocarbon base, an ester base and even a water base. The particles are very small in size (about 10 nm) and coated with a surfactant (oleic acid) to prevent coagulation; therefore, the ferrofluids are very stable and practically neither aggregation nor sedimentation occurs in gravitational and magnetic fields. Hence the concentration of the particles in the mother liquor is constant. Under an

*Walicki, Edward, P-65016 Zielona Góra, ul. Szafrana 11a/7, Poland

**Walicka, Anna, P-65016 Zielona Góra, ul. Szafrana 11a/7, Poland

Akadémiai Kiadó, Budapest

applied magnetic field, the particles are oriented and become the loci of magnetic forces. The contact phenomena at the surface between the solid particles and the liquid carrier disseminate the magnetic stresses in the mass of the ferrofluid. Therefore, a new kind of body forces is introduced when the motion of the fluid is considered. The density and the viscosity of magnetic suspensions differ from those of the mother liquor, as the particle concentration and magnetization change.

The ferrofluids were prepared during the last years and studied first by Rosensweig et al. /1--4/.

In these studies the nonpolar theory of ferrofluids is discussed. Recently the theories of polar and conducting ferrofluids have been created.

The purpose of the present paper is to investigate the steady laminar flow of an electrically nonconducting and nonpolar incompressible ferrofluid in the slot between rotating curvilinear surfaces of revolution having a common axis of symmetry in the presence of a longitudinal magnetic field, as shown in Fig. 1.

The problem is solved under the assumption that the magnetic Reynolds number is small which permits us to neglect the induced magnetic field.

The solution is limited to the analysis of rotational inertia effects and magnetic field on the velocity and pressure distributions in the slot.

2. Basic equations

Let us consider the flow of viscous incompressible and electrically nonconducting ferrofluid through a narrow space between two curvilinear surfaces of revolution with common axis (Fig. 1), from which the inner surface rotates with angular velocity ω_1, and the outer surface — with angular velocity ω_2.

The rotating surfaces are described by function R(x) which denotes the radius of the median surface between the rotating surfaces, plus function h(x) which denotes the distance to each surface from the median, measured along a normal to the median.

An intrinsic curvilinear orthogonal coordinate system x, ϑ, y linked with median surface is shown in Fig. 1.

The physical parameters of the flow are the velocity components v_x, v_ϑ, v_y and pressure p. With regard to axial symmetry of the flow these parameters are not dependent on the angle ϑ. Let the vector of magnetic field $\bar{H}(H_x, 0, 0)$ be tangential to the median surface.

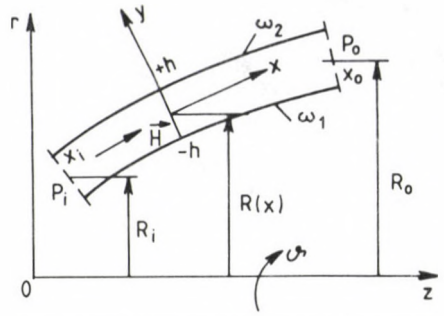

Fig. 1. Slot of small thickness between rotating surfaces of revolution

The governing equations of the steady flow of an electrically non-conducting and incompressible ferrofluid are /4/:
the equation of continuity:

$$\nabla \cdot \bar{V} = 0; \tag{2.1}$$

the equation of momentum:

$$\rho(\bar{V}\nabla)\bar{V} = -\nabla p + \mu\nabla^2\bar{V} + \mu_0 (\bar{M}\nabla)\bar{H}; \tag{2.2}$$

the Maxwell equations:

$$\begin{aligned} \nabla \times \bar{H} &= 0, \\ \nabla \cdot \bar{B} &= 0, \\ \bar{B} &= \mu_0 (\bar{H} + \bar{M}). \end{aligned} \tag{2.3}$$

Here $\bar{V}$ — the velocity vector,
$\bar{H}$ — the magnetic field vector,
$\bar{B}$ — the magnetic induction vector,
$\bar{M}$ — the magnetization,
ρ — the ferrofluid density,
μ — the ferrofluid viscosity,
μ_0 — the magnetic permeability of the free space.

The assumption typical for the flow in a narrow space that:

$$h(x) \ll R(x)$$

and assumption that magnetic Reynolds number is small can be use to make order-of-magnitude arguments for Eqs (2.1)—(2.3).

If the asymptotic transformations have been made as in Refs /5—7/ these equations can be reduced to a simpler form:

$$\frac{1}{R}\frac{\partial(Rv_x)}{\partial x} + \frac{\partial v_y}{\partial y} = 0, \tag{2.4}$$

$$-\rho v_\vartheta^2 \frac{R'}{R} = -\frac{\partial p}{\partial x} + \mu \frac{\partial^2 v_x}{\partial y^2} + \mu_0 M_x \frac{\partial H_x}{\partial x}, \tag{2.5}$$

$$0 = \mu \frac{\partial^2 v_\vartheta}{\partial y^2}, \tag{2.6}$$

$$0 = \frac{\partial p}{\partial y}. \tag{2.7}$$

The "prime" denotes everywhere derivation with respect to x. The order-of-magnitude arguments shows that

$$p(x,y) = p(y). \tag{2.8}$$

After asymptotic transformations the Maxwell equations indicate that for $\bar{H}(H_x, 0, 0)$ there is $\bar{M}(M_x, 0, 0)$ and

$$\begin{aligned} H_x &= H_x(x), \\ M_x &= M_x(x). \end{aligned} \tag{2.9}$$

If the ferrofluid is magnetically nonsaturated, then

$$M_x = \sigma H_x^{-1}, \tag{2.10}$$

for the saturated ferrofluid $\sigma = 1$ and

$$M_x = \sigma; \tag{2.11}$$

where σ is characteristic value of magnetization; it is equal to

$$\sigma = K\, T_c; \tag{2.12}$$

here K — pyromagnetic coefficient, and
T_c — Curie temperature.

Taking into account Eqs (2.9) and (2.10) we may write the last term of Eq. (2.5)

$$\mu_0 M_x \frac{\partial H_x}{\partial x} = \frac{\mu_0 \sigma}{\nu} \frac{dH_x \nu}{dx}. \tag{2.13}$$

The problem statement is complete after specification of boundary conditions. These conditions are stated as follows:

$$v_x(x, \pm h) = 0, \tag{2.14}$$

$$v_\vartheta(x, -h) = R\omega_1, \qquad v_\vartheta(x, +h) = R\omega_2, \tag{2.15}$$

$$v_y(x, \pm h) = 0. \tag{2.16}$$

Moreover, in the inlet and the outlet from the slot the conditions for the pressure are stated as follows:

$$\begin{aligned} p &= p_i \quad \text{for} \quad x = x_i, \\ p &= p_o \quad \text{for} \quad x = x_o \end{aligned} \tag{2.17}$$

thus, x_i — the inlet coordinate and
x_o — the outlet coordinate.

3. Solution of the equations

Integrating the Eqs (2.6) and (2.5) with respect to y, taking into account Eq. (2.13) and determining the arbitrary constants from the boundary conditions (2.15) and (2.14) we obtain

$$v_\vartheta = \frac{R}{2}\left[(\omega_1 + \omega_2) - (\omega_1 - \omega_2)\frac{y}{h}\right], \tag{3.1}$$

$$v_x = \frac{1}{2\mu}\left(\frac{dp}{dx} - \frac{\mu_0\sigma}{\nu}\frac{dH_x}{dx}\right)(y^2 - h^2) -$$

$$- \frac{\rho RR'}{48\mu h^2}\left[(y^4 - h^4)(\omega_1 - \omega_2)^2 - 4h(y^3 - h^2 y)(\omega_1^2 - \omega_2^2) + \right.$$

$$\left. + 6h^2(y^2 - h^2)(\omega_1 + \omega_2)^2\right]. \tag{3.2}$$

The flow rate Q is defined as

$$Q = 2\pi R \int_{-h}^{+h} v_x \, dy. \tag{3.3}$$

Using here the expression (3.2) we obtain after simple transformations

$$\frac{dp}{dx} - \frac{\mu_0\sigma}{\nu}\frac{dH_x}{dx} = -\frac{3\mu Q}{4\pi Rh^3} + \frac{\rho RR'}{4}\left[\frac{1}{5}(\omega_1 - \omega_2)^2 + (\omega_1 + \omega_2)^2\right]. \tag{3.4}$$

Applying the formula (3.4) in the relation (3.2) we get the final expression for velocity component v_x:

$$v_x = -\frac{3Q}{8\pi Rh^3}(y^2 - h^2) - \frac{\rho RR'}{240\mu h^2}\left[(5y^4 - 6h^2y^2 + h^4)(\omega_1 - \omega_2)^2 - \right.$$

$$\left. - 20h(y^3 - h^2 y)(\omega_1^2 - \omega_2^2)\right]. \tag{3.5}$$

Taking into account the expression for velocity v_x in (2.4) and integrating this equation with respect to y we get the formula for velocity component v_y:

$$v_y = \frac{1}{R}\frac{\partial}{\partial x}\left\{\frac{Q}{8\pi h^3}(y^3 - 3h^2 y) + \frac{\rho R^2 R'}{240\mu h^2}\left[y(y^2 - h^2)^2(\omega_1 - \omega_2)^2 - \right.\right.$$

$$\left.\left. - 5h(y^2 - h^2)^2(\omega_1^2 - \omega_2^2)\right]\right\}. \tag{3.6}$$

Note that the velocity components for the present case do not depend on the magnetic field.

To define the pressure distribution let us return to expression (3.4); integrating this expression and applying the boundary conditions (2.17) we have:

$$p = p_i - \frac{3\mu Q}{4\pi}\left[A(x) - A_i\right] + \frac{\rho\Omega^2}{8}(R^2 - R_i^2) + \frac{\mu_o\sigma}{\nu}\left[C(x) - C_i\right], \qquad (3.7a)$$

or

$$p = p_o - \frac{3\mu Q}{4\pi}\left[A(x) - A_o\right] + \frac{\rho\Omega^2}{8}(R^2 - R_o^2) + \frac{\mu_o\sigma}{\nu}\left[C(x) - C_o\right], \qquad (3.7b)$$

where

$$A(x) = \int \frac{dx}{Rh^3}, \qquad A_i = A(x_i), \qquad A_o = A(x_o);$$

$$C(x) = H_x^{\nu}(x), \qquad C_i = C(x_i), \qquad C_o = C(x_o); \qquad (3.8)$$

$$\Omega^2 = \frac{1}{5}(\omega_1 - \omega_2)^2 + (\omega_1 + \omega_2)^2.$$

By subtracting the formulae (3.7) we get the relation for the pressure drop in the slot as follows:

$$\Delta p = p_i - p_o = -\frac{3\mu Q}{4\pi}(A_i - A_o) + \frac{\rho\Omega^2}{8}(R_i^2 - R_o^2) + \frac{\mu_o\sigma}{\nu}(C_i - C_o). \qquad (3.9)$$

Note that the formulae (3.7) and (3.9) for the pressure distribution and the pressure drop may be presented in the following forms:

$$p = p_n + p_f \qquad (3.10)$$

or

$$\Delta p = \Delta p_n + \Delta p_f \qquad (3.11)$$

where

$$p_n = p_o - \frac{3\mu Q}{4\pi}\left[A(x) - A_o\right] + \frac{\rho\Omega^2}{8}(R^2 - R_o^2), \qquad (3.12)$$

$$\Delta p_n = -\frac{3\mu Q}{4\pi}(A_i - A_o) + \frac{\rho\Omega^2}{8}(R_i^2 - R_o^2) \qquad (3.13)$$

are the pressures for nonmagnetic flow, and

$$p_f = \frac{\mu_o \sigma}{\nu}\left[C(x) - C_o\right], \tag{3.14}$$

$$\Delta p_f = \frac{\mu_o \sigma}{\nu}(C_i - C_o) \tag{3.15}$$

are the pressures caused by magnetic field.

4. Examples of application

4.1. Nondimensional form of the solution

Equations (3.1), (3.5) and (3.7) may be nondimensionalized by using the following parameters:

$$\tilde{x} = \frac{x}{R_o}, \qquad \tilde{R} = \frac{R}{R_o}, \qquad \tilde{h} = \frac{h}{h_o}, \qquad \tilde{y} = \frac{y}{h},$$

$$\tilde{v}_x = \frac{v_x}{V_Q}, \qquad \tilde{v}_\vartheta = \frac{v_\vartheta}{V_\omega}, \qquad \tilde{p} = \frac{16(p - p_o)\rho h_o^4}{\mu^2 R_o^2},$$

$$\tilde{A}(\tilde{x}) = A(x)h_o^3, \qquad \tilde{C}(\tilde{x}) = \frac{C(x)}{H\nu_o}, \tag{4.1}$$

$$R_f = \frac{16\pi \mu_o h_o^3 \sigma H \nu_o}{\mu \nu Q}, \qquad R_\lambda = \left(\frac{2h_o}{R_o}\right)\mathrm{Re}, \qquad \mathrm{Re} = \frac{2h_o \rho V_Q}{\mu},$$

$$V_Q = \frac{Q}{4\pi}\frac{1}{R_o h_o}, \qquad V_\omega = R_o \omega_1, \qquad f = \frac{\omega_2}{\omega_1},$$

$$\tilde{\Omega}^2 = \frac{1}{5}(1 - f)^2 + (1 + f)^2, \qquad \pi_\lambda = R_\lambda\left(\frac{V_\omega}{V_Q}\right)^2,$$

where V_Q — the averaged longitudinal velocity in the outlet cross-section,

V_ω — the tangential velocity on the inner surface in the outlet cross-section,

Re — and R_λ are, respectively, the Reynolds and the modified Reynolds numbers,

R_f — the ferrofluid index;

note that always

$$\sigma H_o \nu = H_o^2 .$$

The nondimensional formulation assumes then the form

$$\tilde{v}_x = \frac{3}{2}\frac{1}{\tilde{R}\tilde{h}}(1 - \tilde{y}^2) - \frac{\pi_\lambda}{960}\tilde{R}\tilde{R}'\tilde{h}^2 V_x(\tilde{y}), \tag{4.2}$$

$$\tilde{v}_\vartheta = \tilde{R} V_\vartheta(\tilde{y}), \tag{4.3}$$

$$\left.\begin{aligned} \tilde{p} &= \tilde{p}_n + \tilde{p}_f, \\ \tilde{p}_n &= -12 R_\lambda\left[\tilde{A}(\tilde{x}) - \tilde{A}_o\right] + \frac{R_\lambda \pi_\lambda}{8}\tilde{\Omega}^2(\tilde{R}^2 - 1), \\ \tilde{p}_f &= R_\lambda R_f\left[\tilde{C}(\tilde{x}) - \tilde{C}_o\right], \end{aligned}\right\} \tag{4.4}$$

here

$$\begin{aligned} V_x(\tilde{y}) &= (1 - 6\tilde{y}^2 + 5\tilde{y}^4)(1 - f)^2 + 20(\tilde{y} - \tilde{y}^3)(1 - f^2) \\ V_\vartheta(\tilde{y}) &= \frac{1}{2}\left[1 + f - (1 - f)\tilde{y}\right]. \end{aligned} \tag{4.5}$$

It is easy to see that for $R_f = 0$ one obtains

$$\tilde{p}_f = 0 \qquad \text{and} \qquad \tilde{p} = \tilde{p}_n .$$

To analyse this solution in the particular cases of the flow configuration we assume that

$$H_x = \frac{H_o}{\tilde{R}} \qquad \text{and} \qquad \nu = 1. \tag{4.6}$$

4.2. Throughflow between the conical parallel surfaces

For the conical parallel surfaces shown in Fig. 2, the geometric relations are given as:

$$R = x \sin\alpha, \qquad R_i = x_i \sin\alpha, \qquad R_o = x_o \sin\alpha, \qquad h = \text{const.}$$

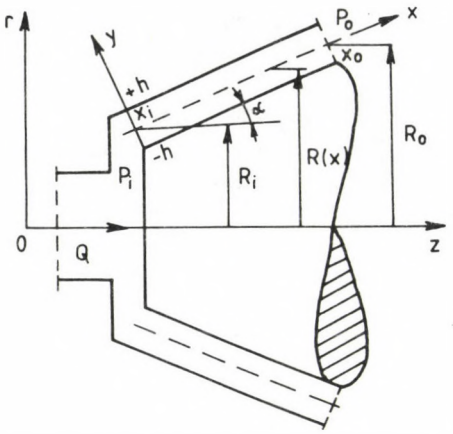

Fig. 2. Slot between conical parallel surfaces

The nondimensional quantities are

$$\tilde{R} = \tilde{x} \sin\alpha, \qquad \tilde{R}_o = 1, \qquad \tilde{x}_o = \frac{1}{\sin\alpha}, \qquad \tilde{h} = 1$$

and the nondimensional formulation is then

$$\tilde{v}_x = \frac{3}{2}\frac{1}{x\sin\alpha}(1 - \tilde{y}^2) - \frac{\pi_\lambda}{960}\tilde{x}\sin^2\alpha\, V_x(\tilde{y}), \tag{4.7}$$

$$\tilde{v}_\vartheta = \tilde{x}\sin\alpha\, V_\vartheta(\tilde{y}), \tag{4.8}$$

$$\tilde{p} = \tilde{p}_n + \tilde{p}_f,$$

$$\tilde{p}_n = -\frac{12R_\lambda}{\sin\alpha}(\ln\tilde{x} - \ln\tilde{x}_o)\frac{R_\lambda}{\beta}\pi_\lambda\tilde{\Omega}^2(\tilde{x}^2\sin^2\alpha - 1), \tag{4.9}$$

$$\tilde{p}_f = R_\lambda R_f\left(\frac{1}{\tilde{x}\sin\alpha} - 1\right).$$

Figures 3 and 4 show the profiles of the velocity component $\tilde{v}_x$ for two values of the coefficient π_λ, namely:

$$\pi_\lambda = 40 \qquad \text{and} \qquad \pi_\lambda = 60$$

for the flow between parallel disks ($\alpha = 90^o$) and for the case when only one of them rotates (f = 0).

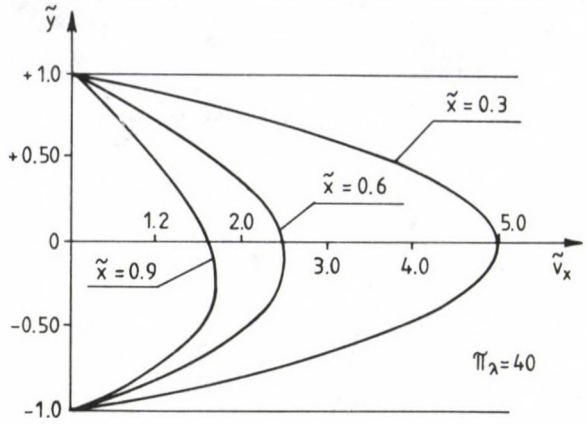

Fig. 3. Dimensionless profiles of the velocity components $\tilde{v}_x$ for the flow between parallel disks for $\pi_\lambda = 40$

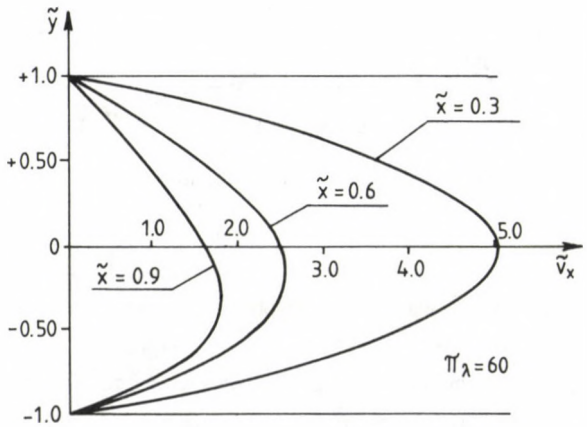

Fig. 4. Dimensionless profiles of the velocity components $\tilde{v}_x$ for the flow between parallel disks for $\pi_\lambda = 60$

It can be seen from these figures that the differences between the profiles of velocity $\tilde{v}_x$ are considerable in the cross-sections lying near the inlet and the outlet to the slot and depend on the coefficient π_λ. The maximum of velocity profiles moves into the direction of rotating disk for increasing values of π_λ and radii. For large values of $\tilde{x}$ or for increasing π_λ ultimately a back flow occurs in the slot. The beginning of the back flow may be decelerated by increasing the flow rate (V_Q increases and π_λ decreases).

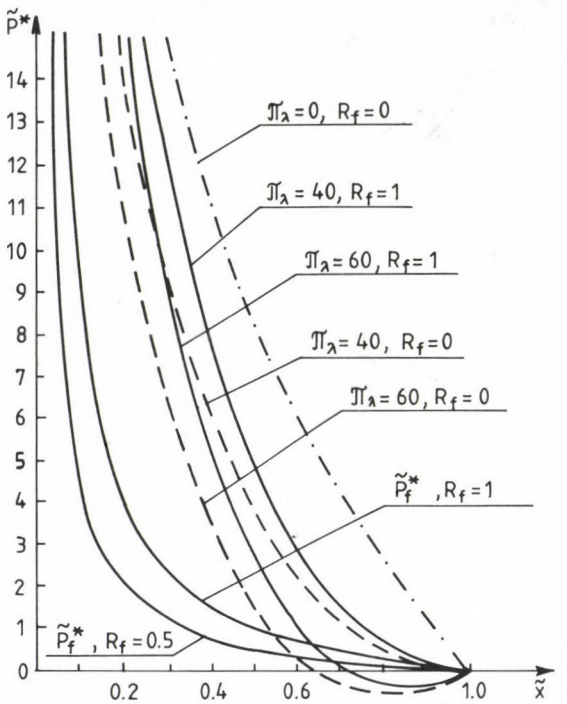

Fig. 5. Dimensionless pressure distributions $\tilde{p}^*$ for the flow between parallel disks

In the following lines a simple physical explanation is given for this property.

In the neighbourhood of the rotating disk the centrifugal forces hurl more and more mass of fluid into the radial direction with increasing radius and angular velocity. With a fixed flow rate only a part of the accelerated mass of fluid can be replaced by the inlet. The difference is compensated by the onset of a back flow at large radii $\tilde{x}$.

This property is also true for angles α different of 90^0 ($\alpha \leqq 90^0$).

It is easy to see that the profiles of velocity $\tilde{v}_\vartheta$ are straight lines.

Figure 5 shows the pressures distributions defined as

$$\tilde{p}_f^* = \frac{\tilde{p}_f}{R_\lambda} \qquad \text{and} \qquad \tilde{p}^* = \frac{\tilde{p}}{R_\lambda}. \tag{4.10}$$

The dash-dot line presents the pressure distribution without inertia effects i.e. the pressure distribution obtained from the formula:

$$\tilde{p}_n^* = -12 \ln \tilde{x}. \tag{4.11}$$

The dashed lines present the pressure distribution for nonmagnetic flow.

The curves for the total pressure (continuous lines) are made for the following value of ferrofluid index:

$$R_f = 1.$$

From this figure, it is clear that the inertia effect is considerable; the pressure distribution varied significantly as indicated by dashed lines.

With increased angular velocity the pressure losses grow larger.

The reaction of magnetic field is seen in the form of pressure growth (continuous lines). This growth, presented by magnetic pressure $\tilde{p}_f^*$, is a function of the ferrofluid index R_f and it can be relatively great; it increases with the increase of R_f.

4.3. Throughflow between the concentric spherical surfaces

For the concentric spherical surfaces shown in Fig. 6, the geometric relations are given as follows:

$$R = R_s \sin\phi\,, \qquad \phi = \frac{x}{R_s}\,, \qquad R_i = R_s \sin\phi_i,$$

$$R_o = R_s \sin\phi_o, \qquad h = \text{const}.$$

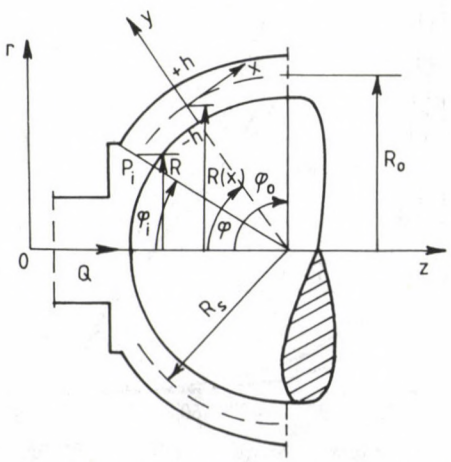

Fig. 6. Slot between concentric spherical surfaces

The nondimensional quantities are (for $\phi_o = 90^o$):

$$\tilde{R} = \sin\phi, \qquad \tilde{R}_o = 1, \qquad \tilde{x} = \phi, \qquad \tilde{h} = 1.$$

The nondimensional formulation assumes the form:

$$\tilde{v}_x = \frac{3}{2}\frac{1}{\sin\phi}(1 - y^2) - \frac{\pi_\lambda}{1920}\sin 2\phi\, V_x(\tilde{y}), \tag{4.12}$$

$$\tilde{v}_\vartheta = \sin\phi\, V_\vartheta(\tilde{v}), \tag{4.13}$$

$$\left.\begin{aligned} \tilde{p} &= \tilde{p}_n + \tilde{p}_f, \\ \tilde{p}_n &= -12R_\lambda \ln \operatorname{tg}\frac{\phi}{2} + \frac{R_\lambda}{8}\pi_\lambda \tilde{\Omega}^2(\sin^2\phi - 1), \\ \tilde{p}_f &= R_\lambda R_f\left(\frac{1}{\sin\phi} - 1\right). \end{aligned}\right\} \tag{4.14}$$

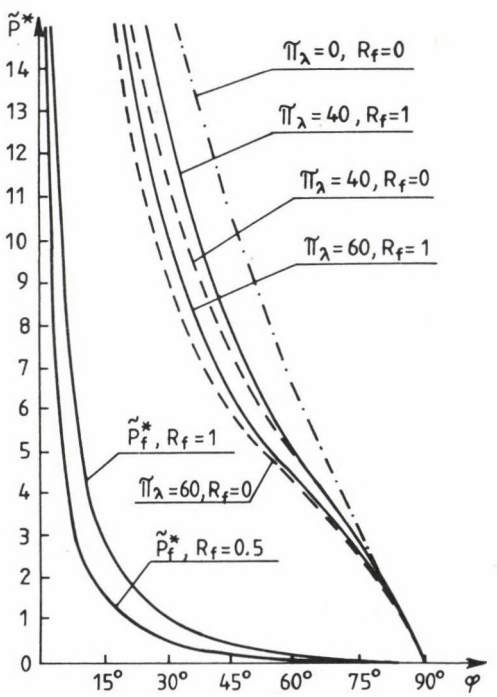

Fig. 7. Dimensionless pressure distributions $\tilde{p}^*$ for the flow between concentric spherical surfaces

Note that the character of changes of the velocity components $\tilde{v}_x$ and $\tilde{v}_\vartheta$ in this case is the same as in the previous one.

Figure 7 presents the magnetic and the total pressure distributions (continuous lines) $\tilde{p}_f^*$ and $\tilde{p}^*$, respectively.

The dash-dot line shows the pressure distirbution without inertia effects, i.e., the pressure distribution obtained from the formula:

$$\tilde{p}_n = -12 \ln \operatorname{tg} \frac{\phi}{2}. \tag{4.15}$$

The dashed lines present the pressure distributions for nonmagnetic flow.

The curves for the total pressure (continuous lines) are made also for $R_f = 1$.

In this case the inertia effect is considerable even so little smaller than that in the previous one; the effect of magnetic pressure is here relatively smaller, too.

5. Conclusions

The analysis of the obtained formulae allow us to confirm that the flow in the slot is generated by two reasons:

— the difference of the pressure at the inlet and the outlet, and,

— the rotational motion of the surfaces (in particularly analysed cases, by rotational motion of the inner surface).

It results from formulae (3.1), (3.5) and (3.6) that the velocity field for the present case of flow is independent on the applied magnetic field.

The profile of tangential velocity v_ϑ for the fixed cross-section (function V_ϑ) is identical with the profile of Couette flow between two moving (in generally) planes.

However, from the formulae for longitudinal velocity v_x it results that the main part has a profile identical with profile of flat Poiseuille flow.

This flow is generated by the difference mentioned above of the pressure and by rotational motion of surfaces. On the main part of longitudinal velocity the part of the secondary flow which is generated by the suction effect of the moving surfaces is imposed.

The secondary flow is described by the second component of the longitudinal velocity v_x and by cross velocity v_y.

From the formulae for pressure distribution it results that the inertia effect is considerable; it causes the pressure losses which growth increases with the increase of angular velocity of rotating surfaces. The influence of inertia forces is more visible in the flow between two disks (surfaces with rectilinear generatrices) than in that between two spheres (surfaces with curvilinear generatrices).

The action of magnetic field is seen in the form of pressure growth (magnetic pressure) which increases with the intensity of this field and it can achieve relatively great values.

REFERENCES

1. Neuringen, J.L. - Rosensweig, R.E.: Ferrohydrodynamics. Phys. Fluids, Vol. 7, No. 12 (1964), 1927—1937

2. Cowley, M.D. - Rosensweig, R.E.: The interfacial stability of a ferromagnetic fluid. J. Fluid Mech., Vol. 30, No. 4 (1967), 671—675

3. Rosensweig, R.E. - Kaiser, R. - Miskolczy, G.: Viscosity of magnetic fluid in magnetic field. J. Colloid and Interface Sci., Vol. 29, No. 4 (1969), 680—686

4. Rosensweig, R.E.: Ferrohydrodynamics. The encyclopedic dictionary of physics. Pergamon Press, 1974

5. Walicki, E.: Viscous fluid flow in a slot of the curvilinear thrust bearing. Rev. Roum. Sci. Techn.-Méc. Appl. Vol. 20, No. 4 (1975), 483—493

6. Walicka, A.: Accurate and asymptotic solutions of simplified sets of equations describing the motion of viscous fluids in a slot bounded by two co-axial surfaces of revolution. WNT, Warszawa 1989

7. Walicka, A.: Integral approaches for the throughflow of a ferrofluid between fixed surfaces of revolution. J. Tech. Phys. Vol. 32, No. 2 (1991), 153—168

Acta Technica Acad. Sci. Hung., 105(4), pp. 357—371 (1993)

INTEGRAL APPROACHES FOR THE FLOW OF A POWER-LAW FLUID IN A SLOT BETWEEN FIXED SURFACES OF REVOLUTION

WALICKI, E.* - WALICKA, A.**

(Received: 2 April 1993)

The steady laminar flow of a power-law fluid is considered, through a narrow space between two fixed surfaces of revolution, having a common axis of symmetry.

To solve this problem the boundary layer equations are used and expressed for the axially symmetric case in a curvilinear orthogonal coordinate system x, ϑ, y connected with one of the surfaces.

The method of integral approaches is used to solve the boundary layer equations.

As a result one obtains the formulae expressing such flow parameters as the velocity components v_x, v_y and the pressure p.

1. Introduction

The radial laminar flows of a viscous newtonian fluid through the narrow space between stationary parallel disks have been the object of theoretical /1, 2, 5/ and experimental studies /2, 3/.

A more general problem of the incompressible viscous flow through the space between surfaces of revolution is considered in /4, 6, 7/.

The problem of viscous Newtonian throughflow between stationary surfaces of revolution shapes of which are described by the functions satisfying any conditions for which similar solutions exist is solved in /4/. This throughflow is examined also in more general way in /6, 7/.

This paper deals with the steady laminer flow of a power-law (Ostwald--de Weale) fluid in the slot of small thickness between fixed curvilinear surfaces of revolution having a common axis of symmetry as shown in Fig. 1.

---

*Walicki, Edward, P-65016 Zielona Góra, ul. Szafrana 11a/7, Poland

**Walicka, Anna, P-65016 Zielona Góra, ul. Szafrana 11a/7, Poland

Akadémiai Kiadó, Budapest

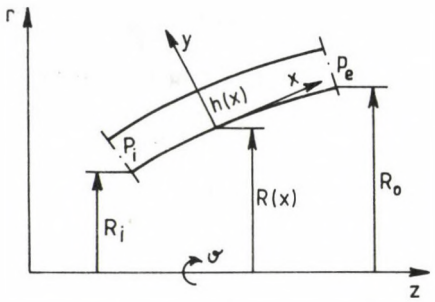

Fig. 1. Slot of small thickness between fixed surfaces of revolution

Basing on the method of integral approaches as in /8/ we have analysed the influence of inertia terms on the pressure distribution in the slot.

2. Basic equations

Let the inner surface be described by function $R = R(x)$ which denotes the radius of this surface. The thickness of the slot is described by function $h = h(x)$ which denotes the distance between the curvilinear surfaces measured along a normal to the inner surface.

An intrinsic curvilinear orthogonal coordinate system x, ϑ, y linked with the inner surface is shown in Fig. 1.

The physical parameters of the flow are the velocity components v_x, v_y and pressure p.

With regard to the axial symmetry of the flow, these parameters are not dependent on the angle ϑ.

The assumption typical for the flow in a narrow space that:

$$h(x) \ll R(x)$$

can be used to make order-of-magnitude arguments in the equations governing the steady flow a power-law fluid. If some asymptotic transformations are made, the same as in /4, 6, 7/, these equations can be reduced to the simpler form:

$$\rho\left(v_x \frac{\partial v_x}{\partial x} + v_y \frac{\partial v_x}{\partial y}\right) = -\frac{\partial p}{\partial x} + \mu \frac{\partial}{\partial y}\left(\left|\frac{\partial v_x}{\partial y}\right|^{n-1} \frac{\partial v_x}{\partial y}\right), \tag{2.1}$$

$$\frac{\partial p}{\partial y} = 0, \tag{2.2}$$

$$\frac{1}{R}\frac{\partial (Rv_x)}{\partial x} + \frac{\partial v_y}{\partial y} = 0. \tag{2.3}$$

The order-of-magnitude arguments shows that

$$p(x,y) = p(x). \tag{2.4}$$

The boundary conditions for the velocity components v_x and v_y are the usual non-slip conditions stated as follows:

$$\begin{aligned} &v_x(x,0) = 0, \qquad v_y(x,0) = 0, \\ &v_x(x,h) = 0, \qquad v_y(x,h) = 0. \end{aligned} \tag{2.5}$$

The boundary conditions for the pressure are:

$$p(x_i) = p_i, \qquad p(x_o) = p_o; \tag{2.6}$$

here x_i — the inlet co-ordinate and
x_o — the outlet co-ordinate.

We will use Eqs (2.1)—(2.3) to investigate the flow field in the slot by the method of integral approaches. Its concept consists in calculating first the solution of Eqs (2.1)—(2.3) in the Reynolds' approximation (without the inertia terms) and then in solving the complete set (with the inertia terms) by using the obtained approximation.

3. Reynolds' approximation

To find the Reynolds' approximation we replace Eq. (2.1) by the equation:

$$\mu \frac{\partial}{\partial y}\left(\left| \frac{\partial v_x}{\partial y} \right|^{n-1} \frac{\partial v_x}{\partial y} \right) = \frac{dp}{dx}; \tag{3.1}$$

here the expression (2.4) was taken into account.

Integrating this equation we get:

$$v_x = \frac{n}{n+1}\left(-\frac{1}{\mu}\frac{dp}{dx}\right)^{\frac{1}{n}}\left[\left(\frac{h}{2}\right)^{1+\frac{1}{n}} - \left|\frac{h}{2} - y\right|^{1+\frac{1}{n}}\right]. \tag{3.2}$$

The flow rate Q is defined as:

$$Q = 2\pi R \int_0^h v_x \, dy$$

and after calculation

$$Q = 2^{-\frac{1}{n}} \pi R h^{2+\frac{1}{n}} \left(\frac{n}{2n+1}\right)\left(-\frac{1}{\mu}\frac{dp}{dx}\right)^{\frac{1}{n}}. \tag{3.3}$$

Applying this formula in Eq. (3.2), we have:

$$v_x = \frac{2^{\frac{1}{n}} Q}{\pi}\left(\frac{2n+1}{n+1}\right)\frac{1}{R\, h^{2+\frac{1}{n}}}\left[\left(\frac{h}{2}\right)^{1+\frac{1}{n}} - \left|\frac{h}{2} - y\right|^{1+\frac{1}{n}}\right], \tag{3.4}$$

and from the continuity equation (2.3) we obtain

$$v_y = \frac{2^{\frac{1}{n}} Q}{\pi}\left(\frac{2n+1}{n+1}\right)\frac{yh'}{R\, h^{3+\frac{1}{n}}}\left[\left(\frac{h}{2}\right)^{1+\frac{1}{n}} - \left|\frac{h}{2} - y\right|^{1+\frac{1}{n}}\right]; \tag{3.5}$$

the prime denotes the derivation with respect to x.

To define the pressure distribution let us turn to the expression (3.3). After simple modification we have the following differential equation for pressure:

$$\frac{dp}{dx} = -\frac{2\mu Q^n}{\pi^n}\left(\frac{2n+1}{n}\right)^n \frac{1}{R^n h^{2n+1}}. \tag{3.6}$$

Integrating Eq. (3.6) and applying the boundary conditions (2.6) we get:

$$p = p_i - \frac{2\mu Q^n}{\pi^n}\left(\frac{2n+1}{n}\right)^n \left[A^{(n)}(x) - A_i^{(n)}\right] \tag{3.7a}$$

or

$$p = p_o - \frac{2\mu Q^n}{\pi^n}\left(\frac{2n+1}{n}\right)^n \left[A^{(n)}(x) - A_o^{(n)}\right] \tag{3.7b}$$

where

$$A^{(n)}(x) = \int \frac{dx}{R^n h^{2n+1}}, \qquad A_i^{(n)} = A^{(n)}(x_i). \qquad A_o^{(n)} = A^{(n)}(x_o). \tag{3.8}$$

By subtracting the formulae (3.7) we obtain the relation for the pressure drop in the slot for Reynolds' approximation:

$$\Delta p_r = p_i - p_o = -\frac{2\mu Q^n}{\pi^n}\left(\frac{2n+1}{n}\right)^n \left(A_i^{(n)} - A_o^{(n)}\right). \tag{3.9}$$

4. Integral approaches

To analyse the influence of inertia terms of Eq. (2.1) on the pressure distribution in the slot we rearrange it to simplify its integration.

For this purpose we multiply equation (2.1) by v_x^k, and the equation of continuity (2.3) by $(\rho v_x^{k+1})/(k+1)$ and add the obtained expressions. As a result we have:

$$\frac{\rho}{k+1}\left[\left(\frac{R'}{R} + \frac{\partial}{\partial x}\right) v_x^{k+2} + \frac{\partial}{\partial y}\left(v_x^{k+1} v_y\right)\right] = -v_x^k \frac{dp}{dx} + \mu n\, v_x^k \left|\frac{\partial v_x}{\partial y}\right|^{n-1} \frac{\partial^2 v_x}{\partial y^2}, \tag{4.1}$$

the prime denotes the differentiation with respect to x.

Integrating this equation across the slot thickness and taking into account boundary conditions (2.5) we obtain the following relation:

$$\frac{\rho}{k+1}\left(\frac{R'}{R} + \frac{\partial}{\partial x}\right) \int_0^h v_x^{k+2} dy = -\frac{dp}{dx} \int_0^h v_x^k dy + \mu n \int_0^h v_x^k \left|\frac{\partial v_x}{\partial y}\right|^{n-1} \frac{\partial^2 v_x}{\partial y^2} dy. \tag{4.2}$$

Introducing auxiliary notations

$$I_{k-2}^{(1)} = \int_0^h v_x^k \left|\frac{\partial v_x}{\partial y}\right|^{n-1} \frac{\partial^2 v_x}{\partial y^2} dy,$$

$$I_k^{(2)} = \int_0^h v_x^k dy, \qquad I_{k+2}^{(3)} = \int_0^h v_x^{k+2} dy \tag{4.3}$$

we can write

$$\frac{\rho}{k+1}\left(\frac{R'}{R}+\frac{\partial}{\partial x}\right) I_{k+2}^{(3)} = - I_k^{(2)} \frac{dp}{dx} + \mu n I_{k-2}^{(1)}. \tag{4.4}$$

Thence we have:

$$\frac{dp}{dx} = \mu n \frac{I_{k-2}^{(1)}}{I_k^{(2)}} - \frac{\partial}{k+1} \frac{\left(\frac{R'}{R}+\frac{\partial}{\partial x}\right) I_{k+2}^{(3)}}{I_k^{(2)}}. \tag{4.5}$$

To evaluate the pressure distribution effectively we must calculate the integralt $I_{k-2}^{(1)}$, $I_k^{(2)}$, $I_{k+2}^{(3)}$.

Taking into account the velocity component v_x defined by Eq. (3.4) and assuming for calculation the following values of k:

$$k = 0 \qquad \text{and} \qquad k = 1$$

one obtains — after integrating Eq. (4.5) — the following formulae for the pressure distribution:

$$p = p_i - \frac{2\mu Q^n}{\pi^n}\left(\frac{2n+1}{n}\right)^n \left[A^{(n)}(x) - A_i^{(n)}\right] - \frac{C_k^{(n)} \rho Q^2}{\pi^2}\left[B(x) - B_i\right] \tag{4.6a}$$

or

$$p = p_o - \frac{2\mu Q^n}{n}\left(\frac{2n+1}{n}\right)^n \left[A^{(n)}(x) - A_o^{(n)}\right] - \frac{C_k^{(n)} \rho Q^2}{\pi^2}\left[B(x) - B_o\right] \tag{4.6b}$$

where

$$B(x) = \frac{1}{(Rh)^2}, \qquad B_i = B(x_i), \qquad B_o = B(x_o);$$

k	0	1
$C_k^{(n)}$	$\frac{1}{4}\left(\frac{2n+1}{3n+2}\right)$	$\frac{3}{4}\frac{(2n+1)^2}{(3n+2)(4n+3)}$

(4.7)

By subtracting the formulae (4.6) we get the relation for the pressure drop in the slot as follows:

$$\Delta p = p_i - p_o = - \frac{2\mu Q^n}{\pi^n}\left(\frac{2n+1}{n}\right)^n \left(A_i^{(n)} - A_o^{(n)}\right) - \frac{C_k^{(n)} \rho Q^2}{\pi^2}(B_i - B_o). \tag{4.8}$$

For n = 1 all above formulae reduce to those obtained in /8/ for the newtonian flow.

5. Examples of applications

5.1. Nondimensional form of the solution

Equations (3.4), (3.5) and (4.6) may be nondimensionalized by using the following parameters:

$$\tilde{x} = \frac{x}{R_o}, \qquad \tilde{R} = \frac{R}{R_o}, \qquad \tilde{h} = \frac{h}{h_o}, \qquad \eta = \frac{y}{h},$$

$$\tilde{v}_x = \frac{v_x}{V_o}, \qquad \tilde{v}_y = \frac{v_y}{V_o}\frac{R_o}{h_o}, \qquad \tilde{p} = \frac{(p - p_o)\,\rho\, h_o^{4n} Q^{2-2n}}{\mu^2 (2\pi)^{2-2n} R_o^{4-2n}}, \tag{5.1}$$

$$\tilde{A}^{(n)}(\tilde{x}) = A^{(n)}(x)\, R_o^{n-1} h_o^{2n+1}, \qquad \tilde{B}(\tilde{x}) = B(x)(R_o h_o)^2,$$

$$R_\lambda = \left(\frac{h_o}{R_o}\right) Re, \qquad R_e = \frac{\rho V_o^{2-n} h_o^n}{\mu},$$

where V_o is the averaged velocity in the outlet cross-section of the slot defined as:

$$V_o = \frac{Q}{2\pi}\frac{1}{R_o h_o},$$

Re and R_λ are, respectively, the Reynolds and the modified Reynolds numbers.

The nondimensional formulation assumes then the form:

$$\tilde{v}_x = 2^{1+\frac{1}{n}} \left(\frac{2n+1}{n+1}\right) \frac{1}{\tilde{R}\,\tilde{h}} \left[\left(\frac{1}{2}\right)^{1+\frac{1}{n}} - \left|\frac{1}{2} - \eta\right|^{1+\frac{1}{n}}\right], \tag{5.2}$$

$$\tilde{v}_y = 2^{1+\frac{1}{n}} \left(\frac{2n+1}{n+1}\right) \frac{\tilde{h}'\eta}{\tilde{R}\,\tilde{h}} \left[\left(\frac{1}{2}\right)^{1+\frac{1}{n}} - \left|\frac{1}{2} - \eta\right|^{1+\frac{1}{n}}\right], \tag{5.3}$$

$$\tilde{p} = -\, 2^{n+1} \left(\frac{2n+1}{n}\right)^n R_\lambda \left[\tilde{A}^{(n)}(\tilde{x}) - \tilde{A}_o^{(n)}\right] - 4\, C_k^{(n)} R_\lambda^2 \left[\tilde{B}(\tilde{x}) - 1\right]. \tag{5.4}$$

5.2. Throughflow between the conical parallel surfaces

For the conical parallel surfaces shown in Fig. 2 the geometric relations are given as:

$$R = x \sin\alpha, \qquad R_i = x_i \sin\alpha, \qquad R_o = x_o \sin\alpha, \qquad h = \text{const.}$$

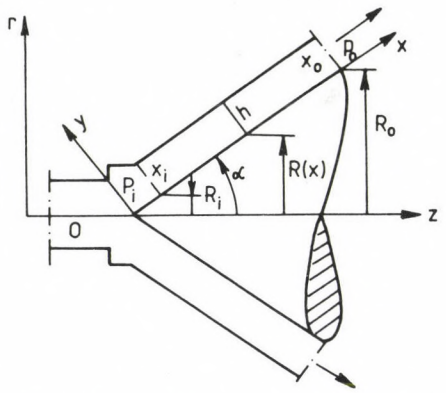

Fig. 2. Slot between conical parallel surfaces

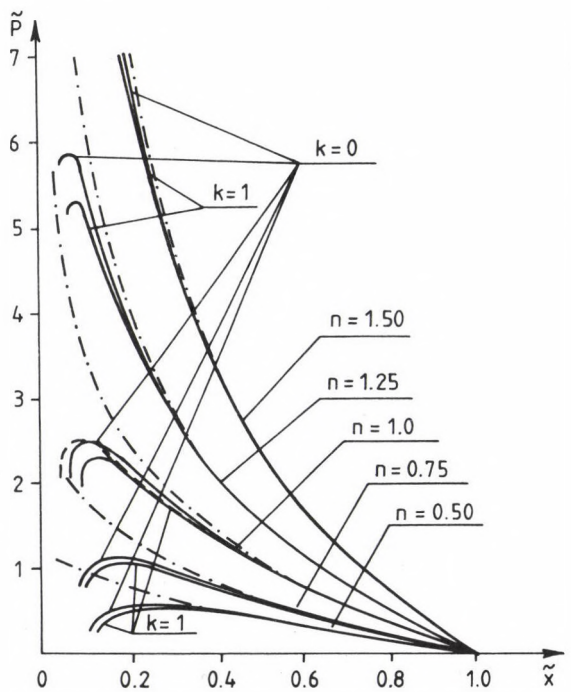

Fig. 3. Dimensionless pressure distributions for the flow between parallel disks for the value of $R_\lambda = 0.12$

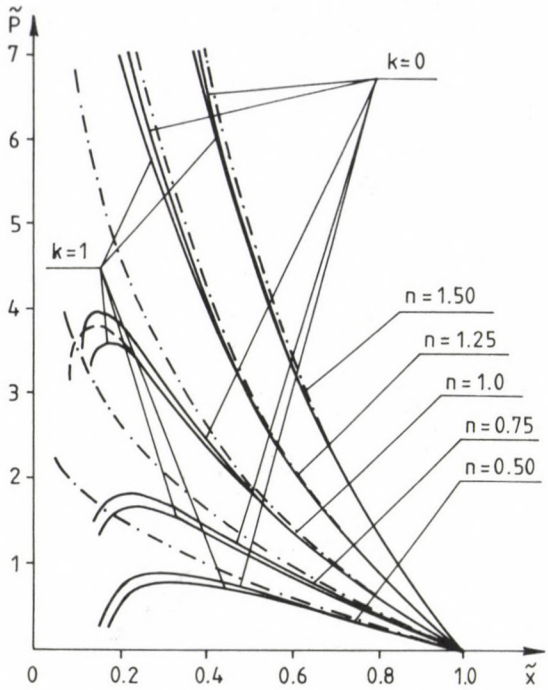

Fig. 4. Dimensionless pressure distributions for the flow between parallel disks for the value of $R_\lambda = 0.24$

The nondimensional quantities are:

$$\tilde{R} = \tilde{x} \sin \alpha, \qquad \tilde{R}_o = 1, \qquad \tilde{h} = 1$$

and the nondimensional formulation assumes the form:

$$\tilde{v}_x = 2^{1+\frac{1}{n}} \left(\frac{2n+1}{n+1}\right) \frac{1}{\tilde{x} \sin\alpha} \left[\left(\frac{1}{2}\right)^{1+\frac{1}{n}} - \left|\frac{1}{2} - \eta\right|^{1+\frac{1}{n}}\right], \tag{5.5}$$

$$\tilde{v}_y = 0, \tag{5.6}$$

$$\tilde{p} = -2^{n+1} \left(\frac{2n+1}{n}\right)^n \frac{R_\lambda}{(1-n)\sin^n\alpha} \left|x^{1-n} - x_o^{1-n}\right| - 4C_k^{(n)} R_\lambda^2 \left(\frac{1}{\tilde{x}^2 \sin^2\alpha} - 1\right). \tag{5.7}$$

Figures 3--5 show the pressure distributions between parallel disks ($\alpha = 90^o$) for three values of the Reynolds number:

$$R_\lambda = 0.12; \qquad 0.24; \qquad 0.6$$

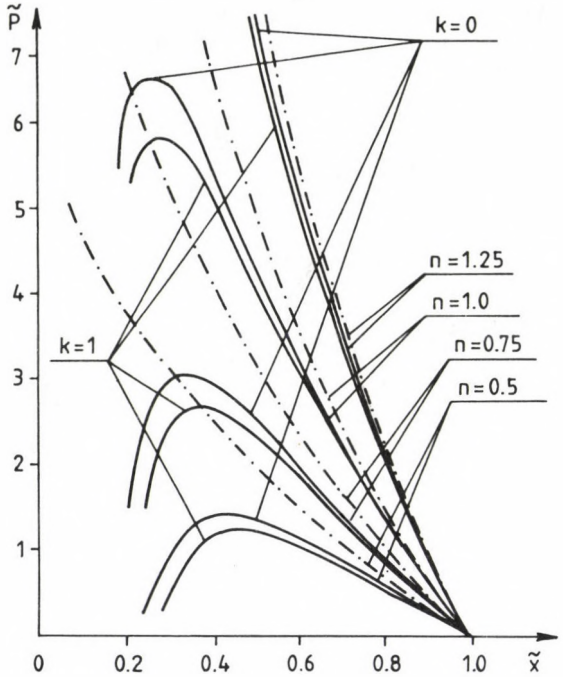

Fig. 5. Dimensionless pressure distributions for the flow between parallel disks for the value of $R_\lambda = 0.6$

for power-law fluid defined by the following values of n:

$$n = 0.5; \quad 0.75; \quad 1.25; \quad 1.5$$

and for Newtonian fluid (n = 1).

The broken "dash-dot" lines present the pressure distributions for Reynolds' approximation obtained from the formula:

$$\tilde{p} = -2^{n+1} \left(\frac{2n+1}{n} \right)^n \frac{R_\lambda}{1-n} \left(\tilde{x}^{1-n} - 1 \right). \tag{5.8}$$

For the Newtonian flow the formula for the pressure distribution in Reynolds approximation has the form:

$$\tilde{p} = -12\, R_\lambda \ln \tilde{x}. \tag{5.9}$$

The dashed lines present the results of experiments given by Chen /3/ for the Newtonian flow.

5.3. Throughflow between concentric spherical surfaces

For the concentric spherical surfaces shown in Fig. 6, the geometric relations are given as:

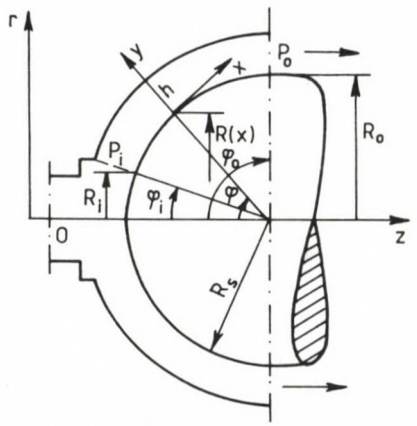

Fig. 6. Slot between concentric spherical surfaces

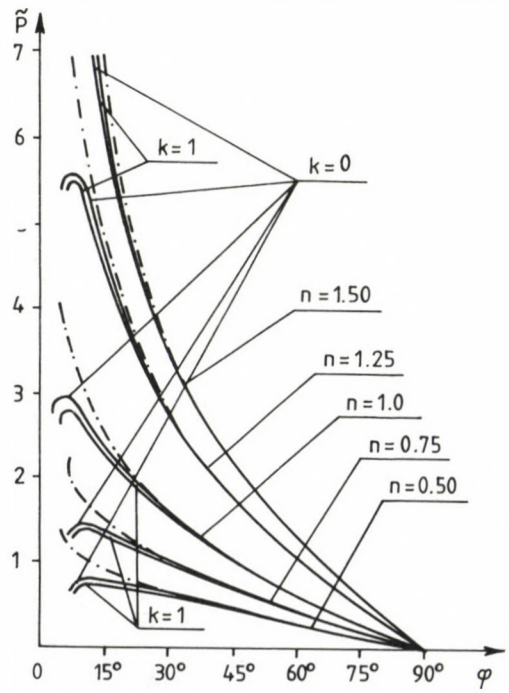

Fig. 7. Dimensionless pressure distributions for the flow between concentric spherical surfaces for the value of $R_\lambda = 0.1$

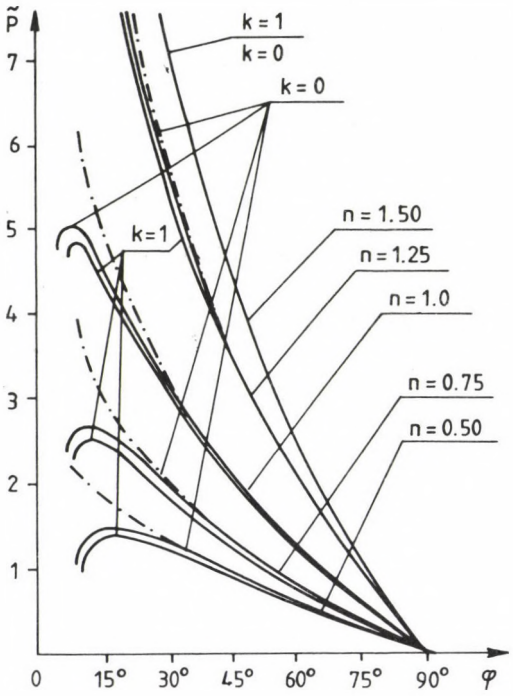

Fig. 8. Dimensionless pressure distributions for the flow between concentric spherical surfaces for the value of $R_\lambda = 0.2$

$$R = R_s \sin\phi, \qquad \phi = \frac{x}{R_s}, \qquad R_i = R_s \sin\phi_i,$$

$$R_o = R_s \sin\phi_o, \qquad h = \text{const.}$$

The nondimensional quantities are (for $\phi_o = 90^o$):

$$\tilde{R} = \sin\phi, \qquad \tilde{R}_o = 1, \qquad \tilde{x} = \phi, \qquad \tilde{h} = 1$$

and the nondimensional formulation is given as:

$$\tilde{v}_x = 2^{1+\frac{1}{n}} \left(\frac{2n+1}{n+1}\right) \frac{1}{\sin\phi} \left[\left(\frac{1}{2}\right)^{1+\frac{1}{n}} - \left|\frac{1}{2} - \eta\right|^{1+\frac{1}{n}}\right], \tag{5.10}$$

$$\tilde{v}_y = 0, \tag{5.11}$$

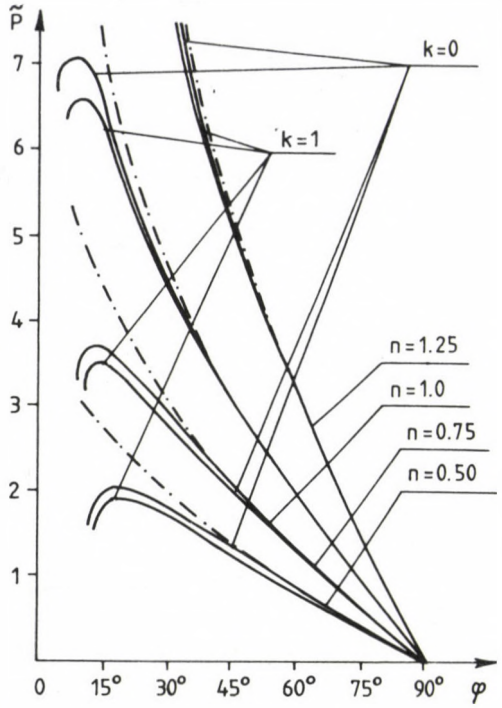

Fig. 9. Dimensionless pressure distributions for the flow between concentric spherical surfaces for the value of $R_\lambda = 0.3$

$$\tilde{p} = -2^{n+1}\left(\frac{2n+1}{n}\right)^n R_\lambda\left[I^{(n)}(\phi) - I^{(n)}(90^o)\right] - 4C_k^{(n)} R_\lambda^2\left(\frac{1}{\sin^2\phi} - 1\right), \qquad (5.12)$$

where:

$$I^{(n)}(\phi) = \int \frac{d\phi}{\sin^n\phi}. \qquad (5.13)$$

Figures 7—9 show the pressure distributions for three values of the Reynolds number:

$$R_\lambda = 0.1; \quad 0.2; \quad 0.3$$

for power-law fluid defined by the following values of n:

$$n = 0.5; \quad 0.75; \quad 1.25; \quad 1.5$$

and for newtonian fluid (n = 1).

The "dash-dot" lines present the pressure distributions for Reynolds approximation obtained from the formula:

$$\tilde{p} = -2^{n+1} \left(\frac{2n+1}{n} \right)^n R_\lambda \left[I^{(n)}(\phi) - I^{(n)}(90^0) \right]. \tag{5.14}$$

For the Newtonian flow the formula for the pressure distribution in Reynolds' approximation has the form:

$$\tilde{p} = -12 R_\lambda \ln \operatorname{tg} \frac{\phi}{2} . \tag{5.15}$$

6. Conclusions

Application of the method of integral approaches to the study of the power-law fluid flow between the surfaces of revolution yields the formulae for the velocity components v_x, v_y and pressure p.

A comparison formulae of this paper for Newtonian flow (n = 1) with those obtained by another method presented in /7/ shows that the velocity components v_x and v_y given by the method used here defined the flow field approximately, the influence of the inertia terms of the momentum equation being disregarded.

The formulae for pressure distributions include the effect of inertia terms. The pressure depends on the modified Reynolds number R and it increases with the magnitude of this number.

A comparison of the pressure distribution made for the special case of the Newtonian flow (n = 1) between parallel disks with the experimental data of Chen /3/ indicates a satisfactory agreement between the theoretical and experimental data.

In conclusion it may be remarked that the approach for k = 1 (energy integral approach) gives the formulae leading to sufficiently accurate values of the pressure distribution in the flow configuration considered. The results obtained by this approximation are better than those obtained for k = 0 for the special case of the flow between parallel disks. It seems that this remark is also true for all the flows of power-law fluids for $n \leqslant 1$.

From Figs 7—9, it is seen that in flows of power-law fluids for $n > 1$ in the slot between surfaces with curvilinear generating lines the pressure distribution can be calculating by using the formulae without the inertia effects, i.e. the formulae for the Reynolds' approximation.

REFERENCES

1. Savage, S.B.: Laminar radial flow between parallel plates. J. Applied. Mech., Trans. ASME, Ser E, Vol. 31, No. 4 (1964), 594—596

2. Peube, J.L. - Che-Pen Chen: Sur l'écoulement radial divergent d'un fluide visqueux incompressible entre deux plans paralleles. C.R. Acad. Sci., Paris, t. 258 (1964), 353—355

3. Che-Pen Chen: Contribution a l'étude expérimentale de l'écoulement radial d'un fluide visqueux incompressible entre deux disques paralleles. J. Mécanique, Vol. 5, No. 2 (1966), 245—259

4. McAlister, K.W., Rice, W.: Flows between stationary surfaces of revolution, having similarity solutions. J. Appl. Mech., Trans. ASME, Ser. E, Vol. 39, No. 2 (1972), 345—350

5. Patrat, J.C.: Contribution a l'étude des pressions dans un écoulement radial divergent. J. Mécanique, Vol. 14, No. 3 (1975), 505—522

6. Walicki, E.: Viscous flow through the clearance between two fixed surfaces of revolution. Archiwum Budowy Maszyn, Vol. 25, No. 2 (1978), 429—436

7. Walicka, A.: Accurate and asymptotic solution of simplified sets of equations describing the motion of viscous fluids in a slot bounded by two co-axial surfaces of revolution. WN-T, Warszawa 1989

8. Walicka, A.: Integral approaches for viscous flow in a slot between fixed surfaces of revolution. UN WSJ Zielona Góra, Mechanika, No. 18 (1993), 123—135

PRINTED IN HUNGARY

Akadémiai Kiadó és Nyomda Vállalat, Budapest

ACTA TECHNICA

Volume 105 Nos 1—4

CONTENTS

BOOK REVIEW

NOTICE TO CONTRIBUTORS

Papers in English* are accepted on condition that they have not been previously published or accepted for publication.

Manuscripts in two copies (the original type-written copy plus a clear duplicate one) complete with figures, tables, and references should be sent to

Acta Technica
Nádor u. 7. I. 118
Budapest, Hungary
H-1051

Although every effort will be made to guard against loss, it is advised that authors retain copies of all material which they submit. The editorial board reserves the right to make editorial changes.

Manuscripts should be typed double-spaced on one side of good quality paper with proper margins and bear the title of the paper and the name(s) of the author(s). The full postal address(es) of the author(s) should be given in a footnote on the first page. An abstract of 50 to 100 words should precede the text of the paper. The approximate locations of the tables and figures should be indicated in the margin. An additional copy of the abstract is needed. Russian words and names should be transliterated into English.

References. Only papers closely related to the author's work should be referred to. The citations should include the name of the author and/or the reference number in brackets. A list of numbered references should follow the end of the manuscript.

References to periodicals should mention: (1) name(s) and initial(s) of the author(s); (2) title of the paper; (3) name of the periodical; (4) volume; (5) year of publication in parentheses; (6) numbers of the first and last pages. Thus: 5. Winokur, A.—Gluck, J.: Ultimate strength analysis of coupled shear walls. American Concrete Institute Journal 65 (1968) 1029-1035

References to books should include: (1) author(s)' name; (2) title; (3) publisher; (4) place and year of publication. Thus: Timoshenko, S.—Gere, J.: Theory of Elastic Stability. McGraw-Hill Company. New York, London 1961

Illustrations should be selected carefully and only up to the necessary quantity. Black-and-white photographs should be in the form of glossy prints. The author's name and the title of the paper together with the serial number of the figure should be written on the back of each print. Legends should be brief and attached on a separate sheet. Tables, each bearing a title, should be self-explanatory and numbered consecutively.

Authors will receive proofs which must be sent back by return mail.

Authors will receive 50 reprints free of charge.

* Hungarian authors can also submit their papers in Hungarian.

HU ISSN 0865-8927